Converting Biomass Feedstocks through Heterogeneous Catalysis: How Compressed Liquid Water Influences Catalytic Activity and Stability

by

Alex Roger Maag

A Dissertation

Submitted to the Faculty of

Worcester Polytechnic Institute

In partial fulfillment of the requirements for the

Degree of Doctor of Philosophy

in

Chemical Engineering

by

_____

April 2019

APPROVED

<table>
<tr><td>_____
Dr. Michael Timko, Advisor
Chemical Engineering Department, WPI</td><td>_____
Dr. Jamal Yagoobi, Committee Member
Mechanical Engineering Department, WPI</td></tr>
<tr><td>_____
Dr. Ravindra Datta, Committee Member
Chemical Engineering Department, WPI</td><td>_____
Dr. Anthony Dixon, Committee Member
Chemical Engineering Department, WPI</td></tr>
<tr><td>_____
Dr. Andrew Teixeira, Committee Member
Chemical Engineering Department, WPI</td><td>_____
Dr. Susan Roberts, Head of Department
Chemical Engineering Department, WPI</td></tr>
</table>

Abstract

Recent technological advances in process intensity and energy efficiency has motivated the use of biomass as a source of sustainable energy. Thermochemical reactions operated in a compressed liquid phase have many process engineering benefits compared to traditional vapor phase reactions, including reduced energy intensive drying steps, reaction intensification and improved thermal management. These process engineering benefits under compressed liquid phase conditions are the greatest for organics diluted in water, such as those derived from biological reactant feedstocks. However, there is a relative lack of thermochemical reactions are operated in a compressed liquid phase when compared to the number of commercial vapor phase processes, and similarly, there are fewer studies evaluating how changing the thermodynamic state of liquid water solvent can influence catalytic reactivity and stability.

Hydrothermal liquefaction (HTL) is one process studied which operates in a compressed liquid phase at 300 °C and 20.7 MPa; capable of breaking down food waste into carbon rich bio-oil, bio-char and residual aqueous phases. Bio-oil can be refined into transportation fuels, but organics partitioned into the HTL water phase reduce oil recovery and require costly water purification steps. Therefore, it is desirable to reduce water-soluble organic HTL products by catalytically shifting the product distribution into the oil phase. Using a heterogeneous metal oxide catalyst, $CeZrO_x$, water-soluble organics were promoted through aldol coupling reactions that increase product molecular weight and hydrophobicity; thereby partitioning HTL oil yields and reducing water-soluble hydrocarbons.

A challenge in developing compressed thermochemical processing of biomass, particularly when feeds are diluted in an aqueous phase, is the limited number of heterogeneous catalysts known to be hydrothermally stable. Zeolites are a class of catalysts with recent interest as a catalyst

for a variety of compressed thermochemical processing technologies. However, many zeolites are prone to framework degradation under aqueous phase conditions at temperatures <200 °C. We evaluate the hydrothermal stability of the ZSM-5 under dense, sub- and supercritical water conditions for 3 hours over a wide treatment times and temperatures ranging from 250 to 450 °C at 25 MPa. Characterization using X-ray diffraction (XRD), electron microscopy, and N_2 sorption indicated that the MFI framework was stable at temperatures ≤ 200 °C and 24MPa pressures for up to 500 hrs, in contrast to many other previously studied frameworks. A non-Arrhenius framework degradation rate observed near water's critical point was consistent with the temperature-dependence of water auto-ionization, as the maximum rate was found to be coincident with co-optimization of thermal and OH– promotion effects. In contrast to the unique framework stability of ZSM-5, acid site densities decreased monotonically with increasing treatment temperature, with treatment at the most extreme conditions (450 °C) leading to >90% decrease in the Brønsted acid site density.

The unique hydrothermal framework stability of ZSM-5 provided an opportunity to deconvolute the role of water on catalytic activity and stability by evaluating the activity of ethanol dehydration to form ethylene under both high and low conversion conditions. Liquid phase ethanol dehydration operated at 375 °C and 24 MPa and high conversion conditions had a 50% loss in ZSM-5 catalytic activity when compared to an analogous vapor phase operation. Zeolite characterization reveals a retained zeolite framework and similar amount of hard coke formation, but a loss in Brønsted acid sites after liquid phase operation, which may contribute to the loss in catalytic activity. When ethanol dehydration is performed under low conversion conditions with an initial water loading in the feed, there is an increase in vapor phase activity but a decrease in the liquid activity. Under all low conversion reaction conditions, the framework loss, acid site loss

and extent of coking was minimal, suggesting that water plays an active role in the intrinsic ethanol dehydration activity. Competitive adsorption Langmuir model verifies a decrease amount of ethanol adsorption on an ideal surface with a compressed bulk liquid phase compared to a vapor phase, which indicates water will competitively adsorb and lower the amount of ethanol access to the active sites in a zeolite.

Acknowledgements

There are many people that have been a positive impact for me throughout my PhD experience. I am particularly grateful for the constant feedback and guidance that Professor Timko has provided me over the last six years. Professor Timko's generosity with his limited time and patience to clearly communicate new ideas has always provided me a good direction for my research and made for a successful graduate school experience. I am also thankful of my graduate committee (Professor Anthony Dixon, Professor Ravindra Datta, Professor Jamal Yagoobi, and Professor Andrew Teixeira) that has given positive comments and critiques in order to help direct of my research. In addition, Professor Geoff Tompsett has been a tremendous mentor and am grateful for the many hours spent training and supporting me throughout the graduate process. I would not have been able to perform the required experimental runs without the constant assistance provided by Doug White and Tom Partington in XRD training, creating custom parts, and assisting when instrumentation failures require fixing. I would like to thank the countless collaborators that have helped me characterize ZSM-5 zeolite after various treatments, including Professor Sisson and Li for SEM imaging and training, Professor Smith of Clark University for 27 Al NMR analysis, Professor Azimi at the University of Toronto for SEM and TEM imaging, Alexander Carl and Professor Grimm for XPS analysis, Professor Bond for acid site characterization.

In addition, I am grateful for the constant discussions and camaraderie with my fellow Timko labmates that made for a fun and productive research environment (Max Tyufekchiev, Avery Brown, Azadeh Zaker, Brendan McKeough, Zijian Ma, Yuanpu Wang, Patricia Guerra and Ziyang Zhang). I would like to thank all of the undergraduates that have assisted me in the research for this dissertation (Ibrahim Abu Muti, Ioodanis Kesisoglou, Nyoca Davis, Abdullah Almaymuni, Louis Ayisi, Deanna Poirier, Andersen DeRosier, and Jeremy Filteau). Lastly, I am particularly

grateful to my family, who have constantly supported me leading up to and throughout graduate school at WPI.

Contents

List of Figures

List of Tables

Chapter 1

Introduction

Recent technological advances in process intensity and energy efficiency has motivated the use of biomass as a sustainable energy source. Thermochemical processing of biomass under compressed liquid phase conditions can intensify biomass conversion reactions and improve its corresponding throughput. In addition, aqueous phase processing of wet biological feedstock can reduce process energy demands by minimizing the cost associated with drying. The process intensification benefits of compressed liquid phase operation are considered in Chapter 3. Improvements in liquid phase thermochemical processing opens up new routes to valorize waste streams such as disposed municipal food, pulp and paper sludge and agricultural residue; feedstocks with an inherently higher moisture content that limits gasification and pyrolysis technologies from being energy effective. Chapter 4 provides an example to convert model food waste into an energy dense bio-oil though hydrothermal liquefaction and improves the energy recovery of the process using a heterogeneous catalyst.

A challenge in converting biomass in a compressed aqueous phase is the limited number of known heterogeneous catalysts that are hydrothermally stable under hot liquid water conditions. Zeolites are a class of catalysts with recent interest as a catalyst for a variety of compressed thermochemical processing technologies. However, many zeolites are prone to framework degradation under aqueous phase conditions, even at temperatures less than about 200 °C.

Therefore, further work is required to understand zeolite stability and degradation mechanisms. Chapter 5 evaluates the hydrothermal stability of a commonly used zeolite, ZSM-5, under compressed liquid phase conditions. In particular, we were interested in understanding ZSM-5 decrystallization at temperatures greater than 250 °C and for exposure times longer than 6 hours (the most aggressive conditions reported in the literature). Many chemical reactions of interest require temperatures > 250 °C and industrially relevant catalyst materials must exhibit framework stability for thousands of hours to be economically viable. Chapter 6 extends the work in previous studies on ZSM-5 stability under hot liquid water conditions to industrial time scales and characterizes both framework and acid site stability

Water is known to act as both a solvent and reactant under many reaction conditions, which can either promote or inhibit the expected activity for many catalysts. Therefore, Chapter 7 assesses ethanol dehydration to form ethylene under compressed liquid phase operation. Ethanol dehydration is traditionally operated in the vapor phase and is highly active and selective using ZSM-5 zeolite. Ethanol dehydration reactions were performed in a continuous phase packed bed reactor catalyzed using ZSM-5 zeolite operated under both liquid and vapor phase (0.1 or 24 MPa), varying weight hourly space velocities (30 − 1200 hr^{-1}) and water loadings (0 − 33 wt%). Comparison of water's influence on catalytic reactivity in liquid compared to vapor phase condition is made. Characterization of ZSM-5 catalyst after reaction evaluates if the catalyst is hydrothermally stable under ethanol dehydration conditions.

Chapter 2

Background and Motivation

2.1 Biomass Conversion Processes

In order to reduce our reliance on crude oil, researchers are seeking alternative, green sources of energy from biological feedstocks such as pulp/paper sludge, food waste, corn stover, sugar cane and cellulosic biomass. Current and developing technologies convert a variety of bio-renewable feedstocks into liquid fuels and commodities through a combination of multiple enzymatic, catalytic, and/or thermochemical processes. The water content inherent within biomass feedstocks, which can range from 18 to 60% of the total weight, is a primary limiting factor preventing biomass conversion processes from becoming economically competitive with petrochemical technologies.[1] Processing wet biomass feedstocks can lead to dilute process streams that require significant processing energy to either dry, heat and/or separate the water from the reactant stream. Discovering novel strategies to handle feedstocks with a large water content has become a recent technological challenge. Bio-based processes are converting highly oxygenated compounds into products, which requires fundamentally different chemistries compared to the conversion of alkanes, paraffin waxes and aromatics typically performed for crude oil sources.

Current technologies overcome the high moisture content in highly oxygenated biomass feeds at different stages of the biomass-to-product process with varying degrees of success. Gasification and pyrolysis technologies initially dry a biomass feed prior to vapor phase processing. Both gasification and pyrolysis technologies require heating of biomass to relatively high temperatures but low residence times to break down and volatilize biomass into a syngas product consisting of methane, carbon monoxide, carbon dioxide and/or hydrogen.[2-4] Syngas can be catalytically condensed into a rich liquid fuel through Fischer Tropsch reaction.[4] Other technologies attempt to separate water from the product at the end of processing, such as biomass pretreatment, thermochemical or enzymatic hydrolysis and fermentation processes. Further economic benefits and limitations of each biomass conversion technology are briefly outlined below.

2.1.1 Gasification technologies

Gasification technologies convert biomass into a syngas mixture under high operating temperatures >350 °C.[5] The ratio of H_2, CO_2 and CO formed largely depends on the operating temperature selected; higher conversions are obtained at elevated temperatures but reduce the energy efficiency of the system.[5] A series of techno-economic analyse compared the economic efficiency of biomass-based processing technologies, defined as the total product cost relative to its energy content as a fuel.[6-9] The processes reviewed included a rational combination of multiple processes in series, which included gasification, pyrolysis, Fischer-Tropsch, enzymatic hydrolysis, and fermentation processes. Gasification technologies combined with a Fischer Tropsch reactor to form liquid fuels were reported to have the most complex processing system that required the greatest initial capital investment.[6] However, combined gasification and Fischer-Tropsch had the lowest operating costs with a sufficiently dry feed, but operating cost was

extremely sensitive to the biomass feedstock costs, which accounted for ~28% of the total operating cost for the process.[6] Therefore, the total efficiency of the system is dependent on the feedstock of choice and its corresponding initial moisture content.

2.1.2 Pyrolysis Technologies

Pyrolysis reactions create either a liquid or a gas product by breaking down organic matter at elevated temperatures in an inert atmosphere. There are several modes of pyrolysis, which include fast, intermediate and slow pyrolysis that create varying fractions of solid, liquid and gas products. Of these, fast pyrolysis processes have been currently commercialized, which requires rapid heating in an inert environment to operating temperatures between 400−600 °C to form a liquid bio-oil product.[10, 11] The pyrolysis bio-oil product is typically acidic with a low heating value, which can cause steel tubing corrosion and significant hydro-treatment costs to upgrade the oil.[12] Analysis by Anex et al.[6] found fast pyrolysis technologies to have the best processing efficiency compared to gasification or enzymatic routes, based on the product energy value. While the economics does account for the lower heating value for pyrolysis oils, it does not account for downstream hydrotreating and hydrocracking costs associated with upgrading the pyrolysis oil. In addition, a NREL report that evaluated pyrolysis processes notes that drying of the feed is essential, and a 7% moisture upper limit has been recommended to maintain high yields and low heating costs.[12] NREL further estimates the required drying energy for biomass to be 3.6 MJ/kg of moisture evaporated, making excessively wet biomass feeds such as municipal food waste not energy efficient for pyrolysis use.[12] McNamare et al.[13] estimated that the available energy in pyrolysis oil is insufficient to offset the energy required for drying at solid loading lower than 25%. Although several studies present pyrolysis as a promising technology for converting waste streams, a review paper by Rollinson et al.[14] presents a more critical analysis of these techno-economic

studies. Rollinson et al.[14] determined that most energy balances make unreasonable assumptions on drying energy costs, heat losses and/or auxiliary energy costs required for a plant, and concludes that the use of economic pyrolysis technologies is more limited in scope.

2.1.3 Liquid-phase Biochemical and Thermochemical Processes

Another route to forming platform chemicals is through liquid phase processing using pretreatment, hydrolysis and fermentation systems. The initial pretreatment step breaks down the cell walls of biomass treatment to form a slurry of carbohydrates for further processing. Common pretreatments include dilute acid, steam explosion, hot water and ammonia recycle percolation; processes that have operating temperature ranging between 160 – 290 °C and reaction times ranging between 1 – 30 min under acidic or basic conditions.[4] After pretreatment, a hydrolysis process breaks down biomass carbohydrates to create a mixture of soluble sugars.[15] The broken down biomass sugars are then fed into batch fermentation reactors to form a variety of alcohols, organic acids, hydrogen or methane species.[15] This process are operated at lower temperatures than pyrolysis and gasification but requires longer residence times.[4] The paper by Anex et al.[6] compared the techno economic analysis of a combined enzymatic hydrolysis and fermentation process to a gasification and pyrolysis process. The enzymatic route had the highest cost per energy content, but this was largely due to the high cost for enzymes. In addition, the analysis by Anex et al.[6] used corn stover with 25% of the weight including water for the biochemical route, while the gasification and pyrolysis routes did not assume a moisture content in their pathways.

In addition to using woody biomass, a significant amount of research has looked into thermochemical routes to convert feedstocks with a higher moisture content, such as food waste or microalgae.[11] Approximately 15 million dry tons of food waste is produced annually in the United States (USA), and 92% of this waste is disposed of in landfills where it decomposes to

produce greenhouse gases and water pollution. Hydrothermal liquefaction (HTL) is an attractive technology capable of converting a broad range of organic compounds, especially those with substantial water content, into energy products.[16] The HTL process converts a ~15 wt% organic slurry at operating temperatures ranging 280 – 375 °C and elevated pressures ranging between 10 – 25 MPa, forming a bio-oil precursor that can be further upgraded to transportation fuels and an aqueous phase containing water-soluble organic impurities.[11] Analysis by Akhtar et al.[17] reviewed several HTL parameters that influence bio-oil yields, including temperature, type of feedstocks, solvent density, pH and residence time. Temperature and solvent type were primary parameters that influenced the HTL activity, with water being the cheapest and most readily available and optimum oil yields at an operating temperature ~250 − 300 °C. Also, the use of homogeneous and heterogeneous catalysts for limiting coke formation or upgrading water-soluble organics has received recent interest.[18]

Despite recent interest and potential benefits of liquid phase operation, the vast majority of data are from studies performed in the vapor phase.[19, 20] There has been a renewed interest in the last decade for non-enzymatic aqueous phase processing of biomass, which can eliminate the initial costs associated with drying the feedstocks by using the water as a solvent. In order to create economical thermochemical processing technologies in a compressed liquid phase, a fundamental understanding of water's role as both a solvent, reactant or in catalyst deactivation is necessary, particularly for organics mixtures with water fractions greater than 25%.

2.2 Thermodynamic Properties of Water

Water has unique thermophysical properties that depend on both temperature and pressure. For example, the ionic product and dielectric constant of liquid water change dramatically as the

temperature increases from room temperature to its critical point.[21, 22] **Figure 2.1** plots the temperature dependence of water's ionic product, extracted from Bandura et al.[21], and dielectric constant extracted from Marrone et al.[23]. **Figure 2.1** shows that at temperatures less than the critical point of water (374 °C), the ionic product increases monotonically with increasing temperature and takes values more than 1,000 times greater than observed at ambient conditions. The ionic product decreases sharply at temperatures greater than water's critical point, reaching values lower than ambient water at temperatures greater than 420 °C. The changing ionic product and dielectric constant properties of liquid phase water can influence molecular reactivity, often leading to unexpected and highly non-Arrhenius behavior especially for reactions involving ionic reaction steps or highly polar transition states.[24-27]
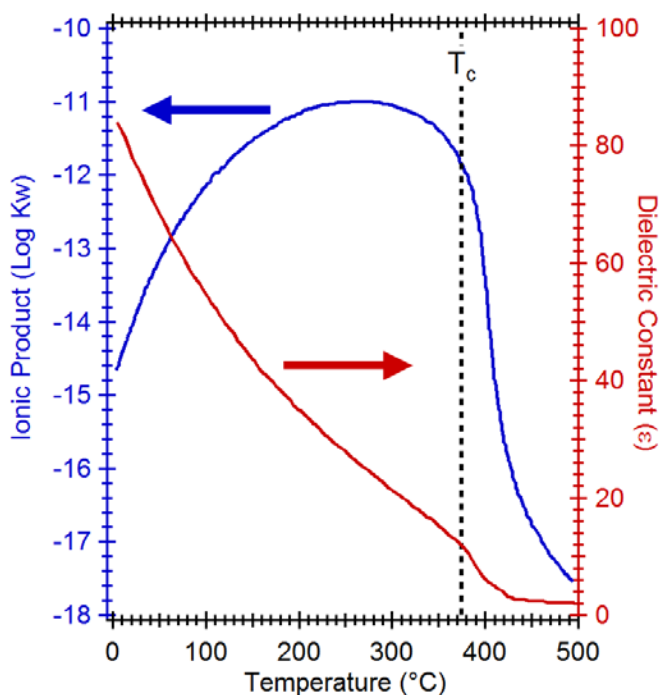
Figure 2.1: Plot ionic product and dielectric constant of water at 24 MPa pressure at varying temperatures. Data was extracted from previous studies by Marrone et al.[23] and Bandura et al.[21]

Previous studies have shown that hot liquid water as a solvent can either promote or suppress ionic reactions.[28-32] A previous study by Tester et al.[28] revealed a non-Arrhenius shift in activity for the hydrolysis of methyl tert-butyl ether (MTBE) under conditions ranging from 150 to 600 °C and 250 atm. Under subcritical conditions, the rate of MTBE hydrolysis increased with increasing temperature. However, a steep decrease in activity occurred above the critical point. It is hypothesized that the ionic reaction is attenuated because liquid water above its critical point becomes incapable of supporting ions, including H^+ and OH^-, as shown by the ionic product in **Figure 2.1**. This study highlights how supercritical water's limited capacity to self-ionize can influence activity. Similarly, Marrone et al.[23] observed a significant loss in methylene chloride hydrolysis under supercritical compared to subcritical conditions. Marrone et al. [23] attributed similar non-Arrhenius activity observations to the temperature dependence of the dielectric constant of water near the critical point, and the resulting effect on polar transition state solvation and subsequent hydrolysis rates of dichloromethane. Therefore, it has been established that water's unusual properties play a role in apparent activity differences between subcritical and supercritical homogenous reactions.

Due to the unique thermophysical properties of water near and above its supercritical state, it is often difficult to assess the role of water on hydrothermal activity, particularly for batch systems with heat up and cool down stages. **Figure 2.2** highlights how the heat up and cool down stages can create significant changes in the ionic product and dielectric constant during a representative reaction performed at super critical water conditions at 400 °C. Based on **Figure 2.2**, the transient heat up and cool down steps will create a local maximum in the ionic product of water. The increase in ionic product during heat-up and cool-down can lead to an increase in reactivity, particularly for acid or base catalyzed reactions. The changes in ionic product and

dielectric constant can also influence catalytic stability, where liquid hydrolysis is known to preferentially degrade many solid acid materials.[33-40] The influence of heat up and cool down stages may play a role in batch reaction studies, but will not influence continuous plug flow reactors that heat up under inert conditions prior to reactant fluid delivery. Therefore, comparing activity or stability studies with a water solvent under either batch or flow conditions can have varying results that may be attributable to the thermochemical properties of water.
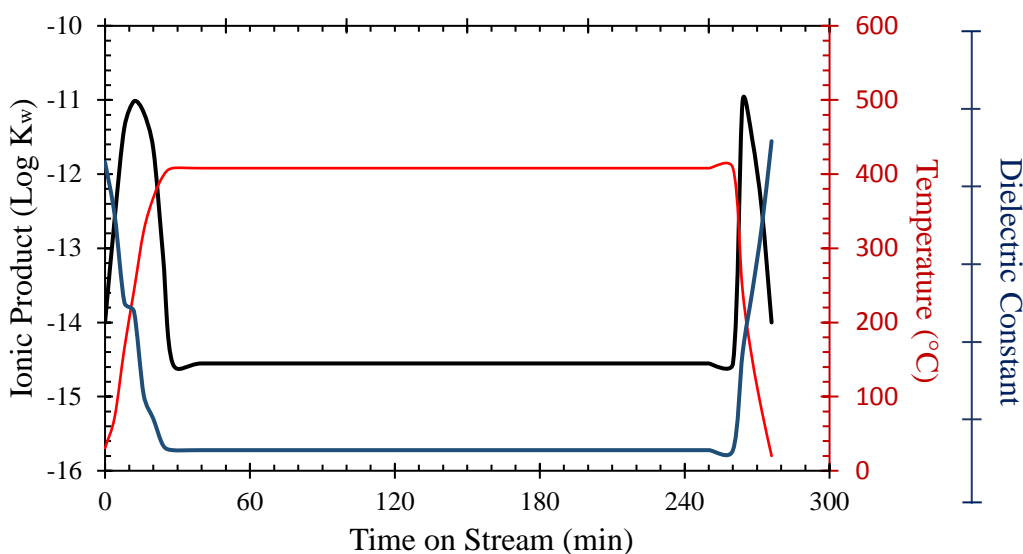
Figure 2.2: A case temperature profile of a batch study diluted in an aqueous phase. The expected ionic product and dielectric constant are overlaid to show the expected changes with temperature as well.

2.3 Hydrothermally Stable Heterogeneous Catalysts

The recent efforts to improve process intensity, separation,[41] and energy efficiency,[42] especially for high moisture content feedstocks,[43, 44] motivate interest in developing catalysts for use in the presence of liquid water phases.[45-49] The fundamental subject of catalyst stability

10

under compressed liquid phase conditions has been studied, with a few classes of materials showing promising results after hot liquid water treatment.

2.3.1 Metal and Metal Oxide Catalysts

Metal oxides are a class of nonporous heterogeneous catalysts with either pure or mixed metal centers that are covalently bonded with oxygen to create strongly cross-linked particles. The structural stability of metal oxides under hot liquid water conditions has been previously studied and considered better than many other commonly used catalyst materials. [50, 51] Under more extreme supercritical water conditions, titania, (TiO_2), zirconia (ZrO_2) and ceria zirconia oxide ($CeZrO_x$) were treated at 500 C and 28 MPa and all retained their crystallinity based on XRD and surface area based on BET.[52] The primary breakdown of metal oxides is considered leaching, which can vary based on the specific metal oxide.[53] Jocs et al.[53] created thermodynamic models for a variety of metal oxides treated in supercritical water at 400 °C and evaluated the expected leaching between a solid particle and bulk fluid. Based on this, study nickel and cobalt metals were prone to oxidation and leaching while other metals such as ruthenium ceria, titania and zirconia are expected to retain their framework stability.[53]

One common metal used in the catalysis of biomass feedstocks is Niobium oxide. Niobium oxide (Nb_2O_5) has been extensively studied as a catalyst for converting biorenewables under hot liquid water conditions, but is known to agglomerate into sintered particles with a lower surface area. Therefore, studies have examined routes to reduce agglomeration by supporting it on silica or alumina materials. Li et al.[54] successfully supported Nb_2O_5 on alumina, which was used as a catalyst with retained catalytic activity over 1000 hrs for hydrating ethylene oxide at 150 °C. Similarly, Nb_2O_5 has been successfully supported on mesoporous silica SBA-15 and retained its framework stability under 200 °C hot liquid water treatment.[55] Platinum has also been supported

on carbon nanotubes with remarkable hydrothermal stability after 450 °C hot liquid water treatment.[56]

2.3.2 Zeolites

Zeolites are a class of microporous aluminosilicate structures with a large surface area, adjustable acidity and can promote product selectivity due to the steric nature of their pore sizes. The zeolite framework has tetrahedrally coordinated silicon and aluminum species bonded together with oxygen linkers to form secondary building units comprising a unit cell. Each zeolite framework has a unique unit cell with varying sized pores. Zeolite channels allow access for reactants or products to diffuse, which can range from 1.7 to 12.1Å in diameter. The steric hindrance within a zeolite pore can allow for size selective product formation relative to other commonly used homogeneous acid catalysts.[57, 58] Zeolites can have strong Brønsted acidity, which is tuned by the amount of Al incorporated in the structure due to catalytic protons balancing the tetrahedrally coordinated internal AlO_4 sites.

The differences in zeolite unit cells creates structures with varying accessible pore volumes and framework densities, as shown in the scatter plot of all zeolite discovered structures in **Figure 2.3**. Inverse relationship between zeolite framework density and accessible pore volume in **Figure 2.3** shows that denser frameworks have less available void volume for reaction to occur in the pore, and conversely larger internal volumes cause a zeolite framework to become less densely packed. In total, there are over 240 unique zeolite frameworks, which are designated using a three letter acronyms. Common zeolites described in this chapter are denoted in **Figure 2.3**, which include MFI for ZSM-5 catalyst, FAU for faujasite catalyst, BEA for H-β catalyst, FER for ferrierite catalyst and MOR for mordenite catalyst.

12
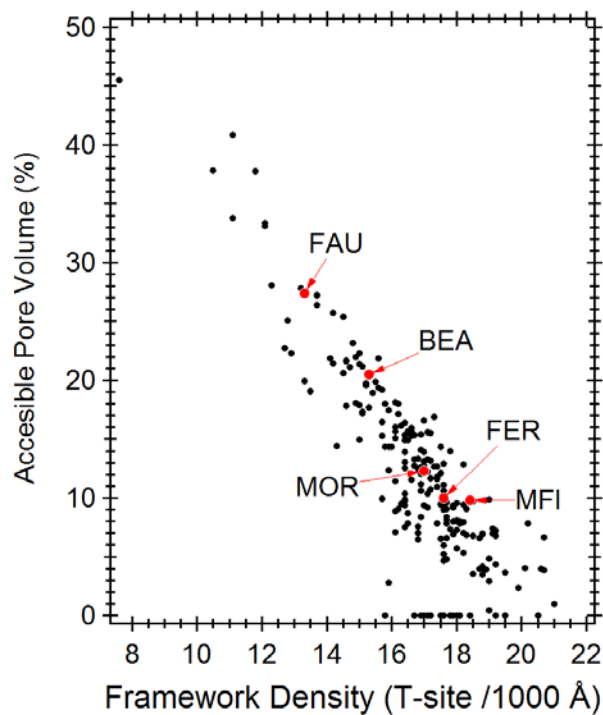
Figure 2.3: Scatter plot of all zeolites frameworks in terms of accessible pore volume relative to its corresponding framework density.

Many aspects of zeolite performance remain incompletely understood in the liquid phase, including even the fundamental question of zeolite stability.[33, 38, 39, 50, 59, 60] Zeolites are considered less hydrothermally stable compared to previously described metal oxides or carbon-based catalysts.[50] The abundant literature on zeolite degradation under acidic and basic[61-67] conditions can provide insight to zeolite's hydrothermal stability under hot liquid water conditions. The two primary mechanisms of zeolite degradation, acid catalyzed dealumination and base catalyzed desilication, are presented in **Scheme 2.1**.[61-75] Base catalysis by OH− selectively cleaves siloxane framework bonds, leading to desilication.[61, 64-67] Desilication of a zeolite in an alkaline medium will often initiate at internal sites[63] and propagate from hydroxyl nest defects introduced into the framework during synthesis or dealumination.[38, 63, 65, 76] The extent of zeolite desilication greatly depends on the zeolite structure and its Si/Al ratio.[77, 78] In

contrast to base catalyzed desilication, numerous studies report that acids promote zeolite dealumination,[65, 67-75] with minimal framework degradation. Framework degradation from dealumination will occur when the Si/Al ratio is low, such as for aluminum rich H-Y zeolite.[79] As shown in **Scheme 2.1,** dealumination in acid solutions occurs via a proton/hydronium catalyzed mechanism that selectively removes Al sites. The complete removal of framework Al species results in a variety of extra-framework hydroxyaluminate complexes that impart Lewis acidity as well as mono, di and/or trivalent Al cations.[68]
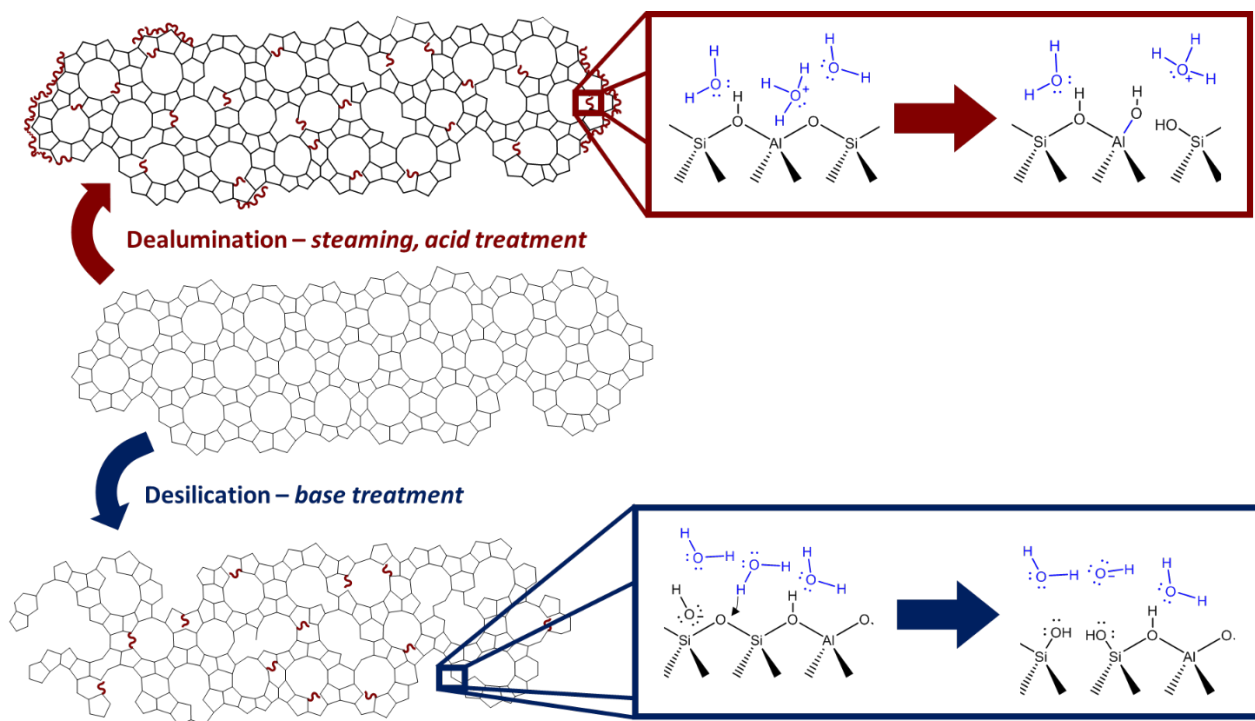
Scheme 2.1: Schematic of acid catalyzed dealumination and base catalyzed desilication mechanisms known during zeolite breakdown under acid, base or steaming conditions.

Similar to acid treatment, framework leaching of aluminum is the predominant form of degradation for steamed H-Y[79-81], H-β[38, 82] and H-ZSM-5 [70, 75, 83, 84] zeolites under a

wide range of temperatures and water vapor partial pressures. However, marginal to negligible degradation of ZSM-5 framework has been previously shown in the literature under steaming conditions ranging from 500 to 570 °C and 12kPa to saturated steam pressure.[70, 75, 85, 86] Studies have reported that liquid water is more aggressive compared to steaming; steaming typically selectively removes Al sites, whereas exposure to liquid water destroys the aluminosilicate framework itself.[33, 37-39, 59, 60] For example, Ravenelle et al.[33] reported that H-Y zeolite lost >90% of its original crystallinity within 6 hours of exposure to liquid water at 200 °C. Similarly, H-MOR,[60] H-β,[60] and ZSM-22[39] were treated in hot liquid water at temperatures up to 250 °C and experienced >25% framework degradation after 72 hours. Unlike HY, H-MOR, and H-β zeolite frameworks, ZSM-5 retained framework crystallinity for up to 72 hours at 200 °C.[60]

The relative stability of ZSM-5 in hot liquid water compared to H-Y, H-β, and H-MOR zeolites suggests that the MFI framework is either thermodynamically or kinetically more resistant to de-crystallization than other frameworks. The MFI framework is composed of unit cells consisting primarily of 5 and 6 membered rings, whereas the H-Y and H-β frameworks have much greater fractions of strained 4-membered rings, and the strain of these rings potentially reduces their kinetic and/or thermodynamic stability compared to MFI framework. Likewise, compared to BEA and MOR, the MFI framework is more densely packed with less accessible volume, as shown in **Figure 2.3**. The densely packed framework may reduce zeolite-water interactions, thereby conferring greater aqueous phase stability to the MFI. Further exploration of ZSM-5 hydrothermal stability is performed in Chapters 5 and 6.

2.4 Functionalized Zeolite for Improved Hydrothermal Stability

Zeolites modified by surface functionalization,[41, 80, 87] have been shown to have improved stability under liquid phase aqueous conditions. For example, silylation of H-β[88] improved the liquid-phase stability in hot liquid water by retaining all crystallinity at 160 °C after 48 hours, with treatment increasing the mesoporosity of the material instead of the general framework destruction observed for the parent. Zapata et al.[89] utilized a biphasic oil/water emulsion for improved recovery of organophilic alkylation products of m-cresol and propanol from the aqueous phase reaction using H-Y zeolite at 200 °C. Cresol conversion was further improved by functionalizing H-Y zeolite with organosilanes to promote cresol adsorption. However, the hydrothermal stability of silylated zeolites is limited. The organosilanes are prone to be hydrolytically cleaved from the zeolite surface under more aggressive hot liquid water treatment temperatures.

In addition to silylation techniques to improve zeolite hydrophobicity/ hydrophilicity and hydrothermal stability, adjustments of zeolite acid sites through metal ion incorporation can improve catalytic function and stability. **Scheme 2.2** shows three types of metal ion incorporation commonly performed in the literature, which are impregnation, ion exchange, and isomorphic substitution. A detailed explanation of each metal ion incorporation is presented below.

2.4.1 Metal impregnation

The first technique shown in **Scheme 2.2** is impregnation, in which a metal species (*M*) associates with a Brønsted acid site by coordinating near adjacent framework oxygen species and/or acid sites. Metal incorporation through impregnation is denoted with a slash "/" between impregnated species and framework structure. Impregnation can reduce Brønsted acid site strength and improve product dissociation, thereby reducing coke formation and improving catalytic

stability.[90, 91] Specifically, phosphorous impregnation in MFI zeolites (P/ZSM-5(30)) has been

shown to improve ethanol dehydration to ethylene selectivity and acid site stability.[92] Similar

acid site stability results were observed with P/ZSM-5(14) during hexane cracking. Nickel is also

a common impregnation metal used to attenuate acid site strength in a zeolite.[93] Gayubo et

al.[93] found that 1 wt% of Ni impregnated into ZSM-5 (Ni/ZSM-5(30)) effectively reduces

ethanol adsorption onto the acid site from 135 kJ mol^{-1} to 125 kJ mol^{-1}, which reduces the

irreversible deactivation of ZSM-5 through coking. Lastly, heavier metals such as iron, cobalt,

molybdenum and chromium have varying effects on the selectivity of vegetable oil hydrolysis

products when operated at 250 – 350 °C under hot liquid water conditions.[94] Impregnation of

iron was shown to promote the formation of larger molecular weight products, while molybdenum

produced lighter hydrocarbon fractions.[94] The main issue with impregnation techniques is that

they are weakly associated with an acid site within the framework, which makes them prone to

leaching upon exposure to aqueous solutions.[95] Previous studies has shown that metal ions will

readily hydrate and dissociate off of a Brønsted acid site, and eventually diffuse out of a zeolite

framework.[95]
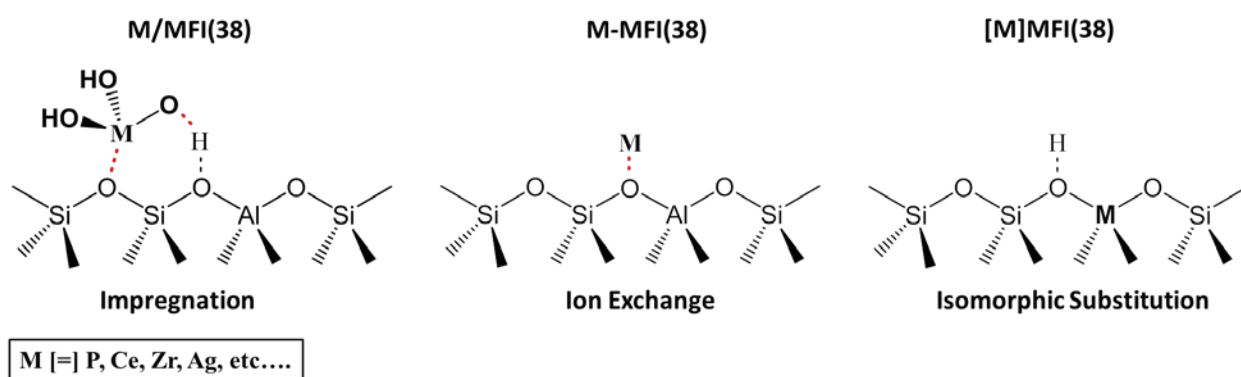
Scheme 2.2: Different forms of metal incorporation into a zeolite framework, impregnation, ion

exchange and isomorphic substitution. The notation used to denote each type of incorporation in

denoted above.

17

2.4.2 Metal ion exchange

Metal incorporation through ion exchange occurs when a metal species, often a monovalent cation, replaces the active Brønsted acidic proton that is charge compensating a tetrahedrally coordinated framework aluminum site. Ion exchange in a zeolite is denoted with a dash "-" between the exchanged species and framework structure. Kubo et al.[96] reported that Cu and Ag ion exchanged into MFI lattice (Ag-ZSM-5(51)) improve the activity of hexane cracking in 30% water by reducing the loss of acid sites via steaming.[96-99] Xiaojing et al.[97] also found that Ag-ZSM-5(40) successfully protects acid sites from degradation at 600 °C and low water concentrations, but saturated steam would start to preferentially remove aluminum species.

While the ion exchanged metal usually has a +1 charge, divalent or trivalent cations have been used to ion exchange multiple Brønsted acid sites that are distributed closely within a zeolite channel. For example, rare earth metals like La have also been shown to improve the steam stability of FAU zeolite through coordination with three acid sites.[100] Other rare earth metals like Ce, Pr and Nd have been shown to protect the FAU zeolite framework when ion exchanged at acid sites.[96, 100] Although ion exchange has stronger association with the framework than impregnation techniques, the metal ion will also leach into solution, particularly at high operating temperatures T > 200 °C upon exposure to aqueous solutions.

2.4.3 Isomorphic substitution

The last form of ion exchange shown in Scheme 1 is isomorphic substitution. Isomorphic substitution (or incorporation) replaces the aluminum center within a zeolite with a different 3^+ cationic metal site. Since the new metal sites are often bonded tetrahedrally, the site can retain Brønsted acidity with a charge-compensating proton. Metal incorporation through isomorphic substitution is denoted with a bracket "[ ]" enclosing the substituted species prior to the framework

designation. Compared to impregnation and ion exchange techniques, isomorphic substitution is less studied due to the relative hydrothermal instability[101] and difficulty in using post synthesis techniques to introduce new metal centers to the zeolite framework. Boron is one of the more popular isomorphic substituted species, in which the metal precursor was added during the crystal synthesis.[101-104] In particular, [B]-ZSM-5 has been used in Beckmann rearrangement[101] and dodecane cracking[104] chemistries, producing weaker trigonal coordinated active relative to conventional [Al]-ZSM-5 zeolite. Carati et al. synthesized BEA and MFI frameworks with Ti metal incorporated within the lattice, and found that [Ti]ZSM-5 was more stable than [Ti]BEA.[105] Shahami et al.[102] successfully incorporated Sn into MFI frameworks to create smaller crystal sizes compared to an identical synthesis technique without a Sn precursor. Next, previous literature studies that apply zeolite chemistry studies under hot liquid water conditions using a variety of post synthesis adjustments are discussed.

2.5 Literature Studies of zeolite catalyzed reactions under hot liquid water conditions

Many recent chemistries attempt to use zeolite catalysts for processing hydrocarbons under hot liquid water conditions. **Figure 2.4** compares the operating temperatures of previous literature studies performed under hot liquid water conditions with different zeolite framework types. The reactions that have been shown to use zeolites under hot liquid water conditions can be broadly separated into six chemistries, which are described in the following sections.
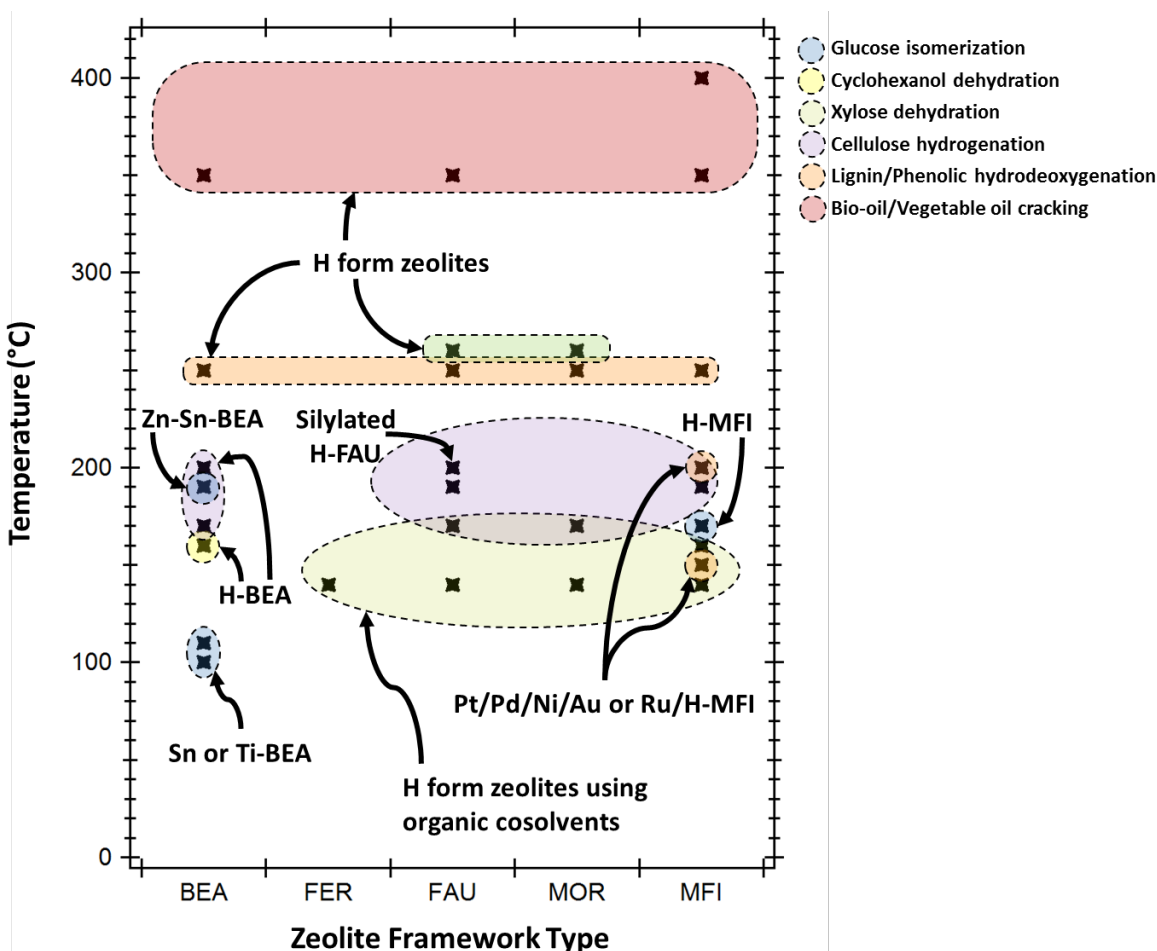
Figure 2.4. Literature overview of that compares the operating temperature of hot liquid water chemistries using different zeolite frameworks at temperatures ≥100 °C.

2.5.1 Hydrogenation of Cellulose

Biomass consists of an entangled network of cellulose, hemicellulose and lignin structures, with a relative abundance of each constituent based on the specific biomass crop. Thermochemical routes to break down cellulosic material into their monomer forms have been explored as an alternative to commonly applied enzymatic catalytic routes.[106-109] For example, previous studies have explored cellulose and hemicellulose hydrolysis and hydrogenation reactions catalyzed with zeolites under compressed liquid phase conditions, as shown in purple in **Figure 2.4**.[37, 106-110] Most hydrolysis and hydrogenation reactions are performed in a batch reactor at

operating temperatures ranging between 140-220 °C and under autogenic pressures using a large cage zeolite to allow cellulose to enter the micropores.[110] Dhepe et al[106] determined H-Y zeolite with a Si/Al of 15 was the most active catalyst in hydrolyzing hemicellulose compared to H-β and H-MOR zeolites, yielding 42% xylose and arabinose. Work by Shrotri et al.[108] found nickel supported on H-β zeolite improved cellulose conversion to sorbitol, mannose and glycerol when compared to pure nickel catalyst during batch reactions at 200 °C and autogenic pressure. However, not all studies found that the zeolites effectively hydrolyze all cellulosic material. Chambon et al.[107] found that H-Y had a negligible effect on catalyzing the breakdown of crystalline cellulose at 190 °C and autogenic pressures, but successfully hydrolyzes the soluble oligomeric species that leach during hydrothermal treatment into glucose monomers and further breakdown products. A mechanistic role of zeolite catalyzed cellulose hydrolysis remains unknown due to the limited amount of studies.

2.5.2 Glucose isomerization

Glucose isomerization has been studied in the literature in order to form both high fructose corn syrup and to form platform chemicals for fuels and other chemicals. The framework of BEA zeolite with incorporated Sn sites has been shown to efficiently isomerize glucose.[48, 111-118] Glucose isomerization was performed under batch conditions ranging between operating temperatures of 100 – 140 °C and autogenic pressures. Sn-β catalyzed glucose isomerization to either fructose, xylose or mannose products from the Sn incorporated Lewis acid centers within the zeolite framework. Under low conversion conditions, Davis et al.[118] also reported stereospecific isomerization of glucose to sorbose using Ti-β zeolite.

Gardner et al.[115] studied ZSM-5 catalyzed glucose to fructose isomerization in liquid water at 190 °C, reporting that catalytic activity was due to formation of trace, water-soluble Al species

attributed to loss from the zeolite. The concentration of aluminum ion species was enhanced with the addition of concentrated sodium hydroxide solution. Since salts are naturally inherent in biomass material, analysis of the feedstock is necessary when testing the catalytic activity on a more representative reactant. In contrast to acid site loss, ZSM-5 maintained its framework crystallinity throughout the reaction process

2.5.3 Xylose and Cyclohexanol dehydration

Several studies have investigated the catalytic activity of zeolites in the dehydration of 5 carbon wood sugars to form furfural, a popular platform chemical for both fuels and commodity chemicals. H-Y, H-β and H-MOR zeolites are the most common zeolite frameworks used to hydrolyze and hydrogenate xylose monomers into furfural.[119, 120] Using similar conditions as cellulose hydrolysis (170 °C and 5 MPa N_2 + autogenic pressure), Dhepe et al.[106] was able to breakdown hemicellulose found in bagasse into C5 species using H-Y, H-β and H-MOR zeolites. H-Y zeolite was shown to be the most active, yielding 40% xylose and arabinose yield and 15% furfural, and largely maintaining its catalytic activity after five reuses.[106] Lessard et al.[121] successfully performed xylose dehydration experiments using a continuous, liquid phase, plug flow reactor setup at the bench scale. The dehydration experiments high conversion (98%) and furfural selectivities (98%) were operated at 260 °C and 5.5 MPa in a toluene-water solvent mixture using H-MOR zeolite as the catalyst. Unlike glucose isomerization and cellulose hydrogenation reactions, H-form zeolites are used for dehydration reactions due to their strong Brønsted acidity.

2.5.4 Phenol hydrodeoxygenation

Hydrodeoxygenation chemistries have been performed using a zeolite under hot liquid water conditions in several studies using a variety of phenolic compounds. Often a hydrogenation

catalyst such as ruthenium is impregnated within the zeolite structure to improve hydrodeoxygenation chemistry. Zhang et al. performed phenol hydrodeoxygenation with ruthenium, palladium or platinum impregnated ZSM-5 at 150 °C and autogenic pressures.[122] From this study, Ru/H-ZSM-5(25) was found to be the most selective in forming cyclohexane, with both the Brønsted acid site and ruthenium metal serving as the active sites for dehydration and hydrogenation reactions, respectively.[122] Similarly, hydrodeoxygenation of guaiacol, a model compound for lignin, has been performed at 250 C and autogenic pressures with 5 MPa of hydrogen pressure using both Ru/H-Y and H-Y zeolites impregnated with both ruthenium and either iron, nickel, copper and zinc.[123] Reactions using Ru-Cu/H-Y zeolite catalyst reported the highest hydrocarbon yield and the highest selectivity to form cyclohexane. Incorporation of a second impregnated metal species, such as copper, attenuated the hydrogenation chemistry, which reduced byproduct formation.[123]

2.5.5 Bio-oil cracking

At temperatures > 250 °C, most studies no longer use metal impregnated or ion exchanged zeolites for catalysis due to their known leaching and use H-form zeolites for cracking chemistries. Specifically, Savages group has studied fatty acid cracking, compounds that are commonly found in plant oils, which can be converted into precursors for transportation fuel.[49]

Other studies have demonstrated improvements in cracking chemistries for fatty acids and algae in hot liquid water conditions to form valuable bio-oils.[49, 124-128] Mo et al. identified ZSM-5 to be the most active in converting fatty acids into aromatic hydrocarbons when compared to the activity of H-Y and H-β zeolites.[124] Further investigations also identified that ZSM-5 undergoes coking but can be regenerated and largely retains its catalytic activity after three reuses.[49]

Mo et al.[49] studied the use of ZSM-5 for catalytic cracking palmitic acid in supercritical water to produce higher value aromatic compounds. Robin et al.[94] studied catalytic cracking of fatty acids in liquid water at 350 °C and reported that the addition of Mo and H-ZSM-5 increased yields of alkenes and aromatics in the gasoline and diesel fuel ranges. Li et al[125] upgraded the bio-oil produced from hydrothermal liquefaction of Nannochloropsis sp using ZSM-5 to reduce the bio-oil oxygen content by an order of magnitude. Duan et al.[128] upgraded algal bio-oil under supercritical water conditions, using ZSM-5 to increase heating value of the oil product.

2.6 Zeolite deactivation through coking

Based on the previous studies that use zeolites under hot liquid water conditions, the selection of zeolite varies with both chemistry and operating temperature. Cracking and dehydration chemistries are performed at elevated operating temperatures >250 °C and the zeolites used do not incorporate additional metal species through ion exchange or wet impregnation. The lack of tuned acid sites is likely due to extensive leaching when operating in hot liquid water at elevated reaction temperatures. However, the strong Brønsted activity that arises from H-form zeolites can lead to further oligomerization and coking that can deactivate a catalyst.[129]

Previous studies have shown that zeolite catalysts initially have high activity but will deactivate over prolonged TOS due to coking,[130] where the extent of coking depends on the specific zeolite framework.[131] Larger pore zeolites, such as H-β and H-Y have reduced Van Der Waal interactions with a given compound,[132] which can allow for strong internal acid sites that rapidly deactivate with polyaromatic coke.[130] For example, ethanol dehydration on medium sized zeolites such as H-ZSM-5, have been shown to be highly selective to ethylene over long periods of time but have also been shown to deactivate via coking after 60 hours of vapor phase reaction at 300 °C.[129] Many studies have looked into routes to reduce coke formation during operation.

The use of nano-sized ZSM-5 helps shorten the diffusion path length and prolongs the time the zeolite remains catalytic before deactivation, particularly under higher water loadings.[133] Similarly, hierarchical zeolites have been shown to also reduce the diffusion path length, which reduces oligomerization reactions and is more selective to ethylene compared to micron sized ZSM-5 crystals at identical operating conditions.[134] Work by Choopun et al.[134] applied nano-ZSM-5 at the pilot scale and was able to regenerate the catalyst during runs to allow the continuous packed bed experiment to run for up to 2000 hrs.[135] The addition or formation of water is also expected to attenuate coke formation and improve the coke stability of zeolites, provided the zeolite is sufficiently hydrothermally stable under reaction conditions. The work in Chapter 7 evaluates the extent of framework, acid site and coking stability of ZSM-5 under ethanol dehydration conditions

References

1.   Hanning, L., et al. *EPSRC Thermal Management of Industrial Processes A Review of Drying Technologies*. 2010.

2.   Hashaikeh, R., I.S. Butler, and J.A. Kozinski, *Selective promotion of catalytic reactions during biomass gasification to hydrogen.* Energy & Fuels, 2006. **20**: p. 2743-2747.

3.   Hashaikeh, R., et al., *Sequential hydrothermal gasification of biomass to hydrogen.* Proceedings of the Combustion Institute, 2005. **30 II**: p. 2231-2237.

4.   Dry, M.E., *The Fischer - Tropsch process: 1950-2000.* Catalysis Today, 2002. **71**: p. 227-241.

5.   Kumar, M., A. Olajire Oyedun, and A. Kumar, *A review on the current status of various hydrothermal technologies on biomass feedstock.* Renewable and Sustainable Energy Reviews, 2018. **81**: p. 1742-1770.

6.   Anex, R.P., et al., *Techno-economic comparison of biomass-to-transportation fuels via pyrolysis, gasification, and biochemical pathways.* Fuel, 2010. **89**: p. S29-S35.

7.   Swanson, R.M., et al., *Techno-economic analysis of biomass-to-liquids production based on gasification.* Fuel, 2010. **89**: p. S2-S10.

8.   Kazi, F.K., J. Fortman, and R. Anex, *Techno-Economic Analysis of Biochemical Scenarios for Production of Cellulosic Ethanol.* National Renewable Energy Laboratory-NREL, 2010: p. 102.

9.   Kazi, F.K., et al., *Techno-economic comparison of process technologies for biochemical ethanol production from corn stover.* Fuel, 2010. **89**: p. S20-S28.

10.   Bridgwater, A.V., D. Meier, and D. Radlein, *An overview of fast pyrolysis of biomass.* Organic Geochemistry, 1999. **30**: p. 1479-1493.

11.   López Barreiro, D., et al., *Hydrothermal liquefaction (HTL) of microalgae for biofuel production: State of the art review and future prospects.* Biomass and Bioenergy, 2013. **53**: p. 113-127.

12.   Ringer, M., et al., *Large-Scale Pyrolysis Oil Production: A Technology Assessment and Economic Analysis.* Renewable Energy, 2006: p. 1-93.

13.   McNamara, P.J., et al., *Pyrolysis of Dried Wastewater Biosolids Can Be Energy Positive.* Water Environment Research, 2016. **88**(9): p. 804-810.

14.   Rollinson, A.N. and J.M. Oladejo, *'Patented blunderings', efficiency awareness, and self-sustainability claims in the pyrolysis energy from waste sector.* Resources Conservation and Recycling, 2019. **141**: p. 233-242.

15.   Chundawat, S.P.S., et al., *Deconstruction of lignocellulosic biomass to fuels and chemicals.* Annual Review of Chemical and Biomolecular Engineering, 2011. **2**: p. 121-45.

16.   Pavlovič, I., et al., *Hydrothermal reactions of agricultural and food processing wastes in sub-and supercritical water: a review of fundamentals, mechanisms, and state of research.* Journal of agricultural and food chemistry, 2013. **61**: p. 8003-8025.

17.   Akhtar, J. and N.A.S. Amin, *A review on process conditions for optimum bio-oil yield in hydrothermal liquefaction of biomass.* Renewable and Sustainable Energy Reviews, 2011. **15**: p. 1615-1624.

18.   Lababpour, A., *Continuous Hydrothermal Liquefaction for Biofuel and Biocrude Production from Microalgal Feedstock.* Chembioeng Reviews, 2018. **5**(2): p. 90-103.

19.   Pour, A.N., et al., *Study on products distribution of iron and iron-zeolite catalysts in Fischer-Tropsch synthesis.* Fuel, 2008. **87**: p. 2004-2012.

20.   Collignon, F. and G. Poncelet, *Comparative vapor phase synthesis of ETBE from ethanol and isobutene over different acid zeolites.* Journal of Catalysis, 2001. **202**: p. 68-77.

21.   Bandura, A.V. and S.N. Lvov, *The ionization constant of water over wide ranges of temperature and density.* Journal of Physical and Chemical Reference Data, 2006. **35**: p. 15-30.

22.   Peterson, A.A., et al., *Thermochemical biofuel production in hydrothermal media: A review of sub- and supercritical water technologies.* Energy & Environmental Science, 2008. **1**: p. 32.

23.   Marrone, P.A., et al., *Solvation effects on kinetics of methylene chloride reactions in sub- and supercritical water: theory, experiment, and ab initio calculations.* Journal of Physical Chemistry A, 1998. **102**: p. 7013-7028.

24.   Lehr, V., et al., *Catalytic dehydration of biomass-derived polyols in sub- and supercritical water.* Catalysis Today, 2007. **121**: p. 121-129.

25.   Y.Arai, T.S., Y.Takebayashi, *Supercritical Fluids: Molecular Interactions, Physcial Properties and New Application.* 2002: p. 1-443.

26.   Klingler, D. and H. Vogel, *Influence of process parameters on the hydrothermal decomposition and oxidation of glucose in sub- and supercritical water.* Journal of Supercritical Fluids, 2010. **55**: p. 259-270.

27.   Savage, P.E. and C. Rearrangements, *Organic Chemical Reactions in Supercritical Water.* Chemical reviews, 1999. **99**: p. 603-622.

28.   Taylor, J., et al., *Multiscale Reaction Pathway Analysis of Methyl tert-Butyl Ether Hydrolysis under Hydrothermal Conditions.* Industrial & Engineering Chemistry Research, 2002. **41**: p. 1-8.

29.   Dinjus, E. and A. Kruse, *Hot compressed water - A suitable and sustainable solvent and reaction medium?* Journal of Physics Condensed Matter, 2004. **16**.

30.   Aida, T.M., et al., *Dehydration of lactic acid to acrylic acid in high temperature water at high pressures.* Journal of Supercritical Fluids, 2009. **50**: p. 257-264.

31.   Shoji, D., et al., *Visualized kinetic aspects of decomposition of a wood block in sub- And supercritical water.* Industrial & Engineering Chemistry Research, 2005. **44**: p. 2975-2981.

32.   Venardou, E., et al., *On-line monitoring of the hydrolysis of acetonitrile in near-critical water using Raman spectroscopy.* Vibrational Spectroscopy, 2004. **35**: p. 103-109.

33.   Ravenelle, R.M., et al., *Stability of zeolites in hot liquid water.* Journal of Physical Chemistry C, 2010. **114**: p. 19582-19595.

34.   Ravenelle, R.M., et al., *Sie-2011-Structural Changes of γ-Al2O3-Supported Catalysts in Hot Liquid Water.pdf.* American Chemical Society, Catalysis, 2011. **1**: p. 552-561.

35.   Pollock, R.A., et al., *Role of liquid vs vapor water in the hydrothermal degradation of SBA-15.* Journal of Physical Chemistry C, 2012. **116**: p. 22802-22814.

36.   Van Pelt, A.H., et al., *Stability of functionalized activated carbon in hot liquid water.* Carbon, 2014. **77**: p. 143-154.

37.   Ennaert, T., et al., *Conceptual frame rationalizing the self-stabilization of H-USY zeolites in hot liquid water.* ACS Catalysis, 2015. **5**: p. 754-768.

38. Zhang, L., et al., *Factors that Determine Zeolite Stability in Hot Liquid Water.* Journal of the American Chemical Society, 2015. **137**: p. 11810-11819.

39. Jamil, A.K., et al., *Hydrothermal Stability of One-Dimensional Pore ZSM-22 Zeolite in Hot Water.* Journal of Physical Chemistry C, 2016. **120**: p. 22918-22926.

40. Zhang, E.M., *Testing the Stability of Cation Exchanged Zeolite ZSM-5 in Hot Liquid Water.* 2017.

41. Zapata, P.A., et al., *Condensation/hydrogenation of biomass-derived oxygenates in water/oil emulsions stabilized by nanohybrid catalysts.* Topics in Catalysis, 2012. **55**: p. 38-52.

42. Liu, G., et al., *Catalytic cracking of supercritical n -dodecane over wall-coated HZSM-5 zeolites with micro- and nanocrystal sizes.* Energy and Fuels, 2012. **26**: p. 1220-1229.

43. Schwartz, T.J., et al., *Bridging the chemical and biological catalysis gap: Challenges and outlooks for producing sustainable chemicals.* ACS Catalysis, 2014. **4**: p. 2060-2069.

44. Elliott, D.C., et al., *Process development for hydrothermal liquefaction of algae feedstocks in a continuous-flow reactor.* Algal Research, 2013. **2**: p. 445-454.

45. Héroguel, F., B. Rozmysłowicz, and J.S. Luterbacher, *Improving Heterogeneous Catalyst Stability for Liquid-phase Biomass Conversion and Reforming.* CHIMIA International Journal for Chemistry, 2015. **69**: p. 582-591.

46. Xian, X., et al., *Catalytic cracking of n-dodecane over HZSM-5 zeolite under supercritical conditions: Experiments and kinetics.* Chemical Engineering Science, 2010. **65**: p. 5588-5604.

47.   Antal, Michael Jerry, et al., *Mechanism and Kinetics of the Acid-Catalyzed Dehydration of 1- and 2-Propanol in Hot Compressed Liquid Water.* Industrial & Engineering Chemistry Research, 1998. **37**: p. 3820-3829.

48.   Román-Leshkov, Y., et al., *Mechanism of glucose isomerization using a solid lewis acid catalyst in water.* Angewandte Chemie - International Edition, 2010. **49**: p. 8954-8957.

49.   Mo, N. and P.E. Savage, *Hydrothermal catalytic cracking of fatty acids with HZSM-5.* ACS Sustainable Chemistry and Engineering, 2014. **2**: p. 88-94.

50.   Xiong, H., H.N. Pham, and A.K. Datye, *Hydrothermally stable heterogeneous catalysts for conversion of biorenewables.* Green Chemistry, 2014. **16**: p. 4627-4643.

51.   Kumar, R., et al., *Ketonization of oxygenated hydrocarbons on metal oxide based catalysts.* Catalysis Today, 2017. **302**: p. 16-49.

52.   Chakinala, A.G., et al., *Catalyst screening for the hydrothermal gasification of aqueous phase of bio-oil.* Catalysis Today, 2012. **195**: p. 83-92.

53.   Jocz, J.N., L.T. Thompson, and P.E. Savage, *Catalyst Oxidation and Dissolution in Supercritical Water.* Chemistry of Materials, 2018. **30**: p. 1218-1229.

54.   Li, Y.C., et al., *Selective catalytic hydration of ethylene oxide over niobium oxide supported on alpha-alumina.* Applied Catalysis a-General, 2004. **272**(1-2): p. 305-310.

55.   Pagan-Torres, Y.J., et al., *Synthesis of Highly Ordered Hydrothermally Stable Mesoporous Niobia Catalysts by Atomic Layer Deposition.* Acs Catalysis, 2011. **1**(10): p. 1234-1245.

56.   de Vlieger, D.J.M., et al., *Carbon Nanotubes: A Promising Catalyst Support Material for Supercritical Water Gasification of Biomass Waste.* Chemcatchem, 2012. **4**(12): p. 2068-2074.

57.   Gendy, T.S., *Simulation of Liquid and Vapour Phase Xylene Isomerization over Deactivating H-Y-Zeolite.* J. Chem. Technol. Biotechnol., 1998. **73**: p. 109-118.

58.   Zheng, S., A. Jentys, and J.A. Lercher, *Xylene isomerization with surface-modified HZSM-5 zeolite catalysts: An in situ IR study.* Journal of Catalysis, 2006. **241**: p. 304-311.

59.   Vjunov, A., et al., *Impact of aqueous medium on zeolite framework integrity.* Chemistry of Materials, 2015. **27**: p. 3533-3545.

60.   Lutz, W., et al., *Investigation and modeling of the hydrothermal stability of technically relevant zeolites.* Adsorption, 2005. **11**: p. 405-413.

61.   Groen, J.C., et al., *Mechanism of hierarchical porosity development in MFI zeolites by desilication: The role of aluminium as a pore-directing agent.* Chemistry - A European Journal, 2005. **11**: p. 4983-4994.

62.   Fodor, D., et al., *Differences between individual ZSM-5 crystals in forming hollow single crystals and mesopores during base leaching.* Chemistry - A European Journal, 2015. **21**: p. 6272-6277.

63.   Verboekend, D. and J. Pérez-Ramírez, *Design of hierarchical zeolite catalysts by desilication.* Catalysis Science & Technology, 2011. **1**: p. 879.

64.   Groen, J.C., et al., *Optimal aluminum-assisted mesoporosity development in MFI zeolites by desilication.* Journal of Physical Chemistry B, 2004. **108**: p. 13062-13065.

65.   Groen, J.C., J.A. Moulijn, and J. Pérez-Ramírez, *Decoupling mesoporosity formation and acidity modification in ZSM-5 zeolites by sequential desilication-dealumination.* Microporous and Mesoporous Materials, 2005. **87**: p. 153-161.

66.   Groen, J.C., et al., *Mesoporosity development in ZSM-5 zeolite upon optimized desilication conditions in alkaline medium.* Colloids and Surfaces A: Physicochemical and Engineering Aspects, 2004. **241**: p. 53-58.

67.   van Donk, S., et al., *Generation, Characterization, and Impact of Mesopores in Zeolite Catalysts.* Catalysis Reviews, 2003. **45**: p. 297-319.

68.   Silaghi, M.-C., C. Chizallet, and P. Raybaud, *Challenges on molecular aspects of dealumination and desilication of zeolites.* Microporous and Mesoporous Materials, 2014. **191**: p. 82-96.

69.   Beyerlein, R.a., et al., *Effect of steaming on the defect structure and acid catalysis of protonated zeolites.* Topics in Catalysis, 1997. **4**: p. 27-42.

70.   Ong, L.H., et al., *Dealumination of HZSM-5 via steam-treatment.* Microporous and Mesoporous Materials, 2012. **164**: p. 9-20.

71.   Triantafillidis, C.S., A.G. Vlessidis, and N.P. Evmiridis, *Dealuminated H−Y Zeolites: Influence of the Degree and the Type of Dealumination Method on the Structural and Acidic Characteristics of H−Y Zeolites.* Industrial & Engineering Chemistry Research, 2000. **39**: p. 307-319.

72.   Masuda, T., et al., *Changes in catalytic activity of MFI-type zeolites caused by dealumination in a steam atmosphere.* Applied Catalysis A: General, 1998. **172**: p. 73-83.

73.   Valtchev, V., et al., *Tailored crystalline microporous materials by post-synthesis modification.* Chemical Society Reviews, 2013. **42**: p. 263-290.

74. Maier, S.M., A. Jentys, and J.A. Lercher, *Steaming of zeolite BEA and its effect on acidity: A comparative NMR and IR spectroscopic study.* Journal of Physical Chemistry C, 2011. **115**: p. 8005-8013.

75. Niwa, M., S. Sota, and N. Katada, *Strong Brønsted acid site in HZSM-5 created by mild steaming.* Catalysis Today, 2012. **185**: p. 17-24.

76. Abelló, S., A. Bonilla, and J. Pérez-Ramírez, *Mesoporous ZSM-5 zeolite catalysts prepared by desilication with organic hydroxides and comparison with NaOH leaching.* Applied Catalysis A: General, 2009. **364**: p. 191-198.

77. Silaghi, M.C., C. Chizallet, and P. Raybaud, *Challenges on molecular aspects of dealumination and desilication of zeolites.* Microporous and Mesoporous Materials, 2014. **191**: p. 82-96.

78. Pérez-Ramírez, J., et al., *Hierarchical zeolites: enhanced utilisation of microporous crystals in catalysis by advances in materials design.* Chemical Society Reviews, 2008. **37**: p. 2530-2542.

79. Cairon, O., *Impacts of Composition and Post-Treatment on the Brønsted Acidity of Steam-Treated Faujasite: Insights from FTIR Spectroscopy.* ChemPhysChem, 2013. **14**: p. 244-251.

80. Chen, K., et al., *Water Interactions in Zeolite Catalysts and Their Hydrophobically-Modified Analogues.* ACS Catalysis, 2015. **5**: p. 7480-7487.

81. Dimitrijevic, R., W. Lutz, and A. Ritzmann, *Hydrothermal stability of zeolites: Determination of extra-framework species of H-Y faujasite-type steamed zeolite.* Journal of Physics and Chemistry of Solids, 2006. **67**: p. 1741-1748.

82. Bernasconi, S., et al., *Formation of mesopores in zeolite beta by steaming: A secondary pore channel system in the (001) plane.* Microporous and Mesoporous Materials, 2003. **66**: p. 21-26.

83. Campbell, S.M., et al., *Dealumination of HZSM-5 Zeolites.* Journal of Catalysis, 1996. **358**: p. 350-358.

84. Datka, J., et al., *Physicochemical and Catalytic Properties of HZSM-5 Zeolites Dealuminated by the Treatment with Steam.* The Journal of Physical Chemistry, 1996. **100**: p. 14451-14456.

85. Jin, L., et al., *An improved dealumination method for adjusting acidity of HZSM-5.* Catalysis Today, 2010. **149**: p. 207-211.

86. Triantafillidis, C.S., et al., *Effect of the degree and type of the dealumination method on the structural, compositional and acidic characteristics of H-ZSM-5 zeolites.* Microporous and Mesoporous Materials, 2001. **47**: p. 369-388.

87. Zapata, P.A., et al., *Silylated hydrophobic zeolites with enhanced tolerance to hot liquid water.* Journal of Catalysis, 2013. **308**: p. 82-97.

88. Prodinger, S., et al., *Improving Stability of Zeolites in Aqueous Phase via Selective Removal of Structural Defects.* Journal of the American Chemical Society, 2016: p. jacs.5b12785.

89. Zapata, P.A., et al., *Hydrophobic Zeolites for Biofuel Upgrading Reactions at the Liquid – Liquid Interface in Water / Oil Emulsions.* Journal of the American Chemical Society, 2012. **134**: p. 8570-8578.

90.   Wang, J., et al., *Improvement of low-temperature hydrothermal stability of Cu/SAPO-34 catalysts by Cu^{2+} species.* Journal of Catalysis, 2015. **322**: p. 84-90.

91.   Li, Y., et al., *DFT study on the accommodation and role of la species in ZSM-5 zeolite.* Microporous and Mesoporous Materials, 2011. **142**: p. 621-628.

92.   Ramesh, K., et al., *Synthesis, characterization, and catalytic activity of phosphorus modified H-ZSM-5 catalysts in selective ethanol dehydration.* Industrial & Engineering Chemistry Research, 2010. **49**: p. 4080-4090.

93.   Gayubo, A.G., et al., *Hydrothermal stability of HZSM-5 catalysts modified with Ni for the transformation of bioethanol into hydrocarbons.* Fuel, 2010. **89**: p. 3365-3372.

94.   Robin, T., J.M. Jones, and A.B. Ross, *Catalytic hydrothermal processing of lipids using metal doped zeolites.* Biomass and Bioenergy, 2017. **98**: p. 26-36.

95.   Caeiro, G., et al., *Stabilization effect of phosphorus on steamed H-MFI zeolites.* Applied Catalysis A: General, 2006. **314**(2): p. 160-171.

96.   Kubo, K., et al., *Comparison of steaming stability of Cu-ZSM-5 with those of Ag-ZSM-5, P/H-ZSM-5, and H-ZSM-5 zeolites as naphtha cracking catalysts to produce light olefin at high temperatures.* Applied Catalysis A: General, 2015. **489**: p. 272-279.

97.   He, X., et al., *The role of silver species on the hydrothermal stability of zeolite catalysts.* Microporous and Mesoporous Materials, 2011. **142**: p. 398-403.

98.   Kubo, K., et al., *Ultra-high steaming stability of Cu-ZSM-5 zeolite as naphtha cracking catalyst to produce light olefin.* Catalysis Communications, 2012. **29**: p. 162-165.

99.   Shi, X., H. He, and L. Xie, *The effect of Fe species distribution and acidity of Fe-ZSM-5 on the hydrothermal stability and SO2and hydrocarbons durability in NH3-SCR reaction.* Cuihua Xuebao/Chinese Journal of Catalysis, 2015. **36**: p. 649-656.

100.   Du, X., et al., *Effect of cation location on the hydrothermal stability of rare earth-exchanged y zeolites.* Catalysis Communications, 2013. **35**: p. 17-22.

101.   Forni, L., et al., *Calcination and deboronation of B-MFI applied to the vapour phase Beckmann rearrangement.* Microporous and Mesoporous Materials, 2007. **101**(1-2): p. 161-168.

102.   Shahami, M., R. Ransom, and D.F. Shantz, *Synthesis and characterization of tin, tin/aluminum, and tin/boron containing MFI zeolites.* Microporous and Mesoporous Materials, 2017. **251**: p. 165-172.

103.   Huang, L., et al., *Effect of acid leaching and catalytic properties of zeolite [Al,B]-MWW utilized as ethene methylation catalyst.* Microporous and Mesoporous Materials, 2016. **223**: p. 230-240.

104.   Sanhoob, M.A., et al., *Steam catalytic cracking of heavy naphtha (C12) to high octane naphtha over B-MFI zeolite.* Applied Catalysis B: Environmental, 2017. **210**: p. 432-443.

105.   Carati, A., et al., *Stability of Ti in MFI and Beta structures: a comparative study.* Microporous and Mesoporous Materials, 1999. **30**(1): p. 137-144.

106.   Dhepe, P.L. and R. Sahu, *A solid-acid-based process for the conversion of hemicellulose.* Green Chemistry, 2010. **12**: p. 2153.

107. Sahu, R. and P.L. Dhepe, *A one-pot method for the selective conversion of hemicellulose from crop waste into C5 sugars and furfural by using solid acid catalysts.* ChemSusChem, 2012. **5**: p. 751-761.

108. Shrotri, A., et al., *Conversion of cellulose to polyols over promoted nickel catalysts.* Catalysis Science & Technology, 2012. **2**: p. 1852.

109. Chambon, F., et al., *Cellulose hydrothermal conversion promoted by heterogeneous Brønsted and Lewis acids: Remarkable efficiency of solid Lewis acids to produce lactic acid.* Applied Catalysis B: Environmental, 2011. **105**: p. 171-181.

110. Guo, F., et al., *Solid acid mediated hydrolysis of biomass for producing biofuels.* Progress in Energy and Combustion Science, 2012. **38**: p. 672-690.

111. Moliner, M., Y. Román-Leshkov, and M.E. Davis, *Tin-containing zeolites are highly active catalysts for the isomerization of glucose in water.* Proceedings of the National Academy of Sciences of the United States of America, 2010. **107**: p. 6164-6168.

112. Bermejo-Deval, R., et al., *Metalloenzyme-like catalyzed isomerizations of sugars by Lewis acid zeolites.* Proceedings of the National Academy of Sciences, 2012. **109**: p. 9727-9732.

113. Bermejo-Deval, R., R. Gounder, and M.E. Davis, *Framework and extraframework tin sites in zeolite beta react glucose differently.* ACS Catalysis, 2012. **2**: p. 2705-2713.

114. Bermejo-Deval, R., et al., *Active sites in Sn-beta for glucose isomerization to fructose and epimerization to mannose.* ACS Catalysis, 2014. **4**: p. 2288-2297.

115. Gardner, D.W., et al., *Insights into the Hydrothermal Stability of ZSM-5 under Relevant Biomass Conversion Reaction Conditions.* ACS Catalysis, 2015. **5**: p. 4418-4422.

116.   Dong, W., et al., *Selective chemical conversion of sugars in aqueous solutions without alkali to lactic acid over a Zn-Sn-Beta lewis acid-base catalyst.* Scientific Reports, 2016. **6**: p. 1-8.

117.   Holm, M.S., et al., *Sn-Beta catalysed conversion of hemicellulosic sugars.* Green Chemistry, 2012. **14**: p. 702.

118.   Gounder, R. and M.E. Davis, *Titanium-Beta Zeolite Catalyze the Stereospecific Isomerization of {D}-Glucose to {L}-Sorbose via Intramolecular {C5}-{C1} Hydride Shift.* ACS Catal., 2013. **3**: p. 1469-1476.

119.   Taarning, E., et al., *Zeolite-catalyzed biomass conversion to fuels and chemicals.* Energy & Environmental Science, 2011. **4**: p. 793.

120.   Xavier, N.M., S.D. Lucas, and A.P. Rauter, *Zeolites as efficient catalysts for key transformations in carbohydrate chemistry.* Journal of Molecular Catalysis A: Chemical, 2009. **305**: p. 84-89.

121.   Lessard, J., et al., *High yield conversion of residual pentoses into furfural via zeolite catalysis and catalytic hydrogenation of furfural to 2-methylfuran.* Topics in Catalysis, 2010. **53**: p. 1231-1234.

122.   Zhang, W., et al., *Hydrodeoxygenation of Lignin-Derived Phenolic Monomers and Dimers to Alkane Fuels over Bifunctional Zeolite-Supported Metal Catalysts.* ACS Sustainable Chemistry & Engineering, 2014. **2**(4): p. 683-691.

123.   Wang, H., et al., *One-Pot Process for Hydrodeoxygenation of Lignin to Alkanes Using Ru-Based Bimetallic and Bifunctional Catalysts Supported on Zeolite Y.* ChemSusChem, 2017. **10**: p. 1846-1856.

124. Duan, P. and P.E. Savage, *Catalytic hydrotreatment of crude algal bio-oil in supercritical water.* Applied Catalysis B: Environmental, 2011. **104**: p. 136-143.

125. Li, Z. and P.E. Savage, *Feedstocks for fuels and chemicals from algae: Treatment of crude bio-oil over HZSM-5.* Algal Research, 2013. **2**: p. 154-163.

126. Mo, N., W. Tandar, and P.E. Savage, *Aromatics from saturated and unsaturated fatty acids via zeolite catalysis in supercritical water.* Journal of Supercritical Fluids, 2015. **102**: p. 73-79.

127. Okuhara, T., *Water-tolerant solid acid catalysts.* Chemical Reviews, 2002. **102**: p. 3641-3666.

128. Duan, P., et al., *Catalytic upgrading of pretreated algal bio-oil over zeolite catalysts in supercritical water.* Biochemical Engineering Journal, 2016. **116**: p. 105-112.

129. Zhang, X., et al., *Comparison of four catalysts in the catalytic dehydration of ethanol to ethylene.* Microporous and Mesoporous Materials, 2008. **116**: p. 210-215.

130. Ramasamy, K.K. and Y. Wang, *Ethanol conversion to hydrocarbons on HZSM-5: Effect of reaction conditions and Si/Al ratio on the product distributions.* Catalysis Today, 2014. **237**: p. 89-99.

131. Madeira, F.F., et al., *Ethanol transformation over HFAU, HBEA and HMFI zeolites presenting similar Br??nsted acidity.* Applied Catalysis A: General, 2009. **367**: p. 39-46.

132. Abate, S., et al., *Disruptive catalysis by zeolites.* Catalysis Science & Technology, 2016. **6**(8): p. 2485-2501.

133. Bi, J., et al., *High effective dehydration of bio-ethanol into ethylene over nanoscale HZSM-5 zeolite catalysts.* Catalysis Today, 2010. **149**: p. 143-147.

134.   Choopun, W. and S. Jitkarnka, *Catalytic activity and stability of HZSM-5 zeolite and hierarchical uniform mesoporous MSU-S ZSM-5 material during bio-ethanol dehydration.* Journal of Cleaner Production, 2016. **135**: p. 368-378.

135.   Wang, F., et al., *Coking behavior of a submicron MFI catalyst during ethanol dehydration to ethylene in a pilot-scale fixed-bed reactor.* Applied Catalysis A: General, 2011. **393**(1-2): p. 161-170.

Chapter 3

Comparative Study of Gaseous and High-Pressure Liquid Reactions in Industrial Chemistry

3.1. Background

According to the U.S. Bureau of Economic Analysis (BEA), chemical manufacturing contributed \$837.3 billion to the U.S. economy in 2017.[1] Related industries, including petroleum and coal, food and beverages, and paper products contributed an additional \$1.7 trillion over the same time period.[1] This productivity comes with substantial environmental cost, as the chemical and petrochemical industry consumed 19×10^9 J (19 GJ) in 2016, making it the single largest energy consumer in the industrial sector.[2] A similar report by the International Energy Agency (IEA)[3] indicated that the chemical industry emitted the equivalent of approximately 900 Mtons of CO_2 in 2016, second only to primary metals production in the industrial sector.[2] Accordingly, the chemical process industries are under intense pressure to maintain profitability as energy costs rise.[2, 4] The IEA defined best practices for energy use reduction that, if implemented, could reduce the energy use in the chemical and petrochemical industry by 6.4 EJ, the equivalent of 21% of the total energy used by the chemical industry in 2004.[3] A 2013 study published by IEA, the International Council of Chemistry Associations, and Society for Chemical Engineering and Biotechnology (DECHEMA) advised that process improvements could reduce energy demand of

the 18 most important chemical products by 20 to 40%, with absolute energy savings of 13 EJ and annual CO_2 emissions reductions of 1 Gt by 2050.[3]

Process intensification (PI) offers the potential to achieve dramatic changes in the chemical industries, in terms of energy use, cost, and waste reduction.[5] In their review, Van Gerven and Stankiewicz[6] list more than six definitions of process intensification, with a common theme for using innovative chemical technologies to develop new processes with reduced cost, volume, energy use, and waste generation than is currently possible. Van Gerven and Stankiewicz[6] describe four basic principles of PI: maximize the effectiveness of intramolecular and intermolecular events, give each molecule the same processing experience, optimize driving forces at every length scale, and maximize synergistic effects from partial processes. Many specific PI approaches have been suggested in the literature[5] including multifunctional reactors,[7] cascade catalysts,[8] reactive separations,[9] periodic, dynamic, and integrated control strategies,[10] structured catalytic particles or reactor internals to promote or control mixing,[11] miniaturization or use of microreactors,[12] and localized use of energy, for example as is possible with ultrasound[13] and microwave technologies.[14]

Manipulation of phase behavior is a special class of PI technology. Engineering of processes consisting of multiple phases can reduce thermodynamic bottlenecks by removing products as they form, for example in reactive separations such as reactive distillation and reactive extraction.[15] For example, Román-Leshkov et al.[16] described the use of reactive extraction into an organic phase to increase the selectivity toward hydroxymethylfurfural produced from fructose dehydration, reporting 80% selectivity at 90% conversion. In the absence of the extraction phase, hydroxymethylfurfural re-polymerizes to form humins, thereby limiting selectivity.[17] Fan et al.[18] reported the use of chemical looping, which is a gas-phase chemical reaction enabled by a

reactive solid intermediate, to produce hydrogen and other products from carbonaceous fuels such as coal. Ma et al.[19] reported ethanol steam reforming in a membrane reactor to increase hydrogen yield by 122% over the traditional reactor configuration.

Reactors containing one or more liquid phases are used commonly in the pharmaceutical industry,[19] yet rarely in the petrochemical industry.[20] However, because the densities of liquid phases are typically at least 100× greater than their vapor phases, the use of liquid phase reactors has potential for PI. In their work on synthetic fuels production, Dahmen et al.[21] find that operation at pressure increases process intensity sufficiently to justify the need for more robust process design. Similarly, biomass feeds, which invariably contain moisture, benefit from operation under liquid phase conditions that reduce or eliminate the need for energy intensive drying steps.[22] Because most petrochemical processes of interest, especially reactions, take place at temperatures above 100 °C, maintaining a liquid phase will generally require operating at a pressure greater than ambient (0.1 MPa). Operation at pressure requires additional energy for pumping and design of process vessels, tubing, and valves with additional wall thickness and/or stronger materials than would be required for operation at or near ambient pressure. However, many petrochemical processes already take place at pressures much greater than ambient,[23, 24] meaning that pressure on its own does not represent an insurmountable roadblock.

This discussion demonstrates that process engineering – and especially reaction engineering – with compressed liquid phases may have potential as a PI technology. However, the effects of operating with a compressed liquid on process energy requirements and costs are less clear. In fact, guidelines for when to consider operating a process under liquid phase conditions have not been commonly applied. Moreover, the effects of thermodynamic phase on rates – especially reaction rates – must play an important role in the decision to design a process for vapor phase (as is typical)

or condensed liquid phase operation. Studies that compare reaction rates in liquid phases to those in vapor phases are scarce, which adds uncertainty to the decision. Jaacks et al. studied ethylene radical polymerization reaction with carbon tetrachloride under both liquid and vapor phase conditions and observed negligible differences in chain propagation with operating pressure.[25] In contrast, Gendy[26] simulated a xylene isomerization in a fixed bed reactor, and reported that isomerization rates in the liquid were less than those in the vapor phase, however, liquid phase isomerization was more catalytically efficient due to reduced oligomerization rates. Similarly, Zhao et al.[27] reported that aqueous phase phenol hydrodeoxygenation followed a different reaction pathway with different kinetic rates compared to previous vapor phase hydrodeoxygenation studies.[28, 29]

The previous discussion indicates that rate factors specific to the reactions/processes under consideration may sometimes complicate analysis; in any event, the effects of thermodynamic phase on rate phenomena must be considered in any serious design. However, rate parameters, especially reaction rates of heterogeneously catalyzed reactions (i.e., fluid-solid reactions) are not easily predicted *a priori* with accuracy. On the other hand, the effect of reaction phase on thermodynamic quantities is more readily predicted.[30] Accordingly, thermodynamic considerations can be used to identify which processes have the potential to benefit from liquid phase operation. If thermodynamic analysis fails to justify operation as a compressed liquid phase, then it should not receive further consideration. On the other hand, if thermodynamic analysis indicates sufficient PI benefits, then further evaluation of reaction rates and ultimately costs may be merited.

In this work, therefore, we describe a thermodynamic and generalized process analysis that can be used to guide decisions on the use of liquid phases in process engineering. A specific focus is

on reaction engineering, as reactors are typically central to overall process design. We consider the effects of density on PI, the energy requirements of liquid phase versus vapor phase processes, thermal management in liquid phases, and cost of intensified reactors to establish guidelines to be used to decide when liquid phase processes may be advantageous over ones operating under vapor phase conditions. Lastly, we introduce several case studies to demonstrate the method. This analysis will guide future work that seeks to use liquid phase operation as a means to reduce process volume, energy requirements, and cost.

3.2. Methods

3.2.1 Property data and models.

All enthalpy and thermal conductivity data were obtained as functions of temperature or pressure from the NIST Chemistry Webbook.[31] Heat capacity (c_p), latent heat of vaporization (ΔH^{vap}), and density (ρ) values for pure water, alkanes, aromatics and cyclohexane were also taken from the NIST Chemistry Webbook.[31] Specifically, c_p and ΔH^{vap} were used to calculate heating costs. All alcohol saturated density values were estimated from the modified Racket equation, as recommended by Spencer et al.[32] Liquid density and enthalpy values for mixtures were modeled using Aspen Plus V8.8 software using the UNIQUAC method.[33] **Table 3.1** lists critical properties of water and other common hydrocarbons used to calculate reduced temperature and pressure conditions for several plots.

Table 3.1. Phase change data of water and common alkanes

Compound	Normal Boiling Point T_b (°C)	Critical Temperature T_c (°C)	Critical Pressure P_c (MPa)
Water	100	374	22.1
Ethane (C$_2$)	−88.6	32.3	4.9

Butane (C$_4$)	0.0	152	3.8
Octane (C$_8$)	125.6	295.8	2.5
Dodecane (C$_{12}$)	215.9	385.1	1.8
Hexadecane (C$_{16}$)	280.9	448.9	1.4

3.2.2 Pumping calculations.

Pumping size and energy requirements for a water stream were performed in order to calculate total energy requirements in **Figure 3.5,** which were estimated using heuristics from a correlation provided by Sarver et al.[34] for a centrifugal pump. Briefly, pump sizing requires calculation of the total dynamic head pressure based on water flow through a pump at atmospheric inlet pressure, varying discharge pressure, and identical suction and discharge tube radii. Pump volume was normalized to the pumping flowrate and used 1 kg min^{-1} of water feed as a basis. The motor efficiency of 76% was estimated based on the Peter and Timmerhaus correlation[35] using a brake horsepower of 0.237 hp and the pumping efficiency was estimated as 55%.

3.2.3 Thermodynamic Equilibrium Calculation

The effect of solvent concentration on the thermodynamic equilibrium for reaction of the form: $A \rightleftharpoons B + S$ is examined, where product species S is also added as a solvent in the feed with reactant A. The calculation is performed using Equation 1:

$$\Delta G_{rxn}^{\circ} = -RT \ln(K_{eq}) = -RT \ln\left(\frac{a_B a_S}{a_A}\right) = -RT \ln\left(\frac{x_B x_S}{x_A}\right) \qquad (1)$$

Where ΔG_{rxn}° is the Gibbs free energy of reaction where all species are in a reference state, R is the gas constant, T is temperature (K) and a_i (referencing the same state as ΔG_{rxn}°) and x_i, are the activity and mole fraction of species i. A, B, and S refer to reactant, product, and solvent/product, respectively. The final equality in Equation (1) requires assumption of ideal solution behavior for

all reactants and products, so that $a_i = x_i$. Redefining Equation (1) using the molar extent of reaction method, the molar conversion (X) at equilibrium is defined using Equation (2):

$$X = \frac{x_{B,e}}{x_{A,e} + x_{B,e}} = \frac{1}{x_{S,e}/e^{-\Delta G^\circ_{rxn}/RT} + 1} \tag{2}$$

Where $x_{i,}$ is the final molar concentration of species i at thermodynamic equilibrium.

3.2.4 Heat transfer calculations.

The convective heat transfer coefficient (h_i) for an inner tube side analysis for a heat exchanger was estimated using the Gnielinski correlation[36] for forced convection in a turbulent, fully developed tube, provided in Equation (3):

$$Nu_D = \frac{h_i D}{k} = \frac{(f/8)(Re_D - 1000)Pr}{1 + 12.7(f/8)^{1/2}(Pr^{2/3} - 1)} \tag{3}$$

Where the Darcy friction factor (f) is estimated using the Petukhov correlation, provided in Equation (4):[37]

$$f = (0.79(Re_D) - 1.64)^{-2} \tag{4}$$

The water properties on the inlet side of the heat exchanger are applied to the entire heat transfer calculation, including constant pressure heat capacity (c_p), density (ρ), thermal conductivity (κ) and viscosity ($\square$). Two scenarios were used to calculate the mass flux (J) normalized heat transfer coefficient for the tube heat exchanger: either constant fluid linear velocity and varying tube dimensions or constant tube dimensions and varying fluid velocity. Both scenarios maintained turbulent flow with Reynolds numbers between 3,000 and 146,000. A description of each scenario is detailed in **Table 3.2**. The ranges in tube diameter and Reynold's number were used in order to either maintain a constant linear velocity as well as turbulent flow. The fluid temperature and pressure was selected to span the range of subcritical water conditions up to its critical point.

Table 3.2. Tube heat exchanger scenarios either constant linear velocity (*v*) or tube diameter (*D*)

Scenario	1: Constant Linear Velocity (*v*)	2: Constant Tube Diameter (D)
Mass flowrate - ṁ (kg/min)	10	10
Linear velocity - v (m/min)	5	varies
Tube diameter - D (m)	varies (0.05 to 2.7 m)	1.26
Inlet fluid T (°C)	varies (100-350)	varies (100-350)
Inner fluid P (MPa)	varies (0.1 to 25)	varies (0.1 to 25)
Tube wall T (°C)	20	20

3.2.5 Pressure vessel cost estimates.

To estimate costs of pressure vessels, reactor wall thickness was first determined using the method recommended by Farr et al.[38] for cylindrical geometry, either using Equation (5):

$$t = P \cdot r / (SE - 0.6P) \qquad (5)$$

for vessels operating at atmospheric pressure or Equation (6) for vessels operating at pressures greater than atmospheric:

$$t = R[(SE + P)/(SE - P)]^{1/2} - r \qquad (6)$$

In these correlations, *t* is the vessel wall thickness, *r* is the vessel internal radius, *S* is the maximum allowable stress of the material, *E* is the joint efficiency factor, commonly estimated as 0.85,[38] and *P* is the internal pressure. The maximum allowable stress is determined based on the yield strength of each material, as reported on technical data sheets.[39-43]

3.3. Results and Discussion

Many, or even most chemical reactions used in the petroleum and petrochemical industries are performed in the vapor phase.[44, 45] Vapor phase operation affords some advantages, chiefly that the reactor can be operated at modest pressure (< 1.0 MPa). However, liquid phase operation can be advantageous, providing benefits with respect to process intensity, energy demand, thermal management, and cost. While some of these benefits may be intuitive, others are not, and

quantifying the trade-offs can help identify where operation in liquid phase can justify the uncertainties in pressure/phase dependent activity change or process safety. Pressurized systems, even at the scale of mico sized capillaries,[24] pose safety concerns that warrant proper risk assessment and minimization.[46] The objective of this work, therefore, was to quantify the potential intensification, energy, and cost benefits of liquid phase operation. The final section describes several representative case studies that provide insight on when liquid phase operation may be worth considering or when vapor phase operation is clearly preferred over the liquid phase.

3.3.1 Process Intensity.

The most important difference between the liquid and vapor phases is that the molecular density of liquids is many times greater than that of vapors, on the order of 10 to 1,000 times greater, depending on the fluid and thermodynamic state. The difference in liquid and vapor phase densities gives rise to a potential increase in process intensity, defined here as the net rate of product formation per unit reactor volume. Using a first order reaction of the form A→B in an isothermal, plug flow reactor (PFR) as an example, the volumetric increase in overall product formation rate can be demonstrated. The reaction rate is defined as $r_a = k_A[A]$, which can be combined with the PFR design equation to yield the familiar equation:[47]

$$V = \int_{C_{A0}}^{C_A} \frac{vA}{r_a} dC_A = \frac{\dot{m}}{\rho k} \ln\left(\frac{1}{1-X}\right) \qquad (7)$$

where $\dot{m}$ is the inlet mass flow rate, v is the fluid linear velocity, A is the reactor cross sectional area, ρ is the fluid density, and k is the reaction rate constant. Equation (7) allows comparison of the volumes required to achieve a desired conversion, X, of two reactor operating under liquid and vapor phase conditions at identical flow rates and temperatures. After cancelation of flow rate and conversion terms to be held constant in the two scenarios, the resulting relationship describing the

ratio of the reactor volumes required for operation at two different densities (e.g., liquid and vapor at different pressures but at the same temperature) is given as:

$$\frac{V_2}{V_1} = \frac{\rho_1 k_2}{\rho_2 k_1} \qquad (8)$$

The ratio of the two reactor volumes depends on both the reaction rate constant and density of the fluid. Interpretation of Equation (8) when comparing two conditions with identical reaction temperatures requires calculation of the respective densities and consideration of the effects of phase and/or density on reaction rate constants. The rate constant of homogeneous reactions can depend on phase due to pressure effects,[48] solvation,[49] and potentially diffusion rates. Except under unusual circumstances, these effects are generally minor.[50] Reaction rate constants of heterogeneous reactions can be influenced by the phase or density of the solvent by several mechanisms, including reactant adsorption energy,[51] competitive adsorption, modification of intrinsic activity,[25, 52] catalyst destabilization[52-54] or fluid-fluid or fluid-solid[55] mass transfer limitations. No general theory exists for predicting the dependence of heterogeneous reaction rate constants on fluid phase. To first order, in many cases the effects of phase on reaction rate constants can be considered to be minor, resulting in simplification of Equation (8) to yield:

$$\frac{V_2}{V_1} = \frac{\rho_1}{\rho_2} = IF \qquad (9)$$

where the intensification factor (*IF*) can be defined as the ratio of volumes of two reactors operating at different densities and/or pressures while provided the same conversion at the same inlet mass flow rate. In fact, while Equation (9) was derived explicitly for reactor engineering, similar considerations could equally be applied to many other processes of interest, for example separations, with only minor adjustments. Under other processes without a reaction, the simplification made in equation 8 would be unnecessary and the intensification factor would be directly related to the corresponding fluid densities.

For comparison of liquid operation to vapor operation, Equation (9) indicates that the resulting

IF exactly equals the inverse ratio of respective densities, which is a natural consequence of the

effect of density on linear velocity and/or reactor residence time. Since the liquid phase density of

a given substance is always greater than its vapor phase density, Equation (9) predicts that a liquid-

vapor *IF* will always be >1, which is consistent with greater process intensity in the liquid phase

than in the vapor. Therefore, in this study, a pressurized, "intensified" phase (terms V_1 and ρ_1 in

Equation (9), irrespective of the phase of the pressurized fluid is compared relative to the same

substance or mixture at atmospheric pressure (0.1 MPa) when calculating *IF* (terms V_2 and ρ_2 in

Equation (9).

Increasing process intensity affords several potential benefits, including decreasing the amount

of material required for process construction, reducing equipment size so that it can be made

transportable, and potentially reducing costs (see Section 3.4). The magnitude of these benefits

depends on the ratio of liquid to vapor densities, which in turn depends on reaction temperatures

and pressures and the thermodynamic behavior of the solvent itself.

Although *IF* will depend on the properties of the solvent or carrier gas, water is a natural choice

as a model, given the importance of water in many processes. **Figure 3.1a** provides plots of *IF*

calculated for pressurized water (either in its liquid or vapor state) at various pressures relative to

the vapor phase water at the same temperature and a fixed pressure of 0.1 MPa. The effects of

thermodynamic conditions are parameterized using reduced temperature (T_r) as the horizontal axis

and plotting data isobarically using reduced pressures (P_r). When comparing the pressurized liquid

state to the vapor state at 0.1 MPa, *IF* is much greater than one, ranging from 1,500 to 2,000, and

is largely independent of pressure except as the critical point is approached and liquid-phase

density becomes a strong function of pressure. For comparison of pressurized vapor states to the

vapor at 0.1 MPa, *IF* varies from 1 to 100 and is highly dependent on pressure, a natural consequence of the compressibility of the vapor phase. Liquid phase isobars of *IF* exhibit a discontinuity when P_r reaches the saturation pressure, an effect that is captured by the vertical lines in **Figure 3.1a**. For $P_r \geq 1$, the liquid and vapor phases can no longer be distinguished from one another as the fluid exists as a supercritical fluid, and the isobars no longer exhibit a vapor-liquid discontinuity. Accordingly, for $P_r \geq 1$, *IF* is strongly temperature dependent, as expected based on the compressibility of fluids near their critical point.
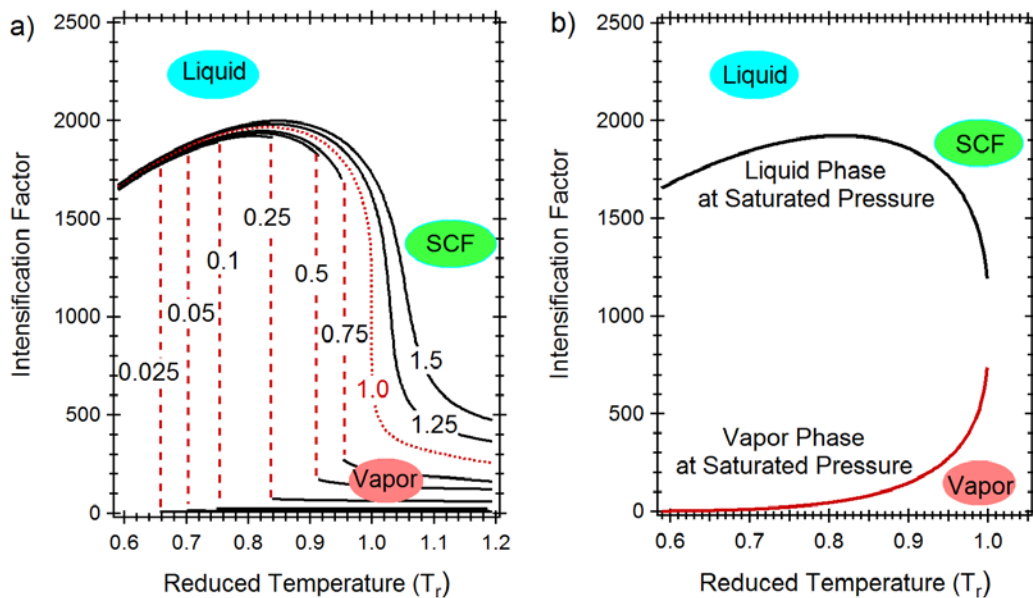
Figure 3.1. Plot of the temperature dependent intensification factor (IF) of water when operating in a compressed phase relative to atmospheric pressure. **Figure 3.1a** plots water's isobaric lines between reduced pressures of $P_c = 0.025$ and 1.5, as indicated in the figure. The red dotted lines in **Figure 3.1a** represent discontinuity in IF between liquid and vapor phase. **Figure 3.1b** compares the IF for water's saturated liquid and vapor lines.

To capture the behavior near the critical point in more detail, **Figure 3.1b** plots a single *IF* curve at varying pressures required for saturated liquid and vapor water phases and again as a function of T_r. Because the difference between saturated liquid and vapor water states is based on the

minimum pressure difference required for phase change, **Figure 3.1b** allows direct comparison of the effect of liquid or vapor state on *IF*. Expectedly, the *IF* determined for saturated phases is always much greater in the liquid phase than in the pressurized vapor. For $T_r < 0.9$, the *IF* of the saturated liquid is approximately $100\times$ greater than in the saturated vapor. For T_r greater than 0.9 but less than 1.0, *IF* of the saturated liquid and vapor phases converge, as expected given the behavior at near-critical conditions. At the critical point, saturated liquid and vapor water states converge into a single supercritical fluid phase. However, increasing pressure can still result in increased process intensity above the critical point, at least relative to a process operating at 0.1 MPa, as shown in **Figure 3.1a** with an increased *IF* with an increase in P_r isobaric lines at conditions where $T_r > 1$.

Figure 3.1 is specific for water, an important solvent yet one with distinctive properties, including unusually high liquid phase density. However, similar intensification considerations apply to all fluids, as the liquid phase of a fluid is always denser than its vapor phase at the same temperature. **Figure 3.2** provides *IF* calculated for saturated liquid phases as a function of T_r for water, alcohol, several aromatic hydrocarbons, and alkane solvents, again relative to vapor phase operation at 0.1 MPa. Provided that $T_r < 0.95$, *IF* of the saturated liquid is always greater than 100, indicating the potential intensity benefits of operating in the liquid phase. Beyond this general observation, several trends emerge. First, as expected, water is an outlier in this analysis, with a greater *IF* than any of the other substances and at all values of T_r. Second, *IF* calculated for the hydrogen bonding alcohols is greater than that of the corresponding alkane with the same number of carbons, a direct consequence of the effects of hydrogen bonding on liquid phase density. On the other hand, *IF* for hydrocarbons decreases with increasing hydrocarbon chain length, a consequence of the comparatively low densities of short-chain compounds in the vapor phase.

Moreover, since the critical points of short-chain compounds are much less than the temperatures and pressures used in petrochemical processes, as shown for alkanes in **Table 3.1**, liquid phase operating conditions may not be as beneficial as suggested simply by consideration of their vapor/liquid density ratios since a distinct liquid phase may not exist at relevant process temperatures. In these cases, the fluid will exist as at supercritical conditions, which can still provide PI benefits relative to operation at 0.1 MPa.
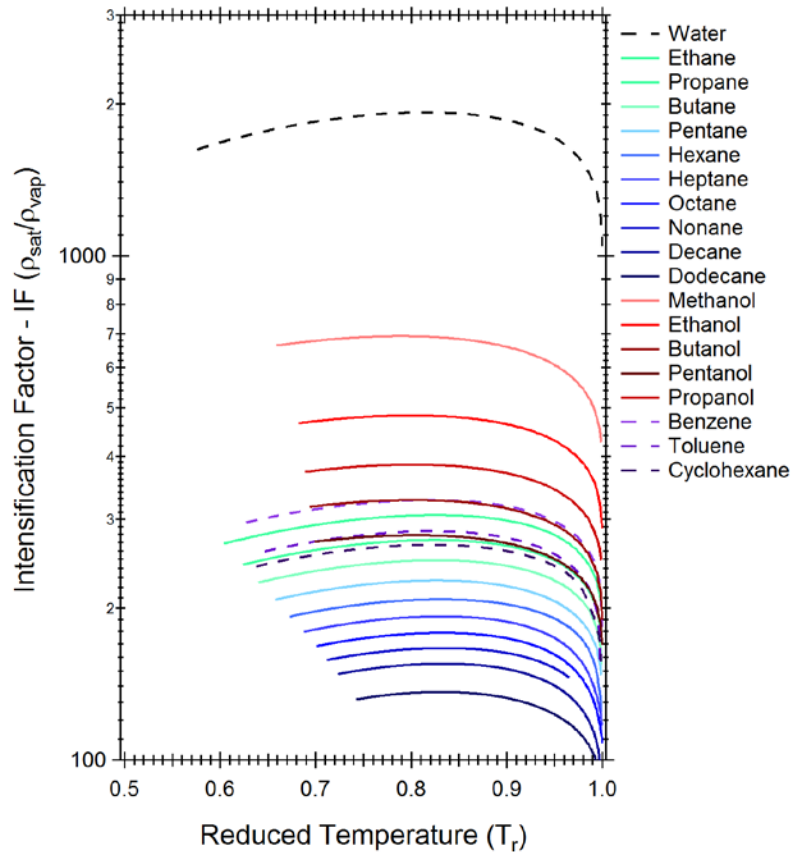
Figure 3.2. Intensification factor (IF) of saturated water and common liquid hydrocarbons at varying reduced temperatures. IF is defined in Equation (9) and is an estimate of the relative volumes of a process operating at 0.1 MPa compared to a pressurized process operating at a saturated pressure but at the same temperature.

Figures 3.1 and 3.2 apply only to situations in which the reactants are dissolved in the solvent phase or vaporized into the carrier gas. The benefits of liquid-phase operation on the process intensity of dispersed solid particles, such as biomass feeds, require separate consideration from feeds that consist of a single fluid phase. The density of the continuous phase does not directly influence process intensity for feeds that include dispersed solid particles. Instead, process intensity is determined by the volume fraction of solids present in the continuous phase. For common processes involving biomass particles, the volume fraction of solids will be on the order of 10-20 vol%,[56] and independent of continuous phase density. So, while processes involving particulate feeds do not receive the *IF* benefit shown in **Figures 3.1 and 3.2**, liquid phase operation can still benefit these processes due to improved energy balance and thermal management, as the next two sections describe.

The *IF* considerations summarized in **Figures 3.1** and **3.2** exclude potential effects of solvent density on reaction equilibrium. In general, these effects minimally influence activity, for example if reactants (or products) are preferentially solvated, resulting in a difference in $\Delta G°_{rxn}$ when liquid and vapor phase conditions are compared. In the special case of the solvent also being a reactant or product of the reaction, solvent density may play a larger role in apparent activity. Hydrolysis and dehydration reactions are particularly important examples. In these cases, increasing water density can either shift equilibrium towards products or towards the reactants, depending on the role of the solvent in the reaction and as a consequence of Le Chatelier's principle.[30]

To evaluate Le Chatelier's effect on a reaction for which the solvent is also a product, consider the model reaction $A \rightleftharpoons B + S$, where species A is the reactant and B is the product, and S is both the solvent and a product. Equation (1), introduced in the Methods, was then used to examine the

effect of x_s on the conversion of A for different values of ΔG°_{rxn}. **Figure 3.3** plots molar equilibrium

conversion (X) of species A at a reaction temperature of 600 K as a function of x_s, calculated at

discrete values of ΔG°_{rxn} ranging from +25 to –25 kJ mol^{-1}. This range was selected as any value

of ΔG°_{rxn} less favorable than 25 kJ mol^{-1} is insensitive to x_s. **Figure 3.3** shows that equilibrium

conversion is most sensitive to x_s when $\Delta G^\circ_{rxn} = 0$ kJ mol^{-1}, with any deviation from this value

resulting in decreased x_s sensitivity. For the cases of most practical interest, $\Delta G^\circ_{rxn} < -10$ kJ mol^{-}
^{1} and the sensitivity of equilibrium conversion to x_s is modest. One important counter example is

the reverse water-gas-shift reaction ($CO + H_2O \rightleftharpoons CO_2 + H_2$), which can be run at equilibrium-

limited conditions. On the other hand, equilibrium conversion of the water-gas shift reaction and

other water or solvent consuming reactions benefit from increasing water density.
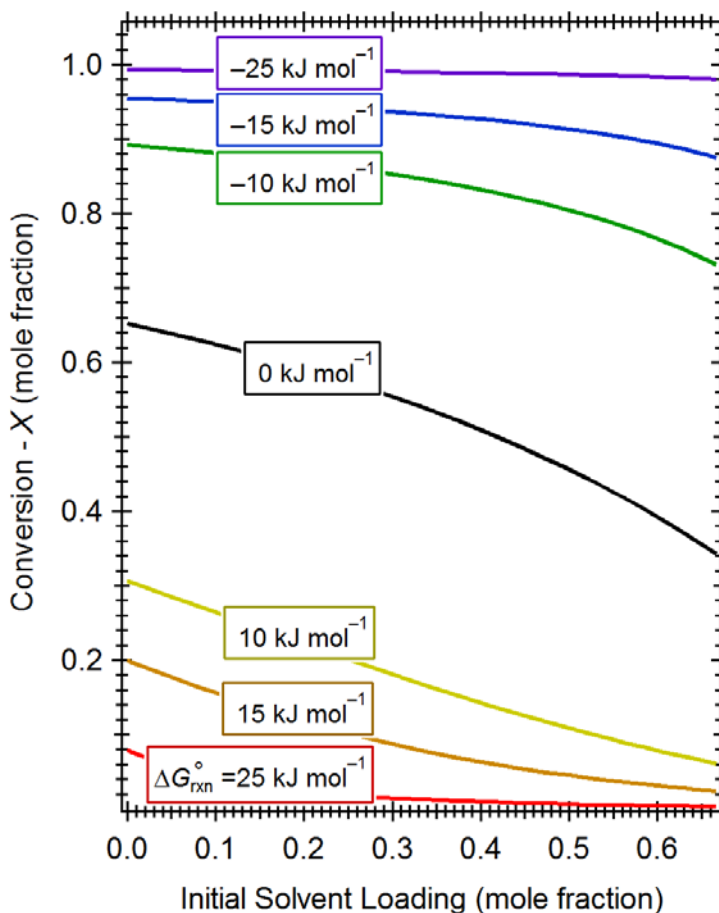
Figure 3.3 The theoretical molar conversions from a thermodynamic equilibrium calculation for chemical reaction A $\rightleftharpoons$ B + S operated at a reaction temperatures of 600 K with varying initial molar solvent (S) loading. Each line is calculated at a constant Gibbs free energy of reaction ΔG_{rxn}°

The method used to generate **Figure 3.3**, summarized previously in Equation (1), assumes ideal gas and/or ideal solution behavior, i.e., K_ϕ or $K_\gamma = 1$.[30] The assumption of ideal gas/ideal solution behavior is required for a simplification that is also broadly applicable, and for detailed analysis these effects should be included. However, the approximation is reasonable to first order, assuming that the reaction mixture is not near a liquid-liquid phase boundary.[57] And, as with temperature, the first-order effect of non-ideal gas or solution behavior will mostly be variation of the equilibrium conversion, but not the dependence of equilibrium conversion on x_s. In terms of applicability, Alexopoulos et al.[58] performed a rigorous thermodynamic analysis of ethanol dehydration to produce ethylene and water, reporting that equilibrium conversion is insensitive to water concentration (x_s) for most practical situations, a consequence of $\Delta G_{rxn}^{\circ} < -10$ kJ mol^{-1} at all temperatures of interest. Similarly, dehydration reactions of carbohydrates are often performed in aqueous mixtures, with no adverse effect on equilibrium conversion.[59, 60] These previous studies therefore support the general point that equilibrium conversion is insensitive to solvent concentration even for reactions for which the solvent is also a reaction product, at least for most practical situations. On the other hand, solvothermal reactions, that is reactions in which the solvent is also a reactant, will benefit from increasing x_s, a direct consequence of the Le Chatelier's principle shown in Figure 3 for solvent producing reactions. Since ΔG_{rxn}° can be calculated with accuracy, Figure 3 is a general guide to determine whether equilibrium conversion considerations eliminate liquid phase operation as a practical option for a given reaction. That stated and as a rule

of thumb, the effect of x_s on equilibrium conversion will not typically be a major design factor, provided that $\Delta G^{\circ}_{rxn} < -25$ kJ mol^{-1} as it often is.

3.3.2 Energy Requirements

Considerations of *IF* suggest that liquid phase operation may have advantages over the vapor phase, especially for fluids and under conditions at which the liquid density is substantially (>100×) greater than the vapor phase. However, compression to form the liquid phase requires energy, and therefore liquid phase operation might reasonably be expected to require more energy than vapor phase, even when the operating temperature is held constant. On the other hand, liquid phase operation avoids additional heating associated with overcoming the latent heat of vaporization, and the net effect on energy consumption between increased pumping and decreased heating costs is therefore uncertain. Considering first the latent heat of vaporization, the enthalpy of water as a function of T_r and at P_r ranging from 0.05 to 1.25 is shown in **Figure 3.4**. For each isobar, the enthalpy exhibits a discontinuity at the vaporization temperature, with the magnitude of the discontinuity equalling the latent heat of vaporization. The latent heat is on the order of 2 MJ kg^{-1} and decreases with increasing pressure. Regardless, at all conditions, the enthalpy of the vapor is much greater than the enthalpy of the liquid phase; avoiding the latent heat of vaporization by operating in the liquid phase therefore decreases overall process heat requirements.
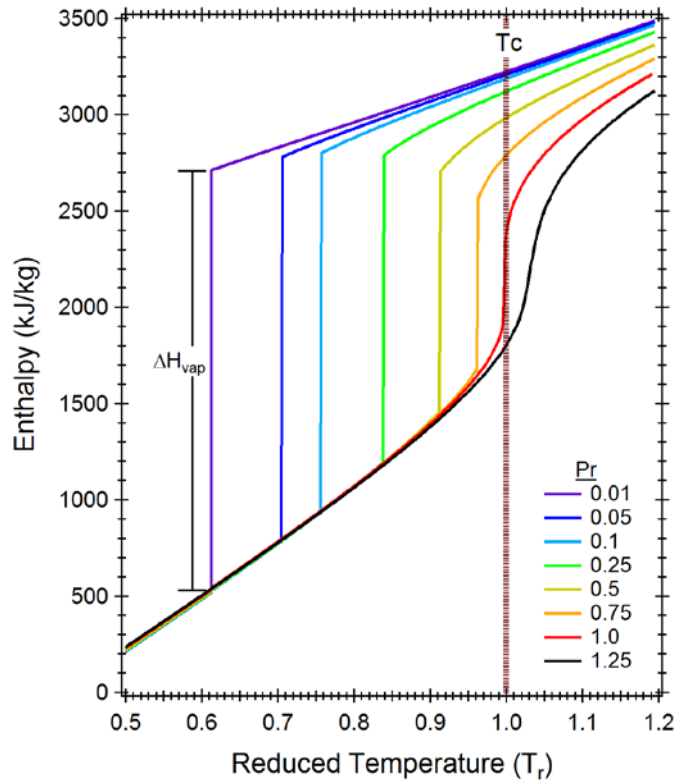
Figure 3.4. Plots of isobaric enthalpies lines of water with varying operating pressures.

Figure 3.4 demonstrates the importance of the latent heat of vaporization on enthalpic

considerations. However, latent heat is only one component of the energy required to operate at a

given temperature and pressure. The complete energy requirement includes pumping to the desired

pressure, followed by vaporization (if required), and heating to the desired temperature. It should

be noted that all pumping energy calculations were performed at an initial temperature and pressure

of 25 °C and 0.1 MPa, since the complete energy calculations for pumping (work) and heating

(enthalpy) are pathway dependent. **Figure 3.5a** is a contour plot of the energy required for liquid

and vapor phase operation as functions of T_r and P_r, calculated for water. In all cases, the energy

required for operating in the liquid phase is less than that required for vapor phase operation,

generally by at least 0.5 MJ kg^{-1}. **Figure 3.5a** suggests that the pumping energy is less than the

sensible heat and latent heat requirements. **Figure 3.5b** plots the fraction of the total energy

required for pumping, confirming that pumping is always less than 15% of the total energy required to operate at a given T_r and P_r, regardless of the state of the working fluid. As expected at a given T_r, pumping is a greater fraction of the total energy in the liquid phase than the vapor; however, the increased pumping energy is more than offset by the avoidance of the latent heat of vaporization. While the results shown in **Figure 3.5** are robust, they are limited to P_r on the order of 1.0. For P_r sufficiently greater than 1.0, pressurized operation will become less energetically favorable than operation at 0.1 MPa, due to increasing pumping costs; however, operation at $P_r \gg$ 1 is not typically relevant to industry and is not shown in **Figure 3.5**.
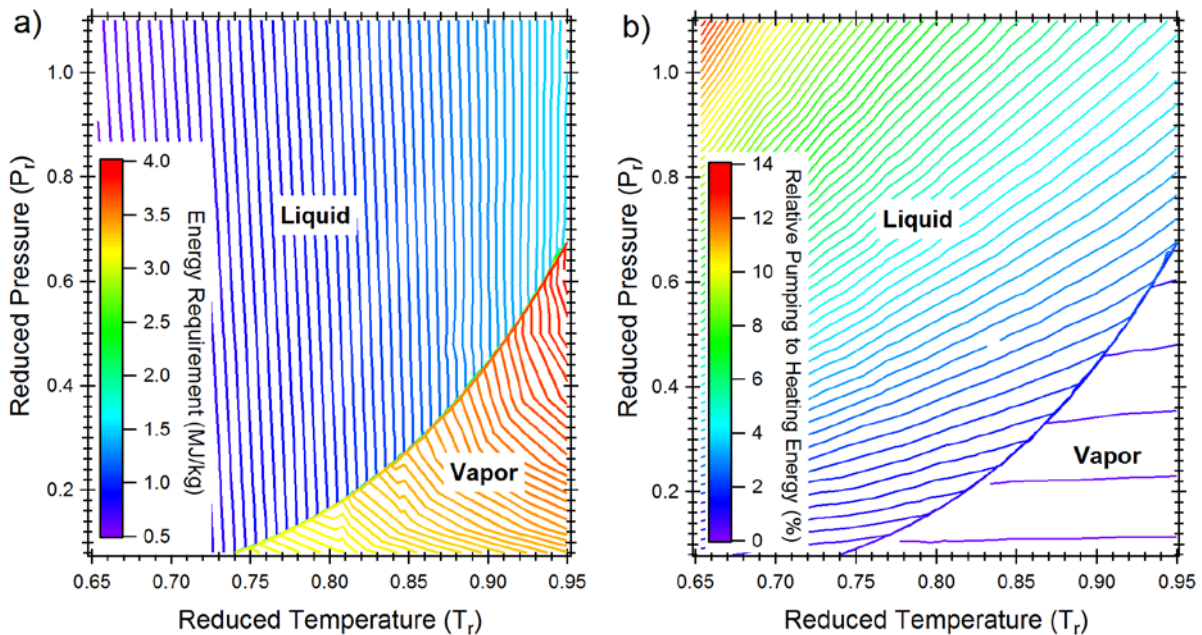
Figure 3.5. a) Contour plot of total energy (in MJ kg^{-1}) required to heat and pump water at varying reduced pressures ($P_r = P/P_c$) and reduced temperatures ($T_r = T/T_c$). b) Contour plot of pumping to heating ratio at varying reduced pressures and reduced temperatures.

The analyse in **Figure 3.4** and **Figure 3.5** are especially important for biomass and mixed waste mixtures. **Table 3.3** lists representative biomass and waste feeds, their higher heating values, and

typical moisture contents. The moisture content of green biomass is greater than 10 wt%, sometimes as great as 95 wt%. **Table 3.3** lists drying energy for the different feeds calculated based on a thermal requirement of 3–4 MJ/kg of water removed.[61] The energy required to dry these feeds is up to 42% of the energy inherent within the feed itself based on its higher heating value. For biomass feeds with moisture content greater than 20 wt%, liquid-phase processes such as hydrothermal liquefaction, aqueous phase reforming, and hydrothermal carbonization are therefore more energetically favorable than vapor-phase processes, such as pyrolysis, torrefaction, and gasification. Similar logic applies for processes aimed at chemical conversion of fermentation products (e.g., ethanol), as the water content of fermentation products is typically greater than 80 wt%.[62, 63]

Table 3.3 Biomass and waste slurry properties and drying energy requirements

Biomass Feed (wet)	Moisture Content (wt%)	Higher Heating Values, HHV (MJ/kg)	Drying Energy[1] (MJ/kg)	Refs
Undried Wood Chips	38-72	5–11.5	1.1–2.9	[64]
Dried Woody Biomass	6–10	15–19	0.2–0.4	[65-68]
Agricultural Residue	10–22	17.5–18.2	0.3–0.9	[69, 70]
Sugarcane Residue	40–75	7–18	1.2–3	[70]
Algae	68 – 95	12–13.4	2–3.8	[71, 72]
Municipal Solid Residue	35 – 85	2.4–11	1.1–3.4	[73-76]

[1]Drying energy estimated as the product of moisture content and the 3-4 MJ/kg operational energy requirement for a rotary dryer, as reported by Hanning et al.[61]

As in the *IF* analysis shown in **Figure 3.1**, the energy analysis shown in **Figure 3.4** and **Figure 3.5** is restricted to water. Since the latent heat of vaporization of water is greater than most other common fluids,[55] the observed trends in energy requirements shown in **Figure 3.5** may not be applicable to other solvents, which warrants further investigation. **Table 3.4** provides latent heat

of vaporization data for several representative fluids, including water. As expected, the heat of

Compound	Reduced Temperature, T_r (Actual Temperature, °C)	Reduced Pressure (P_r)	Heat of Vaporization ΔH_{vap} (MJ kg^{-1})	Saturated Liquid Heat Capacity $C_p^{sat,liq}$ (MJ kg^{-1} K^{-1})	Latent to Sensible Heat Ratio[1] $\Delta H_{vap}/C_p^{sat,liq}\Delta T$
Water	0.6 (115 °C)	0.0076	2.22	.00424	5.5
	0.7 (180 °C)	0.045	2.02	.00441	2.9
	0.8 (244.6 °C)	0.16	1.74	.00482	1.6
	0.9 (309 °C)	0.44	1.34	.00605	0.76
Hexane	0.7 (82 °C)	0.05	0.33	.00252	2.1
	0.9(184 °C)	0.46	0.21	.00327	0.4
Cyclohexane	0.7 (115 °C)	0.062	0.33	.00232	1.5
	0.9 (226 °C)	0.48	0.21	.00311	0.32
Dodecane	0.7 (188 °C)	0.023	0.27	.00285	0.57
	0.9 (319 °C)	0.34	0.17	3.49	0.17
Methanol	0.7 (86.1 °C)	0.027	1.06	3.02	5.3
	0.9 (188.7 °C)	0.39	0.69	4.74	0.86

vaporization for water is an order of magnitude greater than other substances, with the exception of methanol. Nonetheless, the latent heats of vaporization shown in **Table 3.4** are similar in magnitude and generally greater than pumping requirements, indicating that liquid-phase operation will generally be more energy efficient than vapor phase operation. The general benefit of liquid phase operation is further indicated by the fact that the latent heat of vaporization is generally greater than the sensible heat required to reach a desired temperature, as shown in **Table 3.4**. Water is simply an exceptional case in terms of the magnitude of the effect.

Table 3.4. Heat of Vaporization and Heat Capacities of water and other hydrocarbon solvents.
[1]Sensible heat was calculated based on a reference temperature of 20 °C

3.3.3 Thermal Management

While operation in the liquid phase may reduce energy requirements relative to the vapor phase, energy is still required to heat the liquid phase to reaction temperatures. Based on **Figure 3.5**, heating constitutes at least 80% of the total energy and careful heat integration may be important for energy efficiency and/or cost considerations. Heat can be recovered by transferring heat from hot streams to cooler ones via recuperating heat exchangers, e.g., from the hot product stream to cool feed streams. The capital cost of heat exchangers is determined primarily by the total heat transfer area,[77] and, for a given temperature difference, the heat exchanger size depends on various parameters, including the thermal conductivity of the process fluid. For this reason, liquid-phase heat exchanger operation can confer a distinct advantage over the vapor phase, as the thermal conductivity of the liquid phase is much greater than that of the vapor phase.

The mass flux (J) normalized inner heat transfer coefficient (h_i) for double tube counter-current heat exchangers was calculated for liquid and vapor phase heat exchanger operation. Two scenarios are considered, both of which plot isobaric, heat transfer efficiency lines (h_i/J) as a function of the inner tube reduced temperature inlet either for constant fluid velocity (**Figure 3.6a**) or constant heat exchanger cross sectional area (**Figure 3.6b**). The heat exchanger scenario in **Figure 3.6a** maintains turbulent flow by holding linear velocity constant at 500 m min^{-1} while varying the heat exchanger diameter. **Figure 3.6a** indicates that heat transfer efficiency (h_i/J) is 50 to 130% greater in the liquid phase than the vapor phase. Fluid pressure has negligible effect on the mass flux normalized heat transfer coefficient except when phase change occurs, as shown by the discontinuities in isobaric lines when $P_r < 1.0$. The scenario in **Figure 3.6b** maintains turbulent flow at fluid velocities between 0.2 to 575 m min^{-1} while holding the inner tube area constant at 0.1 m^2. For constant inner tube cross sectional area, h_i/J is 1.6 to 3 times greater for liquid phase

operation than for the vapor phase at the same T_r. The improvements in heat transfer in **Figure 3.5** are attributable to a 10× increase in liquid water thermal conductivity, 4.5× increase in dynamic viscosity, and nearly 2000× increase in fluid density relative to vapor phase operation.

When comparing the heat transfer coefficient to the heat transfer efficiency (h_i/J), the improvement shown in **Figure 3.6** is significantly reduced, which is attributable to greater liquid phase densification (increase in IF) compared to vapor phase operation. The fact that liquid phase operation has any improvement in heat transfer efficiency (h_i/J) means that the increase in liquid state heat transfer properties (h_i) has a greater influence than the density. When the temperature difference between the hot and cold fluid are held constant, the increased thermal conductivity of the liquid phase allows either a decrease in heat exchanger size and/or increase in total fluid velocity relative to the vapor phase to achieve the same value of h_i/J.
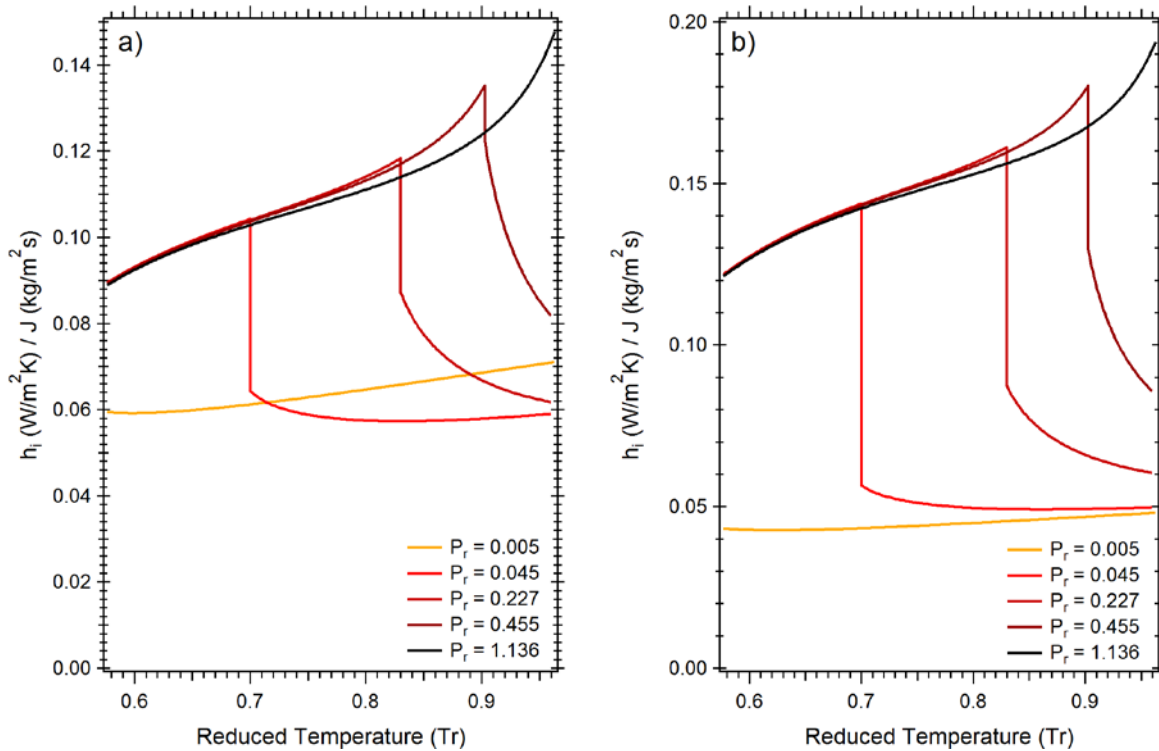
Figure 3.6. Plot of tube-side heat transfer coefficient of water normalized by mass flux (h_i/J) at varying reduced temperatures (0.5 to 0.95) and reduced pressures (0.005 to 1.14 MPa).

Discontinuity in the isobaric lines represents shift from liquid to vapor phase operation. a) plots h_i/J vs T_r at a constant mass flowrate of 200 kg/min and constant fluid linear velocity of 500 m/min. b) plots h_i/J vs T_r with a constant mass flowrate of 50 kg/min and constant inner tube diameter of 0.1 m^2. Further details of the heat exchanger scenarios in both figures is described in the methods section.

As a result of the heat transfer coefficient improvement expected for liquid phase operation, heat exchangers with liquid phase working fluids will be more compact and potentially less costly than those using vapor phase fluids. Moreover, heat exchangers operated at pressures designed for both fluids to remain pressurized as liquids will avoid boiling and condensing films, both of which complicate exchanger design because of flow maldistribution and often reduce thermal effectiveness.[56] Conversely, constructing a heat exchanger for high-pressure operation may require use of greater amounts or more costly materials than would a low pressure equipment. However, since the pressure of the two fluids will equal another, only the outer walls need to be designed to hold pressure.

As with process intensity, heat exchange for solid-fluid process streams is a special case. Of these, biomass slurries are especially important, since heat exchange in hydrothermal liquefaction, carbonization, and gasification is important for energy efficient system designs.[37, 78] In fact, a previous process design analyses of hydrothermal liquefaction operation considered the thermal conductivity of a 33 wt% slurry similar to that of water, but did not explicitly calculate the effect of suspended particles on heat transfer coefficients.[37] The use of slurries consisting of phase change materials has gained attention in the past several years for improving heat exchanger performance,[79] suggesting that heat integration of process involving biomass slurries should be possible. Di Blasi determined that the thermal conductivity of lignocellulose particles is

66

approximately half that of pure liquid water,[80] and the solid loading of a typical slurry ranges between 10 and 20 solid wt%. Assuming that the effective slurry thermal conductivity is the weighted average of the thermal conductivities of the water and biomass components, the presence of biomass particles should reduce the thermal conductivity modestly, by approximately 5-10%. Moreover, when it comes to heat transfer coefficients, the presence of biomass particles should be minor as the continuous phase is primarily responsible for heat transfer. Based on these considerations, heat integration of biomass slurries should be technologically viable, meaning that the thermal management benefits indicated by **Figure 5** should be applicable to biomass slurry streams.

3.3.4 Cost Considerations.

Cost is often the overriding consideration in process design and operation. Previous analysis presented here suggests that liquid phase operation can lead to more compact and energy efficient processes than are possible under vapor phase conditions. However, reactors containing high-temperature liquid phases must be designed to hold pressure. As a result, for a given reactor volume (or diameter if the reactor is tubular), the thickness of the wall will be much greater for liquid phase operation than vapor phase. If the reactor volume is the same under liquid and vapor phase conditions, then the cost of the liquid phase reactor may be many times that of the vapor phase version since reactor cost depends to first order on the amount and cost of the material of construction. **Figure 3.7a** plots the estimated cost of a liquid phase vessel with at a constant internal volume (0.75m inner diameter, 3m long) operated at 25 MPa relative to the cost of a vapor phase vessel constructed of the same material of the same volume as the liquid phase version, but operating at 0.1 MPa. The cost ratio is calculated based on the required reactor thickness for each material of construction, which is dependent on that material's yields strength. The cost is related

water's operating phase (i.e., steam at 0.1 MPa or liquid water at 24 MPa) and plotted as a function of T_r for several different common materials of construction. **Figure 3.7a** clearly shows that liquid-phase reactors are much more expensive than reactors designed for low-pressure vapor phase operation, again if the volumes of the two reactors are equal to one another. The performance of Monel and 316 stainless steel, two common materials of construction, is especially poor.

Figure 3.7a is consistent with the common perception that the cost of pressurized reactors and processes is greater than it is for reactors and processes operating at or near ambient pressure. However, **Figure 3.7a** does not take into account potential process intensity benefits of liquid phase or pressurized operation. **Figure 3.1** indicated that liquid-phase operation has the potential to increase process intensity by as much as a factor of 2,000, which translates into a volume reduction of the same magnitude without sacrificing production rates. Therefore, holding process volume constant in the cost analysis, as is done in **Figure 3.7a**, may be misleading. Accordingly, **Figure 3.7b** re-plots the data in **Figure 3.7a**, but instead of holding constant the reactor volume, reactor volume is reduced using values of *IF* previously provided in **Figure 3.1**. **Figure 3.7b** shows that operation under liquid phase conditions has the potential to reduce process costs relative to vapor-phase
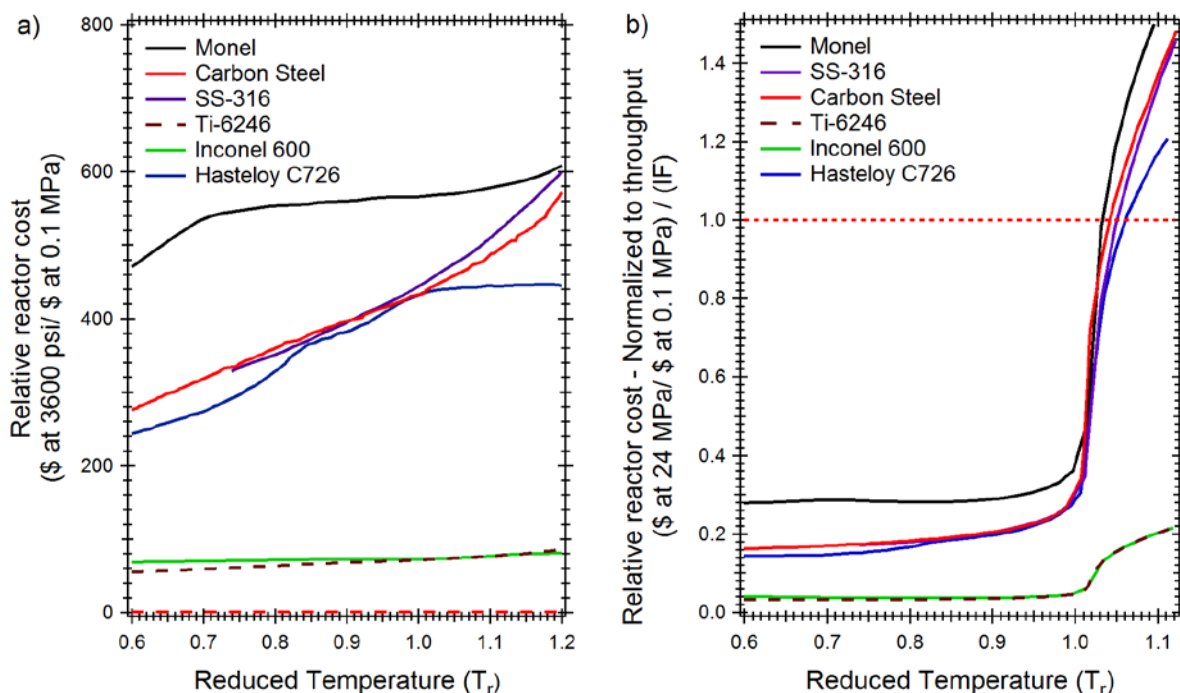
Figure 3.7. a) Relative reactor cost rated to operate at 24 MPa compared to 0.1 MPa at varying reduced temperatures and materials of construction. b) Relative reactor cost normalized to throughput (*IF*) for water. Red dotted line represents identical cost for throughput normalized liquid reactor operated at 24 MPa as vapor phase reactor operated at 0.1 MPa.

operation, assuming that the potential improvements of liquid-phase operation on *IF* can be achieved and provided that the process is operated at $T_r < 1$. For $T_r > 1$, the pressure improvement of *IF* is not sufficient to offset the other costs. On the other hand, for $T_r < 1$, vessels constructed of either Inconel or titanium and designed for high intensity liquid phase operation at 25 MPa have the potential to cost only 5% of that required for vapor phase operation at 0.1 MPa. Lastly, while the analysis shown in **Figure 3.1** is restricted to water, similar considerations apply to many other fluids, albeit with less dramatic effects as outlined in **Figure 3.2**.

While **Figure 3.7** is encouraging, some caveats must be mentioned. First, **Figure 3.7** includes only the capital cost of process vessels. Capital costs also include piping, pumps, valves,

instrumentation, and controls. Of these, the costs of piping should follow trends similar to those shown for process vessels in **Figure 3.7**. The costs of pumps, however, will depend more strongly on pressure than simple vessels, so that the relative costs of these items may partially or even fully offset other potential cost savings.[81] Lastly, as mentioned previously, the process intensity analysis assumes that reaction rate constants are at most weak functions of pressure and/or phase. Some reaction rate constants may be increased by liquid phase operation and others decreased, and selection of liquid phase operation must take this into account. That stated, the potential benefits are sufficient to justify consideration of liquid-phase design in many cases. The next section presents some representative examples that provide some guidance on when liquid-phase operation can be beneficial or when it should be avoided.

3.3.5 Case Studies

The potential energetic and cost benefits of compressed liquid phase operation detailed in previous sections can be applied to several chemical processes. For example, fermentation feedstock upgrading reactions are promising candidates for liquid phase operation due to the high moisture content of the feed and the enthalpic benefit of operating in liquid phase for water-rich feeds. Accordingly, several representative reactions involving upgrading of fermentation products to more valuable products were selected for further analysis, as listed in **Table 3.5**. In addition to providing reactant and product information, **Table 3.5** provides potential *IF* improvement estimated for operating at 25 MPa compared to 0.1 MPa at the same temperature. In all cases, the calculated *IF* associated with liquid phase operation are much greater than one. Glycerol conversion to acrolein[82] is especially striking, as the estimated *IF* for liquid phase operation is 1,100 due to the high water content of the feed (63.8 wt%). For water-free feeds, the benefits of liquid-phase operation are not as significant, but the corresponding *IF* are still >100.

70

Similarly to *IF*, the total heating requirement of a process is improved at higher operating pressures. **Table 3.5** defines energy requirements as an enthalpic ratio equal to the net energy required to operate at 25 MPa ($\Delta H^{25\,\text{MPa}}$) relative to at 0.1 MPa ($\Delta H^{0.1\,\text{MPa}}$) as a vapor state, using 20 °C and 0.1 MPa as a reference state in both cases. Under all conditions, the enthalpy required to heat the reactant mixture to the liquid or supercritical state at 25 MPa is always less than the vapor state at 0.1 MPa. Reactions performed at $T < 350$ °C have the greatest liquid phase enthalpic improvement, requiring only 50–60% of the energy required for vapor phase operation, largely due to avoiding the latent energy required for phase that was shown for water in **Figure 3.4**. Also as shown in **Figure 3.4**, pressure can also reduce thermal requirements when $T_r > 1$, as indicated in **Table 3.5** for acetic acid reforming, acetone-butanol-ethanol deoxygenation, and ethanol condensation. Thermal benefits are greatest for feeds with the greatest water content, as should be expected.

Table 3.5. Case studies considering previously studied vapor phase catalytic upgrading reactions of common fermentation broth products for improvement under high pressure liquid phase conditions.

Reactant	Product	Chemistry	Water Loading (wt%)	Operating Temp (°C)	Space Velocity (hr^{-1})	Catalyst	Reactant Conversion (%)	Product Selectivity (%)	Intensification Factor (IF) $\left(\frac{\rho^{24\,MPa}}{\rho^{0.1\,MPa}}\right)$	Enthalpic Ratio $\left(\frac{\Delta H^{24\,MPa}}{\Delta H^{0.1\,MPa}}\right)$	Ref.
Glycerol	Acrolein	Dehydration	63.8%	320	227 (GHSV)	Rare earth phosphates	76.2%	60-70%	1240	0.50	[82]
Ethanol	Ethyl Acetate	Dehydrogenation	0%	200-260	0.2-50 (LHSV)	Cu:ZnO: ZrO$_2$:Al$_2$O$_3$	60%	80%	440 – 570	0.50 – 0.63	[83]
Ethanol	Butadiene	Condensation	0%	400	1.2 (WHSV)	Ag/MgO-SiO$_2$	50%	41%	310	0.85	[84]
ABE mixture	Liquid fuels	Deoxygenation	0%	400	4.5 (WHSV)	Al$_2$O$_3$	~55%	~35%	310	0.83	[85]
Acetic acid	Syngas	Reforming	43.3%	675-750	3 (WHSV)	Ni/La$_2$O$_3$/ Al$_2$O$_3$	50 – 100%	100%	260 – 270	0.93	[86]

In addition to the IF and thermal benefits of liquid phase operation shown in **Table 3.5**, liquid phase operations of streams involving organic solutions in aqueous solvents can also reduce the energy requirements of product recovery in some instances. Water removal from any of the feed streams shown in **Table 3.5** can be achieved using distillation; however, the energy requirements can be significant given the partial vaporization of water that distillation requires. On the other hand, the products of the reactions in **Table 3.5** are all much less water soluble than the reactants. Therefore, in many cases, operation in the liquid phase has the added benefit of reducing the energy requirements of product recovery. Processes with this potential benefit should be prioritized for closer scrutiny. The examples provided in **Table 3.5** provided guidelines.

On the other hand, attempting liquid-phase operation with one or more components which are not readily compressed into their liquid states will rarely be advantageous except under specific circumstances. Specifically, process requiring hydrogen (e.g., hydrogenation, hydrodeoxygenation, hydrogenolysis) and oxygen (selective oxidation), cannot be analyzed using the methods shown here since gases such as hydrogen and oxygen cannot be compressed to liquid-like densities at typical reaction temperatures (e.g., >100 °C) except at pressures far in excess of those required to compress water and most organic substances. Instead, processes requiring reactions with hydrogen and oxygen typically benefit from having all reactants in the vapor phase. Otherwise, reaction rates will likely be limited by gas-liquid mass transfer rates. The exception to this general rule is when the non-gas reactants cannot easily be vaporized – e.g., if they are non-volatile at reaction temperatures or if vaporization would lead to degradation. In these cases, gas-liquid process conditions may not be avoidable. However, operation under supercritical[87, 88] or gas-expanded liquid conditions[89] – both of which promote gas solubility compared to standard gas-liquid biphasic conditions – may be worth investigating for oxidations and hydrogen reduction

reactions.[90] Under supercritical fluid or gas-expanded liquid conditions, many of the heuristics presented here will be broadly applicable.

In summary, the data in **Table 3.5** clearly indicates that liquid-phase operation will generally lead to significant process intensification for many important reactions. Since process intensity is also related to the energy use and thermal management benefits of liquid phase operation, the analysis in **Table 3.5** strongly suggests liquid-phase operation should be more frequently considered during the early stages of process design than is current practice.

3.4. Conclusions

Compressed liquid phase operation can have clear process engineering benefits, including intensification, energy use, and thermal management improvements compared to vapor phase operation. The extent of improvement depends to first order on the density ratio of the continuous phase in the vapor phase compared to its compressed liquid phase, and proximity to the critical point. Processes which use substances with strong intermolecular associations, including especially hydrogen bonding, as working fluids are especially promising candidates, as the potential intensification improvements can be >100 in many instances and approaching 1,000 specifically for water. Likewise, process energy requirements are nearly always less for liquid phase operation than for the vapor phase, despite the fact that operation at pressure results in greater energy use for fluid compression and pumping. The increased energy consumption required for compression and pumping is more than offset by reductions in latent and sensible heat requirements. Likewise, liquid phase operation can benefit thermal management, as the greater thermal conductivities of liquid phases compared to vapors translates into >50% increases in heat transfer efficiency (h/J). Capital costs are greater for pressurized process vessels of the same volume, but projected improvements in process intensity are sufficient such that the cost of liquid-

phase reactor construction has potential to be less than that required for vapor phase operation at ambient pressure for the same throughput. Several case studies, such as conversion of glycerol to acrolein, show the magnitudes of the benefits that liquid phase operation might provide. Further work is required to understand the effects of continuous phase density and/or thermodynamic state on reaction rate constants, as the present analysis neglected these effects.

Abbreviations

Latin letters

C_p	Heat Capacity
ΔH	Change in enthalpy
T	Temperature
P	Pressure
J	Mass Flux
T	Reactor thickness
r	Reactor internal radius
S	Maximum allowable stress
E	Joint efficiency factor
X	Conversion
$\dot{m}$	Mass flowrate
v	Volumetric flowrate
r_i	Reaction rate
k	Reaction rate constant
C_A	Molar concentration of species A
C_A0	Initial concentration of species A
V	Reactor volume
HHV	Higher heating value
IF	Intensification factor
h_i	inner heat transfer coefficient
f	Fanning friction factor
Re_D	Reynolds number in a tube
Nu_D	Nusselt number in a tube
Pr	Prandlt number
D	Tube diameter
A	Tube cross-sectional area
a_i	Activity of species i
$\Delta G°_{rxn}$	Standard Gibbs free energy of reaction
x_i	Mole fraction of species i
x_{i0}	Initial mole fraction of species i
R	Gas constant

Greek letters

γ_i	Activity coefficient of species i
ρ	Density
v	Viscosity
κ	Thermal Conductivity

Subscripts

b	Boiling point
c	Critical point
r	Reduced variable

Superscript

vap	vapor state
sat, liq	saturated liquid state

References

1. US Department of Commerce, B., Bureau of Economic Analysis, *Gross Output by Industry.* 2018.

2. Agency, I.E., *CO2 Emissions from Fuel Combustion Highlights.* 2016. **15**: p. 1-156.

3. Agency, I.E., *Technology Roadmap: Energy and GHG Reductions in the Chemical Industry via Catalytic Processes.* 2015.

4. Agency, I.E., *Worldwide Trends in Energy Use and Efficiency.* 2007: p. 168.

5. Bielenberg, J. and M. Bryner, *Realize the Potential of Process Intensification | AIChE*, in *Chemical Engineering Progess (CEP)*. 2018.

6. Van Gerven, T. and A. Stankiewicz, *Structure, Energy, Synergy, Time - The Fundamentals of Process Intensification.* Industrial & Engineering Chemistry Research, 2009. **48**: p. 2465-2474.

7. Dautzenberg, F.M. and M. Mukherjee, *Process intensification using multifunctional reactors.* Chemical Engineering Science, 2001. **56**: p. 1549-1555.

8.   Climent, M.J., A. Corma, and S. Iborra, *Mono- and Multisite Solid Catalysts in Cascade Reactions for Chemical Process Intensification.* ChemSusChem, 2009. **2**: p. 500-506.

9.   Stankiewicz, A., *Reactive separations for process intensification: an industrial perspective.* 2003. **42**: p. 137-144.

10.   Nikačević, N.M., et al., *Opportunities and challenges for process control in process intensification.* Chemical Engineering and Processing: Process Intensification, 2012. **52**: p. 1-15.

11.   Gascon, J., et al., *Structuring catalyst and reactor - An inviting avenue to process intensification.* Catalysis Science and Technology, 2015. **5**: p. 807-817.

12.   Charpentier, J.C., *Process intensification by miniaturization.* Chemical Engineering and Technology, 2005. **28**: p. 255-258.

13.   Gogate, P.R., *Cavitational reactors for process intensification of chemical processing applications: A critical review.* Chemical Engineering and Processing: Process Intensification, 2008. **47**: p. 515-527.

14.   Cecilia, R., U. Kunz, and T. Turek, *Possibilities of process intensification using microwaves applied to catalytic microreactors.* Chemical Engineering and Processing: Process Intensification, 2007. **46**: p. 870-881.

15.   Harmsen, G.J., *Reactive distillation: The front-runner of industrial process intensification. A full review of commercial applications, research, scale-up, design and operation.* Chemical Engineering and Processing: Process Intensification, 2007. **46**: p. 774-780.

16.   Roman-Leshkov, Y., J.N. Chheda, and J.A. Dumesic, *Phase Modifiers Promote Efficient Production of Hydroxymethylfurfural from Fructose.* Science, 2012. **312**: p. 1933-1937.

17.   Hu, X., et al., *Reaction pathways of glucose during esterification: Effects of reaction parameters on the formation of humin type polymers.* Bioresource Technology, 2011. **102**: p. 10104-10113.

18.   Fan, L., F. Li, and S. Ramkumar, *Utilization of chemical looping strategy in coal gasification processes.* Particuology, 2008. **6**: p. 131-142.

19.   Ma, R., et al., *Experimental and simulation studies of the production of renewable hydrogen through ethanol steam reforming in a large-scale catalytic membrane reactor.* Chemical Engineering Journal, 2016. **303**: p. 302-313.

20.   Chheda, J.N., G.W. Huber, and J.A. Dumesic, *Liquid-phase catalytic processing of biomass-derived oxygenated hydrocarbons to fuels and chemicals.* Angewandte Chemie - International Edition, 2007. **46**: p. 7164-7183.

21.   Dahmen, N., et al., *High pressure in synthetic fuels production.* Journal of Supercritical Fluids, 2015. **96**: p. 124-132.

22.   Vardon, D.R., et al., *Thermochemical conversion of raw and defatted algal biomass via hydrothermal liquefaction and slow pyrolysis.* Bioresource Technology, 2012. **109**: p. 178-187.

23.   Dry, M.E., *The Fischer - Tropsch process: 1950-2000.* Catalysis Today, 2002. **71**: p. 227-241.

24.   Yanqiao Xiang , Daniel R. Maynes , and M.L.L. *, *Safety concerns in ultrahigh pressure capillary liquid chromatography using air-driven pumps.* Journal of Chromatography A, 2003(991): p. 189-196.

25.   Jaacks, V. and F.R. Mayo, *Liquid-Phase and Vapor-Phase Reactions of Ethylene with Carbon Tetrachloride.* Journal of the American Chemical Society, 1965. **87**: p. 3371-3379.

26.   Gendy, T.S., *Simulation of liquid and vapour phase xylene isomerization over deactivating H-Y-zeolite.* Journal of Chemical Technology and Biotechnology, 1998. **73**(2): p. 109-118.

27.   Zhao, C., et al., *Aqueous-phase hydrodeoxygenation of bio-derived phenols to cycloalkanes.* Journal of Catalysis, 2011. **280**: p. 8-16.

28.   Girgis, M.J. and B.C. Gates, *Reactivities, reaction networks, and kinetics in high-pressure catalytic hydroprocessing.* Ind. Eng. Chem. Res., 1991. **30**: p. 2021-2058.

29.   Furimsky, E., *Catalytic hydrodeoxygenation.* Applied Catalysis A: General, 2000. **199**: p. 147-190.

30.   Tester, J.W. and M. Modell, *Thermodynamics and its Applications 3rd edition*, ed. K.M. Caren. 1997: Prentice Hall PTR.

31.   WebBook, N.C., *Thermophysical Properties of Fluid Systems.* 2018.

32.   Spencer, C.F. and S.B. Adler, *A Critical Review of Equations for Predicting Saturated Liquid Density.* Journal of Chemical and Engineering Data, 1978. **23**: p. 82-89.

33.   Maurer, G. and J.M. Prausnitz, *Derivation and Extension of Uniquac Equation.* Fluid Phase Equilibria, 1978. **2**(2): p. 91-99.

34.   Sarver, J., B. Finkenauer, and Y.A. Liu, *Pump sizing and selection made easy.* Chemical Engineering (United States), 2018. **125**: p. 34-43.

35.   Peters, M.S., K.D. Timmerhaus, and R.E. West, *Plant design and economics for chemical engineers.* 1968.

36.   Gnielinski, V., *Neue Gleichungen für den Wärme- und den Stoffübergang in turbulent durchströmten Rohren und Kanälen.* Forschung im Ingenieurwesen, 1975. **41**: p. 8-16.

37.   Dan Knorr, John Lukas, and Paul Schoen, *Production of Advanced Biofuels via Liquefaction: Hydrothermal Liquefaction Reactor Design*, in *NREL Subcontract Report*. 1966, American Institute of Chemical Engineers: Chicago. p. 285-292.

38.   Farr, J.R. and M.H. Jawad, *Guidebook for the Design of ASME Section VIII Pressure Vessels*. 2001, ASME Press. p. 296.

39.   *Monel Bolts | Monel.*

40.   *Hastelloy Fasteners - Bolts, Screws & Nuts | Hastelloy.*

41.   *INCONEL ® alloy 600.*

42. *Facts & Info │ Techincal Data - Titanium Engineers.*

43. *Process Pipes - Temperature and Allowable Stress.*

44. Sadrameli, S.M., *Thermal / catalytic cracking of hydrocarbons for the production of olefins : A state-of-the-art review I : Thermal cracking review.* Fuel, 2015. **140**: p. 102-115.

45. Matar, S. and L. Hatch, *Chemistry of Petrochemical Processes.* 2000: p. 406.

46. Palluzi, *Compressed gases: managing cylinders safely: follow these recommendations to ensure the safe handling, storage and use of gas cylinders.* Chemical Engineering, 2009. **116**(10).

47. Douglas, J., *Conceptual design of chemical processes.* Journal of Chemical Technology & Biotechnology, 1988. **1110**.

48. Troe, J., *Theory of thermal unimolecular reactions at low pressures. II. Strong collision rate constants. Applications.* The Journal of Chemical Physics, 1977. **66**: p. 4758-4775.

49. Marrone, P.A., et al., *Solvation effects on kinetics of methylene chloride reactions in sub- and supercritical water: theory, experiment, and ab initio calculations.* Journal of Physical Chemistry A, 1998. **102**: p. 7013-7028.

50. Goldsmith, C.F., et al., *Temperature and Pressure-Dependent Rate Coefficients for the Reaction of Vinyl Radical with Molecular Oxygen.* Journal of Physical Chemistry A, 2015. **119**: p. 7766-7779.

51. Sievers, C., et al., *Phenomena Affecting Catalytic Reactions at Solid–Liquid Interfaces.* ACS Catalysis, 2016. **6**: p. 8286-8307.

52. Drago, R.S., S.C. Petrosius, and P.B. Kaufman, *Alkylation, isomerization and cracking activity of a novel solid acid, AlCl2(SG)n.* Journal of Molecular Catalysis, 1994. **89**: p. 317-327.

53. Ravenelle, R.M., et al., *Stability of zeolites in hot liquid water.* Journal of Physical Chemistry C, 2010. **114**: p. 19582-19595.

54.   Lutz, W., et al., *Investigation and modeling of the hydrothermal stability of technically relevant zeolites.* Adsorption, 2005. **11**: p. 405-413.

55.   Peters, M.S. and J.L. Holman, *Vapor–and Liquid–Phase Reactions between Nitrogen Dioxide and Water.* Industrial & Engineering Chemistry, 1955. **47**: p. 2536-2539.

56.   López Barreiro, D., et al., *Hydrothermal liquefaction (HTL) of microalgae for biofuel production: State of the art review and future prospects.* Biomass and Bioenergy, 2013. **53**: p. 113-127.

57.   Prausnitz, J.M., *Molecular thermodynamics of fluid-phase equilibriam.* The Journal of Chemical Thermodynamics, 1986. **2**: p. 600.

58.   Alexopoulos, K., et al., *DFT-based microkinetic modeling of ethanol dehydration in H-ZSM-5.* Journal of Catalysis, 2016. **339**: p. 173-185.

59.   O'Neil, R., et al., *Kinetics of aqueous phase dehydration of xylose into furfural catalyzed by ZSM-5 zeolite.* Industrial and Engineering Chemistry Research, 2009. **48**: p. 4300-4306.

60.   Vjunov, A., et al., *Impact of zeolite aging in hot liquid water on activity for acid-catalyzed dehydration of alcohols.* Journal of the American Chemical Society, 2015. **137**: p. 10374-10382.

61.   Hanning, L., et al. *EPSRC Thermal Management of Industrial Processes A Review of Drying Technologies*. 2010.

62.   Lin, Y. and S. Tanaka, *Ethanol fermentation from biomass resources: Current state and prospects.* Applied Microbiology and Biotechnology, 2006. **69**: p. 627-642.

63.   Nomura, M., T. Bin, and S.-i. Nakao, *Selective ethanol extraction from fermentation broth using a silicalite membrane.* Separation and Purification Technology, 2002. **27**: p. 59-66.

64.   Casal, M.D., et al., *Influence of storage time on the quality and combustion behaviour of pine woodchips.* Energy, 2010. **35**(7): p. 3066-3071.

65.   Nazari, L., et al., *Hydrothermal liquefaction of woody biomass in hot-compressed water: Catalyst screening and comprehensive characterization of bio-crude oils.* Fuel, 2015. **162**: p. 74-83.

66.   Jindal, M.K. and M.K. Jha, *Catalytic Hydrothermal Liquefaction of Waste Furniture Sawdust to Bio-oil.* Indian Chemical Engineer, 2015. **0**: p. 1-15.

67.   Scaling, S., *Hydrothermal liquefaction of various biomass and waste feedstocks for biocrude production: A state of the art review.* Renewable and Sustainable Energy Reviews, 2011. **15**: p. 5218-5223.

68.   Nordgren, D., et al., *Ash transformations in pulverised fuel co-combustion of straw and woody biomass.* Fuel Processing Technology, 2013. **105**: p. 52-58.

69.   Bentsen, N.S., C. Felby, and B.J. Thorsen, *Agricultural residue production and potentials for energy and materials services.* Progress in Energy and Combustion Science, 2014. **40**: p. 59-73.

70.   Koopmans, A. and J. Koppejan, *AGRICULTURAL AND FOREST RESIDUES - GENERATION, UTILIZATION AND AVAILABILITY.* Paper presented at the regional consultation on modern applications of biomass energy, 1998: p. 23.

71.   Yang, Y.F., et al., *Analysis of energy conversion characteristics in liquefaction of algae.* Resources, Conservation and Recycling, 2004. **43**: p. 21-33.

72.   Shakya, R., et al., *Effect of temperature and Na 2 CO 3 catalyst on hydrothermal liquefaction of algae.* Algal, 2015. **12**: p. 80-90.

73.   Maag, A., et al., *Catalytic Hydrothermal Liquefaction of Food Waste Using CeZrOx.* Energies, 2018. **11**: p. 564.

74.   Haarlemmer, G., et al., *Bio-oil Production from Food Processing Residues : Improving the Bio-oil Yield and Quality by Aqueous Phase Recycle in Hydrothermal Liquefaction of*

Blackcurrant (Ribes nigrum L .) Pomace Maxime De n. Energy & Fuels, 2016. **30**: p. 4895-4904.

75.   Lo Mastro, F. and M. Mistretta, *Cogeneration from thermal treatment of selected municipal solid wastes. A stoichiometric model building for the case study on Palermo.* Waste Management, 2004. **24**: p. 309-317.

76.   Chang, Y.M., et al., *Change in MSW characteristics under recent management strategies in Taiwan.* Waste Management, 2008. **28**: p. 2443-2455.

77.   Caputo, A.C., P.M. Pelagagge, and P. Salini, *Heat exchanger design based on economic optimisation.* Applied Thermal Engineering, 2008. **28**: p. 1151-1159.

78.   Tran, K.-Q., *Chapter 10 - Process Intensification and Process Integration for Hydrothermal Processing of Forest Residues and Agricultural Wastes.* Waste Biorefinery, 2018: p. 229-322.

79.   Delgado, M., et al., *Review on phase change material emulsions and microencapsulated phase change material slurries: Materials, heat transfer studies and applications.* Renewable and Sustainable Energy Reviews, 2012. **16**: p. 253-273.

80.   Di Blasi, C., *Physico-chemical processes occurring inside a degrading two-dimensional anisotropic porous medium.* International Journal of Heat and Mass Transfer, 1998. **41**: p. 4139-4150.

81.   GUTHRIE and K. M., *Capital Cost Estimation.* Chem. Eng., 1969. **24**: p. 114-142.

82.   Liu, Q., et al., *Rare earth pyrophosphates: Effective catalysts for the production of acrolein from vapor-phase dehydration of glycerol.* Catalysis Letters, 2009. **127**: p. 419-428.

83.   Inui, K., T. Kurabayashi, and S. Sato, *Direct synthesis of ethyl acetate from ethanol over Cu-Zn-Zr-Al-O catalyst.* Applied Catalysis A: General, 2002. **237**: p. 53-61.

84.   Janssens, W., et al., *Ternary Ag/MgO-SiO2 Catalysts for the Conversion of Ethanol into Butadiene.* ChemSusChem, 2015. **8**: p. 994-1008.

85.   Nahreen, S. and R.B. Gupta, *Conversion of the acetone-butanol-ethanol (ABE) mixture to hydrocarbons by catalytic dehydration.* Energy and Fuels, 2013. **27**: p. 2116-2125.

86.   Basagiannis, A.C. and X.E. Verykios, *Reforming reactions of acetic acid on nickel catalysts over a wide temperature range.* Applied Catalysis A: General, 2006. **308**: p. 182-193.

87.   Japas, M.L. and E.U. Franck, *High Pressure Phase Equilibria and PVT-Data of the Water-Oxygen System Including Water-Air to 673 K and 250 MPa.* Berichte der Bunsengesellschaft für physikalische Chemie, 1985. **89**: p. 1268-1275.

88.   THOMASON, T.B. and M. MODELL, *Supercritical Water Destruction of Aqueous Wastes.* Hazardous Waste, 1984. **1**: p. 453-467.

89.   Lopez-Castillo, Z.K., et al., *Enhanced solubility of hydrogen in CO2-expanded liquids.* Industrial & Engineering Chemistry Research, 2008. **47**(3): p. 570-576.

90.   Jessop, P.G., T. Ikariya, and R. Noyori, *Homogeneous Catalytic-Hydrogenation of Supercritical Carbon-Dioxide.* Nature, 1994. **368**(6468): p. 231-233.

Chapter 4

Catalytic Hydrothermal Liquefaction of Food Waste Using CeZrO$_x$

4.1. Background

A variety of sustainable energy solutions are being developed to displace the use of petroleum-derived fuels that contribute to increasing greenhouse gas levels in the atmosphere. Specifically, the growing demand for transportation fuels has driven alternative energy research for conversion of biomass into fuels [1]. The Energy Independence and Security Act 2007 Renewable Fuel Standards (RFS) program targets the production of 36 billion gallons of renewable fuel by 2022 [2]. Feed costs are a major challenge to economical production of biomass, the Department of Energy (DOE) National Renewable Energy Laboratory reported that the feed constitutes 71.5% of the cost of producing renewable biodiesel from biomass and municipal solid waste [3]. Food waste is an inexpensive, energy dense alternative to lignocellulosic biomass, with the potential to be converted into drop-in transportation fuels with thermochemical properties comparable to petroleum-derived fuels [4]. Repurposing food residues also helps divert material from landfills and reduce life-cycle greenhouse gas emissions caused by the biodegradation of organic waste. According to a recent DOE study, more than 15 million dry tons of food waste is generated annually in the United States (USA), 92% of which is discarded in landfills [5]. Repurposing food

waste for biofuel production would reduce the environmental impact from landfills and reduce global reliance on crude oil.

Thermochemical and biochemical technologies can be used to process complex food wastes, mixtures that consist primarily of carbohydrates, proteins, and oils, but also minor components including minerals and salts [6]. Anaerobic digestion converts organic wastes into methane-rich biogas; however, digestion is a slow process, requiring large reactor volumes and yielding a product that must undergo significant upgrading for many applications [7, 8]. When compared to digestion, gasification more rapidly converts organic wastes into a methane-rich syngas. Fast pyrolysis is the rapid thermal conversion of organic wastes or biomass to energy-rich oils [8]. However, both gasification and pyrolysis require dry feeds and the energy required to dry food waste detracts from the processes [8, 9]. Thermochemical processing via hydrothermal liquefaction (HTL) is an attractive process for food wastes, which is capable of converting a broad range of wet organic solids at moderate temperatures and high pressures without the need for a costly biomass drying step [10]. HTL reactions are carried out at elevated temperatures (250–380 °C) and pressures (7–30 MPa) in a hydrothermal water reaction medium for relatively short residence times (10–60 min) to form a carbon rich bio-oil phase along with an aqueous byproduct phase [11, 12]. HTL has been demonstrated for many organic-rich feeds and at a pilot plant scale of 2000 dry metric tons of waste per day [10].

A major issue in commercializing HTL is that considerable amounts of organic byproducts preferentially partition into the aqueous phase, rather than in the bio-oil phase. Molecules with high oxygen to carbon ratios (e.g., short-chain alcohols, acids, and esters) are particularly likely to exist in the aqueous phase due to their high water solubilities. Loss of organic compounds to the aqueous phase limits the HTL energy yield and necessitates downstream treatment of the water

phase before it can be discharged. In their analysis HTL, Zhu et al. [10] found that economic performance of HTL is most sensitive to loss of carbon to the aqueous phase. HTL process conditions that reduce the production of water-soluble organic compounds can potentially improve energy yield, improve carbon yield, reduce waste treatment costs, and improve process economics.

Homogeneous alkali salts, such as Na_2CO_3, have been reported to improve HTL carbon yield, and that improvement is attributed to suppressing coke formation [10, 13-17]. The limitation with homogeneous catalysts is the costly steps necessary to recover and reuse the catalyst after reaction. In comparison with either non-catalytic HTL or HTL catalyzed homogeneously, reusable heterogeneous catalysts have the potential to improve process economics and energy efficiency. Here, we investigate $CeZrO_x$ as a heterogeneous catalyst during HTL for in situ conversion of small, hydrophilic molecules that would otherwise partition into the aqueous phase, into larger, more hydrophobic molecules that instead partition into the bio-oil phase. $CeZrO_x$ was selected as the heterogeneous catalyst because of the stability of the parent oxides [13, 18], and because it is known to catalyze condensation and coupling reactions [19-21]. In addition, we tested catalyst stability under the harsh reaction conditions required for HTL and performed catalytic activity tests on model organic compounds to investigate the upgrading mechanism. Finally, an energy analysis was performed to compare the benefits of the heterogeneous catalyst to previous work using homogeneous catalysts. This study provides a basis for understanding the use of heterogeneous catalysts for converting food wastes into liquid fuels under HTL conditions.

4.2. Materials and Methods

4.2.1. Materials

All of the HTL experiments used a common food waste feedstock made up of common food items listed in **Table 4.1**. Nutrient data were calculated using USDA data for individual food items found on the Nutrient Data Laboratory website and also listed in **Table 4.1** [22]. Food was mixed together with deionized (DI) water to create a slurry with 15 wt % solids, which was stored under refrigeration between experiments. A 15 wt % reactant slurry was selected based on prior HTL studies with similar solid loadings, and balances process intensity, feed handling, water use, and heat transfer considerations [23].

Cerium zirconium oxide ($CeZrO_x$) nanopowder (99% purity) was purchased from Sigma Aldrich (P/N: 634174) and anhydrous Na_2CO_3 was purchased from Alpha Aesar (P/N: 11552) for use as catalysts. $CeZrO_x$ was calcined at 550 °C in a furnace for at least 1 h prior to use. All of the reactants for model HTL studies and products used for gas chromatography ()analysis were purchased from Sigma Aldrich, with a minimum purity of at least 99%.

4.2.2. Food Waste HTL Reactions

Food waste HTL experiments were performed in a 300 mL stainless-steel bench-top reactor purchased from Parr Instruments (Model 4561) rated for use up to 20.6 MPa and 350 °C. The reactor was heated using an external heating jacket and was equipped with a magnetic stirring drive. Reactor temperature was maintained to within 5 °C of the desired set point using a proportional-integral-derivative (PID) controller. For each experiment, the reactor was loaded with 200 g of slurry and 5 wt % of either $CeZrO_x$ or Na_2CO_3 catalyst. The reactor was sealed and heated for approximately 50 min to 300 °C without any initial pressurization. The reactor temperature was maintained at 300 °C for one hour before cooling to room temperature using a water bath. In the majority of experiments on institutional food waste, the reactor headspace was neither purged nor was it pressurized with inert gas as the goal of institutional food waste tests was to simulate

realistic reactor operation. In a handful of runs, the effect of N_2 pressurization on HTL yields from institutional food waste was tested. The results of these tests indicated that N_2 pressurization had no effect on HTL yields within the limits of experimental uncertainty. Thermal HTL reactions using institutional food waste were performed in duplicate with measured yields agreeing to within ±5%. Catalytic HTL reactions were performed several times using different analytic procedures to ensure data reproducibility. Loss in carbon balance closure in **Figure 4.1** for the uncatalyzed HTL reaction is attributed to the losses during product extraction or charring on the reactor walls, impeller, and other surfaces.

4.2.3. Food Waste HTL Product Analysis

Once cooled, the reactor pressure was recorded and the vessel was depressurized. The gas yield was calculated based on the final gas pressure and the ideal gas law. The molar composition of the gas was assumed to be 80% CO_2, 10% CO and 10% H_2; these values were based on literature sources that showed HTL gas is typically composed of 70–90% CO_2, 5–15% H_2 5–15%, and 5–14% CO [24, 25]. Methane, ethylene, and ethane never accounted for more than 1–2% of HTL gases, and therefore the concentrations of these gases were assumed to be negligible [24, 25].

The liquid and solid HTL products were removed from the reactor into a vacuum filtration funnel fitted with 1.2 μm filter paper. Water and dissolved organics passed through the filter and were set aside for TOC analysis. Oil and solids remaining on the filter paper were washed with acetone to dissolve and collect the oil. The reactor walls and impeller were also washed with acetone to collect any residual material left in the reactor. Acetone was removed from the oil fraction using a rotary evaporator heated to 50 °C. Solids that were left on the filter papers were dried in an oven at 105 °C for 24 h before being ashed in a furnace at 650 °C. All food waste HTL runs had at least a 90% mass balance closure (gravimetric analysis).

Oil and water samples produced during catalytic HTL were analyzed with gas chromatography equipped with a mass spectrometer detector. Water samples were directly injected after filtration, while oil samples were diluted to 4 wt % in acetone, filtered, and then injected. Higher heating values for the oil were obtained with a semimicro calorimeter (25720, Parr, Moline, IL, USA) using O_2. Benzoic acid was used to calibrate the instrument prior to analysis. The CHON content of the oil phase was performed by an outside laboratory (Midwest Microlabs) and obtained using an elemental analyzer. The total organic carbon (TOC) of aqueous HTL samples was outsourced (Flowers Chemical Laboratories) and obtained using a TOC analyzer.

4.2.4. Model Food Waste HTL Reactions

HTL reactions with model compounds were performed at the same reaction conditions as used for actual food waste. A 300 mL Parr reactor was initially loaded with 15 grams of organic model compound, 85 g of water and 5 g of $CeZrO_x$ catalyst. For the mixed model HTL activity runs, a 50 mol % ratio for the two reactants was used as a basis. The reactor was then sealed and purged with nitrogen before loading 7.6 MPa of N_2. Initial N_2 pressurization was selected to provide the most careful control of the composition of the reaction mixture, as the goal of model compounds was the unambiguous identification of specific reaction pathways. The reactor was heated to 300 °C and mixed with an impeller set at approximately 700 revolutions per minute. The reaction proceeded at 300 °C and 20 MPa for one hour before quenching and separating out the aqueous, oil, and solid catalyst phases.

Gas chromatograph with mass spectrometer detection (GC-MS) was used for product identification, based on matches with the National Institute of Standards and Technology mass spectra data base. Product quantification was performed using GC with flame ionization detection (FID). Pure pentanal, 1-octene, 1-nonene and pentanol were used as calibration standards. Trans-

2-decenal was used as a calibration standard for 2-propyl-2-heptenal quantification, as 2-propyl-2-heptenal was not available commercially. Model HTL reactions without activity, labeled "No Product" in **Table 4.3**, had no detectable product peaks in the GC-MS (<0.05% yield). All of the products considered "trace" in **Table 4.3** constituted less than 0.3% of total yield, as estimated from FID peak areas. Reactant conversion reproducibility for tests performed under thermal conditions without a catalyst without a catalyst, with $Ce(NO_3)_4$, or with $CeZrO_x$ was ±5 wt %. Likewise, product yields were reproducible to within ±2 wt %.

4.2.5. Hydrothermal Stability of CeZrO$_x$

A total of 1.0 g of $CeZrO_x$ and 100 mL of water were loaded into a 300 mL stainless-steel batch reactor and initially pressurized with N_2 to 7.6 MPa. The reactor was then heated to 300 °C, which pressurized the vessel to 20.6 MPa. The stability study was performed for 16 or 165 h at 300 °C before quenching the reactor and extracting the catalyst for post-characterization. A small fraction of the water was removed from the reactor and kept for analysis followed by centrifugation and filtration steps to remove the $CeZrO_x$ nanoparticles.

$CeZrO_x$ samples were characterized before and after hydrothermal treatment using a variety of techniques. X-ray diffraction was performed using a Rigaku automatic instrument with the Bragg-Bretano theta-theta configuration. XRD patterns were obtained with a Cu Kα at 27.5 kV and 5 mA. Diffuse reflectance UV-Vis-spectroscopy (DR-UV) analysis was performed on powder $CeZrO_x$ using a ThermoScientific Evolution 300 UV-Vis spectrophotometer equipped with a Praying Mantis diffuse reflection cell. $BaSO_4$ was used as a white reflectance standard. Samples were analyzed over the range from 200 to 1100 nm and plotted using the Kubelka and Munk diffuse reflectance model. Cerium content contained in the leachate obtained from hydrothermal treatment of $CeZrO_x$ was measured using a ICP-MS (inductively coupled plasma with mass

spectrometer detector, NexION 350X, PerkinElmer, Hopkinton, MA, USA). The instrument was calibrated with an ICP standard and the liquid sample was diluted 1/50 in water before analysis for cerium content.

4.3. Results

4.3.1. Hydrothermal Liquefaction (HTL) or Food Waste

Table 4.1. List of solid ingredients in the food waste feedstock and corresponding composition and higher heating value (HHV).

Food Item	Feedstock Percent (Dry Basis)	Feedstock Composition and Heating Values	Value [% or MJ/kg]
American Cheese	12.8	Moisture [%]	73.0
Canned Chicken	14.9	Protein [%]	4.8
Instant Potatoes	10.6	Lipids [%]	5.9
Green Beans	14.9	Carbohydrates [%]	15.9
White Rice	19.1	Ash [%]	0.3
Apple Sauce	22.3	HHV, bone dry [MJ/kg]	24.6
Butter	5.4	HHV, wet [MJ/kg]	6.5

The feedstock used for HTL reactions was a mixture representative of institutional food waste and included seven commonly disposed food items. Selection of a traditional food waste mixture was important due to the varying effects on HTL yields that are influenced by protein, carbohydrate

and fat content [26]. The list of solid ingredients used as the feedstock is included in **Table 4.1**, which also includes nutrient data calculated using values for each individual food item found in the United States Department of Agriculture Food Composition Database [22]. **Table 4.2** shows that the food waste mixture contained 73% moisture, was highly oxygenated, and had a higher heating value (HHV) of 6.5 MJ/kg.

Table 4.2. Food waste feedstock properties and properties of the hydrothermal liquefaction (HTL) water and oil products using different catalysts. Elemental analysis of HTL oil calculated on a dry basis. Reactions carried out at 300 °C under batch conditions for one hour.

Catalyst	C Content [%]	H Content [%]	O Content [%]	N Content [%]	Moisture Content [%]	HHV[1] [MJ/kg]	Energy Recovery [%]	HTL Water TOC [ppm]
Food Waste[2]	58.3	10.3	29.3	2.0	N/A	24.6	N/A	N/A
Thermal	79.0	10.3	6.3	4.4	10.5	35.6	27.6	13,800
5% Na_2CO_3	77.6	10.2	8.4	3.8	11.7	24.2	21.3	24,200
5% $CeZrO_x$	80.8	10.1	4.7	4.5	10.1	31.2	38.8	12,500

[1] Higher heating value (HHV) measured without removing moisture content;
[2] Food waste CHON and energy recovery was calculated on a bone dry basis.

The institutional food waste mixture was upgraded under 3 different conditions: (1) thermally, in the absence of any catalyst; (2) in the presence of Na_2CO_3 as a homogeneous catalyst; and, (3) in the presence of $CeZrO_x$ as a heterogeneous catalyst. $CeZrO_x$ was selected for its known activity for promoting the desired reactions as well as the known liquid-phase hydrothermal stability of metal oxides [27]. Dumesic and coworkers [19-21] have reported both esterification [21] and ketonization [20] reactions that are catalyzed by $CeZrO_x$ under vapor phase conditions. In addition, CeO_2 is known for its redox activity that can assist in upgrading a variety of water soluble oxygenated species [18].

Figure 4.1 compares the carbon distribution of the major food waste HTL products, as oil, aqueous phase carbon, char, and gas. Non-catalytic HTL yielded 38.8% of the carbon in the oil phase, with the aqueous and solid char phases containing 21.7% and 23.6% of the carbon, respectively. The addition of Na_2CO_3 as a catalyst reduced coke formation by 10% relative to the thermal HTL reaction, as shown in **Figure 4.1**, consistent with previous work on food waste HTL [10]. On the other hand, use of $CeZrO_x$, resulted in the greatest amount of carbon recovered in the
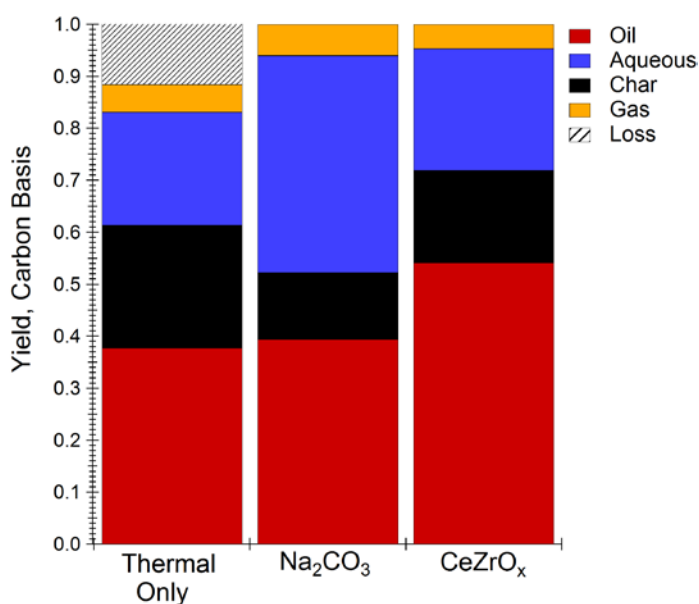
Figure 4.1. HTL yields using different HTL catalysts. Reactions carried out at 300 °C for one hour. Oil, gas, and char yields are calculated on a dry basis. Plots are based on total carbon yield of HTL products.

oil phase and char, while simultaneously rejecting the least amount of carbon to the gas and aqueous phases. All of these results establish the benefits of using $CeZrO_x$ as an HTL catalyst for food waste upgrading.

Table 4.2 compares the properties of bio-oil obtained without catalyst, with Na_2CO_3, and with $CeZrO_x$. The energy recovery obtained using $CeZrO_x$ was 38.8% energy recovery, which is greater

than that obtained either under thermal conditions (27.6%) or with homogeneous catalyst (21.3%), and it is comparable to yields reported for HTL of algae, a feed with much greater energy density than food waste [28]. Although the HHV of oil from HTL reactions is slightly less using $CeZrO_x$ compared to uncatalyzed HTL reactions, the energy recovery improves due to the increased oil yield. In addition, the total organic carbon (TOC) of the water byproduct obtained from $CeZrO_x$ HTL was approximately 50% that obtained under Na_2CO_3 HTL conditions, indicating that the CeZrOx is more effective at reducing the loss of organic compounds to the water phase. The HHV of bio-oil obtained from $CeZrO_x$-catalyzed HTL was 25% greater than that obtained when Na_2CO_3 was used as the catalyst, which is consistent with both the increased carbon content and the decreased moisture content of the $CeZrO_x$ oil product.

4.3.2. Hydrothermal Stability of CeZrOx Catalyst

The data in Section 2.1 indicate that $CeZrO_x$ may improve bio-oil yield and HHV when compared to Na_2CO_3 catalysis, while also reducing the organic content of the aqueous phase. However, activity is only one criterion for a commercial catalyst. In addition to activity, the catalyst must be stable at industrial timescales, a difficult challenge given that many catalyst materials degrade rapidly under HTL process conditions [27]. To be considered hydrothermally stable, a metal oxide catalyst must: (1) retain its crystal structure after hot liquid water (HLW) treatment without any lattice rearrangement; (2) maintain the oxidation state of active metals; and, (3) retain the active metals incorporated at the surface. Batch hydrothermal stability tests were performed to investigate the crystal phase, metal oxidation state, and the leaching stability of $CeZrO_x$ under HLW conditions (>16 h and 300 °C). Relative to reaction conditions (1 h), longer treatment times were used for stability tests (16 h), to provide data under more extreme conditions than were used to acquire the data in **Tables 4.1** and **4.2**.

94

X-ray diffraction was used to study the crystal phase stability of CeZrO$_x$. **Figure 4.2** compares the diffractogram of untreated CeZrO$_x$ and HLW treated CeZrO$_x$ after 165 h at 300 °C. Based on the diffraction peaks located at 30.2, 34 and 50 2θ degrees, the calcined CeZrO$_x$ crystal is in either the cubic or tetragonal phase [29]. No new diffraction peaks appeared with hydrothermal processing, indicating that the crystal lattice was stable under HTL conditions and that no new crystalline phases formed during treatment. Moreover, the peak intensities of calcined and HLW treated CeZrO$_x$ are within 10% of the original material, indicating minimal amorphization during treatment.
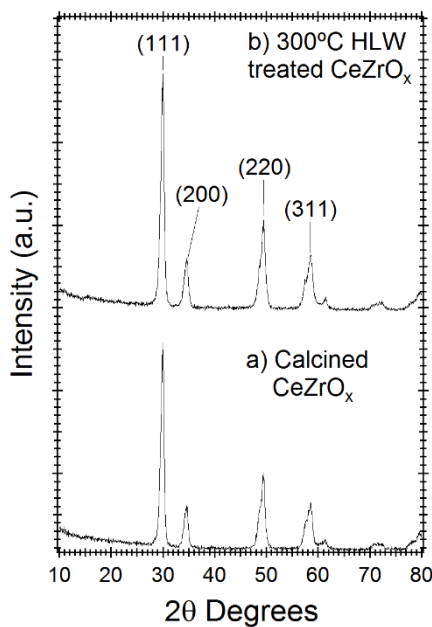
Figure 4.2. X-ray powder diffractogram of (**a**) Calcined CeZrO$_x$ and (**b**) Calcined CeZrO$_x$ treated in HLW for 165 h at 300 °C.

Diffuse reflectance UV-Vis-spectroscopy (DR-UV) can be used to differentiate cerium or zirconium oxides and their oxidation states [30]. **Figure 4.3a** shows the DR-UV spectra of calcined CeZrO$_x$ and 16-h HLW-treated CeZrO$_x$, respectively. Both spectra have broad DR-UV bands centered at 295 nm, with a shoulder at 230–270 nm. Preferential leaching, oxidation, or the

95

reduction of either Ce or Zr would cause this central band to shift, as shown by the work of Damyana et al. [30]. Treatment with HLW does not shift the location or relative intensity of this central band (**Figure 4.3**), indicating that the elemental composition and oxidation state of CeZrO$_x$ were both unchanged by HLW treatment.
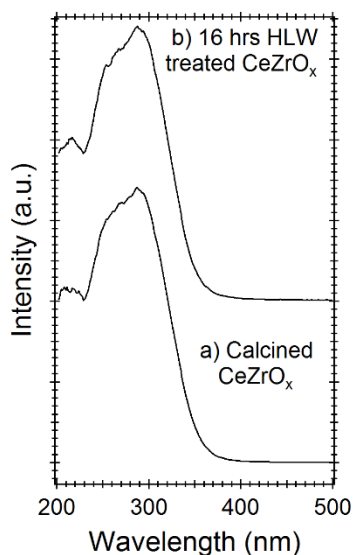
Figure 4.3. Diffuse reflectance UV-Vis-spectroscopy (DR-UV) spectra of (**a**) untreated Cerium zirconium oxide (CeZrO$_x$), and (**b**) CeZrO$_x$ treated in hot liquid water (HLW) for 16 h at 300 °C.

DR-UV is not sensitive to trace metal leaching (<1%) [31]. However, trace leaching can become problematic on extended use. Accordingly, the aqueous phase recovered after hydrothermal treatment of CeZrO$_x$ (again at 300 °C and for 16 h) was analyzed using inductively coupled plasma (ICP) with optical emission spectroscopy (OES). ICP-OES revealed that 0.25% of the cerium present in the catalyst leached into the aqueous phase during treatment. The minimal leaching into water that was observed with ICP-OES again supports the stability of the catalyst in hot, liquid water.

4.3.3. Model Chemistries for HTL Reaction

Relative to the homogeneous catalyst (Na_2CO_3), $CeZrO_x$ improved HTL oil yields, increased the energy recovery of the product, and reduced the TOC content in the water phase. Tests under extreme conditions (300 °C and 16 h) indicated that the catalyst retained crystallinity and underwent only minor leaching under reaction conditions. All of these findings warranted further understanding of $CeZrO_x$ for food waste upgrading. At this point, we sought to confirm that the $CeZrO_x$ catalyst acted by coupling of small oxygenated molecules into larger molecules with reduced oxygen content. Unfortunately, determining the catalytic role of $CeZrO_x$ with a molecularly complex mixture, such as food waste, is a difficult analytical challenge. As a result, data from food waste upgrading did not reveal the mechanism of $CeZrO_x$, or indeed confirm if it acts catalytically at all. For this reason, a series of tests with simple model compounds was performed to confirm the catalytic role of $CeZrO_x$.

$CeZrO_x$ catalyst activity was evaluated for reaction of small oxygenated molecules that are characteristic of food waste. An alcohol (isobutanol), carboxylic acid (propionic acid), aldehyde (pentanal) and ketone (pentanone) were selected for model HTL reactions based on their relative hydrophilicity and abundance in food waste. Moreover, we hypothesized that these reactants might undergo aldol condensation, esterification, and ketonization reactions to a desired product with increased molecular weight and decreased oxygen/carbon ratio [32]. Model HTL reactions were performed under batch conditions described in the Methods and Materials section.

Table 4.3 is a qualitative overview of the results obtained from the model compound HTL reactions, using $CeZrO_x$ as a catalyst. Pentanal was the most active of all model oxygenate reactants. All other compounds, including alcohols, carboxylic acid, and ketones, yielded only trace products (<0.3 wt % yield) in the presence of $CeZrO_x$. Reactions with alcohol and/or

carboxylic acid had no observable reaction products at concentrations greater than our detection limit of 0.05 wt % yield. Reactions with ketones formed only a trace amount of products at concentrations less than 0.3 wt %. **Table 4.3** also lists mixtures consisting of aldehydes and a second compound as "slightly reactive"; in these cases, the observed reactivity was attributed primarily to the aldehyde. The lack of reactivity of acids contrasts with literature reports that show $CeZrO_x$ is active for ketonization and esterification [19-21]. The difference between the current results and those in the literature can be attributed to the high concentration of water present during the HTL reaction as water has been shown to greatly reduce $CeZrO_x$ activity for ketonization and esterification [19]. Apparently, the activity of $CeZrO_x$ towards aldols is less sensitive to water than its ketonization and esterification activity.

Table 4.3. Single and mixed reactant model HTL activity using isobutanol, propionic acid, pentanone, pentanal, and equimolar mixtures of each pair. Reactions performed at 300 °C under batch conditions for one hour.

Model Compounds	Alcohol	Carboxylic Acid	Ketone	Aldehyde
Alcohol (Isobutanol)	No Product			
Carboxylic Acid (Propionic Acid)	No Product	No Product		
Ketone (3-Pentanone)	Trace Product	Trace Product	Trace Product	
Aldehyde (Pentanal)	Slightly Reactive	Slightly Reactive	Slightly Reactive	Reactive

The pentanal reaction activity of CeZrO$_x$ was studied in more detail by quantifying yields of all the major reaction products (>0.3% of total). Specifically, we sought to determine which reactions were being catalyzed and if they would produce products with reduced water solubility compared to the reactants. **Figure 4.4** shows the product distribution obtained for HTL reaction of pentanal in the presence of CeZrO$_x$. First, pentanal conversion was measured at approximately 60%. In comparison, pentanal conversion under uncatalyzed, thermal conditions was about 20%. The main product of catalytic reaction was 2-propyl-2-heptenal; this product constituted 74% of the yield. Other products include pentanol, pentanoic acid, nonene, and octene. Similar products were formed under thermal conditions, albeit with a selectivity to 2-propyl-2-heptanal of only about 50%.
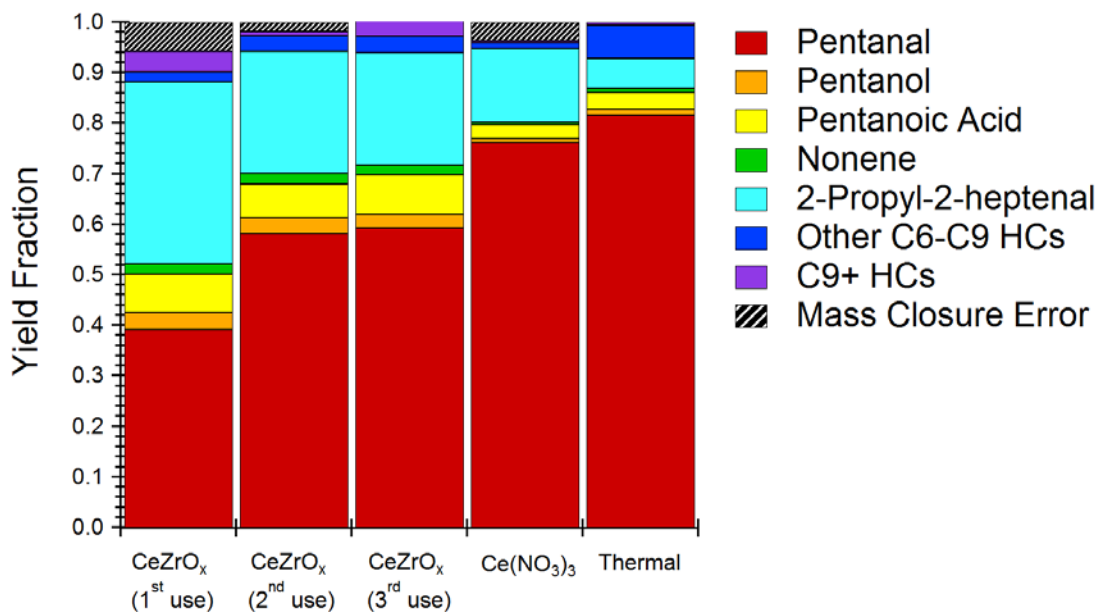
Figure 4.4. Product distribution of model pentanal condensation reaction using CeZrO$_x$ catalyst, Ce(NO$_3$)$_3$ and no catalyst (thermal only). HCs in legend refers to other hydrocarbons

Production of 2-propyl-2-heptenal can be attributed to aldol condensation of pentanal. Aldol condensation with $CeZrO_x$ occurs via base catalyzed formation of an enolate [33]. The enolate couples with another pentanal, and, after dehydration, can form the 2-propyl heptenal product we observed. Aldol condensation is typically base catalyzed, and we therefore surmise that the primary effect of $CeZrO_x$ was to act as a Brønsted base. As desired, the product of aldehyde condensation is much less water soluble than the reactant, having both greater molecular weight and a reduced oxygen content. Given the abundance of aldehydes both in food waste and HTL bio-oil, the results of the model experiments strongly suggest that $CeZrO_x$ catalyzed aldol condensation reactions during the treatment of institutional food waste, thereby improving carbon recovery and reducing loss of carbon to the aqueous phase when compared to the homogeneous catalyst.

Aside from 2-propyl-2-heptenal, $CeZrO_x$ produces 3-nonene, an interesting product given its complete de-oxygenation. Formation of 3-nonene is likely attributable to decarbonylation chemistry of 2-propyl-2-heptanal. Interestingly, the product distribution was not especially dependent on the type of catalyst used, indicating that $CeZrO_x$ acts primarily to increase rates, rather than to alter selectivity. Aside from 2-propyl-2-heptanal, the remaining products were a mixture of alcohol and alkenes, which were likely the products of oxidation, reduction, or condensation reactions, and a pentanoic acid, which was likely produced by oxidation of the aldehyde by cerium oxide [34].

An effective heterogeneous catalyst must be reusable. Accordingly, we evaluated the reusability of $CeZrO_x$ for pentanal upgrading without calcination or regeneration steps in between runs. **Figure 4.4** summarizes the results, showing that pentanal conversion decreased from 60% on first use to about 45% on second and third uses. Selectivity for 2-propyl-2-heptanal remained stable. Reusability tests confirmed that $CeZrO_x$ can be reused with modest loss of activity and without

changing the distribution of products. Based on post-reaction analysis of the catalyst, coke formation was likely a key deactivation mechanism and could be addressed by combusting char and coke produced during HTL reactions to regenerate the catalyst.

Catalyst stability tests indicated minor cerium leaching under HTL conditions; nonetheless, even modest leaching might contribute to homogeneous catalysis, rather than the desired heterogeneous effect. **Figure 4.4** includes the product distribution of pentanal upgrading under HTL conditions using 0.25 wt % $Ce(NO_3)_3$ as a homogeneous catalyst to simulate the effect of leached cerium. The $Ce(NO_3)_3$ concentration was selected based on the amount of cerium leaching quantified during the hydrothermal stability studies of $CeZrO_x$. While 2-propyl-2-heptenal remained the major product when using Ce^{3+} as a catalyst, the overall pentanal conversion reduced from 60% for heterogeneous catalyst to 24% for the homogeneous reaction. The results of catalyst leaching tests again suggest that $CeZrO_x$ acts primarily as a heterogeneous catalyst during HTL chemistry.

4.4. Discussion

Catalytic upgrading of food waste using $CeZrO_x$ as a heterogeneous catalysts yielded a bio-oil with increased carbon content, decreased oxygen content, and increased HHV when compared to the bio-oil produced using a homogeneous catalyst. Its activity was attributed to catalysis of aldol condensation reactions, which have the dual benefit of increasing carbon yield and decreasing the organic content of the aqueous byproduct. Moreover, $CeZrO_x$ exhibited minimal loss of activity on repeated usage. To estimate the potential benefits of the reusable catalyst on HTL, we compared the current results to those presented in the literature.

Table 4.4 compares the energy recovery, oil yield, and oil HHV improvement from the presented food waste catalytic HTL runs with similar studies reported in the literature, using energy recovery as the primary metric of comparison. Inter-comparison of HTL results must take into account the

effects of feed, reaction temperature, and catalyst loading on performance; hence, **Table 4.4** provides data on the experimental conditions relevant to energy recovery analysis. Energy recovery can depend strongly on the feedstock. To account for feedstock dependence, **Table 4.4** provides data on food waste (the current study), vegetable oil, sawdust, and several algae types. Compared to other feeds, vegetable oil has a high energy recovery and mass yield due to the relative ease of converting straight chain lipids into bio-oil compared to carbohydrate-rich steams, such as food waste or biomass. [35] In contrast, lignocellulosic feedstocks, such as sawdust (**Table 4.4**), are more recalcitrant than simple oils and therefore result in lower energy recovery [36]. Algae is a popular candidate as an energy crop for fuel production due to its high growth rate and high energy density, which can be attributed to high lipid content, a component similar to vegetable oil [24]. However, HTL of algae results in lower energy recovery than reported for vegetable oil, likely due to the combined effects of lower operating temperature and more dilute feedstock (6 wt % feed) [34]. Catalytic food waste HTL results in a similar energy recovery compared to microalgae, which is surprising given that microalgae has high lipid content, whereas the food waste mixture used here is primarily composed carbohydrates. The close agreement in the energy recovery for the two feeds may be attributable to the greater reaction temperature used for food waste HTL (250 vs. 300 °C) and the relative effectiveness of the catalyst (zeolites vs. $CeZrO_x$).

   Table 4.4 compares HTL performance based on oil yield improvement and oil HHV to differentiate the effect of feedstock properties from catalytic effects. Oil yield improvement is defined as the ratio of HTL bio-oil yields obtained with the use of a catalyst to that obtained without the use of a catalyst. Similarly, oil HHV improvement is defined as the ratio of HTL bio-oil HHV obtained with the use of a catalyst to that obtained without the use of a catalyst. **Table 4.4** shows that $CeZrO_x$ catalyst improved oil yield by 59% relative to the yield obtained from non-catalytic

HTL of food waste and that the HHV of the thermal and $CeZrO_x$ oils were within 10% of one another. Meanwhile, Na_2CO_3 catalysis had no effect on oil yield and decreased the HHV of the oil product by 68% when compared to the oil obtained from non-catalytic HTL. The net result is that $CeZrO_x$ improves HTL energy yield from 27.6% for the non-catalytic performance to 38.8%, while Na_2CO_3 actually reduces the energy yield.

Next, we compared the results that were obtained for food waste HTL to results reported for other feeds. The relative oil yield and HHV improvements obtained using Na_2CO_3 and $CeZrO_x$ on food waste are similar to those reported in the study by Nazari et al. [36], which used sawdust as a HTL feedstock. The similar performance may be consistent with the fact that carbohydrates dominate the composition of both biomass and food waste, despite the fact that the carbohydrates present in biomass (especially cellulose) are generally more stable than those present in food waste (starch). In contrast, the lipid-rich feeds (vegetable oil, algae) do not benefit as greatly from catalyst addition as the carbohydrate-rich feeds (sawdust and food waste), suggesting that catalysts are not as necessary for efficient energy recovery from the lipid-rich feeds as they are for carbohydrate-rich feeds.

Beyond the single use analysis shown in **Table 4.4**, a re-usable heterogeneous catalyst, such as $CeZrO_x$, has considerable lifetime benefits compared with thermal processes or with processes utilizing homogeneous catalysts. **Table 4.5** provides estimates of the total oil heating value derived from catalytically produced HTL bio-oil obtained between a single use and up to 165 reuses. For single use, the energy yield of $CeZrO_x$ is approximately twice that of Na_2CO_3, 0.24 MJ per gram of catalyst (MJ/g) compared to 0.103 MJ/g. Next, the lifetime of homogeneous catalysts was taken as the equivalent of two uses, as consistent with results reported by Jena et al. [37] that indicate approximately 50% loss of homogeneous catalyst per use. The reusability of $CeZrO_x$ was

estimated to be either 3, 10, 100 or 165 uses. Three uses for $CeZrO_x$ is estimated as a lower limit based on the relative activity maintained in coupling reactions from the model HTL chemistry. The upper range of reusability for $CeZrO_x$ is based on the hydrothermal stability study (i.e., 165 h). The actual lifetime may in fact be greater than that indicated in stability tests because the stability study indicated negligible crystallinity loss after 165 h, at which point the study was terminated. On the other hand, food waste HTL conditions may be more aggressive than hydrothermal conditions, due to the presence of acidic byproducts and heteroatoms, especially sulfur. Therefore, a range between 3 and 165 h of catalyst reuse is used to estimate catalyst lifetime, which takes into account all available data. Using these estimates of catalyst lifetime, the total lifetime energy yield of $CeZrO_x$ after either 3 or 165 uses was estimated at 0.73 MJ/g or 39.9 MJ/g, respectively, as compared to 0.21 MJ/g for Na_2CO_3—a 4 to 200-fold improvement. For comparison, **Table 4.5** provides similar analysis for both homogeneously and heterogeneously catalyzed HTL of different algae types. While the data are scattered by differences in reaction conditions and algae feed characteristics, the lifetime energy recovery obtained using solid $Ca_3(PO_4)_2$ (0.5 MJ/g) is roughly equal to the best results obtained using homogeneous catalysts (i.e., 0.8 MJ/g under optimized conditions using acetic acid) and much better than the typical result, which is in the range of 0.05 MJ/g. This inter-comparison further establishes the benefits of the reusability of heterogeneous catalysts.

In addition to energy efficiency and yield, cost considerations must also be weighed in the overall analysis. Although bulk pricing data for $CeZrO_x$ are not readily available, a simple calculation can be performed. Based on pricing for kg quantities, $CeZrO_x$ is approximately 30-times more expensive per gram than Na_2CO_3, both at purities of 99%. Factoring in the 59% increase in energy yield and considering cost on the basis of energy yield, $CeZrO_x$ is more

economical than Na_2CO_3 when $CeZrO_x$ is reused at least 25 times and Na_2CO_3 is reused twice. While more detailed analysis will require obtaining the bulk pricing data for the two catalysts, the preliminary economic analysis is promising. In summary, therefore, the present study suggests that heterogeneous catalysts such as $CeZrO_x$ have potential for energy efficient and economical promotion of HTL conversion of food waste to energy.

Table 4.4 Comparison of energy recoveries, oil yield improvements and oil HHV improvements with the use of a heterogeneous catalyst.

Feedstock	Temperature (°C) /Catalyst Loading (Dry Feed Basis)	Catalyst	Energy Recovery $\left(\dfrac{HHV_{oil} \times Yield}{HHV_{feed}}\right)$x100	Oil Yield Improvement $\left(\dfrac{Yield_{with\ cat}}{Yield_{thermal}}\right)$	Oil HHV Improvement $\left(\dfrac{HHV_{with\ cat}}{HHV_{thermal}}\right)$
Food Waste	300 °C/33%	$CeZrO_x$	38.8	1.59	0.88
		Na_2CO_3	21.3	1.12	0.68
Vegetable Oil [35]	350 °C/16%	Cr-ZSM5	75.8	0.81	1.01
		Co-ZSM5	70.0	0.73	1.04
		H-ZSM5	77.4	0.79	1.06
Rice Straw [38]	290 °C/5%	Ni/CeO_2	81.6	1.39	1.22
Sawdust [36]	300 °C/20%	Hydrotalcite	52.3	1.82	0.84
		MgO	48.6	1.60	0.93
		Colemanite	57.1	1.92	0.92
Spirunella Algae [37]	350 °C/20%	NiO	56.5	0.76	1.08
Microalgae [34]	250 °C/50%	Nano-Ni/SiO_2	28.9	1.49	1.05
		Zeolite	27.8	1.42	1.06

Table 4.5. Lifetime energy yields for heterogeneous HTL reactions using either a homogeneous or a heterogeneous catalyst. $CeZrO_x$ reuse range based on hydrothermal stability study.

Feedstock	Catalyst	Temperature (°C)/ Residence time (h)	Lifetime Energy Yield [MJ$_{oil}$/g$_{cat}$]		Ref.
			1 Reuse	Expected Reuse [# of Reuses]	
Food Waste	$CeZrO_x$	300 °C/1 h	0.242	0.73 [3×]	Our work
	$CeZrO_x$	300 °C/1 h	0.242	2.42 [10×]	Our work
	$CeZrO_x$	300 °C/1 h	0.242	24.2 [100×]	Our work
	$CeZrO_x$	300 °C/1 h	0.242	39.9 [165×]	Our work
	Na_2CO_3	300 °C/1 h	0.103	0.21 [2×]	Our work
Algae [1]	Na_2CO_3	300–360 °C/0.5–1 h	0.0061–0.362	0.007–0.37 [2×]	[16, 17, 37, 39, 40]
	KOH	300 °C/1 h	0.010–0.014	0.020–0.028 [2×]	[18]
	Acetic Acid	290–300 °C/0.33–1 h	0.007–0.398	0.015–0.80 [2×]	[18, 41]
	Formic Acid	300 °C/1 h	0.012–0.019	0.024–0.038 [2×]	[18]
	$Ca_3(PO_4)_2$	350 °C/1 h	0.250	0.5 [2×]	[40]

[1] Algae results include the following: Spirulina and Chlorella, Microcystis Viridis, Nannochloropsis, Pavlova and Isochrysis, Enteromorpha, and D. Tertiolecta

Another consideration when selecting a heterogeneous catalyst to upgrade a food waste mixture is the inevitable variability in a food waste mixture when applied at a pilot-scale or industrial level. Food waste can have different extents of carbohydrates, proteins, fats and sugars that can have seasonal or regional variability. Oils and sugars are expected to be readily break down to form a bio-oil when compared to the relatively recalcitrant bonds that comprise carbohydrates and proteins. The improvements shown in **Table 4.2** and **4.4** apply to the specific food mixture listed in **Table 4.1**. The best reaction conditions, such as residence time, temperature and/or catalyst loading, to optimize oil yields can vary with the changing

food waste mixture. Proper analysis of the initial food waste allows for any necessary adjustment of the feed prior to hydrothermal liquefaction reactions.

4.5. Conclusions

The conversion of food waste to energy has potential for diverting waste from landfills, a disposal method which contributes to both pollution and greenhouse gas emissions. HTL has shown promise for waste-to-energy conversion, especially for waste streams with high water content. A major challenge for HTL is simultaneously recovering a high quality bio-oil, maximizing energy recovery, and minimizing loss to the aqueous phase. This work establishes $CeZrO_x$ as a heterogeneous catalyst for HTL that yields a bio-oil with improved HHV, increases energy recovery relative to non-catalytic and Na_2CO_3-catalyzed HTL, and reduces the carbon loss to the aqueous phase relative to thermal conditions. Stability tests indicated that the $CeZrO_x$ crystal structure, elemental composition, and oxidation state were stable during exposure to HTL conditions (water at 300 °C for $\geq$16 h), with approximately 0.2% leaching of Ce being measured at the same conditions. Model compound reactions indicated that condensation of aldehydes was the main mechanism of catalytic action, consistent with increased bio-oil HHV and decreased aqueous phase carbon loss observed for the $CeZrO_x$ catalyzed HTL of institutional food waste. The catalyst could be reused up to three times with minimal loss of activity, which was the maximum number tested. Energy analysis indicated that reuse of the heterogeneous catalyst improves lifetime energy recovery by a factor of 200 when compared to single use homogeneous catalyst (39.9 MJ/g for $CeZrO_x$ compared to 0.21 MJ/g for Na_2CO_3). Economically, the heterogeneous catalyst is more cost effective than Na_2CO_3 provided it can be reused at least 25 times. This work suggests that $CeZrO_x$, and possibly other water-stable oxides, have potential for base-catalyzed upgrading of food waste under HTL conditions.

107

References

1.   Administration, U.S.E.I. *International Energy Outlook 2016 Chapter 8: Transportation Sector Energy Consumption*. 2016.

2.   *U.S. Energy Independence and Security Act.* 2007: p. 882.

3.   Davis, R., et al. *Process Design and Economics for the Conversion of Lignocellulosic Biomass to Hydrocarbons: Dilute-Acid and Enzymatic Deconstruction of Biomass to Sugars and Biological Conversion of Sugars to Hydrocarbons*. 2013.

4.   Pavlovič, I., et al., *Hydrothermal reactions of agricultural and food processing wastes in sub-and supercritical water: a review of fundamentals, mechanisms, and state of research.* Journal of agricultural and food chemistry, 2013. **61**: p. 8003-8025.

5.   Energy, U.S.D.o. *Biofuels and Bioproducts from Wet and Gaseous Waste Streams: Challenges and Opportunities*. 2017.

6.   Haarlemmer, G., et al., *Bio-oil Production from Food Processing Residues : Improving the Bio-oil Yield and Quality by Aqueous Phase Recycle in Hydrothermal Liquefaction of Blackcurrant (Ribes nigrum L .) Pomace Maxime De n.* Energy & Fuels, 2016. **30**: p. 4895-4904.

7.   Appels, L., et al., *Anaerobic digestion in global bio-energy production: Potential and research challenges.* Renewable and Sustainable Energy Reviews, 2011. **15**: p. 4295-4301.

8.   Huber, G.W., S. Iborra, and A. Corma, *Synthesis of transportation fuels from biomass: Chemistry, catalysts, and engineering.* Chemical Reviews, 2006. **106**: p. 4044-4098.

9.   Akhtar, J. and N. Saidina Amin, *A review on operating parameters for optimum liquid oil yield in biomass pyrolysis.* Renewable and Sustainable Energy Reviews, 2012. **16**: p. 5101-5109.

10.   Zhu, Y., et al., *Techno-economic analysis of liquid fuel production from woody biomass via hydrothermal liquefaction (HTL) and upgrading.* Applied Energy, 2014. **129**: p. 384-394.

11.   Yan, W.-h.H., et al., *Composition of the bio-oil from the hydrothermal liquefaction of duckweed and the influence of the extraction solvents.* Fuel, 2016. **185**: p. 229-235.

12.   Posmanik, R., et al., *Biomass conversion to bio-oil using sub-critical water: study of model compounds for food processing waste.* Jornal of Supercritical Fluids, 2017. **119**: p. 26-35.

13.   Elliott, D.C., T.R. Hart, and G.G. Neuenschwander, *Chemical processing in high-pressure aqueous environments. 8. Improved catalysts for hydrothermal gasification.* Industrial and Engineering Chemistry Research, 2006. **45**: p. 3776-3781.

14.   Zhu, Y., et al., *Development of hydrothermal liquefaction and upgrading technologies for lipid-extracted algae conversion to liquid fuels.* Algal Research, 2013. **2**: p. 455-464.

15.   Zhang, Y., *Hydrothermal Liquefaction to Convert Biomass into Crude Oil.* Biofuels from Agricultural Wastes and Byproducts, 2010: p. 201-232.

16.   Ross, A.B., et al., *Hydrothermal processing of microalgae using alkali and organic acids.* Fuel, 2010. **89**: p. 2234-2243.

17.   Yang, Y.F., et al., *Analysis of energy conversion characteristics in liquefaction of algae.* Resources, Conservation and Recycling, 2004. **43**: p. 21-33.

18.   Beckers, J. and G. Rothenberg, *Sustainable selective oxidations using ceria-based materials.* Green Chemistry, 2010. **12**: p. 939.

19.   Gärtner, C.A., et al., *Catalytic Upgrading of Bio-Oils by Ketonization.* ChemSusChem, 2009. **2**: p. 1121-1124.

20.   Gaertner, C.A., et al., *Catalytic coupling of carboxylic acids by ketonization as a processing step in biomass conversion.* Journal of Catalysis, 2009. **266**: p. 71-78.

21.   Gaertner, C.A., et al., *Ketonization reactions of carboxylic acids and esters over ceria-zirconia as biomass-upgrading processes.* Industrial & Engineering Chemistry Research, 2010. **49**: p. 6027-6033.

22.   *Welcome to the USDA Food Composition Database.*

23. Elliott, D.C., et al., *Hydrothermal liquefaction of biomass: Developments from batch to continuous process.* Bioresource Technology, 2015. **178**: p. 147-156.

24. Duan, P. and P.E. Savage, *Hydrothermal Liquefaction of a Microalga with Heterogeneous Catalysts.* Industrial & Engineering Chemistry Research, 2011: p. 52-61.

25. Zhang, B., M. Von Keitz, and K. Valentas, *Thermal effects on hydrothermal biomass liquefaction.* Applied Biochemistry and Biotechnology, 2008. **147**: p. 143-150.

26. Zastrow, D.J. and P.A. Jennings, *Hydrothermal Liquefaction of Food Waste and Model Food.* 2013 AIChE Annual Meeting Online Proceedings, 2013. **54**: p. 1-9.

27. Xiong, H., H.N. Pham, and A.K. Datye, *Hydrothermally stable heterogeneous catalysts for conversion of biorenewables.* Green Chemistry, 2014. **16**: p. 4627-4643.

28. Gollakota, A.R.K., N. Kishore, and S. Gu, *A review on hydrothermal liquefaction of biomass.* Renewable and Sustainable Energy Reviews, 2018. **81**: p. 1378-1392.

29. Sánchez Escribano, V., et al., *Characterization of cubic ceria-zirconia powders by X-ray diffraction and vibrational and electronic spectroscopy.* Solid State Sciences, 2003. **5**: p. 1369-1376.

30. Damyanova, S., et al., *Study of the surface and redox properties of ceria-zirconia oxides.* Applied Catalysis A: General, 2008. **337**: p. 86-96.

31. Besson, M. and P. Gallezot, *Deactivation of metal catalysts in liquid phase organic reactions.* Catalysis Today, 2003. **81**: p. 547-559.

32. Kumar, R., et al., *Ketonization of oxygenated hydrocarbons on metal oxide based catalysts.* Catalysis Today, 2017. **302**: p. 16-49.

33.   Postole, G., et al., *Knoevenagel condensation reaction over acid-base bifunctional nanocrystalline CexZr1-xO2 solid solutions.* Journal of Catalysis, 2010. **269**: p. 110-121.

34.   Saber, M., et al., *Catalytic hydrothermal liquefaction of microalgae using nanocatalyst.* Applied Energy, 2016. **183**: p. 566-576.

35.   Robin, T., J.M. Jones, and A.B. Ross, *Catalytic hydrothermal processing of lipids using metal doped zeolites.* Biomass and Bioenergy, 2017. **98**: p. 26-36.

36.   Nazari, L., et al., *Hydrothermal liquefaction of woody biomass in hot-compressed water: Catalyst screening and comprehensive characterization of bio-crude oils.* Fuel, 2015. **162**: p. 74-83.

37.   Jena, U., K.C. Das, and J.R. Kastner, *Comparison of the effects of Na2CO3, Ca3(PO4)2, and NiO catalysts on the thermochemical liquefaction of microalga Spirulina platensis.* Applied Energy, 2012. **98**: p. 368-375.

38.   Chen, D., et al., *Journal of Analytical and Applied Pyrolysis Catalytic hydroliquefaction of rice straw for bio-oil production using Ni / CeO 2 catalysts.* Journal of Analytical and Applied Pyrolysis, 2018.

39.   Shakya, R., et al., *Effect of temperature and Na2CO3 catalyst on hydrothermal liquefaction of algae.* Algal, 2015. **12**: p. 80-90.

40.   Shuping, Z., et al., *Production and characterization of bio-oil from hydrothermal liquefaction of microalgae Dunaliella tertiolecta cake.* Energy, 2010. **35**: p. 5406-5411.

41.   Yang, W., et al., *Direct hydrothermal liquefaction of undried macroalgae Enteromorpha prolifera using acid catalysts.* Energy Conversion and Management, 2014. **87**: p. 938-945.

Chapter 5

Effects of Temperature Varying Solvent Properties on ZSM-5 Degradation in Hot Liquid Water

5.1. Background

Interest in the use of zeolites as solid acid catalysts in liquid water has intensified in recent years for both technological and scientific reasons. Technologically, performing chemistry in the presence of liquid water can reduce the energy required for processing wet feeds that require drying if processed using non-aqueous techniques.[1, 2] Recent work by Zaker et al.[3] has shown that water effectively disrupts chemical pathways that lead to production of undesirable coke products. Similarly, several studies have demonstrated that zeolites, in particular ZSM-5, promote formation of gases, short-chain alkanes, and aromatics from upgrading of fatty acids, algae bio-oil, and vegetable oil in liquid water at temperatures near or greater than its critical point (374 °C).[4-7]

Scientifically, many aspects of zeolite performance remain incompletely understood in the liquid phase, including even the fundamental questions of the role of water on catalytic activity and stability.[8-17] For example, Eckstein et al.[18] reported that phenol alkylation rates decreased in the presence of water, suggesting that the effect was due to competitive adsorption between phenol and water for the same active sites. Liu et al.[19] reported a synergistic effect between homogeneous acid (H_3PO_4) and H-□ zeolite in their studies of cyclohexanol dehydration, with measured dehydration rates much greater for the tandem catalyst than observed for either catalyst

acting separately and suggesting a direct promotional role for water. However, zeolite activity in hot liquid water is often convoluted by stability. Strikingly, several recent studies suggest that ZSM-5 degradation products, including soluble aluminum and nanosized aluminosilicate fragments, act as the catalyst under aqueous-phase conditions, rather than the zeolite itself.[20, 21] In a more subtle example of the convolution between activity and stability, Vjunov et al.[22] reported that the activity of H-☐ for alcohol dehydration decreased after aging in liquid water, attributing their finding to precipitation of silica that blocked access to framework aluminum acid sites. Similarly, Zaker et al.[3] found that the presence of water near its critical point reduced the dodecane cracking activity of ZSM-5 under high conversion conditions and that zeolite H-Y and H-☐ activity retained negligible activity under similar conditions. All of these observations were coincident with either partial (ZSM-5) or complete (H-Y and H-☐☐ framework decrystallization due to water-promoted degradation.

Previous studies on liquid water stability have typically focused on a single temperature or a narrow range of temperatures.[9-11, 15] In doing so, the remarkable temperature dependence of water's thermophysical properties is neglected.[23] Water is typically considered a polar solvent with good capacity for solubilizing most ionic molecules (salts), a low affinity for hydrocarbons, and with a pH of 7 when neutral. However, the properties of water are not constant with respect to temperature, but instead vary considerably.[23, 24] For example, the ionic product of water increases with increasing temperature from its familiar value of 1×10^{-14}, and reaches a maximum at approximately 350 °C that is more than 100 times greater than observed at ambient conditions.[23] At temperatures greater than the critical point, the ionic product decreases sharply with increasing temperature.[23] The net effect is to modulate the rates of acid/base catalyzed reactions, without addition of mineral acids or bases.[25, 26] Similarly, the dielectric constant of water decreases

steadily from 80.1 at room temperature to approximately 1 at the critical point, potentially affecting the rates of reactions that proceed via polarized transition states.[24] The unusual temperature dependence of water's thermodynamic properties has been linked to a non-Arrhenius temperature dependence of molecular reaction rates and unexpected phase behavior.[27] Similar effects on thermodynamic and kinetic behavior of zeolites are reasonable to expect, but have not previously been investigated.

To address gaps in our understanding of water-zeolite interactions and their effects on zeolite stability, ZSM-5 was treated in hot liquid water at temperatures ranging from 250 to 450 °C. ZSM-5 was selected based on previous work by Zaker et al.[3] that suggested it retained >75% of its original crystallinity even when exposed to dense, supercritical water at 400 °C for 2 hours. Post-run characterization evaluated changes in framework properties, aluminum composition, and chemistry. These data were first evaluated to quantify the stability of ZSM-5 compared to other frameworks, establishing MFI as a model framework for studying temperature effects on liquid phase stability. Next, degradation rates were analyzed using solution models of chemical reactivity to examine the effects of water-zeolite interactions and temperature dependence. These results advance the current understanding of zeolite degradation in liquid water and suggest new avenues for future work to stabilize zeolites in this important solvent.

5.2. Experimental Section

5.2.1 Materials.

Binderless ZSM-5 zeolite powder (2 ☐m crystals) with Si/Al=38 was obtained from ACS Materials. Prior to use, catalysts were heated in an oven set to 100 °C for at least one hour followed by calcination in an oven set to 550 °C for at least 16 hours under ambient air conditions. Water

115

was deionized to 17.9 MΩcm prior to use. Ethanol (99%, Sigma Aldrich) was used as a reactant in dehydration studies after dehydration over Type 5A molecular sieves.

5.2.2 Catalyst Stability Experiments

Catalyst stability tests were performed in a pressurized flow-through reactor. A detailed description of the catalytic packed bed setup is provided in the Appendix A. At the start of each experiment, the oven temperature was increased to the desired set point while maintaining a constant nitrogen flow through the reactor. A nitrogen flow was used during heat-up (and cool-down) to provide careful control of the temperature history of the zeolite when exposed to liquid water.[28] Upon reaching the desired operating temperature, de-ionized water was pumped into the system at a flow rate of 4 ml min^{-1} (Eldex, Optos pump). The water was maintained in the liquid state within the flow reactor using a back pressure regulator (Equilibar H6P) set to 25 MPa, which is greater than the critical pressure of water. The water was fed sequentially through the preheat tubing, catalyst tube, chilled tubing section, and 2 filters (15 and 2 μm) before exiting the system. After 3 hours, the water flow was discontinued and nitrogen was used to expel water from the reactor zone before cooling down the system. The reactor was depressurized once the reactor temperature reached 60 °C.

5.2.3 Material Characterization.

ZSM-5 was characterized before and after hydrothermal treatment using a range of established techniques: scanning electron microscopy (SEM) and energy dispersive x-ray spectroscopy (EDS), X-ray diffraction (XRD), N_2 gas sorption, transmission electron microscopy (STEM), X-ray photoelectron spectroscopy (XPS), diffuse reflectance infrared Fourier transform spectroscopy (DRIFTS), ^{29}Si and ^{27}Al solid-state NMR, temperature-programmed surface reactions of isopropylamine, and Fourier transform infrared (FTIR) spectroscopy of ZSM-5 with adsorbed

pyridine. Detailed descriptions of all characterization techniques are included in the methods sections of Appendix A.

5.3. Results

The experimental study was to characterize ZSM-5 framework degradation and acid site loss associated with hot liquid water treatment. ZSM-5 was selected as previous work suggested its framework was more stable than other common frameworks such as H-□ and H-Y.[8, 10] The Si/Al ratio was selected as 38:1 as previous studies have reported the hydrothermal activity of materials with similar Al content[5, 6, 29] and because computational methods[30] and experimental studies have found ZSM-5 stability to be weakly dependent on Al content and optimized in the range from 25 to 100. Tests were performed over the temperature range from 200 to 450 °C and 25 MPa. The pressure was selected to maintain water as a liquid, subcritical, or dense supercritical phase conditions, with the density of water varying smoothly but non-linearly from 0.82 g cm^{-3} at 200 °C to 0.11 g cm^{-3} at 450 °C.[23] Treated samples were subsequently analyzed for changes in crystallinity, textural properties, and acid site density to assess the degradation of the zeolite framework (Section 5.3.1) and aluminum composition and chemistry (Section 5.3.2) during treatment in hot liquid water.

5.3.1 Framework Stability

XRD determined the retained crystallinity of treated ZSM-5. **Figure 5.1a** shows representative XRD data for calcined ZSM-5 and ZSM-5 treated in hot liquid water for 3 hours at temperatures ranging from 250 to 450 °C. The sharp peaks associated with the MFI framework are apparent in all spectra, suggesting that ZSM-5 retains at least partial crystallinity even after treatment at 450 °C. Likewise, no new peaks appear after treatment, suggesting that water treatment does not promote formation of new crystalline phases.

Figure 5.1b provides degree of crystallinity data determined by integration of ZSM-5 crystalline peaks (22.5–25 2□□degrees).[31] The degree of crystallinity is based on the ratio of the integrated areas of treated relative to untreated ZSM-5 samples. The area of untreated ZSM-5 samples is reproducible to within 3% and the error bars are standard deviations from multiple ZSM-5 stability runs at a given temperature. At temperatures less than 325 °C, crystallinity loss is less than the estimated limits of experimental uncertainty based on repeated experiments at every condition (±7%) and consistent with previous reports on ZSM-5 stability in liquid water.[9, 10] At temperatures greater than 325 °C, ZSM-5 crystallinity decreases after treatment. Due to the siliceous composition of the ZSM-5 used here, decreasing peak intensities is a qualitative sign of decrystallization via a pathway of framework desilication involving hydroxyl (OH^-) catalyzed hydrolysis of Si─O bonds, as quantified elsewhere,[10, 12, 15, 17] and is not associated with selective Al loss.[32, 33] Depending on the treatment temperature, ZSM-5 crystallinity decreases by 10 to 20%, reaching a minimum retained crystallinity of about 80% at a temperature of approximatley 420 °C. For temperatures greater than 420 °C, ZSM-5 retains greater than 90% of its original crytallinity. Interestingly, the crystallinity minimum coincides roughly, but not exactly, with the critical tempeature of water (374 °C).
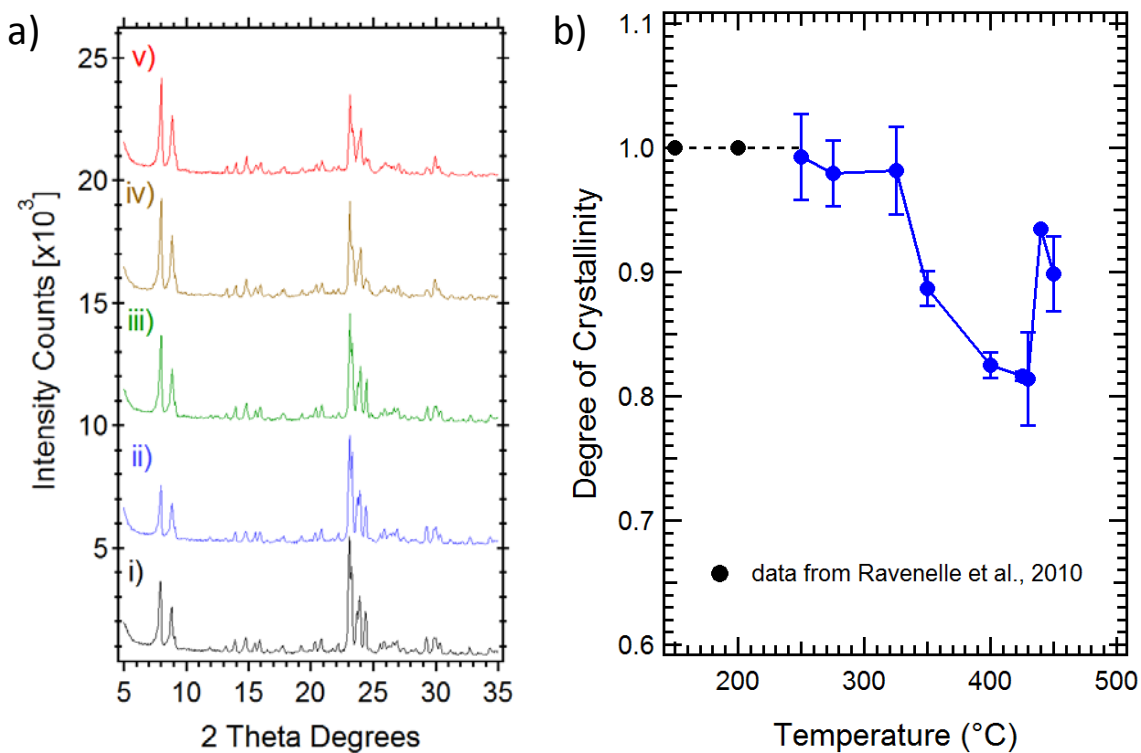
Figure 5.1. (a) XRD pattern of ZSM-5 samples of (i) calcined and (ii-v) hydrothermally treated samples for three hours at 250 °C, 325 °C 400 °C and 450 °C respectively. (b) Corresponding degree of crystallinity for ZSM-5 calculated between 22.5-25.0 2θ degrees at different treatment temperatures relative to a reference calcined ZSM-5, ▲ are from Ravenelle et al.[10] for ZSM-5 at a Si/Al ratio between 15-40.

The observed temperature dependence of framework degradation is unusual and, assuming that our data reflect degradation rates, stand in apparent contradiction to the well-established Arrhenius relationships between reaction rate and temperature.[34] The observation was consistent over multiple, independent experiments, mitigating doubt of its reproducibility. The crystallinity loss at 450 °C was slightly greater than at 440 °C, suggesting resumption of the expected Arrhenius behavior after the aforementioned disruption occurring over the temperature range from 375 to 425 °C. The non-Arrhenius trend in framework degradation shares many qualitative features reported previously for homogeneous reactions in water near its critical point.[27] The Discussion

119

section addresses the scientific and technological implications[6, 35, 36] of this observation in more detail. To examine the framework behavior shown in **Figure 5.1b** in more detail, ZSM-5 samples were further analyzed using electron microscopy and gas sorption.

Figure 5.2 shows representative SEM micrographs obtained from imaging calcined zeolite (a) and zeolites treated in liquid water at 250 (b), 325 (c), and 450 °C (d). The calcined ZSM-5 consists of ~2 μm crystallites with smooth surfaces and sharp edges, as is typically reported for commercial zeolites.[10, 12, 37] The crystal sizes of the sample treated at 250 °C are similar to the original material, albeit with rounded edges and bearing surface cavities with diameters in the range of 50-100 nm. **Figure 5.2b** highlights several of the pits on the ZSM-5 surface. The surface cavities observed in samples treated at 250 °C are qualitatively similar to features arising from desilication under strong alkali conditions at treatment temperatures less than 100 °C, as observed by Groen et al.[38] Similarities between alkali conditions and the enhanced natural concentrations of OH⁻ in liquid water at elevated temperatures is explored further in the Discussion section.

Unlike samples treated at 250 °C, which exhibit modest textural changes, ZSM-5 treated at 325 °C (**Figure 5.2c**) undergoes noticeable degradation, with the crystal "a" dimension retaining its original size (1-2 μm) but with the thickness in the "b" dimension decreasing from approximately 0.5 μm to approximately 100 nm. Consistent with the observations made for ZSM-5 treated at 325 °C, Fodor et al.[39] reported preferential degradation of (010) facets during ZSM-5 treatment in alkali conditions, with subsequent formation of flat crystals. The surfaces of ZSM-5 particles treated at 325 °C retain smooth edges and, unlike samples treated at 250 °C, do not exhibit surface cavities. Presumably, the stronger desilication conditions completely remove surface layers over the course of the 3-hour treatment, leaving behind no evidence of surface cavities.
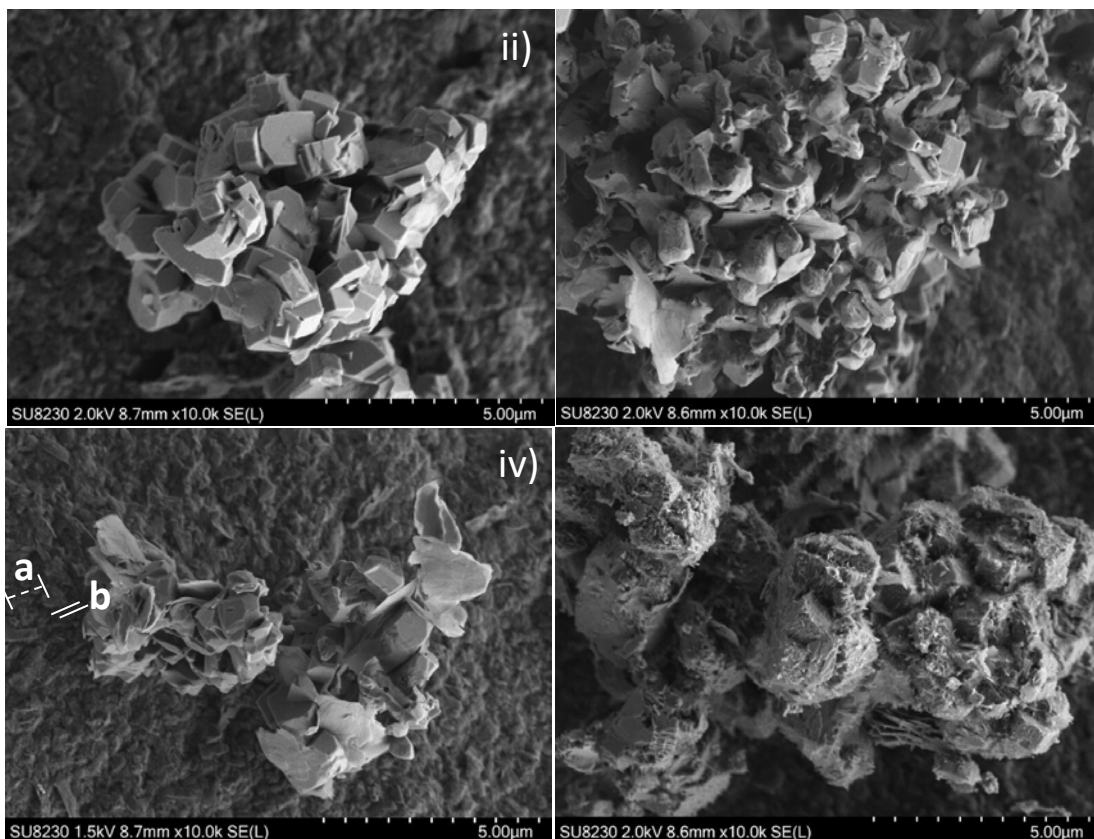
Figure 5.2. SEM images of ZSM-5 samples i) untreated, ii) 250 °C treated, iii) 325 °C and iv) 450 °C treated samples in hot liquid water. "a" and "b" dimensions are labeled in white to denote the change in crystal thickness

The surfaces of ZSM-5 particles treated at 450 °C are visibly rough with the appearance of nanoscale needle-like features. Previous studies of zeolite degradation in hot liquid water reported increased surface roughness,[10, 11, 15] consistent with the surfaces of ZSM-5 treated in liquid water at 450 °C here. The appearance of surface needles and retention of bulk crystallinity (**Figure 5.1b**) after treatment in water at 450 °C are new observations, suggesting quantitative and potentially qualitative differences in degradation mechanisms at these conditions compared to 250 and 325 °C.

Treated samples were analyzed for surface composition using EDS. Images obtained using EDS, shown in **Figure A.2** in the Appendix, indicate increased Al density of ZSM-5 crystals treated at 250 and 325 °C, consistent with deposition of an amorphous alumina phase on the surface. In contrast, the Al composition of the needles observed at 450 °C was similar to that of the parent ZSM-5, again consistent with different mechanisms and rates at these conditions.

STEM determined the effects of liquid water treatment on the internal ZSM-5 framework, specifically the integrity of crystal lattices during the hot liquid water treatment. [28, 38, 40, 41] **Figure 5.3** provides representative bright-field images obtained from STEM analysis of calcined ZSM-5 (3a) and samples treated in hot liquid water at 325 (3b), 400 (3c), and 450 °C (3d). The STEM image of calcined ZSM-5 reveals a straight channel lattice structure that lacks any obstructions or blurriness, as expected for straight MFI channels. After treatment at all temperatures, the internal lattice lines of ZSM-5 retain their original straightness and remain intact and unbroken. A lack of blurriness or bumps in the internal lattice lines of all treated samples strongly indicates that neither does the framework does collapse during liquid water treatment nor does the water treatment induce formation of internal mesopores.

In contrast with the images shown in **Figure 5.3**, Vjunov et al.[17] treated H-β zeolite in hot liquid water at 160 °C for 48 hours and observed a combination of lattice distortions as well as dark pockets attributed to formation of amorphous domains. Even more extremely, Zapata et al.[12] reported near total collapse of the H-Y lattice after 20 hr treatment in hot liquid water at 200 °C. The retention of the internal lattice after hot liquid water treatment is consistent with the XRD data shown in **Figure 5.1**, supporting the conclusion that the ZSM-5 framework retains many of its microporous crystalline features during exposure to hot liquid water.
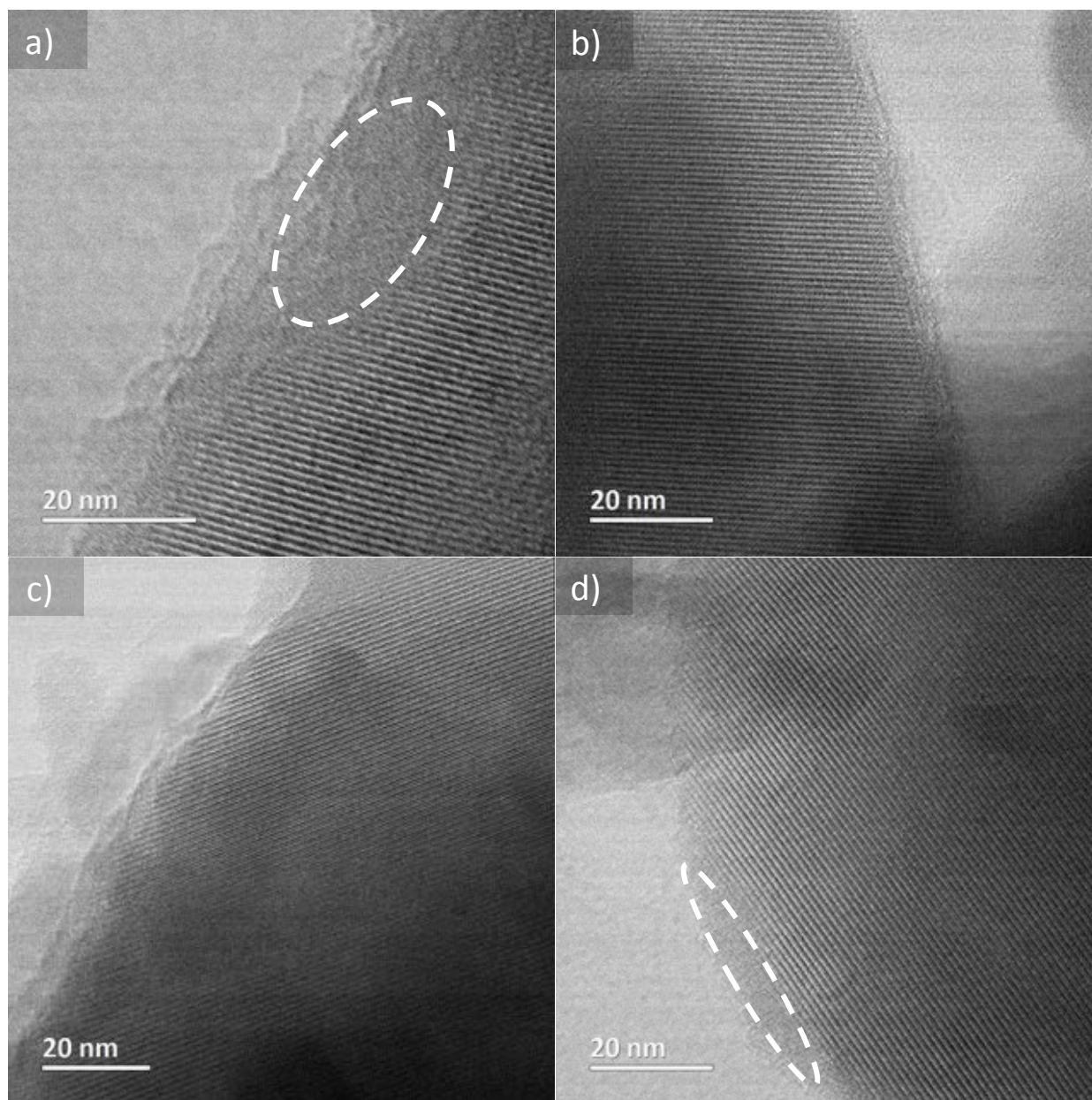
Figure 5.3. STEM images of ZSM-5 samples a) untreated, b) 325 °C treated, c) 400 °C treated and d) 450 °C treated samples in hot liquid water.

While STEM indicates that water treatment does not noticeably alter internal features, comparison of the external crystal surfaces in **Figure 5.3** reveals significant differences in surface texture. The untreated ZSM-5 crystal contains a 5-10 nm region on its surface lacking crystal lattice lines, as shown within the white circle in **Figure 5.3a**. Untextured surface regions in TEM have

been previously attributed to an amorphous silica overlayer.[42] In comparison with the calcined sample, the thickness of the overlayer decreases after hot liquid water treatment at 325 (3b), and 400 °C (3c). Interestingly, and consistent with the unusual crystallinity behavior shown in **Figure 5.1**, the ZSM-5 surface remains untextured after water treatment at 450 °C (**Figure 5.3d** – denoted with a white circle), which may be consistent with the persistence of the amorphous layer at these conditions. Previous studies have suggested that the presence of an amorphous silica external layer may protect the zeolite interior from degradation.[15, 17] Here, it appears the amorphous silica layer observed on untreated ZSM-5 may play a sacrificial role, serving to protect the crystalline interior. The net result of zeolite surface degradation would therefore be competition between amorphous silica dissolution and framework amorphization, a topic that the Discussion section revisits. The STEM results are consistent with SEM images that show a sample treated at 450 °C (**Figure 5.3d**) retains a similar crystallite size as the original calcined sample (3a), while the 325 °C treated sample significantly reduces in size (3c). In summary, the STEM images indicate that the severity of water treatment on amorphous overlayer removal does not increase monotonically with increasing temperature, instead exhibiting a local maximum at temperatures in the vicinity of water's critical temperature.

As STEM analysis occurs over spatially limited distances, analysis is limited by the number of images that can be obtained and analyzed. Accordingly, N_2 sorption was used as a technique to investigate the effects of liquid water treatment on ZSM-5 surface area and micro/meso-porosity. Appendix A contains a much more detailed description of the qualitative features of the N_2 isotherms, while the main text focuses on interpretation of quantitative information obtained from the N_2 isotherms.

Figure A.3 in the Appendix shows representative N_2 isotherms obtained from analysis of ZSM-5 and samples treated in hot liquid water at various temperatures. In all cases, the N_2 sorption data appeared as IUPAC-type-II isotherms, consistent with the microporous characteristics of samples. Minor qualitative differences were present in the isotherms, but they do not influence the overall analysis.

The *t*-plot method[43] was used to extract quantitative textural data from the isotherms shown in **Figure A.3** in the Appendix. **Table 5.1** lists the calculated pore size and surface area results from the *t*-plot method. The data in **Table 5.1** indicate an increase in mesoporosity, but no change in ZSM-5 micropore area of ZSM-5 treated by liquid water at $T \leq 250$ °C, consistent with the XRD results shown in **Figures 5.1a** and **5.b**. Similarly, Ravenelle et al.[10] reported no change in the micropore volume of ZSM-5 after a six-hour treatment in hot liquid water at 200 °C.

Table 5.1. Texture properties of ZSM-5 after hydrothermal treatment in liquid water at different temperatures.

Sample Treatment	Relative [a] Crystallinity	$S_{\text{t-plot, micro}}$ [b] (m^2/g)	$S_{\text{t-plot,ext}}$ [b] (m^2/g)	$S_{\text{micro}}/S_{\text{ext}}$ [b] ratio	V_{micro} [b] (cm^3/g)	V_{meso} [c] (cm^3/g)
Calcined	1.00	326	35.6	9.2	0.168	0.049
250 °C	0.99	350	138.3	2.5	0.183	0.19
275 °C	0.98	193	72.8	2.6	0.098	0.120
325 °C	0.98	221	62.6	3.5	0.113	0.096
350 °C	0.89	257	67.1	3.8	0.130	0.103
430 °C	0.81	285	58.8	4.8	0.141	0.088
450 °C	0.90	287	49.4	5.8	0.139	0.074

[a] Relative crystallinity from ratio of treated with calcined material; [b] micropore surface area and volume are calculated using the *t*-plot method; [c] the mesopore volume is calculated from the difference between the micropore volume and the total volume at $P/P_0 = 0.95$.

As shown in **Table 5.1**, the micropore surface area, $S_{\text{t-plot, micro}}$, decreased from 326 m^2 g^{-1} to 192 m^2 g^{-1} due to treatment at 275 °C. After treatment at temperatures greater than 275 °C, the micropore area increases monotonically with increasing treatment temperature, reaching a value of 286 m^2 g^{-1} after treatment at 450 °C. The micropore area after treatment follows similar trends as observed for crystallinity (**Figure 5.1b**), as increasing the treatment temperature did not lead to monotonic increases in zeolite degradation but instead indicated a more complex relationship between zeolite degradation and temperature. **Figure A.4** in the Appendix plots the total, micropore, and external sorption-determined surface area values as a function of retained crystallinity that shows the complex relationship between these different zeolite characteristics. Again consistent with **Figure 5.1b**, the most significant loss in ZSM-5 crystallinity and micropore surface area occurred at intermediate treatment temperatures, from 300 to 400 °C.

In contrast to the internal surface area, the external surface area increases with increasing treatment temperature for temperatures less than 275 °C and then decreases gradually from 73 to 49 m^2 g^{-1} over the range from 275 to 450 °C. The increase in external surface area observed for the sample treated at 250 °C may be consistent with the formation of surface cavities that SEM revealed (**Figure 5.2b**) and the exfoliation of the amorphous overlayer suggested by comparison of TEM images of calcined ZSM-5 with those obtained from samples treated in liquid water at 325 °C. Again, the textural results provided from N$_2$ sorption in **Table 5.1** are consistent with superior framework stability under supercritical water conditions relative to subcritical temperatures >250 °C.

4.3.2 Acid Site Stability

The next step was to study the fate of aluminum after liquid water treatment, and the resulting effect on Brønsted acid sites (BAS) and Lewis acid sites (LAS). IR, XPS, ^{27}Al-NMR (and ^{29}Si-

NMR), and titration methods were used to develop a composite picture of aluminum chemistry. Starting with IR plotted in **Figure 5.4**, the IR spectrum of the calcined sample exhibits the expected bands characteristic of BAS (3618 cm^{-1}) along with surface silanol groups (3746 cm^{-1}).[41, 44] With increasing treatment temperatures, the intensity of the band associated with BAS decreased in parallel with the appearance of a band attributable to extra-framework alumina, EFAL, at 3660-3690 cm^{-1}.[45] The decreasing intensity of bands associated with BAS and the increasing intensity of the EFAL band is consistent with zeolite dealumination and reminiscent of spectra reported for steam-treated ZSM-5.[46] Qualitatively, the ratio of the Brønsted acid band intensity to the EFAL band intensity decreases approximately threefold after treatment at 400 °C. In contrast to the dramatic changes observed in the EFAL and Brønsted acid bands, the intensity of the silanol band remains relatively unchanged by treatment, consistent with previous studies of ZSM-5 degradation under dealuminating conditions.[47, 48]
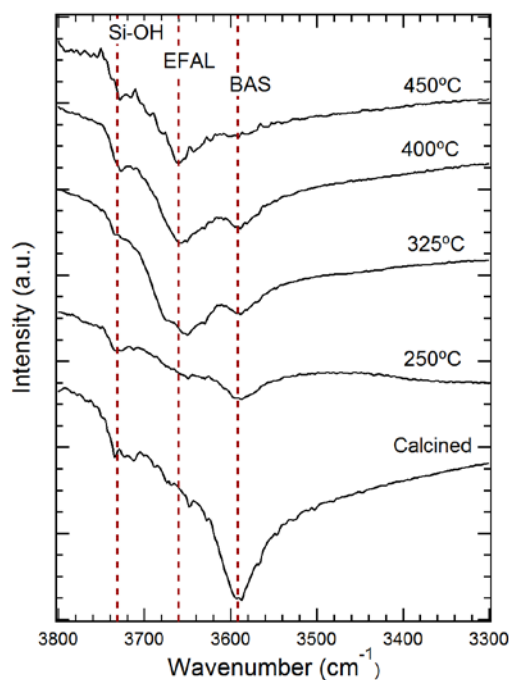
Figure 5.4. DRIFTS diffraction spectra of a) ZSM-5 untreated, b) 250 °C treated, c) 325 °C treated, d) 400 °C treated and e) 450 °C treated samples in hot liquid water

XPS quantified the change in near-interfacial aluminum content due to the high-temperature treatments. **Figure 5.5** presents XP spectra of the Al 2p region for calcined zeolite and for zeolite samples treated at 325 and 400 °C. **Figure 5.5** demonstrates that the intensity of the Al 2p band (centered at 76.5 eV) increases monotonically with increasing treatment temperature from the "initial" value of the calcined sample. In contrast with the Al 2p features, spectra for the Si 2p photoelectron region that correspond to each respective scan in Fig. 5 reveal only nominal changes as shown in **Fig. A.5** in the Appendix. **Figure 5.5** further includes approximate Si/Al ratios as determined from total feature areas for each Si 2p and Al 2p spectral region that are corrected by instrument-specific sensitivity factors.[49] The calculated Si/Al ratio decreases from an initial value of 58 to 4.3 after treatment at 400 °C. Considering the surface sensitivity of XPS, the decrease in the Si/Al ratio is consistent with migration of aluminum atoms from bulk to near-interfacial sites concomitantly with treatment temperature. Similar to the present results shown for liquid treatment, previous studies of ZSM-5 treated in steaming conditions have reported Al surface partitioning.[46, 50, 51] In contrast, previous studies of zeolite stability in hot liquid water with H-Y and H-β do not determine Al migration.[10, 11] On the other hand, Jamil et al.[15] studied ZSM-22 stability after treated in hot liquid water at 250 °C and associated shifts in Al coordination from ^{27}Al NMR and reduced pore access obtained from nitrogen sorption to Al surface enrichment that led to surface pore blocking. The interpretation by Jamil et al.[15] is consistent with the present XPS results, which is expected given the high structural similarity of the ZSM-5 (MFI) and ZSM-22 (TON) frameworks.
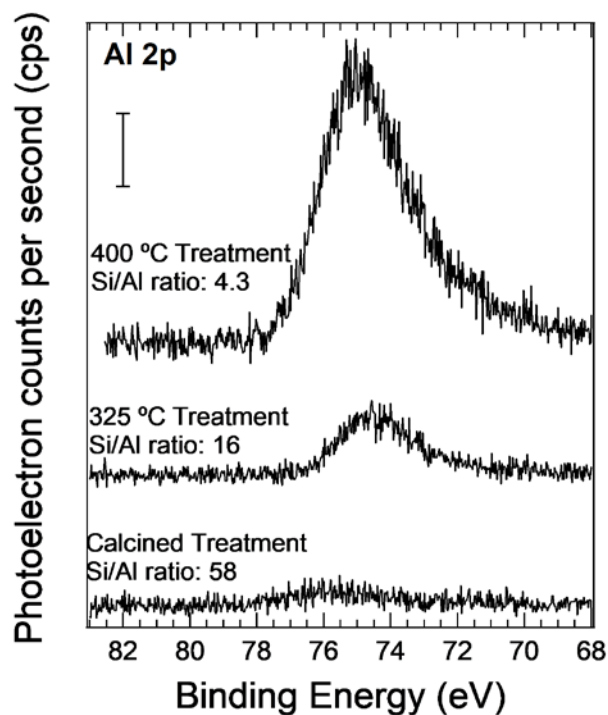
Figure 5.5. Al 2p XP spectra of untreated (bottom), 325 °C treated (middle), and 400 °C treated (top) ZSM-5 samples in hot liquid water. The corresponding surface Si/Al ratios are inset into each respective spectrum. Scale bar represents 100 counts per second (cps) for all spectra.

^{27}Al NMR was used to quantify bulk Al content and investigate the coordination of the aluminum atoms. **Figure 5.6** shows ^{27}Al NMR spectra obtained from analysis of calcined ZSM-5 and samples treated in hot liquid water. **Figure A.6** contains ^{29}Si NMR data, which are consistent with the Al data shown in **Figure 5.6**. As expected from previous studies,[48, 52] the ^{27}Al NMR spectrum of the parent ZSM-5 contains a major peak at 50 ppm, attributable to BAS in the tetrahedral coordination state, and a minor one at 0 ppm, attributable to EFAL in octahedral coordination. Peaks observed at 10 ppm are attributable to contamination from trace aluminum content of the NMR rotor, do not arise from the ZSM-5 sample, and are easily separated from the peaks of interest. **Figure A.7** in the Appendix contains more information on data interpretation.
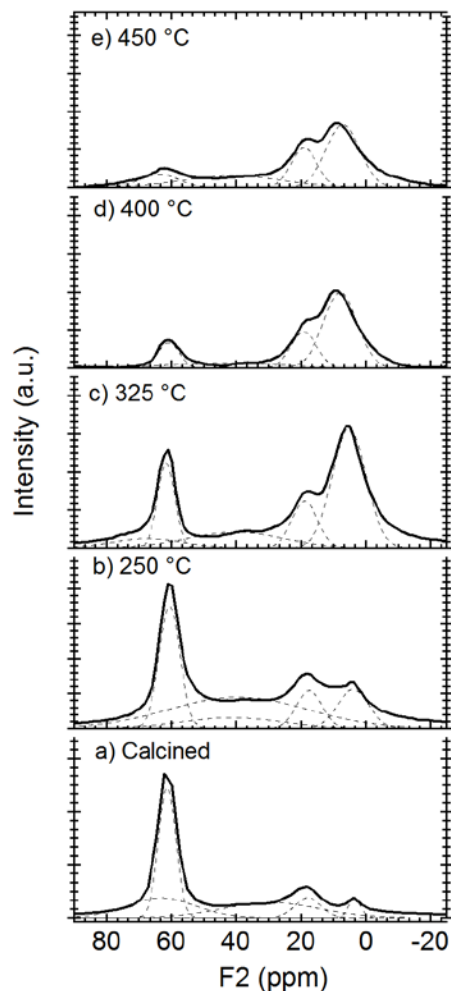
Figure 5.6. 1-D ^{27}Al NMR spectra for a) untreated, b) 250 °C treated c) 325 °C treated, d) 400 °C treated, e) 450 °C treated ZSM-5 samples in hot liquid water

After treatment in hot liquid water, the intensity of the EFAL peak at 0 ppm increases and the intensity of the framework peak at 50 ppm decreases, consistent with ZSM-5 dealumination.[33, 51] Consistent with conclusions drawn from IR and XPS analysis, the ^{27}Al NMR spectra are qualitatively similar to those obtained from analysis of ZSM-5 treated under dealuminating steam or acid conditions.[46, 51, 53] Given the complimentary information provided by IR, XPS, and ^{27}Al NMR for the ZSM-5 samples studied herein and their similarity to samples dealuminated under either steam or acidic conditions, we surmise that, as in acid catalyzed dealumination, the

overall mechanism of dealumination in hot liquid water consists of hydrolysis of Si─O─Al bonds followed by migration to the surface and formation of EFAL. As with desilication, the thermal conditions of hot liquid water and the intrinsic acidity of the solvent makes it a dealumination solvent without addition of mineral acids.

Table 5.2 provides quantitative data obtained by integration of the ^{27}Al NMR spectra shown in **Figure 5.6**. In the original sample, the Si/Al ratio is approximately 20:1. The bulk Si/Al ratio decreases with increasing treatment temperature, consistent with removal of internal Al during treatment resulting in an overall decrease in the bulk Al content of the sample. After treatment at 450 °C, Al content was less than the detection limit of the instrument (i.e., Si/Al > 700). In fact, ^{29}Si NMR spectra of treated zeolite (See A.6d in the Appendix) resemble silicalite,[32] suggesting near quantitative dealumination of the MFI framework. Likewise, the ratio of tetrahedral (BAS) to octahedral (EFAL) sites decreases with increasing treatment temperature, from a ratio of 13.7 in the original sample to 0.16 in the sample treated at 400 °C, an 85-fold decrease. Interestingly, the ratio of tetrahedral to octahedral Al sites is greater in the sample treated at 450 °C compared to the

Table 5.2. Quantified ^{27}Al NMR of H-ZSM5 relative Al site population and Si/Al ratio after hot liquid water treatment.

Sample Temp (°C)	^{27}Al Tetrahedral Al sites	^{27}Al Octahedral Al sites	^{27}Al Si/Al ratio
Calcined	93.2	6.8	19.5
250	61.5	38.5	66.4
325	47.8	52.2	36.5
400	13.9	86.3	435.6
450	22.2	77.8	>700

one treated at 400 °C. This observation, along with the enrichment of surface Al species observed with XPS, may suggest that Al removal from the surface (octahedral sites) follows a different mechanism than Al removal from the interior (tetrahedral sites), potentially due to differences in water access.

Pyridine-IR[45] and isopropylamine titration[54] were performed to quantify the ratio of BAS to Lewis acid sites (LAS) and the absolute density of BAS of the treated samples. **Figure A.8** (in the Appendix) shows IR spectra obtained from analysis of ZSM-5 with adsorbed pyridine. **Table 5.3** summarizes the results, showing that the ratio of BAS to LAS decreases from 9.8 for the calcined material to 1.4 for ZSM-5 treated in liquid water at 450 °C. **Table 5.3** provides quantitative results obtained from isopropylamine titration. The BAS density of the calcined sample is 570 μmol g^{-1}, consistent with the range of acid site densities previously reported for ZSM-5 acidity with Si/Al ratios similar to the one studied here.[55-57] After treatment in hot liquid water at 350 °C, the BAS density decreases by a factor of 3; treatment at 450 °C reduces BAS density by nearly 98% compared to the calcined version. These results are consistent with all measurements previously presented here (e.g., IR and ^{27}Al NMR) and show that BAS are clearly much less stable than the ZSM-5 framework itself during hot liquid water treatment.

Table 5.3. Acid properties of ZSM-5 after treatment in hot liquid water.

Sample Description	BAS[a]/LAS[b,c]	BAS density[d] (μmol g^{-1})	LAS[e] density (μmol g^{-1})
Calcined ZSM-5	9.8	570	58
ZSM-5 (350 °C)	3.8	167	44
ZSM-5 (450 °C)	1.4	14	10

[a] Brønsted acid site, BAS; [b] Lewis acid site, LAS; [c] BAS/LAS determined from pyridine FTIR; [d] BAS density determined directly from isopropylamine titration, [e] LAS density determined from pyridine FTIR and isopropylamine titration.

Table 5.3 also provides quantitative results for LAS densities, which presumably are associated with EFAL species previously observed in both IR and ^{27}Al NMR. Interestingly, trends apparent in octahedrally coordinated EFAL, as determined by ^{27}Al NMR, contradict those observed for LAS density, as obtained from isopropylamine titrations. Similar to the trends observed for BAS, the total amount of LAS decrease with increasing liquid water treatment temperatures, as shown in **Table 5.3**. In contrast, ^{27}Al NMR reveals a monotonic increase in octahedrally coordinated aluminum EFAL up to 400 °C. Kuel et al.[58] have shown a similar discrepancy between the acid site concentrations of steam treated BEA zeolite measured using ^{27}Al NMR and ammonia TPD techniques. The discrepancy between ^{27}Al NMR and ammonia TPD measurements is likely attributable to formation of inactive EFAL species, as noted previously by Loefller et al.[47]

5.4. Discussion

The focus of this work was to understand the effects of zeolite-water interactions and the temperature dependence of water properties on ZSM-5 degradation. Before that analysis could be undertaken, we first needed to establish ZSM-5 degradations mechanisms in hot liquid water and that its stability was sufficient for a meaningful rate analysis. In terms of understanding water dependent ZSM-5 breakdown, the challenge was to determine the relative importance of the two main zeolite degradation mechanisms, desilication and dealumination, and whether they proceeded independently of one another or as an integrated mechanism. Framework degradation data provide insight into the relative importance of desilication on ZSM-5 degradation. XRD indicated that the framework retained >80% of its original crystallinity at all conditions and N$_2$ sorption indicated retention of >65% of original micropore area (as estimated using the *t*-plot method). Surface

features including crystal thinning and the appearance of cavities observed using electron microscopy resemble those reported after alkali promoted desilication of ZSM-5.[38, 39]

Under alkali conditions, the decrystallization process of siliceous ZSM-5 is generally considered to occur via a desilication mechanism involving Si─O bond hydrolysis,[10, 11] and our observations are consistent with this observation. Unlike other zeolites, which undergo internal decrystallization and framework collapse when exposed to hot liquid water,[10, 17] only the external surfaces of MFI show signs of degradation, and the internal framework itself is relatively unperturbed during treatment. Instead, the STEM images in **Figure 5.3** indicate that ZSM-5 framework degradation involves removal of a sacrificial external layer, followed by sequential external amorphization. ZSM-5 degradation under alkali conditions (0.05 – 0.2 M NaOH treatment at temperatures of 60 – 80 °C) obeys similar framework degradation behavior, which includes external surface roughening and pitting as observed here in hot liquid water.[59, 60] STEM and SEM images and XRD spectra of hot liquid water treated ZSM-5 are therefore consistent with a desilication mechanism, which likely originates at crystal surfaces.

Al characterization methods show that ZSM-5 undergoes dealumination, with subsequent deposition of aluminum as EFAL on the zeolite surface. Unlike desilication, which seems to be most severe at approximately 400 °C, dealumination rates appear to increase monotonically with increasing temperature. Whereas the MFI framework retains >80% of its original crystallinity after treatment in liquid water, BAS density decreases by >90%. DRIFTS (**Figure 5.4**), and XPS (**Figure 5.5**) indicate surface enrichment of Al species with liquid water treatment. ^{27}Al NMR (**Figure 5.6**) and ^{29}Si NMR (**Figure A.6**) indicate increasing Si/Al content of the bulk zeolite with increasing treatment temperature, and conversion of internal tetrahedral Al sites to external

octahedral sites. Al−O presumably bonds hydrolyze during water treatment, removing aluminum from the bulk crystal and permitting its migration to the crystal surface as EFAL.

In order for the zeolite to become more siliceous, water treatment must eventually remove EFAL from the zeolite surface, similar to removal of the amorphous silica layer removal previously described. EDS (**Figure A.2**) shows agglomeration of aluminum on the surfaces of ZSM-5 treated at 325 and 400 °C, consistent with migration of internal Al to the surface. At 450 °C, surface enrichment of Al is not observed, potentially suggesting that rates of Al surface migration and dissolution are comparable to one another at this temperature.

Preferential hydrolysis of framework Al−O bonds has been previously shown as the primary mechanism for ZSM-5 breakdown under both acidic and steaming conditions.[41, 46, 52, 53, 61] Consistent with our observations of ZSM-5 treated in hot liquid water, steam and acidic treatment of ZSM-5 reduce BAS density and promote formation of EFAL,[47, 51, 62] while largely retaining framework crystallinity[33, 52] and enriching crystal surface Al species.[46, 51] All of these observations are consistent with results obtained from IR, XPS and ^{27}Al NMR analysis of ZSM-5 treated in hot liquid water.

Consideration of all available experimental data suggests that ZSM-5 degradation in hot liquid water occurs via parallel desilication and dealumination pathways, combining aspects of acid/steam treatment with those generally observed under alkali conditions. Bulk dealumination does not appear to promote internal framework collapse, consistent with previous findings by Ong et al.[30] Since dealumination must initiate primarily at internal sites, the desilication and dealumination processes seem to be proceed independently of one another. **Figure 5.7** summarizes the analysis as a single schematic, showing that removal of a sacrificial amorphous silica layer followed by surface-initiated desilication occurs in parallel with bulk dealumination and deposition
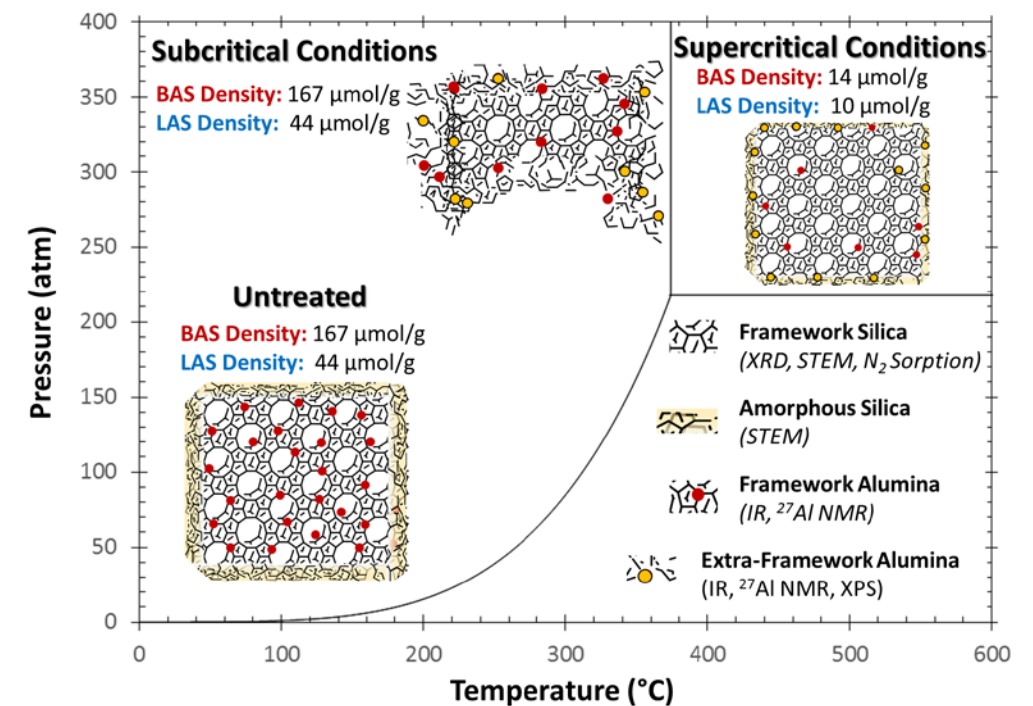
Figure 5.7. Schematic representation of ZSM-5 desilication and dealumination under subcritical and supercritical water treatment overlaid on a P-T phase diagram. BAS and LAS densities are denoted with red and orange dots, respectively. Amorphous silica is denoted in yellow outer coatings.

of EFAL on the crystal surface. Desilication is most severe over the temperature range from 350-420 °C; in contrast, the extent of dealumination increases monotonically with increasing temperature.

Having reached a conclusion on the mechanism of ZSM-5 degradation in hot liquid water, we set out to gain insight into its relative stability compared with other frameworks by quantitative analysis of degradation rates. A major challenge is that the various literature studies investigated different treatment times, ranging from as short as 30 min (this study for Y and β - as shown in **Figure A.1C** and **A.1D**) to as long as 48 hours in the study by Lutz et al.[9] Intercomparison of these data therefore requires a model to normalize results to a common treatment time. Ravenelle

et al.[10] obtained time-resolved data of HY crystallinity after hot liquid water treatment, which allowed testing of different kinetic models. Detailed analysis of literature data, described in the Appendix and summarized in **Figure A.9**, indicated that zeolite degradation rates reported by Ravenelle et al.[10] could be modeled adequately using a pseudo-first order rate law, an approach analogous to that used by Hartman and Fogler in their analysis of zeolite degradation rates in acid solutions at temperatures less than 100 °C. Accordingly, the kinetic model becomes:

$$ln\left[\frac{X(t)}{X(t=0)}\right] = -k_{app}t \qquad (1)$$

where X is a zeolite characteristic (taken either as crystallinity index determined from XRD or Si/Al ratio determined from ^{27}Al-NMR). The slope of the pseudo-first order plot can be taken as k_{app}, the degradation rate constant. Eqn. (1) was used to estimate k_{app} for all available experimental data; estimated values of k_{app} were then used to predict the degree of crystallinity retention after a treatment time of 10 hours, a time selected as an intermediate value compared to the available data.

Figure 5.8 plots predictions of retained crystallinity after 10 hours as a function of treatment temperature for all zeolite frameworks for which liquid water stability data are available. In addition to MFI data, which have been shown previously in **Figure 5.1**, **Figure 5.8** includes new data obtained as part of this study for MOR, FER, and FAU, as well as literature data for MFI,[10] BEA,[17] MOR,[9] FER,[9] and FAU.[10, 11] Error bars in **Figure 5.8** denote stability ranges as obtained from studies of zeolites with varying Si/Al content. Unlike ZSM-5 stability, which seems to be largely independent of its composition,[9] Y and β stability are strongly dependent on Al content, as shown in **Figure 5.8**. **Figure 5.8** makes clear that MFI is the most stable framework of any for which data are available. Interestingly, the stability of FER and MOR are comparable to one another, though less than that of MFI. BEA and FAU are clearly the least stable frameworks shown in **Figure 5.8**. Furthermore, MFI is the only framework which exhibits unusual behavior

near the critical point, which is likely due to the fact that is the only one stable enough for this behavior to be resolved.

The structures of the frameworks studied to date (MFI, FAU, BEA, MOR, and FER) provide some clues that can help explain their hydrothermal stability relative to one another. In particular, we focused on the densities of 4-, 5-, and 6-membered rings in the various structures, as determined by analysis of the International Zeolite Association database.[63] **Table A.1** summarizes the results of the structural analysis. In particular, the MFI framework is composed of unit cells consisting primarily of 5 and 6 membered rings, whereas the FAU and BEA frameworks have much greater fractions of strained 4-membered rings. Quantum calculations suggest that the strain of 4-membered rings reduces their kinetic and/or thermodynamic stability compared to 5- and 6-membered rings.[64, 65] To first order, therefore, the relative densities of 5- and 6-membered rings compared to 4-membered rings seems to be a reasonable predictor of zeolite stability in hot liquid water.

The analysis of ring structures does not fully explain all observations of zeolite stability. For example, FER contains two-dimensional pores with zero 4-membered rings, yet it is less stable than MFI, which contains three dimensional pores with 16 4-membered rings per unit cell.[63] The relative stability of ZSM-5 compared to FER may be attributable to the ability of MFI to undergo dealumination without amorphizing Previous stability studies on FER,[66] FAU[67, 68] and BEA[58] frameworks under acidic or steaming conditions show that dealumination creates defects that eventually lead to formation of internal mesopores and/or loss of crystallinity, whereas MFI largely retains its original framework after dealumination.[33, 52] Since hot liquid water appears to promote desilication and dealumination simultaneously, decoupling of these phenomena in ZSM-5 may be an important factor in its relative stability compared to other zeolites

studied to date. Consistent with this analysis, Prodinger et al.[69] reported that internal silanization

of H-β removes defect sites and greatly increases zeolite stability in hot liquid water, suggesting

that defect sites play a major role in the initiation of de-crystallization. On the other hand, ZSM-5

stability seems to benefit from the presence of an amorphous surface layer, an effect which may

not be shared by other zeolites. Again, defects, their locations, and their propagation all appear to

play important roles in zeolite degradation in hot liquid water.

Figure 5.8 establishes MFI as a model for studying water-zeolite interactions as it is predicted

to retain >50% of its original crystallinity even at the most severe conditions. In terms of

dealumination, ZSM-5 retains sufficient BAS density (or Al content) to permit dealumination rate

analysis at all temperatures. A quantitative analysis was required to understand the importance of

the non-linear temperature dependence of water properties on ZSM-5 degradation, the main goal

of this study. Here, we focused on kinetic aspects of degradation rates. In addition, we considered

thermodynamic analysis, which is summarized in the SI. Since previous analysis suggested that

desilication and dealumination occurred in parallel, independent pathways, Equation 1 was used

to determine value of k_{app} for both crystallinity loss (as measured by XRD) and aluminum loss (as

measured by ^{27}Al NMR) at all temperatures at which data were available. We then performed a

simple Arrhenius analysis of these values of k_{app}, using the familiar equation:

$$ln(k_{app}) = \ln(A) - \frac{E_A}{RT} \qquad (2)$$

where all variables retain their usual meanings. **Figure 5.9a** plots the temperature dependence on

ZSM-5 desilication (black squares), revealing a non-Arrhenius temperature relationship. The de-

crystallization analysis exhibits a poor fit ($r^2 = 0.75$) and data above the critical point do not fall

on the same trend line as data below the critical point. In addition, the estimated activation energy

of 45 kJ mol^{-1} is much less than expected for Si–O bond hydrolysis of zeolites.[70] Similarly, the
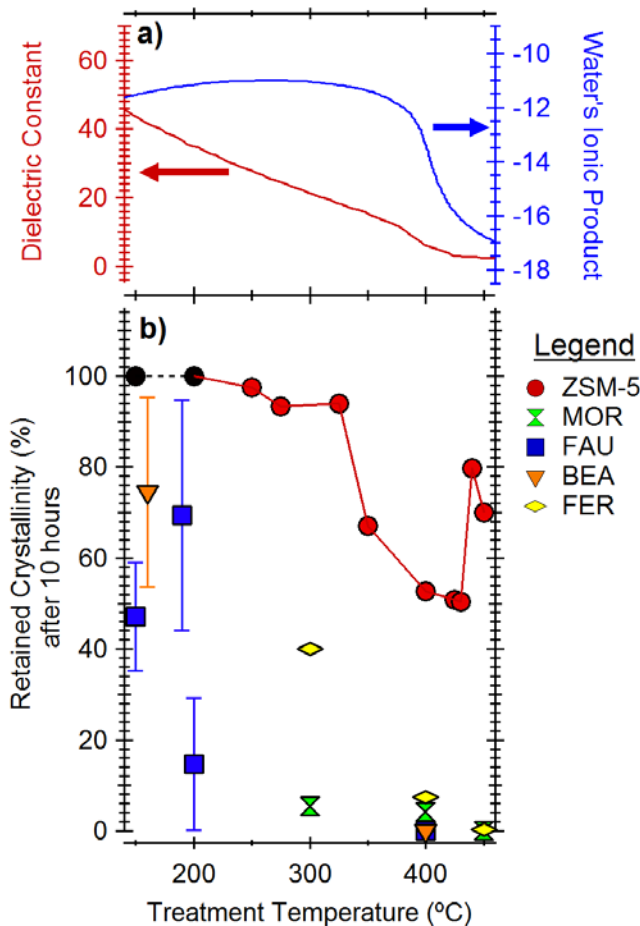
Figure 5.8. Plot of extrapolated retained crystallinity of hot liquid water treated ZSM-5 compared to previous literature studies on MOR, FAU, BEA and FER frameworks. FAU data is taken from Ravenelle et al.[10] and Ennaert et al.[11], MOR and FER from Lutz et al.[9] and BEA taken from Vjunov et al.[17] The dielectric contant and K_w of compressed liquid water are included in the plot on top and denoted in red and blue lines respectively.

Arrhenius analysis for acid site loss, shown in **Figure 5.9a** (red circles), shows noticeable deviation from linearity at $T = 400$ °C. Furthermore, the dealumination activation energy estimated from **Figure 5.9a** is l 23.2 kJ mol^{-1}, again much less than expected.[70] The non-Arrhenius temperature dependence on zeolite degradation shown in **Figure 5.9a** suggests that the effect of temperature is
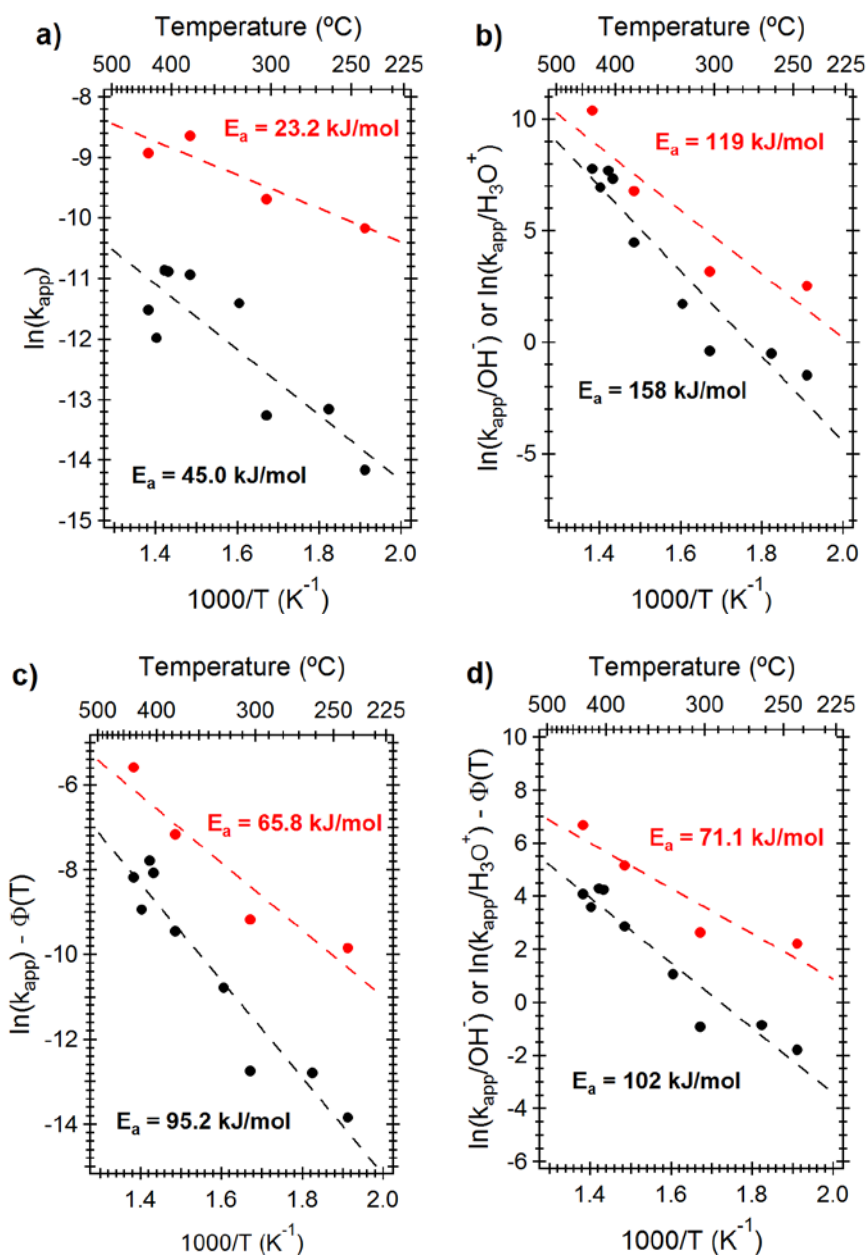
Figure 5.9. Plots of ZSM-5 degradation rates of both decrystallization (black squares) and dealumination (red circles) a) using a simple Arrhenius analysis, b) an adjusted Arrhenius analysis assuming water as the sole source of OH⁻ or H⁺ and accounting for the temperature dependence of K_W, c) an adjusted Arrhenius analysis accounting for the temperature dependence of dielectric constant using the Kirkwood correlation factor, and d) an adjusted Arrhenius analysis accounting for the temperature dependence of both K_W and dielectric constant.

141

more subtle than the usual thermal effect – as originally anticipated when we undertook this study. In fact, **Figure 5.8** overlays the auto-ionization and dielectric constants of pure water over ZSM-5 degradation rate data; the overlay shows that some of the non-Arrhenius rate behavior is coincident with temperatures at which K_W and ε exhibit non-linear temperature variation. Accordingly, we set out to evaluate more complex rate models that incorporate the temperature dependence of water's physical properties.

We turned to the literature on the role of water on the rates of molecular reactions to guide our analysis of ZSM-5 degradation rates. For example, Taylor et al.[27] found that non-Arrhenius behavior for methyl-tert-butyl (MTBE) hydrolysis in sub- and supercritical water, explaining their results by invoking acid/base catalyzed hydrolysis and the temperature varying values of K_W using a global rate expression of the form:

$$-\frac{d[X(t)]}{dt} = k_{app}[X(t)] = A \cdot exp\left[\frac{E_a}{RT}\right][\text{H}^+][X(t)] \qquad (3)$$

where $X(t)$ is the reactant concentration and $[\text{H}^+] = [\text{OH}^-] \approx K_W^{1/2}$. Following the treatment by Taylor et al.[71] equation (3) assumes that the activity coefficient of H^+ is approximately 1. Rearrangement of equation (3) can put the expression of the form:

$$ln\left(\frac{k_{app}}{[H^+]}\right) = \ln(A) + \frac{E_a}{RT} \qquad (4)$$

Assuming that desilication proceeds via Si−O hydrolysis as the rate determining step and that dealumination via Al−O hydrolysis permits quantitative analysis using Equation (4). Similar to C−O bond hydrolysis, desilication is generally promoted by alkali, meaning that desilication rates could exhibit non-Arrhenius behavior in liquid water due to self-dissociation and subsequent OH^- promoted Si─O bond hydrolysis. and can have significant changes in degradation based on the aqueous-phase OH^- concentration.[38, 72, 73] Similarly, dealumination is promoted by acids,

meaning that H^+ liberated by self-dissociation of water could plausibly catalyze the Al−O bond hydrolysis associated with dealumination.

Equation (4) suggests plotting k_{app} data after normalization by either $[H^+]$ (dealumination) or $[OH^-]$ (desilication) to obtain a straight line with intercept corresponding to $-E_a/R$. **Figure 5.9b** presents the results of this analysis for desilication (black squares) and for dealumination (red circles). The trend line obtained for desilication is linear over several orders of magnitude ($r^2 = 0.90$) and data above and below the critical point are equally well fit. The slope of the best-fit line for desilication data corresponds to an activation energy of approximately 160 kJ mol^{-1}, which is in better agreement with literature values of Si−O bond hydrolysis relative compared to the value obtained from the simple Arrhenius analysis shown in **Figure 5.9a**.[70] As with desilication, the dealumination data (red circles) shown in **Figure 5.9b** are linearized by $[H^+]$ normalization, though the normalized dealumination data retain more scatter than do the normalized desilication data. Quantitatively, the dealumination data in **Figure 5.9b** correspond to an activation energy of 120 kJ mol^{-1}, which is in reasonable agreement with the previous value of 190-260 kJ mol^{-1} estimated using DFT.[70] Acid/base normalization of degradation rates therefore results in qualitative improvement in data fits and quantitative agreement with expected values of Si−O and Al−O bond hydrolysis activation energies, especially when the inherent uncertainties of both the experimental values and DFT estimates are taken into account.

Although incorporating $[OH^-]$ concentration improves the linearity of the Arrhenius fit, the data in **Figure 5.9b** are not randomly scattered around the best-fit line, instead showing systematic under-prediction at intermediate temperatures. The systematic bias suggests that other factors aside from OH^- concentration may play secondary roles in Si−O bond hydrolysis. We focused our attention on the potential role of the solvent to stabilize polar transition states.[74, 75] Marrone et

al.[76] described the effect of water dielectric constant on the non-Arrhenius relationship governing dichloromethane hydrolysis in sub- and supercritical water. The dielectric constant varies from approximately 80.1 at room temperature to 1 at the critical point, as shown in **Figure 5.8**, meaning that it can exert a temperature-dependent effect on reactions which proceed via polar transition states. While dealumination and desilication transition states involved in zeolite degradation are not as well defined as their molecular analogs, previous computational analysis predicts that hydrolysis of Si−O and Al−O bonds proceeds via polarized transition states.[70] Marrone et al.[76] proposed combining Kirkwood dielectric continuum solvation theory with transition state theory to account for the temperature dependence of desilication and dealumination rates arising from the temperature dependence of the dielectric constant:

$$ln\left(k_{app}\right) = \ln(A) - \frac{E_A}{RT} + \Phi(T) \qquad (5)$$

where $\Phi(T)$ is the Kirkwood correlation factor. The Kirkwood correlation factor estimates the effects of the dielectric constant (ϵ_i) on the stabilization of the polar transition state for reactions of the type A + B →P, assuming that the solvent behaves as a continuum:

$$\Phi(T) = -\frac{1}{RT}\left(\left(\Delta G_\epsilon^{vac} - \Delta G_{\epsilon_a}^{vac}\right) + \frac{N_A}{4\pi\epsilon_0}\left(\frac{\frac{\epsilon_a-1}{2\epsilon_a+1}\left[\frac{\mu_{\ddagger,\epsilon_a}^2}{r_{\ddagger,\epsilon_a}^3} - \frac{\mu_A^2}{r_A^3} - \frac{\mu_B^2}{r_B^3}\right]}{-\frac{\epsilon-1}{2\epsilon+1}\left[\frac{\mu_{\ddagger,\epsilon}^2}{r_{\ddagger,\epsilon}^3} - \frac{\mu_A^2}{r_A^3} - \frac{\mu_B^2}{r_B^3}\right]}\right)\right) \qquad (6)$$

where μ_i is the dipole moment r_i is the ionic radii (r_i) of either the reactant (denoted with the subscripts "A") the product (denoted with the subscript "B") or the transition state (denoted with $\ddagger$ subscript). In addition, ΔG_ϵ is the change in Gibbs free energy relative to vacuum and ϵ is the dielectric constant of water solvent. In a molecular reaction, equating ϵ with the bulk dielectric constant of the solvent is unambiguous. For reactions proceeding in molecular-scale micropores, the local value of the dielectric constant is less clear. In the case of desilication, which

characterization data indicate occurs primarily at zeolite surfaces, using the bulk dielectric constant may be justified. For dealumination, which must occur primarily in the micropores themselves, using the bulk dielectric constant is less clear. However, no data are available to develop a model of the molecularly confined dielectric constant, meaning that no clear alternative is available. Accordingly, we used the bulk dielectric constant for analysis of both desilication and dealumination rates.

For this study, the dipole moments (μ_i), ionic radii (r_i) are considered to be weak functions of temperature, allowing them to be lumped together into a single factor, W:

$$\Phi(T) = -\frac{1}{RT}\left(\left(\Delta G_\epsilon^{vac} - \Delta G_{\epsilon_a}^{vac}\right) + W\left(\frac{\epsilon_a - 1}{2\epsilon_a + 1} - \frac{\epsilon - 1}{2\epsilon + 1}\right)\right) \qquad (7)$$

Neglecting the temperature dependence of the dipole moments of the reactants is reasonable; Gubskaya and Kusalik[77] indicate that the dipole of water varies only 10% over the range from 273 to 373 K. The temperature dependence of the transition state dipole is less clear; however, the present analysis must necessarily neglect it, as calculating the temperature dependent dipole moment of the Al−O and Si−O transition states is beyond the scope of this study. Instead, as with equating the micropore dielectric constant with the bulk value, we sought to determine if Kirkwood theory, when combined with the bulk dielectric constant of water, has the correct form for empirical description of desilication and dealumination rates.

To test the use of Kirkwood theory to describe degradation rates, Equations (5-7) were used without inclusion of the [OH⁻] or [H⁺] correction shown previously and using W as a best-fit parameter. **Figure 5.9c** contains plots of the desilication (black squares) and dealumination (red circles) rate constants analyzed using Kirkwood theory. Overall, the fits obtained from Kirkwood theory are inferior to those found using the [OH⁻] or [H⁺] correction. Quantitatively, the corresponding desilication (95.2 kJ mol⁻¹) and dealumination (65.8 kJ mol⁻¹) were in poor

agreement with values expected from simulation.[78] **Figure 5.9c** indicates that Kirkwood theory on its own is not sufficient to explain measured dealumination and desilication rates.

Based on the success of the [OH$^-$] or [H$^+$] correction, we next decided to combine it with Kirkwood theory:

$$ln\left(\frac{k_{app}}{[H^+]}\right) = \ln(A) - \frac{E_A}{RT} + \Phi(T) \qquad (8)$$

where all variables have been previously defined. **Figure 5.9d** contains Arrhenius-style plots of desilication (black squares) and dealumination (red circles) rate constants, analyzed using both the Kirkwood correction and K_W normalization. Desilication rates shown in **Figure 5.9d** are well described by the acid/base-modified Kirkwood theory, with a single outlier data point and a slope corresponding to an activation energy 100 kJ mol^{-1}. Similarly, the dealumination analysis in **Figure 5.9d** provides a good fit for the available data, with the residual scatter consistent with experimental error. The dealumination activation energy determined from the modified Kirkwood approximation is 70 kJ mol^{-1}, which is less than predicted from simulations, but not unreasonably so given the level of approximation required for the analysis. On the other hand, the correlation constants (r^2) obtained using the Kirkwood approximation are similar to those obtained from acid/base adjustment of Arrhenius theory, indicating that Kirkwood theory may not be required to explain experimental observations. The challenge, shown in **Figure 5.8**, is that K_w and ε exhibit similar temperature behavior to one another. **Figure 5.9d** therefore suggests that explaining ZSM-5 degradation rates in liquid water requires accounting for [OH$^-$] or [H$^+$], and that future work can evaluate the benefits of including the temperature dependence of the dielectric constant in the rate analysis.

The present analysis provides guidance to prolong zeolite lifetimes in hot liquid water. For example, addition of dilute hydrochloric acid could be used to decrease desilication rates, consistent with the study by Ennaert et al.[11] On the other hand, attempts to reduce desilication rates run the risk of increasing dealumination rates, since dealumination rates are often observed to be acid promoted. In addition, assuming that the solvent indeed plays a role in stabilizing Si–O and/or Al–O transition states, decreasing the effective dielectric constant may stabilize zeolites in liquid phases containing water. Assuming that solvent polarity influences degradation rates, a nonpolar co-solvent might be added to the reaction mixture to decrease its effective dielectric constant and the auto-ionization constant of water; indeed, several previous groups may have inadvertently used this approach by studying zeolite activity under conditions where a significant hydrocarbon co-solvent was present as a reactant.[79-81] In these cases, preservation of zeolite crystallinity at conditions which this study predicts should result in >50% decrystallization, may be due to the effect of the co-solvent/reactant on the dielectric constant and K_W. This suggests that mechanical de-watering, rather than drying, to reduce water content of aqueous or moist feeds may be an energy efficient strategy that permits prolonged use of zeolites, especially since physical de-watering is typically less energy intensive than thermal drying.[82]

4.5. Conclusion

To address fundamental knowledge gaps in the effects of the thermodynamic properties of water on zeolite stability, ZSM-5 degradation was studied in liquid water at temperatures over the range from 250 to 450 °C, with specific emphasis on the stability of the framework, retention of acid sites, and the activity of the material following treatment. The ZSM-5 framework remains stable when treated for 3 hours in hot liquid water at temperatures less than 325 °C. When treated at

temperatures greater than 325 °C, ZSM-5 crystallinity decreases and textural properties show signs of framework degradation. The temperature dependence of crystallinity and changes in textural properties are non-monotonic, with 400 °C being the most aggressive conditions studied. ZSM-5 decrystallization appears to initiate at the crystal surface. Instead, exposure to hot liquid water appears to remove a sacrificial amorphous silica overcoat.

ZSM-5 degradation appears to proceed via parallel desilication and dealumination pathways. Crystallinity (XRD) and dealumination (^{27}Al NMR) data were analyzed using a first-order kinetic model to estimate degradation rate constants as functions of temperature. These rate constants were then used to compare the stability of MFI with other frameworks that have been studied, namely FAU, BEA, MOR, and FER. This analysis clearly established MFI as the most stable framework studied to date, with its relative lack of strained 4-membered rings compared to the other frameworks the likely source of its stability. Ring strain alone did not explain all observed stability trends, specifically the greater stability of MFI compared to FER, despite the complete absence of 4-membered rings in the FER framework. Based on analogies with framework stabilities measured under alkali, acid, and steaming conditions, differences in defect chemistry, location, and tendency to propagate were suggested as a secondary factor governing zeolite stability in liquid water.

The temperature dependencies of desilication and dealuminate rate data were analyzed and found not to follow typical Arrhenius behavior, suggesting that temperature plays more than a thermal role in determining ZSM-5 degradation rates in liquid water. We re-analyzed the data using the temperature-dependent values of K_W and ε, and recovered Arrhenius behavior with corresponding activation energies estimated as 102─158 for desilication and 71.1─119 kJ mol^{-1} for dealumination. Mechanistically, this analysis suggests that OH$^-$ and H$^+$ formed by auto-ionization from water influence desilication (OH$^-$) and dealumination (H$^+$) rates, similar to behavior

observed at treatment temperatures less than 100 °C but with addition of alkali or acid promoters. Additionally, water seems to solvate the polar transition states involved in Si─O and Al─O bond hydrolysis, as this effect is capture – at least in part – by including the temperature-dependent values of ε using a Kirkwood-modified Arrhenius analysis. These results point to the importance of temperature-varying properties on zeolite stability in hot liquid water, provide a framework for understanding these effects, and point to new avenues for work in this active research field.

5. References

1. Toor, S.S., et al., *Hydrothermal liquefaction of biomass: A review of subcritical water technologies.* Energy, 2011. **36**: p. 2328-2342.

2. Peterson, A.A., et al., *Thermochemical biofuel production in hydrothermal media: A review of sub- and supercritical water technologies.* Energy & Environmental Science, 2008. **1**: p. 32.

3. Zaker, A., et al., *Zeolite Catalyzed Cracking of Dodecane in Supercritical Water: Lewis and Brønsted Acidity Article.* Catalysis Today, 2018.

4. Robin, T., J.M. Jones, and A.B. Ross, *Catalytic hydrothermal processing of lipids using metal doped zeolites.* Biomass and Bioenergy, 2017. **98**: p. 26-36.

5. Duan, P., et al., *Catalytic upgrading of pretreated algal bio-oil over zeolite catalysts in supercritical water.* Biochemical Engineering Journal, 2016. **116**: p. 105-112.

6. Mo, N. and P.E. Savage, *Hydrothermal catalytic cracking of fatty acids with HZSM-5.* ACS Sustainable Chemistry and Engineering, 2014. **2**: p. 88-94.

7.   Li, Z. and P.E. Savage, *Feedstocks for fuels and chemicals from algae: Treatment of crude bio-oil over HZSM-5.* Algal Research, 2013. **2**: p. 154-163.

8.   Xiong, H., H.N. Pham, and A.K. Datye, *Hydrothermally stable heterogeneous catalysts for conversion of biorenewables.* Green Chemistry, 2014. **16**: p. 4627-4643.

9.   Lutz, W., et al., *Investigation and modeling of the hydrothermal stability of technically relevant zeolites.* Adsorption, 2005. **11**: p. 405-413.

10.   Ravenelle, R.M., et al., *Stability of zeolites in hot liquid water.* Journal of Physical Chemistry C, 2010. **114**: p. 19582-19595.

11.   Ennaert, T., et al., *Conceptual frame rationalizing the self-stabilization of H-USY zeolites in hot liquid water.* ACS Catalysis, 2015. **5**: p. 754-768.

12.   Zapata, P.A., et al., *Silylated hydrophobic zeolites with enhanced tolerance to hot liquid water.* Journal of Catalysis, 2013. **308**: p. 82-97.

13.   Lutz, W., et al., *Hydrothermally resistant high-silica Y zeolites stabilized by covering with non-framework aluminum species.* Microporous Materials, 1997. **12**: p. 131-139.

14.   Bakare, I.A., et al., *Hydrothermal stability of MTT zeolite in hot water: The role of La and Ce.* Microporous and Mesoporous Materials, 2016. **233**: p. 93-101.

15.   Jamil, A.K., et al., *Hydrothermal Stability of One-Dimensional Pore ZSM-22 Zeolite in Hot Water.* Journal of Physical Chemistry C, 2016. **120**: p. 22918-22926.

16.   Zhang, L., et al., *Factors that Determine Zeolite Stability in Hot Liquid Water.* Journal of the American Chemical Society, 2015. **137**: p. 11810-11819.

17.   Vjunov, A., et al., *Impact of aqueous medium on zeolite framework integrity.* Chemistry of Materials, 2015. **27**: p. 3533-3545.

18.   Eckstein, S., et al., *Elementary steps and reaction pathways in the aqueous phase alkylation of phenol with ethanol.* Journal of Catalysis, 2017. **352**: p. 329-336.

19.   Liu, Y., et al., *Enhancing the catalytic activity of hydronium ions through constrained environments.* Nature Communications, 2017. **8**: p. 14113.

20.   Gardner, D.W., et al., *Insights into the Hydrothermal Stability of ZSM-5 under Relevant Biomass Conversion Reaction Conditions.* ACS Catalysis, 2015. **5**: p. 4418-4422.

21.   Kruger, J.S., V. Nikolakis, and D.G. Vlachos, *Aqueous-phase fructose dehydration using Brønsted acid zeolites: Catalytic activity of dissolved aluminosilicate species.* Applied Catalysis A: General, 2014. **469**: p. 116-123.

22.   Vjunov, A., et al., *Impact of zeolite aging in hot liquid water on activity for acid-catalyzed dehydration of alcohols.* Journal of the American Chemical Society, 2015. **137**: p. 10374-10382.

23.   Bandura, A.V. and S.N. Lvov, *The ionization constant of water over wide ranges of temperature and density.* Journal of Physical and Chemical Reference Data, 2006. **35**: p. 15-30.

24.   Kruse, A. and E. Dinjus, *Hot compressed water as reaction medium and reactant. 2. Degradation reactions.* Journal of Supercritical Fluids, 2007. **41**: p. 361-379.

25.   Venardou, E., et al., *On-line monitoring of the hydrolysis of acetonitrile in near-critical water using Raman spectroscopy.* Vibrational Spectroscopy, 2004. **35**: p. 103-109.

26.   Hunter, S.E. and P.E. Savage, *Recent advances in acid- and base-catalyzed organic synthesis in high-temperature liquid water.* Chemical Engineering Science, 2004. **59**: p. 4903-4909.

27.   Taylor, J., et al., *Multiscale Reaction Pathway Analysis of Methyl tert-Butyl Ether Hydrolysis under Hydrothermal Conditions.* Industrial & Engineering Chemistry Research, 2002. **41**: p. 1-8.

28.   Serrano, D.P., et al., *Influence of the calcination treatment on the catalytic properties of hierarchical ZSM-5.* Catalysis Today, 2012. **179**: p. 91-101.

29.   Mo, N., W. Tandar, and P.E. Savage, *Aromatics from saturated and unsaturated fatty acids via zeolite catalysis in supercritical water.* Journal of Supercritical Fluids, 2015. **102**: p. 73-79.

30.   Muraoka, K., W. Chaikittisilp, and T. Okubo, *Energy Analysis of Aluminosilicate Zeolites with Comprehensive Ranges of Framework Topologies, Chemical Compositions, and Aluminum Distributions.* Journal of the American Chemical Society, 2016. **138**: p. 6184-6193.

31.   ASTM, *Standard Test Method for Determination of Relative Crystallinity of Zeolite ZSM-5 by X-Ray Diffraction.* ASTM International: D4758-01, 2015. **05**: p. 3-5.

32.   Fyfe, C.a., G.C. Gobbi, and G.J. Kennedy, *Investigation of the conversion (dealumination) of ZSM-5 into silicalite by high-resolution solid-state 29Si and 27Al MAS NMR spectroscopy.* Journal of Physical Chemistry, 1984. **88**: p. 3248-3253.

33.   Ong, L.H., et al., *Dealumination of HZSM-5 via steam-treatment.* Microporous and Mesoporous Materials, 2012. **164**: p. 9-20.

34.   Beyerlein, R.A., et al., *The Engineering of Chemical Reactions.* Topics in Catalysis, 1997: p. 27-42.

35.   Héroguel, F., B. Rozmysłowicz, and J.S. Luterbacher, *Improving Heterogeneous Catalyst Stability for Liquid-phase Biomass Conversion and Reforming.* CHIMIA International Journal for Chemistry, 2015. **69**: p. 582-591.

36.   Román-Leshkov, Y., et al., *Mechanism of glucose isomerization using a solid lewis acid catalyst in water.* Angewandte Chemie - International Edition, 2010. **49**: p. 8954-8957.

37.   Fodor, D., et al., *Role of defects in pore formation in MFI zeolites.* Journal of Physical Chemistry C, 2015. **119**: p. 5447-5453.

38.   Groen, J.C., et al., *Mechanism of hierarchical porosity development in MFI zeolites by desilication: The role of aluminium as a pore-directing agent.* Chemistry - A European Journal, 2005. **11**: p. 4983-4994.

39.   Sano, T., et al., *Effect of framework aluminum on the dissolution process of ZSM-5 zeolite crystal.* Microporous Materials, 1997. **12**: p. 71-77.

40.   Fodor, D., et al., *Differences between individual ZSM-5 crystals in forming hollow single crystals and mesopores during base leaching.* Chemistry - A European Journal, 2015. **21**: p. 6272-6277.

41.   Triantafillidis, C.S., et al., *Effect of the degree and type of the dealumination method on the structural, compositional and acidic characteristics of H-ZSM-5 zeolites.* Microporous and Mesoporous Materials, 2001. **47**: p. 369-388.

42.   Reitmeier, S.J., et al., *Enhancement of sorption processes in the zeolite H-ZSM5 by postsynthetic surface modification.* Angewandte Chemie - International Edition, 2009. **48**: p. 533-538.

43.   LIPPENS, B.C. and J.H. Boer, *Studies on pore systems in catalysts V. The t method.* Journal of Catalysis, 1965. **4**: p. 319-323.

44.   Trombetta, M., et al., *An FT-IR study of the internal and external surfaces of HZSM5 zeolite.* Applied Catalysis A: General, 2000. **192**: p. 125-136.

45.   Jin, F. and Y. Li, *A FTIR and TPD examination of the distributive properties of acid sites on ZSM-5 zeolite with pyridine as a probe molecule.* Catalysis Today, 2009. **145**: p. 101-107.

46.   Datka, J., et al., *Physicochemical and Catalytic Properties of HZSM-5 Zeolites Dealuminated by the Treatment with Steam.* The Journal of Physical Chemistry, 1996. **100**: p. 14451-14456.

47.   Loeffler, E., et al., *Study of Different States of Nonframework Aluminum in Hydrothermally Dealuminated H-ZSM-5 Zeolites unsing Diffuse Reflectance I.R. Spectroscopy.* Zeolites, 1990. **10**: p. 266-271.

48.   Kumar, S., et al., *Influence of mild dealumination on physicochemical, acidic and catalytic properties of H-ZSM-5.* Journal of Molecular Catalysis A: Chemical, 2000. **154**: p. 115-120.

49.   Briggs, D., *Handbook of X‑ray Photoelectron Spectroscopy CD Wanger, WM Riggs, LE Davis, JF Moulder and GE Muilenberg Perkin‑Elmer Corp., Physical Electronics Division,.* Surface and Interface Analysis, 1981.

50.   Marschmeyer, S. and H. Papp, *Surface analysis of a hydrothermally treated H-ZSM-5 zeolite.* Surface and Interface Analysis, 1997. **25**: p. 660-666.

51.   Campbell, S.M., et al., *Dealumination of HZSM-5 Zeolites.* Journal of Catalysis, 1996. **358**: p. 350-358.

52.   Niwa, M., S. Sota, and N. Katada, *Strong Brønsted acid site in HZSM-5 created by mild steaming.* Catalysis Today, 2012. **185**: p. 17-24.

53. Kooyman, P.J.J., P. van der Waal, and H. Van Bekkum, *Acid dealumination of ZSM-5.* Zeolites, 1997. **18**: p. 50-53.

54. Farneth, W.E. and R.J. Gorte, *Methods for Characterizing Zeolite Acidity.* Chemical Reviews, 1995. **95**: p. 615-635.

55. Kellicutt, A.B., et al., *An examination of the intrinsic activity and stability of various solid acids during the catalytic decarboxylation of γ-valerolactone.* Catalysis Science & Technology, 2014. **4**: p. 2267.

56. Ferreira Madeira, F., et al., *Ethanol transformation into hydrocarbons on ZSM-5 zeolites: Influence of Si/Al ratio on catalytic performances and deactivation rate. Study of the radical species role.* Applied Catalysis A: General, 2012. **443-444**: p. 171-180.

57. Mlekodaj, K., et al., *Porosity and accessibility of acid sites in desilicated ZSM-5 zeolites studied using adsorption of probe molecules.* Microporous and Mesoporous Materials, 2014. **183**: p. 54-61.

58. Kuehl, G.H. and H.K.C. Timken, *Acid sites in zeolite Beta: Effects of ammonium exchange and steaming.* Microporous and Mesoporous Materials, 2000. **35**: p. 521-532.

59. Van Bokhoven, J.A., et al., *Stepwise dealumination of zeolite Beta at specific T-sites observed with 27Al MAS and 27Al MQ MAS NMR.* Journal of the American Chemical Society, 2000. **122**: p. 12842-12847.

60. Su, L., et al., *Creating mesopores in ZSM-5 zeolite by alkali treatment: A new way to enhance the catalytic performance of methane dehydroaromatization on Mo/HZSM-5 catalysts.* Catalysis Letters, 2003. **91**: p. 155-168.

61.   Groen, J.C., J.A. Moulijn, and J. Pérez-Ramírez, *Decoupling mesoporosity formation and acidity modification in ZSM-5 zeolites by sequential desilication-dealumination.* Microporous and Mesoporous Materials, 2005. **87**: p. 153-161.

62.   Maijanen, A., E. Derouane, and J. Nagy, *FT-IR and Solid State NMR Investigation of Surface Hydroxyl Groups on Dealuminated ZSM-5.* Applied Surface Science, 1994. **75**: p. 204-212.

63.   *Database of Zeolite Structures.*

64.   Groen, J.C., et al., *Mesoporous beta zeolite obtained by desilication.* Microporous and Mesoporous Materials, 2008. **114**: p. 93-102.

65.   Petrovic, I., et al., *Thermochemical study of the stability of frameworks in high silica zeolites.* Chemistry of Materials, 1993. **5**: p. 1805-1813.

66.   Pellet, R.J., et al., *Isomerization of n-butene to Isobutene by Ferrierite and Modified Ferrierite Catalysts.* Journal of Catalysis, 1995. **157**: p. 423-435.

67.   Dimitrijevic, R., W. Lutz, and A. Ritzmann, *Hydrothermal stability of zeolites: Determination of extra-framework species of H-Y faujasite-type steamed zeolite.* Journal of Physics and Chemistry of Solids, 2006. **67**: p. 1741-1748.

68.   Kawai, T. and K. Tsutsumi, *A Study on the Surface Silanol Groups Developed by Hydrothermal and Acid Treatment of Faujasite Type Zeolites.* Journal of colloid and interface science, 1999. **212**: p. 310-316.

69.   Prodinger, S., et al., *Improving Stability of Zeolites in Aqueous Phase via Selective Removal of Structural Defects.* Journal of the American Chemical Society, 2016: p. jacs.5b12785.

70. Malola, S., et al., *Detailed reaction paths for zeolite dealumination and desilication from density functional calculations.* Angewandte Chemie - International Edition, 2012. **51**: p. 652-655.

71. Taylor, J.D., J.I. Steinfeld, and J.W. Tester, *Experimental Measurement of the Rate of Methyl tert -Butyl Ether Hydrolysis in Sub- and Supercritical Water.* Industrial & Engineering Chemistry Research, 2001. **40**: p. 67-74.

72. Ogura, M., et al., *Alkali-treatment technique - New method for modification of structural and acid-catalytic properties of ZSM-5 zeolites.* Applied Catalysis A: General, 2001. **219**: p. 33-43.

73. Verboekend, D. and J. Pérez-Ramírez, *Design of hierarchical zeolite catalysts by desilication.* Catalysis Science & Technology, 2011. **1**: p. 879.

74. Townsend, S.H., et al., *Solvent Effects During Reactions in Supercritical Water.* Industrial and Engineering Chemistry Research, 1988. **27**: p. 143-149.

75. Wong, M.W., M.J. Frisch, and K.B. Wiberg, *Solvent Effects 1. The Mediation of Electrostatic Effects by Solvents.* J. Am. Chem. Soc., 1991. **113**: p. 4776-4782.

76. Marrone, P., *1998 Marrone thesis.pdf*. 1998.

77. Gubskaya, A.V. and P.G. Kusalik, *The total molecular dipole moment for liquid water.* Journal of Chemical Physics, 2002. **117**: p. 5290-5302.

78. Silaghi, M.C., C. Chizallet, and P. Raybaud, *Challenges on molecular aspects of dealumination and desilication of zeolites.* Microporous and Mesoporous Materials, 2014. **191**: p. 82-96.

79. Sahu, R. and P.L. Dhepe, *A one-pot method for the selective conversion of hemicellulose from crop waste into C5 sugars and furfural by using solid acid catalysts.* ChemSusChem, 2012. **5**: p. 751-761.

80. O'Neil, R., et al., *Kinetics of aqueous phase dehydration of xylose into furfural catalyzed by ZSM-5 zeolite.* Industrial and Engineering Chemistry Research, 2009. **48**: p. 4300-4306.

81. Deepa, A.K. and P.L. Dhepe, *Lignin Depolymerization into Aromatic Monomers over Solid Acid Catalysts Lignin Depolymerization into Aromatic Monomers over Solid Acid Catalysts.* ACS Catalysis, 2015. **5**: p. 365-379.

82. Chen, G., P.L. Yue, and A.S. Mujumdar, *Sludge dewatering and drying.* Drying Technology, 2002. **20**: p. 883-916.

Chapter 6

Thermal and Temporal Effects on ZSM-5 Framework and Acid Site Stability under Hot Liquid Water Conditions

6.1 Background

Recent interest in process intensification technologies, particularly for converting biomass derived feedstocks into platform chemicals, has motivated interest in compressed liquid phase reactions.[1-3] Many studies use water as a low cost reaction medium at elevated temperatures, which eliminates the energy costs associated with reducing the high moisture content of common biological feedstocks.[1-3] In order to convert organic products diluted in an aqueous solvent, selecting a catalyst that is both active and hydrothermally stable at industrial timescales is required.

Previous studies have selected zeolites as effective catalysts for converting organics under compressed liquid water conditions.[1-8] Zeolites are microporous aluminosilicate structures comprised of a silica-linked structure with catalytically active aluminum sites incorporated within the framework.[8, 9] Brønsted activity in a zeolite arises from a charge compensating hydrogen cation at each framework aluminum sites. In particular, Zaker et al.[10] found that the addition of water attenuated coke formation during cracking of dodecane, a model compound for the petrochemical industry.[11] Compared to the number of vapor phase, zeolite activity and hydrothermal stability studies,[12-16] there are relatively few that evaluate zeolite use in the liquid phase.[8, 17]

Previous hot liquid water (HLW) stability studies have reported that H-β and H-Y zeolites, with either reduced defects or optimized Si/Al ratios, can result in a partially retained framework crystallinity after short periods of HLW treatment at temperatures of 200 °C.[18, 19] In one case, Ennaert et al.[20] reported that USY (Si/Al=19) zeolite successfully retained 88% of its original crystallinity after 24 hours of HLW treatment at 190 °C. However, most reported frameworks are unable to retain at least half of their original crystallinity for more than 12 hours of hot liquid water treatment at temperatures greater than 200 °C.[21] Jamil et al.[22] studied the HLW framework stability of ZSM-22 at 250 °C, conditions where more than half of its original framework crystallinity was lost after 32 hours, but recovered its crystallinity after 144 hours of treatment. However, the recovery in crystallinity was attributed to the formation of a co-crystallized MFI phase, a result that highlights the metastability of the MFI framework in hot liquid water conditions compared to other frameworks.[22] In fact, MFI is the only framework shown to retain crystallinity at treatment temperatures of 240 °C after 72 hours, with only a slight influence of the framework Si/Al ratio.[21] Therefore, ZSM-5 is the most promising catalyst, based on its relative framework hydrothermal stability under compressed liquid water conditions.

This study evaluates the framework crystallinity of ZSM-5 under elevated treatment temperatures and/or prolonged treatment times, up to 350 °C or ~1000 hrs. Based on the previous work in Chapter IV that revealed the unique hydrothermal stability of ZSM-5 after 3 hours of HLW treatment, this work extends the current understanding of ZSM-5 HLW stability to industrial time scales. After treatment, the ZSM-5 framework is characterized using a variety of complementary techniques: X-ray diffraction (XRD), N_2 sorption, scanning electron microscopy (SEM), and transmission electron microscopy (TEM) imaging. In addition, analysis of acid site stability after HLW treatment was performed using infrared spectroscopy (DRIFTS) and nuclear magnetic

160

resonance (^{27}Al NMR). These post-run characterization techniques help assess how treatment temperatures influence ZSM-5 framework and acid sites at prolonged, industrial time-scales.

6.2 Experimental Section

6.2.1 Materials

Binderless ZSM-5 zeolite powder (2μm crystals) with Si/Al=38 were obtained from ACS Materials. Prior to use, catalysts were first heated to 100 °C for at least one hour followed by calcination at 550 °C for at least 16 hrs. Water was de-ionized to 17.9 MΩ cm prior to use.

6.2.2 Catalyst Treatment

Reactions were performed in a 100 ml stainless steel Parr batch reactor. A total of 1g of the calcined zeolite was loaded with 50 mL of DI water. The system was purged with nitrogen gas five times and initially pressurized to 1000 psi before being heated to the desired temperature. Once the set temperature was reached, additional nitrogen gas was delivered until the batch reactor was at 3000 psi. When the desired time was met, the heater and agitator were powered off. The reactor was cooled in an ice bath and slowly depressurized inside the fume hood. The mixture in the reactor was removed and dried in an oven at 60 °C for 15 hrs.

6.2.3 Material Characterization

ZSM-5 was characterized before and after hydrothermal treatment by: scanning electron microscopy (SEM), X-ray diffraction spectrometry (XRDS), N_2 gas sorption, transmission electron microscopy (TEM), Diffuse Reflectance Infra-Red Fourier Transform Spectroscopy (DRIFTS), and ^{29}Al and ^{27}Si magic angle spinning nuclear magnetic resonance (MAS-NMR). SEM provided information on zeolite external crystal surfaces and particle morphology. SEM images were captured using Hitachi SU8230 scanning electron microscope with a cold field

emission source. The samples were mounted on the stub holder using carbon paste. No conductive coatings were applied to the specimens.

Sample crystallinity provides a relative quantitative measure of zeolite degradation. X-ray diffraction was performed using a Rigaku automatic instrument with the Bragg-Bretano theta-theta configuration. Diffractions were taken with a Cu Kα at 27.5kV and 5mA. Analysis was performed over the range from 5-80° 2Θ with a 0.5 step size and 1s dwell time. Crystallinity for each sample was determined from the sum of peak intensities between 22.5-25 2Θ degrees, as designated by ASTM method D5758-01. The 22.5-25 2Θ range includes the prominent ZSM-5 peaks that correspond to the (051), (313) and (033) planes.

Zeolite samples for STEM characterization were crushed using a mortar and pestle. The crushed powder was placed on a 200 mesh copper grid with a holey carbon support film. Secondary electron (SE), bright field (BF), and high angle annular dark field (HAADF) images were captured with a Hitachi HF-3300 microscope operated at an accelerating voltage of 300 kV.

Infrared spectroscopy on treated ZSM-5 samples was performed using a Thermo Nicolet Magna 560 with a SpectraTech DRIFTS cell. Samples were analyzed over the range from 4000 to 400 cm^{-1}, at a resolution of 2 cm^{-1}, and an accumulation of 96 scans. The DRIFTS cell was loaded and flattened with ZSM-5 before purging with N_2 for 10 minutes. 20 °C increments at 10-15 min intervals were ran until 100 °C, where it was held for 30 minutes before raising 50 °C increments to 550 °C. Gas sorption was performed using an ASIQ iQ Quantachrome Instrument is used to determine surface micropore area, external surface area, and micropore volume. Approximately 0.025g of a ZSM-5 sample was first were outgassed with a thermal ramp of 2 °C/min, holding for 20 minutes at 80 °C, 100 °C and 120 °C before a final ramp to 350 °C for 10 hours. The degassed sample were incrementally dosed with nitrogen at 77 K from a p/p_0 range of 10^{-6} to 1. Isotherms

were analyzed using the t-plot method to determine, micropore area and volume. Mesopore volume was calculated using the difference between micropore volume and total adsorbed nitrogen at p/p_0 = 0.99.

All ^{27}Al NMR spectra were collected at 9.4 T on a Varian INOVA spectrometer, using a resonance frequency of 104.17 MHz. ^{27}Al data were collected using a 2.5 mm double resonance Chemagnetics MAS probe with a spinning rate of 16 kHz. A one-pulse experiment with a 1.0 µ/s long $\pi/6$ pulse and a 1.0 s recycle delay was used for the one-dimensional ^{27}Al spectra. All ^{27}Al spectra were referenced to aqueous aluminum nitrate (0 ppm). All ^{27}Al NMR data were processed with the program RMN.[23] Line shape fitting of the ^{27}Al 1D MAS spectra was performed using the program DMFIT.[24]

6.3 Results

A fundamental requirement to have a stable zeolite catalyst is the retention of framework stability, especially important for aggressive hot liquid water (HLW) conditions, particularly at industrial time scales. Batch hydrothermal stability studies with treatment times ranging between 3 to 1000 hr treatment times and treatment temperatures between 150 to 350 °C were selected to assess the degradation rate of ZSM-5. For the hydrothermal stability study, ZSM-5 catalyst with Si/Al ratio of 38 is selected, which is consistent with our previous study and within the range found to be the most stable.[21] Following HLW treatment, ZSM-5 powder was characterized for changes in bulk crystallinity (XRDS), surface morphology (SEM), porosity and internal structure (gas sorption and TEM). In addition to framework stability, the retention of Brønsted acid site is required to maintain catalytic activity. Acid sites within ZSM-5 catalysts are characterized for changes in acid sites by site functionality using infrared spectroscopy (IR) and by acid site

163

coordination using ^{27}Al NMR analysis. The results from these characterization techniques provide a detailed picture on ZSM-5 framework and acid site stability under liquid water conditions.

6.3.1 X-Ray Diffraction

X-ray diffraction (XRD) is a bulk characterization technique commonly used to identify the specific structure or phase of an ordered solid. Representative XRD diffractograms of both untreated and HLW treated ZSM-5 samples are provided in **Figure B.1** in the Appendix and reveal sharp crystalline peaks characteristic of ZSM-5, without significant peaks associated with other zeolite frameworks. XRD can also determine an averaged sample crystallinity by assessing the extent of long-range order across a representative amount of crystals in a powder sample. A retained crystallinity index (CI) is quantified from the ratio of select diffractogram peak areas of a treated sample relative to its reference untreated sample, defined for ZSM-5 as the prominent peak areas between 22.5 and 25 2Θ degrees.[25] The CI calculated from XRD diffractograms is used to assess the hydrothermal stability of ZSM-5 after HLW treatment. **Figure 6.1** plots the time dependency of CI measured at temperatures ranging between 150 °C to 350 °C and times ranging between 3 to 1000 hrs on a logarithmic time scale. The treatment time and temperature ranges were selected based on the aggressiveness of degradation in HLW conditions and error bars are based on the sensitivity of the XRD instrument in determining the bulk crystallinity of untreated ZSM-5.
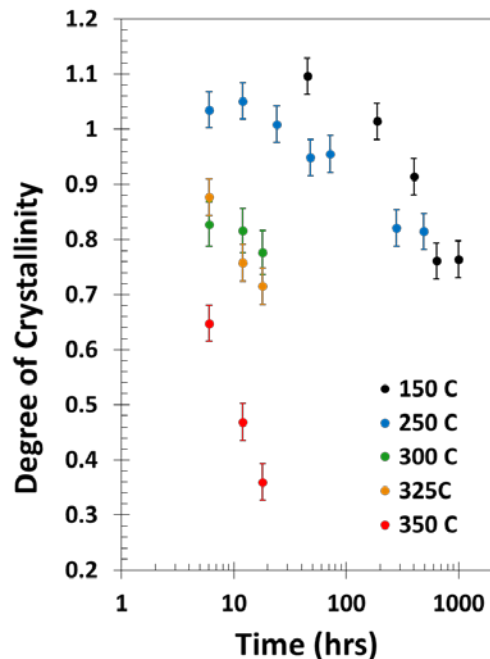
Figure 6.1: XRD pattern of H-ZSM-5 treated samples treated over time at a) 150 °C, b) 250 °C, c) 300 °C, d) 325 °C and e) 350 °C

At temperatures ≤ 250 °C and treatment times ≤ 100 hrs, treated ZSM-5 samples either largely retained or have a slight increase in their CI. However, CI losses greater than 10% are observed for all ZSM-5 samples treated at 150 °C after 200 hrs or treated at 250 °C after 100 hrs. The crystallinity index of 150 °C and 250 °C treated ZSM-5 samples continue drop after 500 hrs and 256 hrs, respectively, before leveling off and retaining a CI of ~80% for at least 100 hrs. The lack of continual CI loss after prolonged HLW treatment is a qualitative sign of ZSM-5 reaching a second state of relative framework stability, a unique result not previously observed in zeolite hydrothermal stability studies.[18-22] The XRD diffractograms of ZSM-5 treated after prolonged treatment times retain the peaks that correspond with ZSM-5 and does not form any additional phases.

In contrast to ZSM-5 treatment temperatures ≤ 250 °C, **Figure 6.1** shows that ZSM-5 samples treated in HLW at 300 °C, 325 °C and 350 °C do not degrade below 90% CI in less than 6 hrs. In addition, ZSM-5 samples treated at or above 300 °C have continual framework degradation, based on CI, for up to 20 hrs. **Figure 6.1** also reveals that increasing the HLW treatment temperature on ZSM-5 has an increasingly more aggressive effect on framework degradation, with 65% of the original CI lost after a 20 hr ZSM-5 treatment at 350 °C. The temperature dependence of framework degradation at T > 250 °C is more consistent with Arrhenius relationships between temperature and reaction rate compared to the unusual CI trends observed at T ≤ 250 °C. To evaluate which mechanism HLW treatment time and temperature influences crystal surface framework degradation, treated ZSM-5 samples were imaged using scanning electron microscopy.

6.3.2 Scanning Electron Microscopy

Scanning electron microscopy (SEM) images are able to visualize textural changes between untreated and treated ZSM-5 zeolite crystal surfaces. **Figure 6.2** visualizes changes in zeolite crystal roughness and size with both treatment time and temperature. Untreated ZSM-5 crystals are primarily hexagonal structures, approximately 2 µm in length with minor amounts of crystals having irregular shape or size. In addition, untreated crystals have clear edges and smooth surfaces, with small amounts of intercrystalline melding. Comparing **Figure 6.2a, c, e and f** shows the effect of HLW treatment time when operated at 350 °C. **Figure 6.2c** reveals minor zeolite crystal surface changes after 6 hrs of hot liquid water treatment, with slight rounding of the crystal edges and an increased density of crystals < 2 µm in length. In contrast, **Figure 6.2f** and **Figure 6.2e** reveal textural changes for ZSM-5 crystals treated at 350 °C for 12 and 18 hrs, respectively. ZSM-5 crystals treated at 350 °C for ≥ 12 hrs have few regions with smooth surfaces or clear edges, an instead have large, thin protrusions surrounding the remaining crystals. When comparing ZSM-5

SEM images with increasing treatment time, textural changes are shown that indicate framework surface instability in more aggressive HLW conditions, with major changes occurring after six hours.
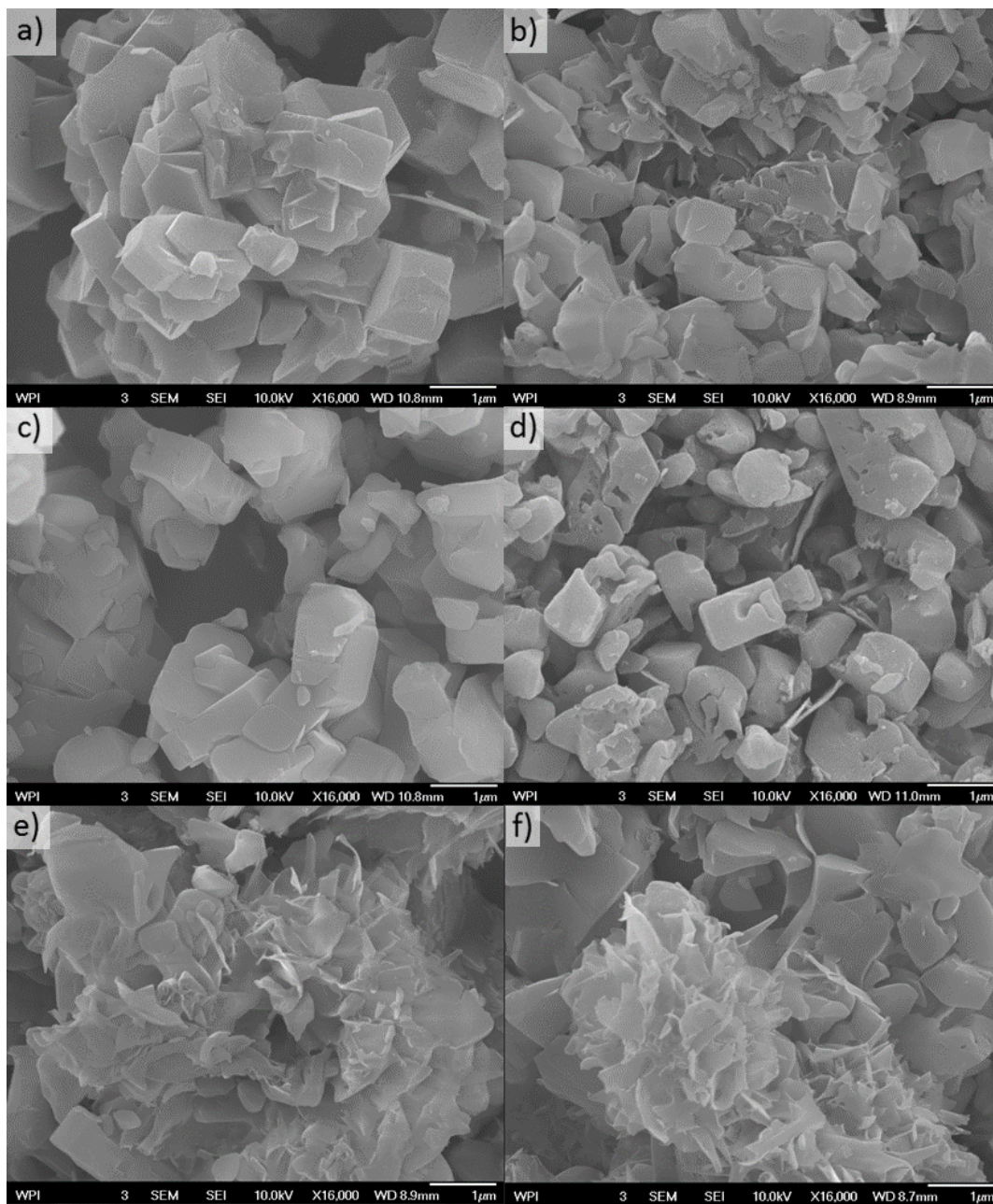
Figure 6.2: SEM images of a) untreated ZSM-5 and b-e) treated ZSM-5 samples in HLW at b) 250 °C for 12 hrs, c) 350 °C for 6 hrs, d) 300 °C for 12 hrs, e) 350 °C for 18 hrs and f) 350 °C for 12 hrs.

Comparing SEM images between **Figure 6.2a,b,d, and f** shows changes in ZSM-5 crystal surface with varying HLW treatment temperature after 12 hrs. Comparing the untreated ZSM-5 crystals in **Figure 6.2a** to those treated at 250 °C in **Figure 6.2b** reveals a slight decrease in average crystal size and increase in edge smoothness. Similarly, ZSM-5 treated at 300 °C for 12 hrs in **Figure 6.2d** demonstrated minimal changes to ZSM-5 crystal size, however an increase in surface roughness compared to crystals treated at reduced temperatures was observed. In addition, ZSM-5 crystals treated at 300 °C lack the large depositions observed with ZSM-5 treated at 350 °C for 12 hours in **Figure 6.2f**. Distinguishing the structural nature of the depositions from SEM images alone is challenging, and could be reasonably described as either small degraded ZSM-5 crystals or amorphous residue deposited on the crystal surface. Next, nitrogen sorption is used to further elucidate structural changes of HLW treated ZSM-5 crystals and newly formed depositions.

6.3.3 Nitrogen Sorption

Nitrogen sorption is a characterization technique used to investigate textural changes of ZSM-5 samples after HLW treatment, including pore volume, surface area and micro/meso-porosity. **Figure 6.3** provides representative nitrogen sorption isotherms after 12 hrs of subcritical water treatment. All of the isotherms in **Figure 6.3** can be classified with an IUPAC type IV isotherm, with a relatively strong N_2 sorption at both low and high points of the p/p_0 range.[26] These isotherms for ZSM-5 zeolites describe both microposity near the low $p/p_0 < 10^{-4}$ region pertaining to gas-zeolite interactions as well as mesoporosity at $p/p_0 > 10^{-1}$ associated with gas-gas molecular interactions.[26] Qualitatively, **Figure 6.3** shows the untreated sorption data has strong adsorption in the region $p/p_0 < 10^{-4}$, with no curvature or hysteresis loop in the region $p/p_0 > 0.1$, which indicates a microporous solid without considerable mesoporosity.[27] The treated samples show a drop in total N_2 sorption in the micropore region along with an increase in adsorption in the

mesoporous region for some samples. An increase in N_2 adsorption in the mesopore region is most significant for ZSM-5 treated at 300 °C, consistent with formation of mesopores from surface roughening observed in **Figure 6.2d**. The drop in sorption per gram of treated sample is consistent with smaller microporous zeolite crystals with a greater surface to volume ratio as well as the formation of a residue with a lower surface area lacking in microporosity. Evaluating the micropore and external surface area trends of treated ZSM-5 is achieved through analysis of the N_2 sorption isotherms.
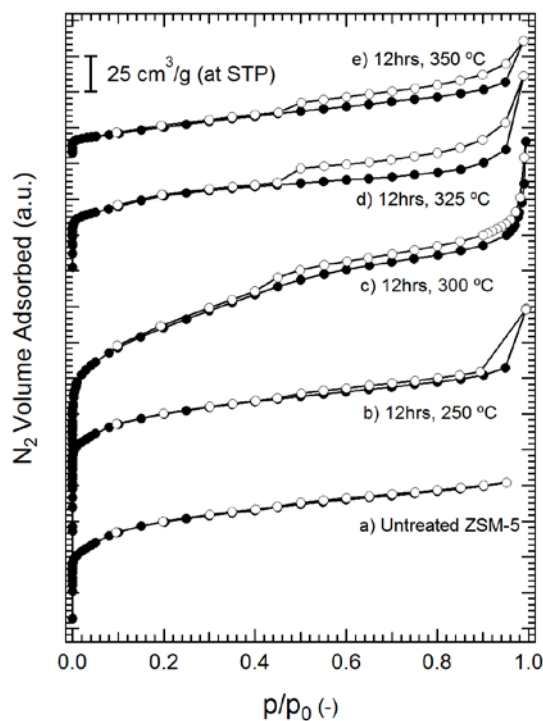
Figure 6.3: N_2 sorption isotherms of a) untreated H-ZSM-5 and (b-e) H-ZSM-5 samples treated for 12 hours in HLW conditions at b) 250 °C c) 300 °C d) 325 °C and d) 350 °C

Micropore and external surface area of the treated ZSM-5 samples are calculated from the N_2 isotherms using the t-plot method for quantitative analysis and tabulated in the Appendix B.[28] **Figure 6.4** plots the changes in micropore and external surface area for HLW treated ZSM-5

samples. **Figure 6.4a** shows treated ZSM-5 samples either largely retain or have a drop in total micropore surface area. Consistent with bulk crystallinity from XRD, ZSM-5 samples treated at 150 and 250 °C maintain a micropore surface area ranging between 270 and 350 m^2/g with no apparent trend with treatment time. The lack of change in microporosity is consistent with the retained bulk crystallinity index previously reported with XRD. However, **Figure 6.4b** reveals an increase in external surface area for ZSM-5 treated at temperature $\leq$ 250 °C, with a 100% increase in total external surface area for ZSM-5 treated at 250 °C for 492 hrs. The increase in ZSM-5 external surface area accessibility after 150 – 250 °C HLW treatment could be attributed to smaller crystals or surface roughening without any amorphous deposition that would influence the total microporosity.

A significant loss in microporosity of ZSM-5 samples treated at temperature > 250 °C is shown in **Figure 6.4a**. At the elevated ZSM-5 treatment temperatures, the total loss in microporosity increases with both increasing treatment time and temperature. The greatest loss in microporosity is shown after HLW treatment at 350 °C for 18 hours, which has 10% of the untreated micropore area, and is consistent with losses in bulk crystallinity observed from XRD. An increase in total external surface area is observed for ZSM-5 samples treated at T > 250 °C but lacks a clear trend with treatment time such as ZSM-5 samples treated at T $\leq$ 250 °C. Analysis of the complicated relationship between external surface area and HLW treatment time is revisited in the discussion section. The loss in microporosity and extent of amorphous deposits is further evaluated using TEM imaging.
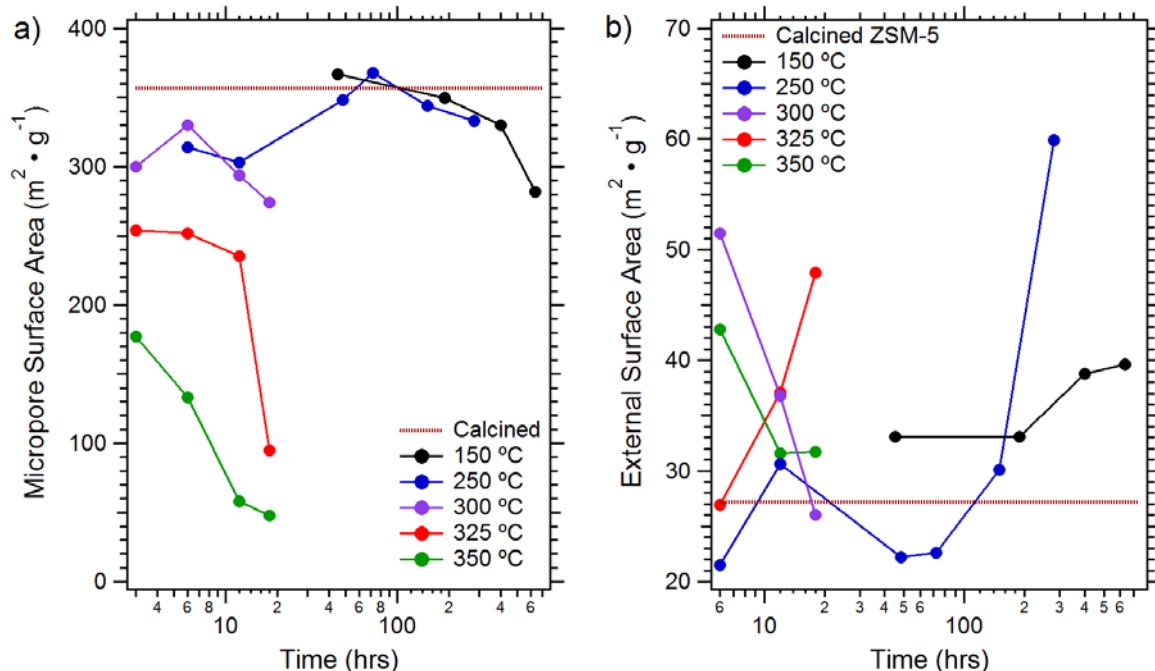
Figure 6.4: t-plot analysis of N_2 sorption isotherms for determining a) micropore surface area and b) External surface area of H-ZSM-5 samples treated for 6 – 600 hrs in HLW conditions ranging between 150 – 350 °C.

6.3.4 Transmission Electron Microscopy

TEM images are able to discern both textural changes on external roughness as well as internal changes in zeolite lattice lines between untreated and treated ZSM-5 crystal samples. Untreated ZSM-5 samples shown in **Figure 6.5a** reveals a relatively smooth crystal surfaces with uniform lattice lines within the internal crystal structure. Similarly, treated ZSM-5 samples in **Figure 6.5b-d,** which correspond with HLW treatments at 150 °C for 636 hrs, 250 °C for 492 hrs, and 300 °C for 12 hrs, respectively, show similar zeolite surface and lattice properties compared to the untreated ZSM-5 images. A lack of blurriness or bumps in the straight lattice lines suggests a lack of internal mesoporosity in the samples of both untreated and treated ZSM-5. TEM suggests that any framework degradation based on XRD or sorption will likely occur from the crystal surface.

Next, infrared spectroscopy is used to evaluate the hydrothermal stability of acid sites of treated ZSM-5.
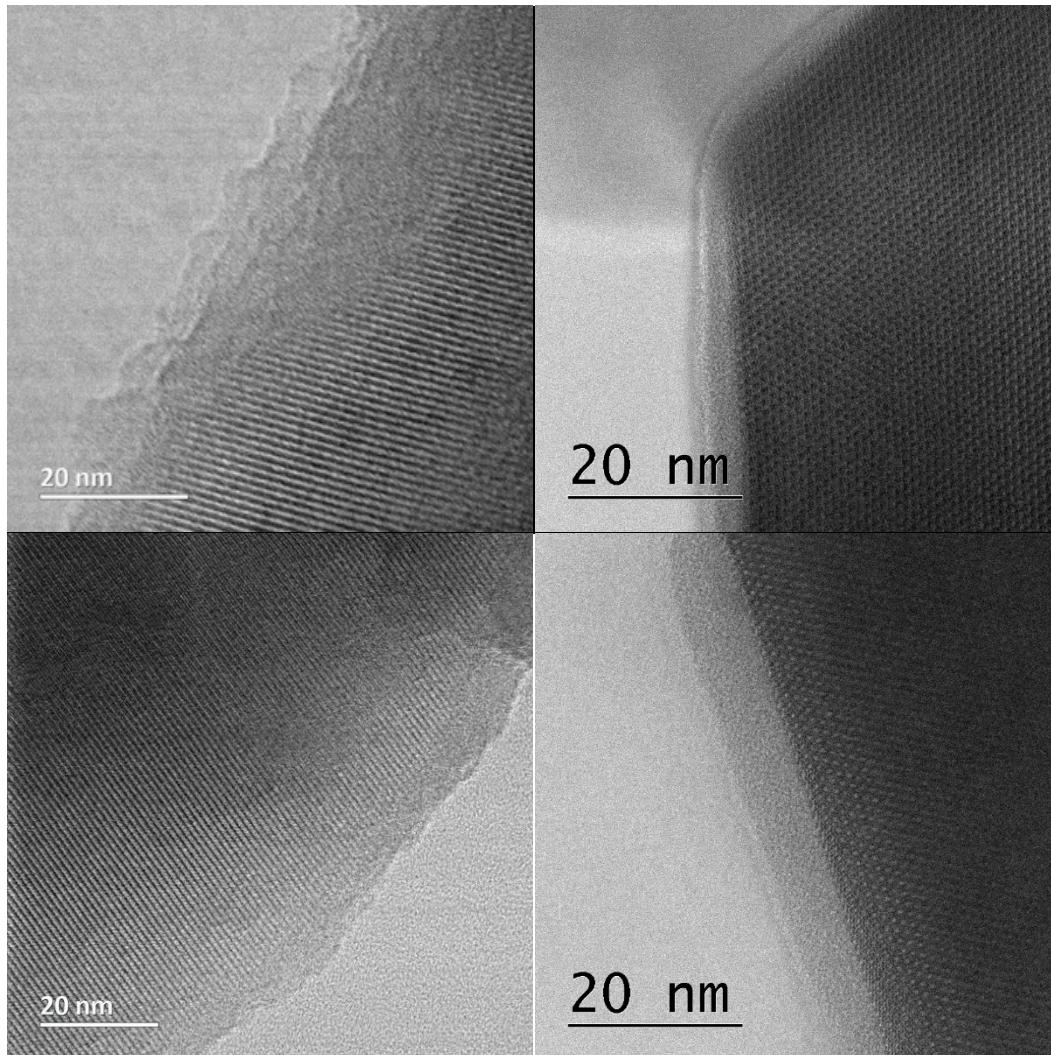
Figure 6.5: Transmission electron microscopy brightfield images of a) untreated ZSM-5 sample and ZSM-5 samples treated at b) 150 °C for 636 hrs c) 250 °C for 492 hrs and d) 300 °C for 12 hrs

6.3.5 Infrared Spectroscopy

Infrared spectroscopy allows for the investigation of ZSM-5 acid site loss associated with HLW treatments. **Figure 6.6** presents the IR spectra of untreated and HLW treated ZSM-5 samples, evaluating the effect of both varying treatment time and temperature. The wavenumber position of infrared bands can identify key functional groups, while shifts in band location or relative intensity can describe chemical changes of the sample. IR bands located at 3600 cm^{-1}, 3660 cm^{-1} and 3720 cm^{-1} correspond to the OH stretching modes of bridging hydroxyl groups, extra framework aluminum (EFAL) species and isolated silanol groups, respectively.[29-31] The bridging hydroxyl band located at 3600 cm^{-1} are Al-O-H stretching modes associated with ZSM-5 Brønsted acidity, while the isolated silanol band located at 3720 cm^{-1} is associated with Si-OH stretching modes on the crystal surface.[30, 31]

IR analysis of untreated ZSM-5, presented in **Figure 6.6a-d**, expectedly shows a strong Brønsted acid band with negligible amounts of extra-framework aluminum or isolated silanol groups. **Figure 6.6a** plots the IR bands for ZSM-5 treated at 150 °C for up to 991 hrs, revealing the retention of the Brønsted acid site (BAS) band at 3600 cm^{-1} and a lack of bands associated with either EFAL or isolated silanol species. **Figure 6.6b** plots bands for 150 °C HLW treatment, revealing a continual increase in the EFAL band for ZSM-5 treated at 250 °C, which becomes roughly equivalent in intensity compared to the Brønsted acid site band after treatment for 492 hrs. Based on **Figure 6.6a and b**, ZSM-5 Brønsted acid site loss begins at industrially meaningful timescales between 150 °C and 250 °C, but will partially retain Brønsted acidity even after 492 hrs at 250 °C. In contrast, **Figure 6.6c** shows BAS loss after 3 hrs of 300 °C HLW treatment, with the EFAL OH stretching mode having a more intense band compared to the Brønsted acid site OH stretching mode after 12 hrs of treatment. HLW treatment at 350 °C **Figure 6.6d**, shows a

predominant EFAL band with a small shoulder associated with Brønsted acid sites at all treatment times. The temperature dependency on acid site loss is clearly shown by comparing the partially, or even completely, retained Brønsted acid site band at treatment temperatures $\leq 250\,°C$ compared to the almost complete loss in Brønsted acid sites after 6 hours of HLW treatment at $350\,°C$. Next, ^{27}Al NMR was used to quantify the remaining Brønsted acid and extra framework aluminum species for HLW treated ZSM-5 samples.
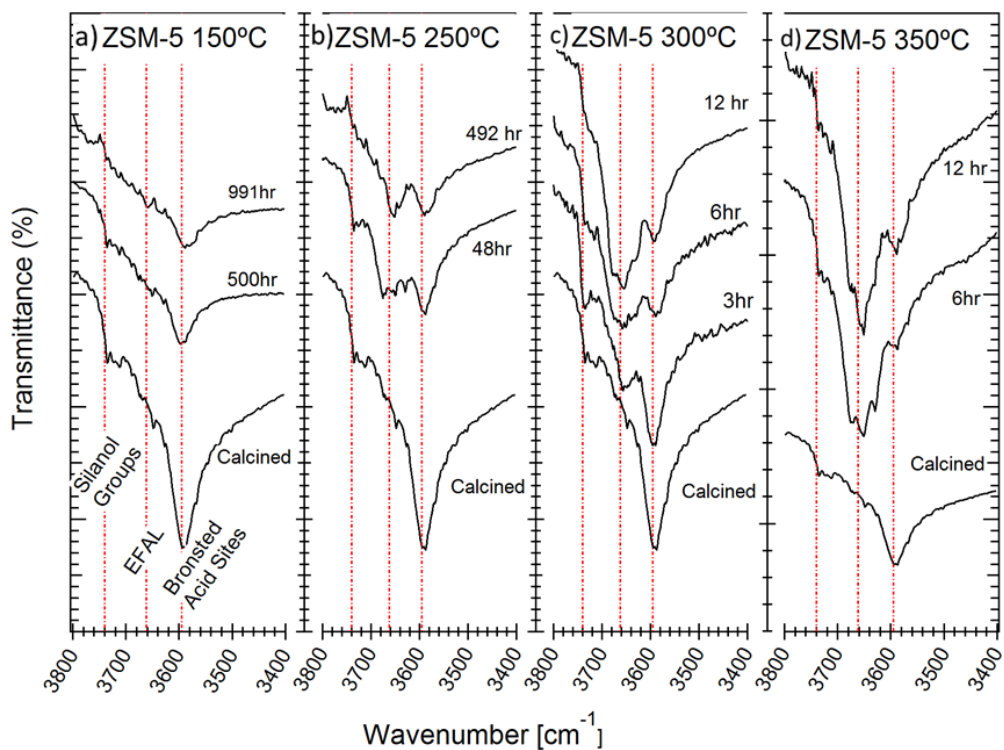
Figure 6.6: Infrared spectroscopy of calcined and a) 150 °C treated, b) 250 °C treated, c) 300 °C treated and d) 350 °C HLW treated ZSM-5 samples. Treatment times are denoted next to the corresponding spectra, which ranges between 3 and 991 hrs.

6.3.6 ^{27}Al NMR Spectroscopy

^{27}Al NMR was used to quantify the ratio of tetrahedral and octahedrally coordinated aluminum in treated ZSM-5 samples, which are listed in **Table 6.2.** Untreated ZSM-5 is reported to have 93.2% of the aluminum in a tetrahedral coordination, which is consistent with the majority residing within the zeolite framework as Brønsted acid sites. After hot liquid water treatment at 150 °C for 636 hrs, ZSM-5 retains most of the framework aluminum, with less than a 2% drop in tetrahedrally coordinated Al sites. The ^{27}Al NMR result for ZSM-5 treated at 150 °C is consistent with the retained Brønsted acid site peak shown in **Figure 6.6**.

Table 6.1. Quantified ^{27}Al NMR of ZSM5 relative Al site population and after hot liquid water treatment.

Sample Treatment Time/Temp (hr, °C)	^{27}Al Tetrahedral Al sites	^{27}Al Octahedral Al sites
Untreated	93.2	6.8
636 hr, 150 °C	91.8	8.2
12 hr, 250 °C	59.2	36.9
48 hr, 250 °C	56.9	43.1
280 hr, 250 °C	42.8	57.2
18 hr, 300 °C	36.8	63.2
6 hr, 350 °C	7.2	92.8
18 hr, 350 °C	7.4	92.6

In contrast to ZSM-5 treated at 150 °C, the amount of tetrahedral Al sites of ZSM-5 treated at 250 °C for 12 hours drops to 59.2%. This is also consistent with IR, which shows that the

175

formation of octahedral Al sites corresponds with the formation of extra framework alumina stretching modes in **Figure 6.6**. This loss in framework Al sites for ZSM-5 treated at 250 °C for 12 hrs corresponds with more than a 30% drop to untreated ZSM-5 zeolite after 12 hours of hot liquid water treatment. Further ZSM-5 treatment times at 250 °C do not show a similar rate of framework Al loss, as 48 and 280 hours treatments have 56.9 and 42.8% of tetrahedral Al sites. **Table 6.1** reports increased losses in framework Al sites with increasing treatment temperatures ≥ 250 °C. ZSM-5 treated at 300 °C for 18 hours has 36.8% of the Al in tetrahedral coordination, 350 °C treated ZSM-5 after 6 and 18 hrs had approximately 7% of the Al in tetrahedral coordination. The results presented in Table 2 reveal that hydrothermal loss in framework aluminum will start at T > 150 °C and is strongly temperature dependent.

6.4 Discussion

6.4.1 Framework Degradation

The focus of this work is to understand the thermal and temporal dependence of ZSM-5 degradation under HLW conditions. This study reveals that ZSM-5 samples treated in HLW at temperatures ≤ 250 °C are recalcitrant towards framework breakdown. XRD and sorption analysis reveal that 150 – 250 °C HLW treated samples retain most of their framework crystallinity and microporosity for up to 500 hours. After 150 – 250 °C HLW treatment, the ZSM-5 framework has an increase in total external surface area, as shown in **Figure 6.4**. With prolonged HLW treatment times at 150 – 250 °C, N_2 sorption also reveals a slight loss in ZSM-5 microporosity. In contrast to the low temperature treatments, ZSM-5 treated in HLW temperatures > 250 °C has a monotonic decrease in crystallinity in XRD and microporosity in N_2 sorption. Consistent with trends in XRD and sorption, SEM images of HLW treated ZSM-5 samples reveal an increase in surface roughness and crystal breakdown with increasing treatment times and temperatures. In contrast, TEM images

reveal that even prolonged HLW treatment leads to no internal framework breakdown under all treatment times and conditions, consistent with previous work in Chapter IV that established ZSM-5 HLW degradation occurs via crystal surface decrystallization at temperatures > 250 °C.

ZSM-5 treated at relatively short treatment times and aggressive HLW temperatures can have identical XRD bulk crystallinities with samples that experienced prolonged treatments at milder HLW temperatures, comparing these samples using SEM, TEM and sorption characterization techniques reveals clear textural differences between them. ZSM-5 crystals that are degraded to similar relative crystallinities in **Figure 6.7** reveal the differences in crystal size and roughness; consistent with the complexity presented with N_2 sorption in **Figure 6.4b**. A slight increase in external surface area in **Figure 6.4b** for ZSM-5 treated at 150 °C is consistent with the change in ZSM-5 crystals treated at 636 hrs at 150 °C observed in **Figure 6.7a** when compared to untreated ZSM-5 image in **Figure 6.2a**. However, **Figure 6.7b** reveals ZSM-5 crystals treated at 250 °C at the same CI show signs of particle agglomeration and formation of needles, similar to features previously shown for samples treated at 350 °C after 12 hrs in **Figure 6.2e**. The lack of time dependent trends in external surface area observed for ZSM-5 treated at temperatures ≥ 250 °C in **Figure 6.4b** are likely influenced by simultaneous needling, agglomeration and formation of amorphous residues. Therefore, the observed particle agglomeration in **Figure 6.7b** may explain the sharp drop in external surface area at treatment temperatures > 72 hrs observed in **Figure 6.4b**. The crystal size for samples treated to a similar CI at 325 °C for 12 hrs lack particle agglomeration observed for 250 °C treated ZSM-5, however an increase in smaller needles and surface roughness is observed. The increase in external surface area for all treated ZSM-5 samples at T ≥ 250 °C relative to untreated ZSM-5 is consistent with observed surface roughening and formation of needle-like features.
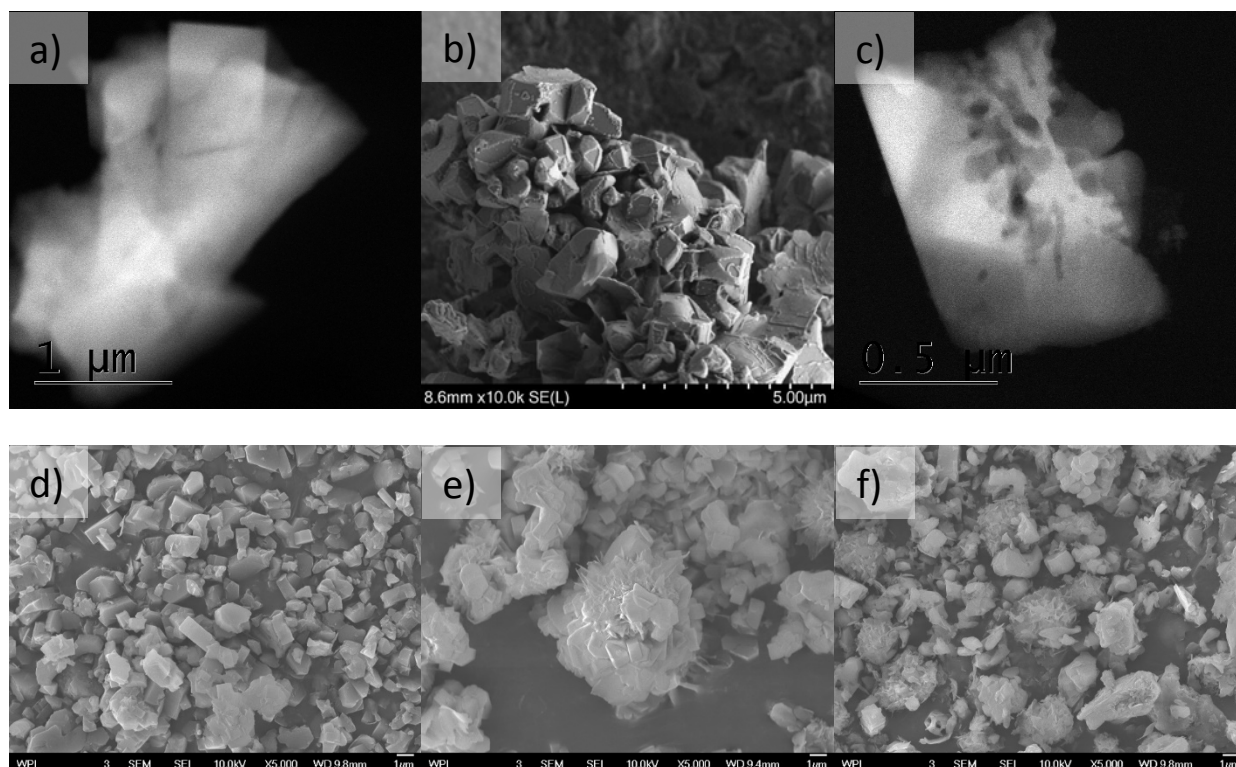
Figure 6.7: TEM and SEM images of treated ZSM-5 samples with similar crystallinity index between 77 and 82%. Darkfield TEM images are of ZSM-5 treated at a) 150 °C for 636 hrs and c) 300 °C for 12 hrs. SEM images are of ZSM-5 samples treated at b) 250 °C for 492 hrs, d) 150 °C for 636 hrs, e) 250 °C for 280 hrs, and f) 325 °C for 12 hrs. Different magnifications are used for a, b, and c and the scale bars for each image are denoted at the bottom

An increase in surface roughness and loss in zeolite crystallinity is due to framework hydrolysis through a desilication mechanism. Previous studies have identified that zeolite desilication occurs through a base catalyzed mechanism using alkali mediums.[32-42] Ennaert et al.[20] were able to reduce framework desilication of HY under hot liquid water treatment with the addition of dilute acid, which shifted water's ionic equilibrium to produce less hydroxyl ions that can catalyze framework breakdown. When comparing ZSM-5 desilication after HLW treatment to other zeolite frameworks, there are significant changes in where framework degradation occurs in the zeolite

lattice. Frameworks HY and H-β undergo internal decrystallization and framework collapse when exposed to liquid water, while ZSM-5 only shows signs of degradation from the external surface and the internal framework itself is relatively unperturbed during prolonged treatment, consistent with the previous work after three hour treatment times in Chapter IV.

In addition, the observed changes in ZSM-5 treated under hot liquid water conditions differs from ZSM-5 treated under alkali conditions. Work done by Fodor et al.[43] revealed internal spots of amorphization using TEM when treated in 0.1 M NaOH at 80 °C. A follow up paper by Fodor et al.[44] revealed that internal defects in ZSM-5 are the primary source for the propagation of internal framework degradation, but even defect free synthesized silicalite treated at 0.1 M NaOH at 80 °C will form degradation holes after 24 hours of hot liquid water treatment, similar to ZSM-5 treated in hot liquid water at 325 C in **Figure 6.7c**. Therefore, ZSM-5 internal lattice is uniquely stable under hot liquid water conditions when comparing it to other HLW frameworks or even ZSM-5 under more basic degradation conditions.

Following a similar rate analysis of zeolite decrystallization performed in Chapter 5, the time dependence of XRD crystallinity is fitted for each temperature and included in **Figure B.2** in the Appendix. The framework degradation rate an approximately first order with respect to the relative crystallinity, consistent with the data for HY degradation in the work by Ravenelle et al.[18] The corresponding rate constant for ZSM-5 treated under hot liquid water conditions at 300 °C, 325 °C and 350 °C are 0.0129 hr^{-1}, 0.0192 hr^{-1} and 0.0565 hr^{-1}, respectively. An Arrhenius analysis is performed and plotted in **Figure B.3** in the Appendix, using the estimated rate constants that also incorporates the temperature dependency on the ionic concentration of water. Based on this analysis, ZSM-5 framework degradation under batch conditions is estimated to have an activation energy of 144 kJ/mol, similar to previously determined activation energy of 158 kJ/mol for ZSM-

5 framework degradation under HLW flow conditions. The consistent rate constants and activation energies between thermal and temporal studies under batch and flow conditions indicates that the framework degradation occurs with a first order dependence on crystallinity under subcritical water conditions.

6.4.2 Acid Site Degradation

In contrast to the complex temperature dependence of ZSM-5 crystallinity after HLW treatment, acid site loss rapidly occurs at internal acid sites. Based on both ^{27}Al NMR and IR, show there is a negligible loss in framework aluminum after 636 hrs of hot liquid water treatment at 150 °C. At treatment temperatures > 150 °C, infrared spectroscopy reveals loss in Brønsted acid sites occurs in conjunction with the formation of stretching modes attributed to extra framework alumina. The acid site loss in ZSM-5 after HLW treatment is consistent with a dealumination mechanism. Previous studies have identified that zeolite dealumination occurs through an acid catalyzed process which has been shown to occur when treated under acidic or steaming conditions.[30, 45-50] Work by Muller et al.[51] identified that acid site losses occur in acidic conditions and can depend on the crystal size, Si/Al ratio and number of defects in the zeolite.

Similar to the thermal trends in framework degradation under subcritical conditions, acid site loss is also temperature dependent, as shown in **Figure 6.6** and **Table 6.1**. ZSM-5 degradation after 3 hrs of hot liquid water treatment in Chapter 4 revealed acid site dealumination formed Al complexes that diffuse through the MFI framework to the crystal surface and eventual leaching of Al sites under flow conditions. The extent of dealumination was shown to be temperature dependent regardless of subcritical or supercritical reaction conditions. The relative ratio of framework to extra-framework alumina species in ZSM-5 monotonically decreases with increasing treatment temperature, but is less sensitive to treatment times for the treated samples

180

characterized in ^{27}Al NMR. Quantitative acid site loss for ZSM-5 treated at 250 °C with varying treatment time reveals that the majority of framework aluminum loss occurs within the first 6 hrs, followed by a much slower rate of dealumination for the following 276 hrs. A similar observation is made for 6 and 12 hr HLW treated ZSM-5 at 350 °C, where a significant loss in acid sites occurs after 6 hrs with low to negligible losses in the following 6 hrs of treatment. A similar observation was made by Kooyman et al.[52], who found the extent of dealumination for ZSM-5 treated under acidic conditions (1N HCl) was insensitive to treatment time. This is in contrast to the observed loss in crystallinity, which occurs over several hours of HLW treatment. The rapid initial dealumination rate followed by a slower prolonged rate of acid site loss could be due to extra framework alumina species protecting the remaining acid sites. A previous study by Yu et al.[53] identified Brønsted and extra framework alumina are in close proximity to each other in a ZSM-5 zeolite after dealumination, which can increase acid strength. The existence of these complexes may also reduce access to water for hydration reactions to occur. The presence of organic species in addition to the water solvent may play a similar role in protecting framework acid sites for degradation, which would be more representative of a reaction mixture. Alternatively, the retention of the remaining Al sites after prolonged treatment could be due to a specific Al siting within the MFI framework that is more recalcitrant to dealumination. Regardless of the mechanistic cause for the retention of remaining Al sites under prolonged HLW treatment, the initial acid loss is highly temperature sensitive and a majority amount of Brønsted acid sites are lost after hot liquid water treatment at 300 °C. Therefore, acid site stabilization strategies are required for reactions that want to fully utilize all Brønsted acid sites under hot liquid water conditions greater than 250 °C.

6.5 Conclusion

In this study, ZSM-5 framework degradation is examined under elevated treatment temperatures and/or prolonged treatment times, up to 350 °C or ~1000 hrs. XRD revealed ZSM-5 largely retains framework crystallinity under prolonged exposure to hot liquid water at temperature ≤ 250 °C. Further framework characterization using N_2 sorption, scanning electron microscopy (SEM), and transmission electron microscopy (TEM) imaging revealed that degradation occurs from the crystal surface and leads to surface roughening and particle agglomeration with increasing treatment temperatures and times. The textural surface trends of framework degradation can vary with different treatment times and temperature, even for ZSM-5 samples with identical crystallinity values from XRD.

In addition, analysis of acid site stability after HLW treatment was performed using infrared spectroscopy (IR) and nuclear magnetic resonance (^{27}Al NMR). Results indicate that acid site loss occurs rapidly within the first 6 hours followed by a much slower rate of dealumination with prolonged treatment times. These post-run characterization studies extend the current understanding of ZSM-5 hydrothermal stability, particularly how treatment temperature influences ZSM-5 framework and acid sites at prolonged, industrial time-scales.

References

1. Mo, N. and P.E. Savage, *Hydrothermal catalytic cracking of fatty acids with HZSM-5.* ACS Sustainable Chemistry and Engineering, 2014. **2**: p. 88-94.

2. Mo, N., W. Tandar, and P.E. Savage, *Aromatics from saturated and unsaturated fatty acids via zeolite catalysis in supercritical water.* Journal of Supercritical Fluids, 2015. **102**: p. 73-79.

3. Savage, P.E., P. Duan, and P.E. Savage, *Hydrothermal Liquefaction of a Microalga with Heterogeneous Catalysts Hydrothermal Liquefaction of a Microalga with Heterogeneous Catalysts.* Industrial & Engineering Chemistry Research, 2011: p. 52-61.

4. Sahu, R. and P.L. Dhepe, *A one-pot method for the selective conversion of hemicellulose from crop waste into C5 sugars and furfural by using solid acid catalysts.* ChemSusChem, 2012. **5**: p. 751-761.

5. Dong, W., et al., *Selective chemical conversion of sugars in aqueous solutions without alkali to lactic acid over a Zn-Sn-Beta lewis acid-base catalyst.* Scientific Reports, 2016. **6**: p. 1-8.

6. Zhao, C. and J.A. Lercher, *Upgrading pyrolysis oil over Ni/HZSM-5 by cascade reactions.* Angewandte Chemie - International Edition, 2012. **51**: p. 5935-5940.

7. Robin, T., J.M. Jones, and A.B. Ross, *Catalytic hydrothermal processing of lipids using metal doped zeolites.* Biomass and Bioenergy, 2017. **98**: p. 26-36.

8. Ennaert, T., et al., *Potential and challenges of zeolite chemistry in the catalytic conversion of biomass.* Chemical Society Reviews, 2016. **45**: p. 584-611.

9. Yilmaz, B. and U. Müller, *Catalytic applications of zeolites in chemical industry.* Topics in Catalysis, 2009. **52**: p. 888-895.

10. Zaker, A., et al., *Evidence of heterogeneous catalytic activity of ZSM-5 in supercritical water for dodecane cracking.* Catalysis Today, 2018. **317**: p. 2-11.

11. Zaker, A., et al., *Zeolite Catalyzed Cracking of Dodecane in Supercritical Water: Lewis and Brønsted Acidity Article.* Catalysis Today, 2018.

12. Beyerlein, R.a., et al., *Effect of steaming on the defect structure and acid catalysis of protonated zeolites.* Topics in Catalysis, 1997. **4**: p. 27-42.

13. Kuehl, G.H. and H.K.C. Timken, *Acid sites in zeolite Beta: Effects of ammonium exchange and steaming.* Microporous and Mesoporous Materials, 2000. **35**: p. 521-532.

14. Bazyari, A., et al., *Effects of steaming-made changes in physicochemical properties of Y-zeolite on cracking of bulky 1 , 3 , 5-triisopropylbenzene and coke formation.* Fuel Processing Technology, 2009. **90**: p. 1226-1233.

15. Ong, L.H., et al., *Dealumination of HZSM-5 via steam-treatment.* Microporous and Mesoporous Materials, 2012. **164**: p. 9-20.

16. Kubo, K., et al., *Ultra-high steaming stability of Cu-ZSM-5 zeolite as naphtha cracking catalyst to produce light olefin.* Catalysis Communications, 2012. **29**: p. 162-165.

17. Xiong, H., H.N. Pham, and A.K. Datye, *Hydrothermally stable heterogeneous catalysts for conversion of biorenewables.* Green Chemistry, 2014. **16**: p. 4627-4643.

18. Ravenelle, R.M., et al., *Stability of zeolites in hot liquid water.* Journal of Physical Chemistry C, 2010. **114**: p. 19582-19595.

19. Zhang, L., et al., *Factors that Determine Zeolite Stability in Hot Liquid Water.* Journal of the American Chemical Society, 2015. **137**: p. 11810-11819.

20. Ennaert, T., et al., *Conceptual frame rationalizing the self-stabilization of H-USY zeolites in hot liquid water.* ACS Catalysis, 2015. **5**: p. 754-768.

21.	Lutz, W., et al., *Investigation and modeling of the hydrothermal stability of technically relevant zeolites.* Adsorption, 2005. **11**: p. 405-413.

22.	Jamil, A.K., et al., *Hydrothermal Stability of One-Dimensional Pore ZSM-22 Zeolite in Hot Water.* Journal of Physical Chemistry C, 2016. **120**: p. 22918-22926.

23.	Grandinetti, P., *RMN, Version 1.3.0; The Ohio State University: Columbus, OH,.* 2005, The Ohio State University, Columbus.

24.	Massiot, D., et al., *Modelling one- and two-dimensional solid-state NMR spectra.* Magnetic Resonance in Chemistry, 2002. **40**: p. 70-76.

25.	ASTM, *Standard Test Method for Determination of Relative Crystallinity of Zeolite ZSM-5 by X-Ray Diffraction.* ASTM International: D4758-01, 2015. **05**: p. 3-5.

26.	Donohue, M.D. and G.L. Aranovich, *Classification of Gibbs adsorption isotherms.* Advances in Colloid and Interface Science, 1998. **76**: p. 137-152.

27.	Abelló, S., A. Bonilla, and J. Pérez-Ramírez, *Mesoporous ZSM-5 zeolite catalysts prepared by desilication with organic hydroxides and comparison with NaOH leaching.* Applied Catalysis A: General, 2009. **364**: p. 191-198.

28.	Voogd, P., J.J.F. Scholten, and H. van Bekkum, *Use of the t-plot-De Boer method in pore volume determinations of ZSM-5 type zeolites.* Colloids and Surfaces, 1991. **55**: p. 163-171.

29.	Jin, F. and Y. Li, *A FTIR and TPD examination of the distributive properties of acid sites on ZSM-5 zeolite with pyridine as a probe molecule.* Catalysis Today, 2009. **145**: p. 101-107.

30. Triantafillidis, C.S., et al., *Effect of the degree and type of the dealumination method on the structural, compositional and acidic characteristics of H-ZSM-5 zeolites.* Microporous and Mesoporous Materials, 2001. **47**: p. 369-388.

31. Trombetta, M., et al., *An FT-IR study of the internal and external surfaces of HZSM5 zeolite.* Applied Catalysis A: General, 2000. **192**: p. 125-136.

32. Verboekend, D., et al., *Hierarchical zeolites by desilication: Occurrence and catalytic impact of recrystallization and restructuring.* Crystal Growth and Design, 2013. **13**: p. 5025-5035.

33. Verboekend, D., G. Vilé, and J. Pérez-Ramírez, *Hierarchical y and USY zeolites designed by post-synthetic strategies.* Advanced Functional Materials, 2012. **22**: p. 916-928.

34. Verboekend, D. and J. Pérez-Ramírez, *Design of hierarchical zeolite catalysts by desilication.* Catalysis Science & Technology, 2011. **1**: p. 879.

35. Groen, J.C., J.A. Moulijn, and J. Pérez-Ramírez, *Alkaline posttreatment of MFI zeolites. From accelerated screening to scale-up.* Industrial & Engineering Chemistry Research, 2007. **46**: p. 4193-4201.

36. Groen, J.C., et al., *Alkaline-mediated mesoporous mordenite zeolites for acid-catalyzed conversions.* Journal of Catalysis, 2007. **251**: p. 21-27.

37. Groen, J.C., et al., *Direct demonstration of enhanced diffusion in mesoporous ZSM-5 zeolite obtained via controlled desilication.* Journal of the American Chemical Society, 2007. **129**: p. 355-360.

38.   Tan, Q., et al., *Synthesis, characterization, and catalytic properties of hydrothermally stable macro-meso-micro-porous composite materials synthesized via in situ assembly of preformed zeolite Y nanoclusters on kaolin.* Journal of Catalysis, 2007. **251**: p. 69-79.

39.   Tao, Y., H. Kanoh, and K. Kaneko, *Developments and structures of mesopores in alkaline-treated ZSM-5 zeolites.* Adsorption, 2006. **12**: p. 309-316.

40.   Groen, J.C., J.A. Moulijn, and J. Pérez-Ramírez, *Decoupling mesoporosity formation and acidity modification in ZSM-5 zeolites by sequential desilication-dealumination.* Microporous and Mesoporous Materials, 2005. **87**: p. 153-161.

41.   Groen, J.C., et al., *Mesoporosity development in ZSM-5 zeolite upon optimized desilication conditions in alkaline medium.* Colloids and Surfaces A: Physicochemical and Engineering Aspects, 2004. **241**: p. 53-58.

42.   Ogura, M., et al., *Formation of Uniform Mesopores in ZSM-5 Zeolite through Treatment in Alkaline Solution.* Chemistry Letters, 2000: p. 882-883.

43.   Fodor, D., et al., *Differences between individual ZSM-5 crystals in forming hollow single crystals and mesopores during base leaching.* Chemistry - A European Journal, 2015. **21**: p. 6272-6277.

44.   Fodor, D., et al., *Role of defects in pore formation in MFI zeolites.* Journal of Physical Chemistry C, 2015. **119**: p. 5447-5453.

45.   Cairon, O., *Impacts of Composition and Post-Treatment on the Brønsted Acidity of Steam-Treated Faujasite: Insights from FTIR Spectroscopy.* ChemPhysChem, 2013. **14**: p. 244-251.

46.   Jin, L., et al., *An improved dealumination method for adjusting acidity of HZSM-5.* Catalysis Today, 2010. **149**: p. 207-211.

47. Masuda, T., et al., *Changes in catalytic activity of MFI-type zeolites caused by dealumination in a steam atmosphere.* Applied Catalysis A: General, 1998. **172**: p. 73-83.

48. Jin, Y., et al., *Mesopore modification of beta zeolites by sequential alkali and acid treatments: Composition-dependent T-atoms removal behavior back donating to hierarchical structure and catalytic activity in benzene alkylation.* Microporous and Mesoporous Materials, 2017. **248**: p. 7-17.

49. Li, J., et al., *Interconnected Hierarchical ZSM-5 with Tunable Acidity Prepared by a Dealumination-Realumination Process: A Superior MTP Catalyst.* ACS Applied Materials and Interfaces, 2017. **9**: p. 26096-26106.

50. Niwa, M., S. Sota, and N. Katada, *Strong Brønsted acid site in HZSM-5 created by mild steaming.* Catalysis Today, 2012. **185**: p. 17-24.

51. Muller, M., G. Harvey, and R. Prins, *Comparison of the dealumination of zeolites beta, mordenite, ZSM-5 and ferrierite by thermal treatment, leaching with oxalic acid and treatment with SiCl4 by 1H, 29Si and 27A1 MAS NMR.* Microporous and Mesoporous Materials, 2000. **34**: p. 135-147.

52. Kooyman, P.J.J., P. van der Waal, and H. Van Bekkum, *Acid dealumination of ZSM-5.* Zeolites, 1997. **18**: p. 50-53.

53. Yu, Z., et al., *Brønsted/lewis acid synergy in H-ZSM-5 and H-MOR zeolites studied by 1H and 27Al DQ-MAS solid-state NMR spectroscopy.* Journal of Physical Chemistry C, 2011. **115**: p. 22320-22327.

Chapter 7

Apparent and Intrinsic Ethanol Dehydration Kinetics under Liquid Phase Conditions

7.1. Background

The need to reduce our dependence on crude oil feedstocks has motivated green technology studies that convert biological feedstocks into fuels and chemicals.[1, 2] Ethanol is the largest produced platform chemical derived from fermentation of renewable sources. Improvements in agricultural cultivation and fermentation processes has cause a significant increase in bio-based ethanol production, creating a surplus and driving ethanol costs down.[3, 4] One existing green alternative in Brazil dehydrates ethanol derived from the fermentation of sugars derived from sugarcane to form ethylene at the industrial scale.[2, 5] The demand for ethylene is currently the largest produced polymerization precursor used in the production of plastics, detergents and lubricants.[6] While the bio-based ethanol dehydration process has been applied at the industrial scale, it only contributes 0.2% of the total ethylene demand, with the vast majority of ethylene produced from the cracking of petroleum-derived compounds. Therefore, further improvements are required on the ethanol dehydration process to compete with ethylene produced from crude sources.

High feed costs and process inefficiencies limit bio-based ethanol as an economic alternative to crude oil for ethylene production. The current ethanol dehydration process delivers a 50-wt% ethanol and water mixture to a boiler that is vaporized to the desired reaction temperature. Ethanol dehydration is a highly endothermic process with a narrow temperature range between 350 and 400 °C to selectively form ethylene when operated using a microporous catalyst.[2] Due to both the temperature dependent ethylene selectivity and high endothermicity, industrial scale processes can be heat transfer limited by the characteristics of the reactor system. The current ethanol dehydration technology converts the gas stream of ethanol through a series of four heaters and adiabatic reactors, which limits the total conversion and allows for reheating of the process flow to maintain the narrow temperature range.

Mohsenzadeh et al.[7] performed a techno-economic analysis on the conventional ethanol to ethylene process and determined that the current process is not economical without ethanol subsidies for a plant in Sweden. Excluding ethanol feed costs, an estimated 26% of the operating costs would arise from the utilities costs associated with heating, compressing, pumping and steam delivery. In addition, an estimated 20% of the capital cost goes to the reactors and furnaces when you exclude holding tanks for reactants and products, with the remaining costs are associated with quenching, compressing and caustic washes for product recovery and stripping columns for ethylene purification. As of the study performed in 2017, ethanol costs would need to be half as much or ethylene prices twice as much in order to break even with current technologies. An estimated 10% of the ethanol price is associated with transportation costs.

We propose that operating ethanol dehydration in a compressed liquid phase will intensify the dehydration process by improving heat transfer, product and energy recovery. A significant amount of energy that goes into the system is associated with heating the water solvent that is

cofed with ethanol. Chapter 3 evaluated the process intensification benefits of operating under a compressed liquid phase instead of commonly applied gas phase conditions. Energy benefits outline how the use of liquid water eliminates a significant amount of energy to overcome water's heat of vaporization. In addition, the improve thermal management under liquid phase operation would allow the reactor systems to deliver heat to the reaction more efficiently than under vapor phase operation. Therefore, process improvements in converting ethanol to ethylene under a compressed liquid phase could reduce the substantial capital costs associated with multiple reactors and furnaces as well as utility operating costs for heating.[7]

The process intensification benefits previously reported in Chapter 3 assumed that reactant phase has negligible effect on catalytic activity. This assumption is not always applicable, as operating pressure/phase has been shown to influence a reaction's intrinsic activity.[8] Pressure/phase dependence of catalytic activity has been attributed to changes in adsorption energies, solvation behavior, reaction pathways, acid/base concentrations, and stabilizing intermediates that can lead to an increase[8] or decrease[9] in catalytic activity. Although some studies have explored chemistries under compressed liquid phase conditions, few have compared the activity of a single catalytic reaction under both liquid and vapor phase operation.[10, 11] Therefore, we sought to explore the limitations and benefits of a compressed, liquid relative to vapor phase operation on catalytic activity using ethanol dehydration as our model chemistry.

In this study, we seek to evaluate whether a change in ethanol dehydration activity occurs when operating under a compressed liquid phase instead of the commonly studied gas phase reaction conditions. Bench scale ethanol dehydration reactions were performed in a continuous phase packed bed reactor catalyzed using ZSM-5 zeolite. Ethylene activity was compared when operated under both liquid and vapor phase (0.1 or 24 MPa) and varying weight hourly space velocities (47

- 946 hr $^{-1}$) and water loadings (0 - 33 wt%). In addition, a low conversion study is performed to examine the intrinsic activity of both liquid and vapor phase reaction conditions is performed. Post-run catalyst characterization and competitive adsorption models assess how the extent of coking, framework and acid site loss may play a role in either diffusion, intrinsic or deactivation mechanisms during ethanol dehydration reactions under the vapor or liquid phase.

7.2. Experimental Section

7.2.1 Materials

ZSM-5 zeolite with a Si/Al ratio = 38 was supplied by ACS Materials (P-38). Water was deionized to 17.9 MΩ cm prior to use. Anhydrous ethanol was purchased from Sigma Aldrich. DI water was used as an added solvent for all reactions.

7.2.2 High Conversion Reactor Setup

High activity ethanol dehydration experiments was performed using a packed bed reactor configuration. A 3/8" ID Sitec reactor tubing was initially filled with 0.5g of ZSM-5 zeolite that was contained using a 2 µm porous stainless steel frit. Ethanol and water was pumped through an initial preheat loop at varying flowrates (0.5 to 2 ml/min) using HPLC pumps (Eldex 5935 Optos pump) prior to being delivered to the catalytic reactor bed. The reaction was performed at 375 °C with varying space velocities (47 − 946 hr^{-1}) and ethanol to water feed ratios (0 − 33 vol% water loading). After conversion over the reactor bed, the product mixture was pumped through a cooling line, stainless steel filters, and then depressurized through a backpressure regulator before liquid and gas phase stream separation.

7.2.3 Low Conversion Reactor Setup

Low conversion reactions were performed on a continuous flow setup similar to the high conversion reactor system. A ¼" Swagelok reactor tube was initially filled with 0.05-0.1g of ZSM-5 zeolite that was contained with a 2 µm porous stainless steel frit. Ethanol and water were pumped at 0.5 to 2 ml/min using an Eldex pump into an initial heated reactor zone. The preheat and reactor zones were both inserted in an aluminum block that was conductively heated using a PID controlled 500W cartridge heater. Reactions were performed at temperatures ranging between 200 and 350 °C at either 100% or 66 vol% ethanol feed. After conversion over the reactor bed, the product mixture was pumped through a cooling line, stainless steel filters, then depressurized through a backpressure regulator and separated into a liquid and gas phase streams.

7.2.4 Gas and Liquid phase Analysis

Gas phase analysis was performed by delivering the gas product to an online Shimadzu GC-2014 with a Rt-Q-Bond fused silica PLOT column (30m length, 0.25 mm ID). The gas was diluted with a 250 ml/min flow of helium and was injected on the GC every 10 minutes to obtained ethylene and/or volatilized diethyl ether yields. Liquid phase products were analyzed offline with a Shimadzu GC-2030 instrument using a Rt-U-Bond fused silica PLOT column (30m length, 0.32 mm ID) to determine ethanol conversions and diethyl ether yields.

7.2.5 ZSM-5 Catalyst Characterizations

Characterization of ZSM-5 both before and after ethanol dehydration reactions is performed using temperature programmed oxidation (TPO), infrared spectroscopy (IR), x-ray diffraction (XRD) and nitrogen sorption.

Infrared spectroscopy on treated ZSM-5 samples was performed using a Thermo Nicolet Magna 560 with a SpectraTech DRIFTS cell. Samples were analyzed over the range from 4000 to 400 cm^{-1}, at a resolution of 2 cm^{-1}, and an accumulation of 96 scans. The DRIFTS cell was loaded and flattened with ZSM-5 before purging with N_2 for 10 minutes. 20 °C increments at 10-15 min intervals were run until temperatures reached 100 °C, where it was held for 30 minutes before raising by 50 °C increments to 550 °C.

Gas sorption was performed using an ASIQ iQ Quantachrome Instrument to determine surface micropore area, external surface area, and micropore volume. Approximately 0.025g of a ZSM-5 sample was first outgassed with a thermal ramp of 2 °C/min, holding for 20 minutes at 80 °C, 100 °C and 120 °C before a final ramp to 350 °C for 10 hours. The degassed sample was incrementally dosed with nitrogen at 77 K from a p/p_0 range of 10^{-6} to 1. Isotherms were analyzed using the t-plot method to determine, micropore area and volume. Mesopore volume was calculated using the difference between micropore volume and total adsorbed nitrogen at $p/p_0 = 0.99$.

The coke yield was determined by analyzing the solid product using temperature programmed oxidation with a TGA 209 F1 Libra from Netzch (temperature program of 30 − 800 °C with a rate of 10 °C min^{-1} and a mixture oxygen, 4 sccm, and nitrogen, 8 sccm).

Sample crystallinity provides a relative quantitative measure of zeolite degradation. X-ray diffraction on de coked ZSM-5 was performed using a Rigaku automatic instrument with the Bragg-Bretano theta-theta configuration. Diffractions were taken with a Cu Kα at 27.5kV and 5mA. Analysis was performed over the range from 5 − 80° 2Ө with a 0.5 step size and 1s dwell time. Crystallinity for each sample was determined from the sum of peak intensities between 22.5

$-$ 25 2Θ degrees, as designated by ASTM method D5758-01. The 22.5 $-$ 25 2Θ range includes the prominent ZSM-5 peaks that correspond to the (051), (313) and (033) planes.

7.2.6 High Conversion Reactor Model

In order to calculate reaction rate constants, a plug flow reactor model was applied to the results obtained from the high conversion ethanol dehydration reactions with varying space velocity. For ethanol to ethylene reaction kinetics, it is assumed to be irreversible and 1st order with respect to ethanol to form ethylene, which makes the kinetic rate equation of the form:

$$r_{EtOH} = -k_1[C_{EtOH}]$$

Where the reaction rate of ethanol to ethylene (r_{EtOH}) is known, while its dependence on ethanol concentration (C_{EtOH}) and the ethanol dehydration reaction rate constant (k_1) are unknown. In order to obtain the concentration of ethanol at a given conversion, the system is assumed selective to ethylene, which allows a stoichiometric equation to be written in the form:

$$C_{EtOH} = \frac{F_{EtOH,0}}{v} = C_{EtOH,0}\left(\frac{1-X}{1-\varepsilon X}\right)$$

Where the molar conversion of ethanol (*X*), initial molar ethanol concentration ($C_{EtOH,0}$), and the variable volume factor ($\varepsilon = 0.38$) are all known. The model assumed the system was operated as an isothermal and isobaric plug flow reactor. Under these assumptions, the plug-flow design equation was simplified as:

$$V = F_{EtOH,0}\int_0^X \left(\frac{dX}{-r_{EtOH}}\right)$$

Where the knowns are total reactor volume (*V*) and initial molar flowrate of ethanol ($F_{EtOH,0}$).
Using these three equations, the reaction rate constant was determined from the following
combined equation in Matlab:

$$k_1 = \frac{F_{EtOH,0}}{V * C_{EtOH,0}}\left[(1 + \varepsilon)ln\frac{1}{1 - X} - \varepsilon X\right]$$

7.2.7 Fugacity Calculation and Langmuir Adsorption Equation

   To model adsorption of water and ethanol on a zeolite surface, a 2D, competitive adsorption
Langmuir model was applied for the analysis. The model assumed an adsorbed species behave
ideally, with only water (A) or ethanol (B) adsorbing to the same sites (S):

$$A + BS \overset{K(T)}{\longleftrightarrow} B + AS$$
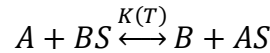
Where A and B are water and ethanol in the bulk phase and AS and BS are water and ethanol
adsorbed onto the surface (S). To account for the nonideality of the bulk phase water/ethanol
mixture, the thermodynamic adsorption equilibrium, K(T), was defined as the ratio of activities of
adsorbed and bulk ethanol/water species of the form:

$$K(T) = \prod_{i}^{n} a_i^{v_i} = \frac{a_A^S a_B^b}{a_A^b a_B^S} = \frac{[AS]a_B^b}{a_A^b[BS]} = \frac{[AS]x_B^b\widehat{\emptyset}_B}{[BS]x_A^b\widehat{\emptyset}_A}$$

Where a_i^b is the activity of species i in the bulk phase and a_i^S is the activity of species i adsorbed
on the surface. The model assumes that adsorbed species behave ideally, so that the adsorbed
species activities can be assumed as their corresponding mole fractions and simplifies as the molar
concentrations (either [AS] or [BS]). The activity of ethanol and water in the bulk can be calculated
based on the product of their corresponding bulk mole fractions x_i and mixture fugacity
coefficients $\widehat{\emptyset}_i$. The fugacity coefficients are calculated using the Peng Robinson equation of state

with the Wong Sandler mixing rule and UNIQUAC model for the activity coefficient (PRSV2 + UNIQUAC + WS model); a model developed by Restrepo et al.[12] that accurately fit ethanol water and ethylene VLE experimental results at 200 °C and pressure up to 16 MPa. Applying the equation of state to obtain the mixture fugacity coefficient and the adsorption Langmuir isotherm model, the molar coverage of ethanol, θ_B, can be defined as:

$$\theta_B = \frac{K\dfrac{\widehat{\emptyset}_A x_A^b}{\widehat{\emptyset}_B x_B^b}}{K\dfrac{\widehat{\emptyset}_A x_A^b}{\widehat{\emptyset}_B x_B^b} + 1}$$

The thermodynamic adsorption equilibrium constant between ethanol and water is set to 7, based on previous ethanol and water adsorption selectivity studies.[13] Based on this equation, the coverage of ethanol θ_B can be estimated at varying water to ethanol molar loadings in the bulk phase $\dfrac{x_A^b}{x_B^b}$.

7.3. Results

7.3.1 Effect of Space velocity

A comparison of vapor and liquid phase ethanol dehydration activities was obtained at varying feed space velocities using the high conversion reactor system. **Figure 7.1** plots the ethanol dehydration conversion when operated at 375 °C and varying ethanol feed space velocities between 47 to 946 hr^{-1}. The reactant flow was delivered to the packed bed reactor zone at a 2:1 volumetric ratio of ethanol to water. Under these operating conditions, **Figure 7.1** reveals that under all conditions, the steady state ethanol conversions were between 20 and 100%, and an ethylene selectivity of >98% was obtained. Expectedly, at increased space velocities, both liquid and vapor phase reactions had lower reduced ethylene yields. When operating ethanol dehydration

197

at the same space velocity, **Figure 7.1** reveals a $10 - 50\%$ increase in vapor phase ethanol conversion relative to liquid phase operation.
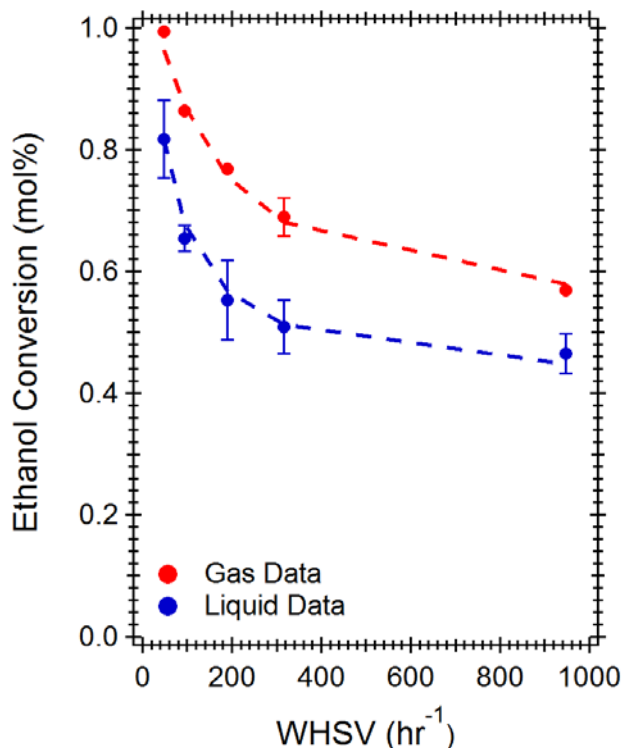
Figure 7.1: Ethanol conversion during the dehydration reaction from a 2:1 volumetric ratio of ethanol:water reactant flow performed at 375 °C and WHSV ranging between 47 and 946 hr^{-1}. Red squares denote reactions performed under 0.1 MPa while blue circles denote reactions performed under 24 MPa of pressure

To quantify the relative loss in apparent activity, the plug flow reaction was modeled by combining a first order kinetic, stoichiometric and plug flow reactor system of equations, as described in the methods section. The reaction was assumed to be first order with respect to ethanol and the reactor system was assumed to operate both isothermally and isobarically. The model for liquid and vapor phase reaction is shown as blue and red dotted lines in **Figure 7.1**, respectively, and fits the data set. Based on these fits, the reaction rate constants for liquid and vapor phase

reactions are 2.25 mol·(g hr)$^{-1}$ and 5.34 mol·(g hr)$^{-1}$, respectively. Therefore, the apparent reaction rate constant for liquid phase reaction is approximately 50% less than for operation under vapor phase conditions.

The apparent drop in liquid phase activity shown in **Figure 7.1** is unusual based on expected process engineering intensification benefits when delivering a compressed liquid phase ethanol reactant compared to the traditional vapor phase feed at the same mass flowrate. Delivering ethanol into a packed bed reactor in a compressed liquid phase effectively increases the ethanol concentration and increases the residence time when compared to a vapor phase reaction, which will have a less dense feed with a greater linear velocity. An increase in reactant residence time (lower WHSV) is expected to increase overall conversion, as shown by the trend in either vapor or liquid phase operation with varying WHSV in **Figure 7.1**. However, the expected compressed phase process benefits are not reflected in the apparent activity of ethanol on ZSM-5.

The apparent loss in catalytic activity with operating phase observed in **Figure 7.1** can be the result of several phenomena, which include pressure or phase effects attenuating the catalytic activity of ZSM-5, coking dynamics of the crystal surface or pores or deactivation through framework or acid site loss. Interactions between the catalyst and either the reactant, solvent or product could result in the observed changes between vapor and liquid phase operation. Of these, the unusual thermodynamic properties of water are likely causing the change in catalytic activity, either directly influencing the intrinsic activity by participating in the reaction or indirectly through catalyst deactivation. Specifically, water ionic product and dielectric constant vary nonlinearly with temperature and pressure and widely differ under steam and liquid water conditions.[8, 14, 15] A shift in the phase of water has been previously shown to either stabilize or destabilize active site transition states, effectively changing the intrinsic activity of ZSM-5 with pressure.[8]

199

Similarly, work by Phillips et al.[16] reported an addition of 10% water to a vapor phase ethanol dehydration reaction using ZSM-5 increased its catalytic activity to form ethylene, a result attributed to a shift in the reaction mechanism from bimolecular to unimolecular when water adsorbed to an acid site. Next, a study that varies the initial water loading in the reactant flow is performed to assess the influence of water on liquid and vapor phase activity.

6.3.2 Effect of water loading

In order to evaluate the role of water on activity, we performed a series of experiments at low space velocities. We selected a WHSV of 47 hr^{-1} based on the previous results that indicated the difference between liquid and vapor phase runs was minimal and was at the highest conversions. **Figure 7.2** plots the effect of water loading on both liquid and vapor phase ethanol dehydration reactions. Similar to the study with varying space velocity, the selectivity to form ethylene was >98% under all conditions. **Figure 7.2** reveals a lack of trends on activity with initial water loading for both liquid and vapor phase operation. Similar to the results observed with varying space velocity in **Figure 7.1**, vapor phase operation was more active than the liquid phase, with vapor phase ethanol conversions ranging between 91 – 98% compared to the 78 – 91% range of liquid phase ethanol conversions. However, the initial water loading had minimal influence on both liquid and vapor phase ethanol dehydration activity.
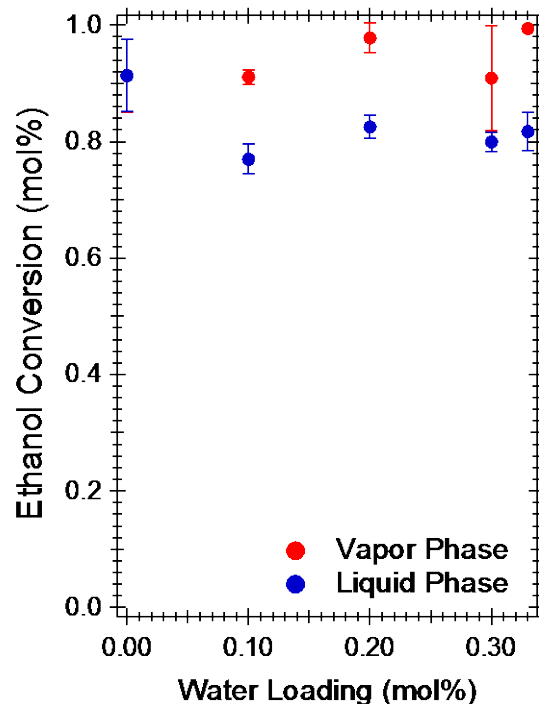
Figure 7.2. Ethanol conversion during the dehydration reaction performed at 375 °C and a WHSV of 47 h^{-1} with varying initial volumetric water loading ranging between 0 and 33%. Red squares denote reactions performed under 0.1 MPa while blue circles denote reactions performed under 24 MPa of pressure

The lack of change with water loading indicates that water does not influence the catalytic activity when comparing liquid and vapor phase reactions. Alternatively, the influence of water could be difficult to assess because it is formed during the reaction, which masks any changes that may occur with varying initial water loading. Assuming that water may not be playing a direct role in activity, characterizing ZSM-5 after the reaction may point to indirect factors that are causing the change in activity. Specifically, the change in activity could be associated with differing dynamics of coke formation either on the crystal or in the micropores. Relative to SAPO-34 and NiAPO-34, coke formation during ethanol dehydration has been shown to be a primary mechanism of deactivation for ZSM-5.[17] The rate of aromatization and oligomerization could be pressure

dependent, which would lead to increased diffusion limitations for liquid phase runs and cause the observed loss in activity. Next, coked and de-coked ZSM-5 samples from select dehydration experiments are characterized in order to evaluate whether catalyst framework stability, acid site stability and/or coke formation influence the apparent vapor and liquid phase activities.

7.3.3 Effect of Catalyst Deactivation

In order to evaluate the influence of zeolite framework and acid site stability on activity, a series of post run characterization techniques are performed on both coked and de-coked ZSM-5 samples. **Table 7.1** lists the different textural properties based on N_2 sorption of coked post-run ZSM-5 samples. **Table 7.1**. reveals a similar loss in total surface area and micropore volume for coked ZSM-5 samples after both liquid and vapor phase reactions with a 66 vol% initial ethanol feed. This is an expected result, as coke has been previously shown to occur both inside micropores and on the catalyst surface.[18] Castaño et al. analyzed the coke formed in ZSM-5 during polyethylene cracking, and determined that soluble coke species were located in the pore based on IR, sorption and Raman characterization.[18]

Table 7.1. Texture properties of ZSM-5 after high conversion ethanol dehydration reaction conditions. Both liquid or vapor phase and either 100% or 66 % ethanol feed volumetric concentrations.

Postrun ZSM-5 Sample Treatment	$S_{t\text{-plot,ext}}$[a] (m2/g)	$S_{t\text{-plot,ext}}$[a] (m2/g)	V_{micro}[a] (cm3/g)
67% Liquid *(Coked)*	128	25.5	0.05
67% Vapor *(Coked)*	120	17.5	0.06

[a]External surface area, micropore surface area, and volume of de-coked ZSM-5 calculated using the t-plot method

Table 7.2 evaluated the crystallinity and textural properties of post-run ZSM-5 samples after decoking. Based on **Table 7.2**, all treated ZSM-5 frameworks retain >88% of their original crystallinity from XRD, based on the crystallinity of untreated ZSM-5. Similarly, nitrogen sorption analysis found comparable ZSM-5 surface areas after all reaction conditions, with total micropore surface areas ranging between $303 - 341$ m^2 g^{-1} , external surface areas ranging between $22 - 40$ m^2 g^{-1}, and the micropore volumes ranging between $0.155 - 0.163$ cm^3 g^{-1}. The sample treated with 66 vol% ethanol feed in the liquid phase had the lowest micropore surface area and volumes while 100 vol% ethanol feed in the vapor phase had the greatest micropore surface area. The differences in XRD and nitrogen sorption between each run can be considered minimal and are consistent with a metastable catalyst framework under ethanol dehydration reaction conditions.

Table 7.2. Texture properties of ZSM-5 after high conversion ethanol dehydration reaction conditions. Both liquid or vapor phase and either 100% or 66 % ethanol feed volumetric concentrations.

| Postrun ZSM-5 Sample Treatment	Relative [a] Crystallinity (%)	$S_{t-plot,ext}$ [b] (m^2/g)	$S_{t-plot,ext}$ [b] (m^2/g)	V_{micro} [b] (cm^3/g)	Total Coke [c] (wt%)	Hard Coke (wt%)
Untreated ZSM-5	N/A	322	39	0.16	N/A	N/A
100% EtOH Liquid	88%	326	33	0.16		
100% EtOH Vapor	94%	341	25	0.16		
67% EtOH Liquid	89%	303	33	0.16	5.3%	2.0%
67% EtOH Vapor	97%	313	22	0.16	1.7%	1.4%

[a] Relative crystallinity based on postrun ZSM-5 samples after decoking compared to crystallinity of untreated material; [b] External surface area, micropore surface area, and volume of de-coked ZSM-5 calculated using the t-plot method;
[c] Percentage of coke determined gravimetrically from difference between coked and de-coked ZSM-5 samples.

Table 7.2 shows that the extent of total coking for post run ZSM-5 samples with a 67% ethanol feed change between liquid and vapor phase operating conditions. However there is a difference in the type of coke formed during ethanol dehydration, which can be classified as either soft or hard coke. Distinguishing between soft and hard coke can be done by evaluating in what temperature range coke is oxidized from ZSM-5 zeolite during temperature-programmed oxidation (TPO). Soft coke is oxidized and degassed at a temperature range between $200 < T < 400$ °C and hard coke will be removed at $400 < T < 650$ °C under an oxygen rich environment. Although the total coke varies with operating conditions, **Table 7.2** reveals that the amount of hard coke is more similar between liquid and vapor phase reactions.

Previous work has shown that hard coke primarily causes pore blockage and diffusion limitation effects. A previous study on in situ IR analysis of coke formation during ethanol dehydration discovered that coke forms from alkene precursors that aromatize into methylated benzenes within channel intersections of the MFI lattice, resulting in pore blockage and diffusion limitations.[19] Other experimental studies have identified ethylene as the precursor to coke formation as well.[20, 21] Experimental results for ethanol to hydrocarbons at 400 °C were fitted by a kinetic model, which found the rate constant for ethylene production influenced coke formation the most, indicating that ethylene is a coke precursor species. Since ethylene is what is considered to be the precursor to oligomerization and aromatization, the soft coke in the 67% ethanol fed into a liquid phase reactor is likely straight chain alkenes that reside in the pore but is still mobile and not actively blocking the pores. Based on this assumption, the soft coke formed is unlikely to result in diffusion limitations. Therefore, due to a similar extent of hard coke formation, it is unlikely that differences in diffusion limitations due to coke formation is the primary cause for the activity difference observed in **Figure 7.1** and **Figure 7.2**.

Lastly, infrared spectroscopy (IR) is used to evaluate the influence of operating phase and ethanol feed concentration on the ZSM-5 acid sites stability after each run. **Figure 7.3** presents IR spectra of untreated and post run, decoked ZSM-5 samples under vapor and liquid phase conditions. The different IR bands in **Figure 7.3** correspond to different stretching modes of acid sites and silanol species within ZSM-5. A loss in Brønsted acid sites occurs via zeolite dealumination, which is the preferential hydrolysis of the Si–O–Al framework bonds that removes aluminum and creates extra framework alumina species (EFAL); commonly shown to occur steaming and acidic aqueous conditions. [22-24] The IR band located at 3600 cm^{-1} corresponds to the OH stretching modes of Brønsted acid sites, the band located at 3660 cm^{-1} corresponds to EFAL species, and the band located at 3720 cm^{-1} corresponds to the surface silanol groups.[25]
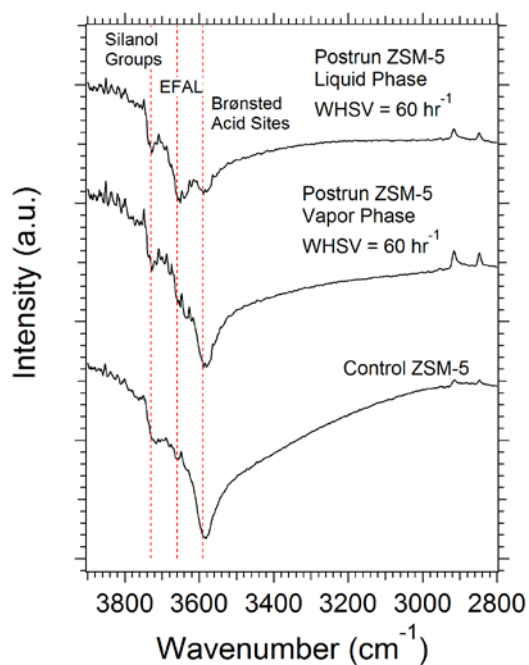
Figure 7.3: Infrared spectroscopy of calcined ZSM-5 and post run ZSM-5 after high conversion ethanol dehydration experiments operated at 375 °C and a 66 vol% ethanol feed in both the compressed liquid phase and vapor phase conditions. The treatment phase is denoted next to the corresponding spectra.

The untreated ZSM-5 spectra in **Figure 7.3** reveal a strong peak Brønsted acid band at 3600 cm$^-$^{1} with minor bands associated with extra-framework aluminum (EFAL) and isolated silanol groups at 3660 and 3720 cm^{-1}, respectively. When comparing ZSM-5 samples after 100% and 66% ethanol fed vapor phase reactions to the untreated ZSM-5 spectra, the Brønsted acid site band is retained with no noticeable increase in bands associated with EFAL or silanol nest species. In contrast, both spectra for ZSM-5 after liquid phase reactions have an observable loss in the Brønsted acid band and a corresponding formation of EFAL species, which suggests the acid site is stable under vapor phase conditions but less stable under hot liquid water conditions. The partial retention of framework acid sites may correspond with the remaining activity observed under liquid phase conditions. Previous analysis in Chapter 6 has shown that acid sites are rapidly lost under hot liquid water treatment at 250 °C within six hours and then remain stable for over 200 hrs. Next, ethanol dehydration is performed under low conversion conditions to minimize water formation and evaluate the intrinsic activity of ZSM-5 by removing any potential diffusion limitations.

7.3.4 Effect of Conversion

To confirm the loss of acid sites as the primary deactivation mechanism that is influencing catalytic activity, a second series of experiments is performed under low conversion conditions. Operating under low conversion conditions will decrease the concentration of water formed during the reaction and therefore minimize the extent of dealumination during the reaction. Low conversion is performed on a similar but scaled down reactor setup which allows for more accurate ethylene and ethanol measurements compared to the higher activity reactor system. Four dehydration experiments are performed, 100% ethanol feed under vapor and liquid phase

206

conditions and 66 vol% ethanol feed under vapor and liquid phase, to accurately evaluate the role of water and fluid phase on the intrinsic activity of ethanol on ZSM-5.

Figure 7.4 plots the results from the intrinsic activity in an Arrhenius plot. Figure 7.4 shows that reactions with an undiluted ethanol feed have similar activities and calculated activation energies of 55.3 and 60.8 kJ/mol for vapor and liquid phase runs, respectively. However, the results performed with an initial 66 vol% ethanol feed have varying activity with operating phase. A vapor phase run with 66 vol% ethanol in water delivered as the feed has a slight increase in catalytic activity compared to the vapor phase run without an initial water loading. In contrast, ethanol dehydration runs performed in the liquid state with a 66 vol% initial ethanol feed had a significant decrease in activity compared to the other vapor and liquid phase runs. At operating temperatures >250 °C, the apparent turnover frequency for liquid phase runs with 33 vol% initial water loading was 3-10 times less than other reaction conditions shown in Figure 7.4. Therefore, the results presented in Figure 7.4 clearly indicate that a combination of water in the liquid phase has a deactivating effect on the intrinsic activity of ethanol dehydration. Based on the previous results on acid site loss under high conversion conditions, the natural next step is to explore ZSM-5 hydrothermal stability under low conversion conditions.
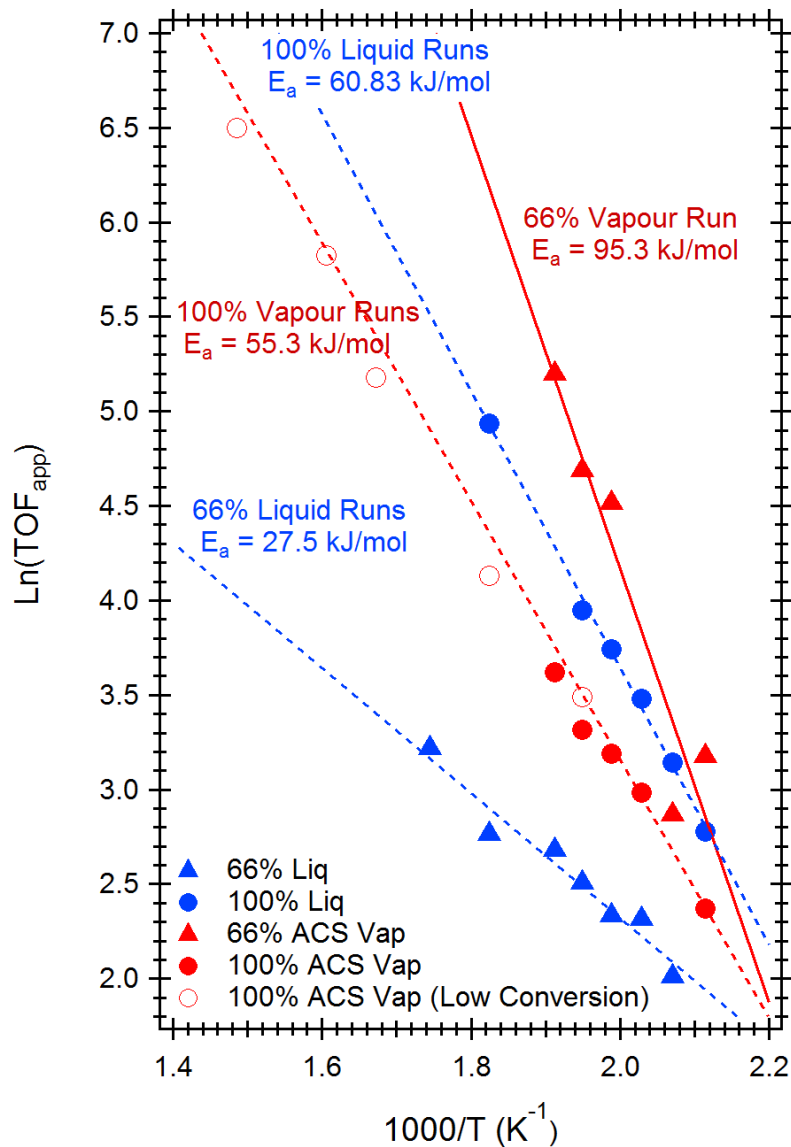
Figure 7.4: Arrhenius plot of intrinsic ethanol dehydration runs operated under a) vapor phase conditions with 100% ethanol feed, b) vapor phase conditions with 66 vol% ethanol feed, c) liquid phase conditions with 100% ethanol feed, and d) liquid phase conditions using 66 vol% ethanol feed.

Table 7.3. Texture properties of ZSM-5 after low conversion ethanol dehydration reaction conditions. Both liquid or vapor phase and either 100% or 66 % ethanol feed volumetric concentrations.

Postrun ZSM-5 Sample Treatment	Relative Crystallinity [a] (%)	$S_{\text{t-plot, micro}}$ [b] (m^2/g)	$S_{\text{t-plot,ext}}$ [b] (m^2/g)	V_{micro} [b] (cm^3/g)	Coke[c] (wt%)
Untreated ZSM-5	N/A	322	39.2	0.159	N/A
100% EtOH Liquid	90.5%	266	28.8	0.169	9.54%
100% EtOH Vapor	90.5%	331	15.2	0.126	9.46%
67% EtOH Liquid	92.8%	309	33.2	0.161	7.20%
67% EtOH Vapor	90.2%	375	25	0.179	9.80%

[a] Relative crystallinity based on postrun ZSM-5 samples after decoking compared to crystallinity of untreated material; [b] External surface area, micropore surface area, and volume of de-coked ZSM-5 calculated using the t-plot method;
[c] Percentage of coke determined gravimetrically from difference between coked and de-coked ZSM-5 samples.

The crystallinity and textural properties of post run and de-coked ZSM-5 zeolite from the intrinsic reaction conditions are included in **Table 7.3**. Similar to the high conversion conditions, the zeolite framework is largely retained after ethanol dehydration, with all ZSM-5 samples having a relative crystallinity value >90%. Also, minimal changes in micropore and external surface area from N_2 sorption are observed when comparing untreated and treated ZSM-5 samples. The extent of coke formation was also similar in all treated ZSM-5 samples, with weight percentages of coke between 7.2 and 9.8%. This suggests that framework stability and coke formation are not influencing the apparent change in intrinsic ethanol dehydration activity.

Infrared spectroscopy (IR) of de-coked ZSM-5 zeolite after each low conversion reaction conditions is performed to evaluate ZSM-5 acid sites stability. **Figure 7.5** presents IR spectra of untreated and post run, decoked ZSM-5 samples under vapor and liquid phase conditions. Interestingly, ZSM-5 retains Brønsted acid sites under all operating conditions. This is in contrast to the loss in ZSM-5 Brønsted acid sites after high conversion reactions after liquid phase operation, which was considered a possibility for loss in catalytic activity. However, the loss in liquid phase ethanol dehydration activity with a 66 vol% ethanol feed cannot be attributed to a loss in acid sites based on the retained acid sites in **Figure 7.5** under all intrinsic operating conditions.
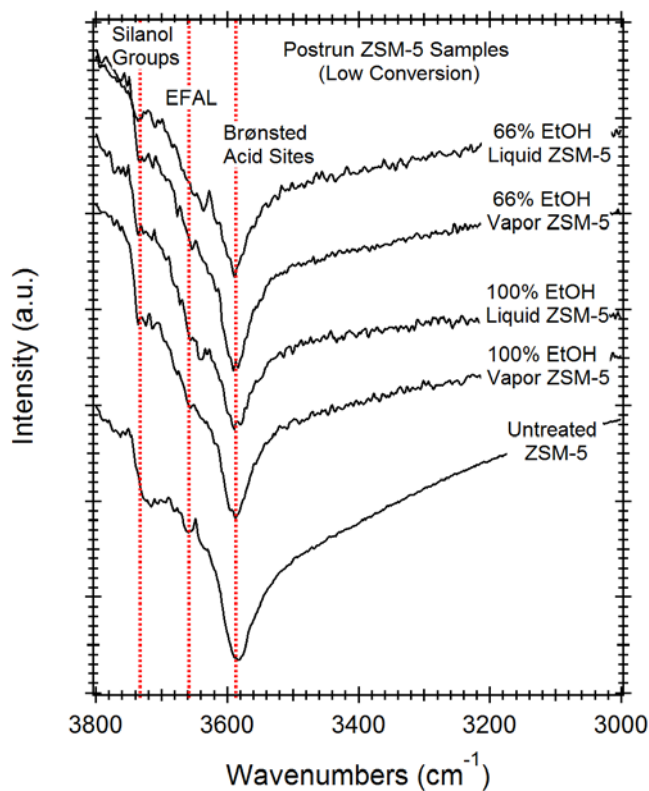
Figure 7.5: Infrared spectroscopy of calcined and post run ZSM-5 after low conversion ethanol dehydration experiments operated at reaction conditions under both compressed liquid and vapor phase conditions. Ethanol dehydration reaction conditions (Phase and ethanol feed concentration) of treated ZSM-5 sample are denoted next to the corresponding spectra.

210

7.4. Discussion

The combination of results presented in **Figure 7.2, Figure 7.4** and **Table 7.3** can help evaluate the role of space velocity, coking and water on the apparent activity for ZSM-5. **Figure 7.1** reveals a reduced ethanol dehydration activity when operated in the liquid relative to vapor phase at 375 °C over a range of high conversion space velocities. **Figure 7.2** shows that the activity under high conversion conditions is largely insensitive to the initial water loading in the reactant feed. The ZSM-5 characterized after reactions at high conversions indicates that loss of acid sites may contribute to the loss in liquid phase activity, which is caused by dealumination via acid site hydrolysis reactions. The amount of hard coke formed after ethanol dehydration reactions remains constant for each high conversion run, which suggests coking does not cause the difference in vapor to liquid phase activity.

The results presented in **Figure 7.4** show differing trends in intrinsic ethanol dehydration activity with varying operating phase and initial water loading compared to high conversion conditions. Ethanol dehydration performed under 100% ethanol loading in the vapor and liquid phase have similar activities, as shown in **Figure 7.4**. However, significant decrease in activity for a 66 vol% ethanol feed in the liquid phase is observed. The results presented in **Figure 7.4** clearly identify that a change in ethanol dehydration activity can be associated with pressure, but only in the presence of water.

Interestingly, the vapor phase run operated with a 66 vol% ethanol feed under low conversion conditions in **Figure 7.4** revealed a slight increase in catalytic activity compared to the vapor phase run without an initial water loading. Previous studies have provided evidence that modifying the strength of BAS can improve the zeolite steady state activity for ethanol dehydration. The vapor phase result is consistent with Phillips et al., report an improvement in steady state ethanol

dehydration activity using ZSM-5 with the addition of up to 25% water. Phillips et al. attribute the improvement to water association at each acid site, which attenuates acid site strength and reduces the initial loss in activity due to coking. Therefore, a balance between ZSM-5 framework and coking stability is tunable with water content during a reaction.

Operating under low conversion conditions allows a deconvolution between diffusion and intrinsic factors on ethanol dehydration activity. Low temperature reaction conditions ensure that the intraparticle diffusion is no longer limited and allow evaluation of the intrinsic ZSM-5 activity. This also will help evaluate the role of water on the apparent change in activity without confounding effects such as water's role in acid site loss or coke formation. The results from low conversion reactions in **Figure 7.4** reveals liquid water inhibits ZSM-5 ethanol dehydration activity without a loss in Brønsted acid sites or coke inhibition, based on ZSM-5 characterization presented in **Table 7.3** and **Figure 7.5**. The lack of change in framework, acid site and coking with varying intrinsic reaction conditions eliminates any indirect influence water may play on ethanol dehydration and suggests that water is an active participant influencing the change in liquid relative to vapor phase activity.

While the results in **Figure 7.2** indicate that high conversion, ethanol dehydration activity is independent with respect to water loading, the results do not necessarily contradict the low conversion results in **Figure 7.4,** which indicate water has a direct influence on intrinsic reactivity. An important note is that while the initial water loading may vary significantly between 0 and 33 vol%, a significant amount of water is formed during the ethanol dehydration. The water produced during ethanol dehydration will initially reside at the catalyst acid sites, which could effectively poison the catalyst and lower the expected per site activity. In addition, due to the microporous nature of ZSM-5 zeolite, an increase in water formation within the crystal lattice could lead to pore

212

intracrystalline diffusional effects. Lastly, in addition to the change in the relative water/ethanol content within the micropores, the change in water content on the ZSM-5 crystal surface could influence activity through competitive adsorption between the crystal surface and bulk fluid phase. Water's role in acid site poisoning, intracrystalline diffusion and competitive adsorption can all be dependent on the operating pressure and phase, which makes the role of water on catalytic activity difficult to assess when performed under high ethanol conversion conditions. Therefore, the experimental results in **Figure 7.2** do not accurately assess how water influences ethanol dehydration intrinsic activity; and whether water role differs between liquid and vapor phase operation.

Once possible explanation for the apparent difference in activity is that water adsorbs and deactivates the catalyst differently under vapor and liquid phase conditions. This can occur due to differences in water and ethanol adsorption on the ZSM-5 surface. A Langmuir isotherm model for water and ethanol on an ideal 2D surface is performed in order to evaluate the effect of phase on the adsorption of ethanol and water adsorption. Both ethanol and water species are assumed to adsorb to the same sites and behave ideally. Differences in the non-ideality between ethanol and water in the bulk phase at elevated temperatures and pressures are taken into account using the Peng Robinson equation of state and Wong Sandler mixing rule. Further details on the Langmuir model are provided in the Methods section.

Figure 7.6 details the differences in ethanol surface coverage with varying water loading for a liquid phase adsorption at 300 °C, liquid phase adsorption at 350 °C and vapor phase adsorption at 300 °C. Based on the ideal, Langmuir model, ethanol is expected to be adsorbed at >80% of the surface sites at molar water loadings <50% for all operating conditions. All three model cases, vapor phase at 300 °C, liquid phase at 300 °C and liquid phase at 350 °C, have similar ethanol

adsorptions at low water loadings. However, there are clear differences in the relative amount of adsorbed ethanol at water loadings greater than 50 mol%. The greatest ethanol surface coverages at water loadings >50% between the three cases in **Figure 7.6** is for 300 °C vapor phase operation. Based on **Figure 7.6**, a molar water:ethanol loading of 70%, which roughly corresponds with a 33% volumetric water:ethanol loading, results in a 30% difference in ethanol surface coverage at 300 °C between liquid and vapor phase conditions. This can be attributed to the non-ideal interactions of water and ethanol, which cause a nonlinear pressure dependence of ethanol to water adsorption selectivity. In addition to the pressure and phase dependency on ethanol adsorption, the competitive adsorption Langmuir model between ethanol and water has a temperature dependence. Specifically the 70 molar percent water loading shown in **Figure 7.6** reveals a ~15% increase in ethanol surface coverage when comparing the 300 and 350 °C conditions.
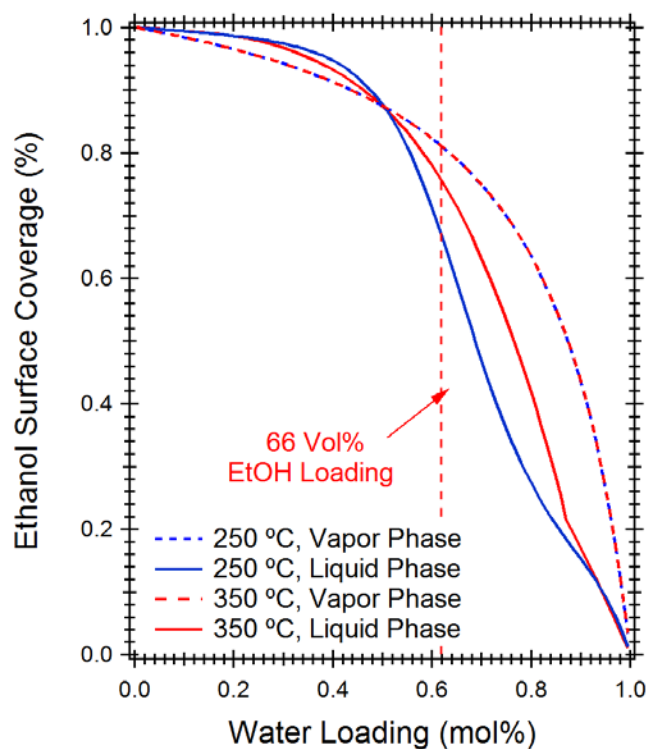
Figure 7.6: Simulated ethanol surface adsorption coverages with varying water loadings (mol%).

The results from the intrinsic activity observed in **Figure 7.4** are consistent with a competitive adsorption explanation based on the model presented in **Figure 7.6**. At low water loadings, the ethanol surface coverage based on the Langmuir model doesn't appreciably change between operating pressure and temperature, primarily having a the surface nearly saturated with ethanol. This is similar to the results shown for 100 vol% ethanol loading in the vapor and liquid phase in **Figure 7.4**, that shown similar intrinsic activities. At 66 vol% ethanol loading in the vapor phase, there is a slight increase in intrinsic activity, which is not unexpected considering the ethanol surface coverage is modelled to remain above 80% (molar loading of 61%).

However, **Figure 7.4** reveals a considerable loss in intrinsic activity at 33 vol% water loading under liquid phase conditions, a result that is consistent with the competitive adsorption model reporting a significant drop in ethanol surface coverage. The ethanol surface coverage also increases with increasing temperature at the same initial water loading, which suggests competitive adsorption of water will have less of a role on activity at higher operating temperatures. Therefore, under higher conversions, the loss in liquid phase ethanol dehydration activity could be due to multiple factors, including acid site loss and competitive adsorption of water

Conclusions

Liquid phase ethanol dehydration operation was compared to the traditional vapor phase activity with varying water loading, temperature and space velocity. After fitting the high conversion activity results to a first order kinetic model, liquid phase activity was 50% of vapor phase runs, independent of initial water loading. ZSM-5 characterization after reaction revealed similar coke formation between liquid and vapor phase runs with a loss in acid sites only for liquid phase runs performed with 66 vol% initial water loading. In contrast, ZSM-5 retained framework and acid sites under low conversion ethanol dehydration runs, but had a shift in activity with the initial

water loading. Without any water added to the feed, both liquid and vapor phase runs had identical catalytic activity. However, a decrease in activity under liquid phase operation and increase in activity under vapor phase conditions was observed under low conversion conditions. The observation was consistent with a competitive adsorption of water and ethanol on the catalyst surface. An ideal Langmuir isotherm modelling the nonideal adsorption of ethanol and water in the liquid phase revealed a preferential increase in water adsorption in the liquid phase, consistent with the observed results under low conversion conditions. The Langmuir isotherm also reveals an increase in ethanol adsorption under liquid phase operation with a 30 molar percent water loading, suggesting liquid phase operation can improve ethanol adsorption under some operating conditions.

References

1.   Morschbacker, A., *Bio-Ethanol Based Ethylene.* Polymer Reviews, 2009. **49**: p. 79-84.

2.   de Andrade Coutinho, P.L., et al., *Braskem's Ethanol to Polyethylene Process Development.* Catalytic Process Development for Renewable Materials, 2013: p. 149-165.

3.   Lin, Y. and S. Tanaka, *Ethanol fermentation from biomass resources: Current state and prospects.* Applied Microbiology and Biotechnology, 2006. **69**: p. 627-642.

4.   Goldemberg, J., *The Brazilian Biofuels Industry.* Biotechnology for Biofuels, 2008. **1**: p. 6.

5.   Briens, C., J. Piskorz, and F. Berruti, *Biomass Valorization for Fuel and Chemicals Production -- A Review.* International Journal of Chemical Reactor Engineering, 2008. **6**.

6.   Fan, D., D.J. Dai, and H.S. Wu, *Ethylene formation by catalytic dehydration of ethanol with industrial considerations.* Materials, 2013. **6**: p. 101-115.

7.   Mohsenzadeh, A., A. Zamani, and M.J. Taherzadeh, *Bioethylene Production from Ethanol: A Review and Techno-economical Evaluation*, in *ChemBioEng Reviews*. 2017. p. 75-91.

8.   Marrone, P.A., et al., *Solvation effects on kinetics of methylene chloride reactions in sub- and supercritical water: theory, experiment, and ab initio calculations.* Journal of Physical Chemistry A, 1998. **102**: p. 7013-7028.

9.   Zhao, C., et al., *Aqueous-phase hydrodeoxygenation of bio-derived phenols to cycloalkanes.* Journal of Catalysis, 2011. **280**: p. 8-16.

10.   Jaacks, V. and F.R. Mayo, *Liquid-Phase and Vapor-Phase Reactions of Ethylene with Carbon Tetrachloride.* Journal of the American Chemical Society, 1965. **87**: p. 3371-3379.

11.   Gendy, T.S., *Simulation of liquid and vapour phase xylene isomerization over deactivating H-Y-zeolite.* Journal of Chemical Technology and Biotechnology, 1998. **73**(2): p. 109-118.

12.   Llano-Restrepo, M. and Y.M. Muñoz-Muñoz, *Combined chemical and phase equilibrium for the hydration of ethylene to ethanol calculated by means of the Peng-Robinson-Stryjek-Vera equation of state and the Wong-Sandler mixing rules.* Fluid Phase Equilibria, 2011. **307**: p. 45-57.

13.   Zhang, K., et al., *Adsorption of water and ethanol in MFI-type zeolites.* Langmuir, 2012. **28**: p. 8664-8673.

14.   Taylor, J.D., J.I. Steinfeld, and J.W. Tester, *Experimental Measurement of the Rate of Methyl tert-Butyl Ether Hydrolysis in Sub- and Supercritical Water.* Industrial & Engineering Chemistry Research, 2001. **40**: p. 67-74.

15.   Taylor, J.D., *Hydrothermal Chemistry of Methylene Chloride and MTBE: Experimental Kinetics and Reaction Pathways by Hydrothermal Chemistry of Methylene Chloride and MTBE : Experimental Kinetics and Reaction Pathways by*. 2001. p. 220.

16. Phillips, C.B. and R. Datta, *Production of Ethylene from Hydrous Ethanol on H-ZSM-5 under Mild Conditions.* Industrial & Engineering Chemistry Research, 1997. **36**: p. 4466-4475.

17. Zhang, X., et al., *Comparison of four catalysts in the catalytic dehydration of ethanol to ethylene.* Microporous and Mesoporous Materials, 2008. **116**: p. 210-215.

18. Castano, P., et al., *Insights into the coke deposited on HZSM-5, H beta and HY zeolites during the cracking of polyethylene.* Applied Catalysis B-Environmental, 2011. **104**(1-2): p. 91-100.

19. Golabek, K., et al., *Ethylene formation by dehydration of ethanol over medium pore zeolites.* Spectrochim Acta A Mol Biomol Spectrosc, 2018. **192**: p. 464-472.

20. Ramasamy, K.K. and Y. Wang, *Ethanol conversion to hydrocarbons on HZSM-5: Effect of reaction conditions and Si/Al ratio on the product distributions.* Catalysis Today, 2014. **237**: p. 89-99.

21. Aguayo, A.T., et al., *Catalyst Deactivation by Coke in the Transformation of Aqueous Ethanol into Hydrocarbons. Kinetic Modeling and Acidity Deterioration of the Catalyst.* Industrial & Engineering Chemistry Research, 2002. **41**: p. 4216-4224.

22. Niwa, M., S. Sota, and N. Katada, *Strong Brønsted acid site in HZSM-5 created by mild steaming.* Catalysis Today, 2012. **185**: p. 17-24.

23. Jin, L., et al., *An improved dealumination method for adjusting acidity of HZSM-5.* Catalysis Today, 2010. **149**: p. 207-211.

24. Ong, L.H., et al., *Dealumination of HZSM-5 via steam-treatment.* Microporous and Mesoporous Materials, 2012. **164**: p. 9-20.

25. Isernia, L.F., *FTIR study of the relation, between extra-framework aluminum species and the adsorbed molecular water, and its effect on the acidity in ZSM-5 steamed zeolite.* Materials Research, 2013. **16**: p. 792-802.

Chapter 8

Conclusions and Recommendations

The objective of this study was to investigate the role of heterogeneous catalyst stability and activity for compressed aqueous phase reactions operated at the process scale. Compared to the amount of vapor phase chemistries, relatively few compressed liquid phase reactions are operated at the industrial scale. The results presented in this thesis evaluate benefits of operating in a compressed liquid phase compared to traditional vapor phase chemistries. The work presented in Chapter 3 summarizes process intensification, enthalpic and energy recovery benefits when operating in a compressed liquid phase for common biomass processing chemistries. Estimated process engineering benefits arise from significant phase dependent changes in a fluid's thermodynamic properties such as density, heat capacity, viscosity and conductivity. Process intensification improvements are the greatest between steam and compressed liquid water. Therefore, process engineering benefits using compressed liquid phase conditions are the greatest for upgrading organics that are diluted in an aqueous stream using a heterogeneous catalyst, such as those derived from biological reactant feedstocks.

Chapter 4 provides an example reaction for converting organics in a dilute aqueous feed under compressed liquid phase conditions using a heterogeneous catalyst; which is the catalytic upgrading of food waste through hydrothermal liquefaction. An estimated 1.3 billion tons is wasted globally each year, which decompose in municipal landfills leading to aquatic and air pollution.

Hydrothermal liquefaction (HTL) is a process capable of breaking down food waste into carbon rich bio-oil, bio-char and residual aqueous phases at elevated pressures. Bio-oil can be refined into transportation fuels, but organics partitioned into the HTL water phase reduce oil recovery and require costly water purification steps. Therefore, it is desirable to reduce water-soluble organic HTL products by catalytically shifting the product distribution into the oil phase. Batch HTL reactions on representative consumer food waste at 300 °C and 20.7 MPa using $CeZrO_x$ revealed an improvement in energy recovery compared to an uncatalyzed HTL reaction. To understand the role of $CeZrO_x$ in the conversion of food waste, model reactions under HTL conditions were performed using water-soluble organics with different functionalities commonly found in food waste mixtures as the reactants. From this study, it was concluded that $CeZrO_x$ promotes aldol coupling reactions that increase product molecular weight and hydrophobicity; thereby partitioning HTL oil yields by reducing water-soluble hydrocarbons.

A required underlying assumption made in comparing vapor phase chemistry to an analogous liquid phase operation in Chapter 3 is that the operating phase does not influence a reaction's chemical kinetics. This assumption is not applicable for all reactions of interest, particularly for heterogeneous catalysis where a phase change can alter solid-fluid interactions that shift thermodynamic transition states, kinetic rate limiting steps, and/or mass and heat transport phenomena. In addition to mechanistic changes when operating a reaction in a compressed liquid compared to vapor phase, changes in irreversible catalyst deactivation are also phase dependent. For example, zeolites have different extents of framework and acid site loss when treated in steam or hot liquid water. Many commonly used zeolite frameworks have little to no framework stability under hot liquid water conditions and completely dissolve at temperatures ≤ 200 °C. However, ZSM-5 was previously shown to retain its crystallinity under hot liquid water treatment

temperatures up to 200 °C. Therefore, the unique hydrothermal stability of ZSM-5 provided an opportunity to deconvolute the relationship between stability and catalytic activity under reaction temperatures commonly used for upgrading bio-based feedstocks.

The stability of the ZSM-5 framework and its acid sites were studied in Chapter 5 under dense, sub- and supercritical water conditions for 3 hours over a wide temperature range from 250 to 450 °C at 25 MPa. Accordingly, X-ray diffraction (XRD), electron microscopy, and N2 sorption indicated that the MFI framework was stable at temperatures less than 325 °C. Above this temperature, the same methods indicated surface-initiated framework amorphization, which reached a maximum rate at approximately 400 °C. The non-Arrhenius framework degradation rate was consistent with the temperature-dependence of water auto-ionization, as the maximum rate was found to be coincident with co-optimization of thermal and OH– promotion effects. Acid site densities, on the other hand, decreased monotonically with increasing treatment temperature, with treatment at the most extreme conditions (450 °C) leading to >90% decrease in the Brønsted acid site density. The results presented in Chapter 5 answer many open questions in the literature on the stability of zeolites in liquid water; and suggest new approaches for stabilizing zeolites under these aggressive conditions.

Chapter 5 reveals that after three hours of hot liquid water treatment, the framework and acid sites of ZSM-5 are largely retained up to 250 °C but will hydrolyze at reaction conditions greater than 250 °C. However, the study does not assess the kinetics of ZSM-5 acid site and framework degradation. Chapter 6 extends the current understanding of ZSM-5 HLW stability to industrial time scales by studying the framework crystallinity of ZSM-5 under elevated treatment temperatures up to 350 °C and prolonged treatment times up to ~1000 hrs. From the batch stability studies, ZSM-5 retains its framework crystallinity for up to 500 hrs of hot liquid water treatment

at treatment temperatures ≤ 200 °C and 24MPa pressures, in contrast to many other previously studied frameworks. At hot liquid water treatment temperatures ≥ 250 °C, the zeolite framework follows a first order degradation rate, which amorphizes from the crystal surface. The loss in framework and acid sites with hot liquid water treatment time and temperature reported in Chapter 5 can be considered the most aggressive conditions for an aqueous reaction, as organic within a reactant feed will protect the zeolite framework and acid sites from hydrolysis.

Chapter 7 applies the current understanding of ZSM-5 framework and acid site stability from Chapters 5 and 6 by evaluating the activity of ethanol dehydration under both high and low conversion conditions. Ethanol dehydration is typically performed in the vapor phase, so this study aims to operate in a compressed liquid phase in order to promote the process intensification benefits detailed in Chapter 3. Despite the expectations that liquid phase operation would improve the activity of ethanol when compared to vapor phase operation due to the densification of the reactant, the opposite effect was observed, with a 50% loss in activity when operated at 375 °C and 24 MPa. Zeolite characterization reveals a retained zeolite framework and similar amount of hard coke formation, but a loss in Brønsted acid sites after liquid phase operation, which may contribute to the loss in catalytic activity. Operating ethanol dehydration under low conversion conditions allows a deconvolution of water role in the intrinsic reactivity from its role in irreversible catalyst deactivation through acid site hydrolysis. The results reveal similar activity for liquid and vapor phase operation without any initial water loading. However, when ethanol dehydration is performed under low conversion conditions with an initial water loading in the feed, there is an increase in vapor phase activity but a decrease in the liquid activity. Under all low conversion reaction conditions, the framework loss, acid site loss and extent of coking was minimal, suggesting that water plays an active role in the intrinsic ethanol dehydration activity.

Competitive adsorption Langmuir model verifies a decrease amount of ethanol adsorption on an ideal surface with a compressed bulk liquid phase compared to a vapor phase, which indicates water will competitively adsorb and lower the amount of ethanol access to the active sites in a zeolite.

Appendix A

Effects of Temperature Varying Solvent Properties on ZSM-5 Degradation in Hot Liquid Water

The Supporting Information contains: 1) detailed descriptions of experimental methods; 2) X-ray diffractograms (XRD) of hot liquid water treated zeolite frameworks, 3) SEM-EDS images, 4) nitrogen adsorption isotherms and analyses; 5) analysis of microporosity, surface area, and crystallinity data to show their inter-relationships; 6) Si 2p XPS spectra of treated ZSM-5; 7) 1D ^{29}Si NMR spectra of hot liquid water treated ZSM-5; 8) 2D Al MQMAS NMR spectra; 9) pyridine IR spectra of hot liquid water treated ZSM-5 samples; 10) Kinetic analysis of literature studies on degradation of MFI and other zeolite frameworks; and 11) temperature effects on ZSM-5 degradation and silica solubility.

A.1. Detailed Experimental Protocol

A.1.1 Catalytic Packed Bed Setup

The catalytic packed bed setup used for ZSM-5 stability and activity studies consists of an AISI type 316 stainless steel Sitec tube (5.2 mm ID, 9.5mm OD) and peripheral equipment. The tube could hold approximately 0.5 grams of catalyst, and a 0.2 μm porous frit was press fit on one end of the tube to contain the zeolite powder. Both ends of the tube were pressure sealed into Sitec tees, which served as the inlet and outlet of the flow reactor. The entire assembly along with a

section of stainless steel tubing (10 m × 0.1 cm i.d) was placed inside a temperature-controlled oven (HP 5890 gas chromatogram oven). Temperatures on the tube surface and inside both the inlet and outlet tees were logged to within ±1 °C using k-type thermocouples (Omega Engineering).

A.1.2 Batch Stability Measurements

A catalytic batch reactor setup was used to evaluate the hydrothermal stability of zeolite frameworks other than ZSM-5. Zeolites were purchased from Zeolyst, including frameworks HY (CBV-760, Si/Al = 30), Hβ (CP814C, Si/Al = 19), mordenite (CBV 21A Si/Al = 10), and ferrierite (CP914C, Si/Al = 10). Each was calcined at 550 °C in air prior to use. The batch reactor setup consisted of a 300 ml AISI type 316 stainless steel Parr Reactor (Model 452HC2) and peripheral equipment. The batch reactor was loaded with 0.5 g of zeolite and 100 ml of deionized water, pressure sealed, and loaded into the reactor assembly. The reactor was initially pressurized to 2.7–10.3 MPa using N_2, which was varied to reach a pressure >25 MPa after heating. The reactor was constantly stirred with an impeller and heated to the desired temperature using an induction heater. The reactor temperature was logged to within ±1 °C using a J-type thermocouple (Omega Engineering). The total heat-up time was between 30-50 min and varied with the final temperature. The desired temperature of the zeolite and water mixture was maintained for three hours before quickly (~5 min) quenching the reaction with ice water. The reactor was then depressurized, the contents filtered to recover the zeolite, and the zeolite was dried in a 60 °C oven. The catalysts were characterized using X-ray diffraction described later in Section 1.3.

A.1.3 Catalyst Characterization

X-ray diffraction was performed using a Rigaku automatic instrument with the Bragg-Bretano theta-theta configuration. Diffractions were taken with a Cu Kα at 27.5kV and 5mA. Analysis was

performed over the range from 5-80 2θ degrees with a 0.5° step size and 1 s dwell time. Crystallinity for each sample was determined from the sum of peak areas between 22.5-25 2θ degrees, as specified by ASTM method D5758-01.[1] The degree of crystallinity of a given sample was calculated from the ratio of these integrated peak areas of the treated sample to an untreated reference.

SEM images were captured using Hitachi SU8230 scanning electron microscope with a cold field emission source. The samples were mounted on the stub holder using carbon paste. No conductive coatings were applied to the specimens so that concurrent EDS measurements could provide composition data of the actual ZSM-5 surface.

Zeolite samples for STEM characterization were crushed using a mortar and pestle. The crushed powder was placed on a 200 mesh copper grid with a holey carbon support film. Secondary electron (SE), bright field (BF), and high angle annular dark field (HAADF) images were captured with a Hitachi HF-3300 microscope operated at an accelerating voltage of 300 kV.

Gas sorption was performed using an ASIQ iQ Quantachrome Instrument to determine surface area and micropore volume. Zeolite (0.025 g) was added to a glass bulb and the sample was degassed following a temperature ramp of 2 °C min^{-1} with 15-min temperature holds at 60, 80, 100 and 120 °C before increasing to 350 °C, where the temperature was maintained for 5 hours. The analysis procedure dosed nitrogen as the adsorbate into the sample cell cooled with liquid N_2 and obtained 60 isothermal P/P_0 points ranging from 5.5×10^{-7} to 1 followed by 15 desorption points between P/P_0 of 1 to 0.1. Micropore and external surface area were determined by applying the t-plot method to model the adsorption isotherm between P/P_0 of 0.15 to 1.

DRIFTS was performed using a Thermo Nicolet Magna 560 with a SpectraTech DRIFTS cell. The DRIFT cell was loaded with ZSM-5, and then purged with N_2 for 10 minutes. The temperature

was increased in 20 °C increments at 10-15 min intervals until 100 °C, where it was held for 30 minutes before increasing in 50 °C increments until reaching 550 °C. Samples were analyzed over the range from 4000 to 600 cm^{-1}, at a resolution of 2 cm^{-1}, and an accumulation of 96 scans at 550 °C.

XPS was performed using a PHI Model 5600 MultiTechnique instrument controlled with AugerScan software. ZSM-5 samples were initially pelletized with a PIKE die kit and degassed prior to analysis. After introducing the sample, the chamber was evacuated to a pressure less than 5×10^{-9} Torr. X-rays from a monochromated Kα line at 1486.6 eV were directed towards the sample at 90° with respect to the analyzer. Survey scans were performed at 0.5 eV per step and 50 ms. Sensitivity factors of 0.193 for Al 2p and 0.283 for Si 2p were used to obtain surface Si/Al ratios, as described previously.[2]

All ^{27}Al and ^{29}Si NMR spectra were collected at 9.4 T on a Varian INOVA spectrometer, using resonance frequencies of 104.17 MHz and 79.41 MHz, respectively. ^{29}Si data were collected using a 7.5 mm double resonance Chemagnetics MAS probe with a spinning rate of 4 kHz. A one-pulse experiment with a $\pi/6$ pulse at a pulse length of 2.1 µs and recycle delay of 12 s was used. All ^{29}Si spectra were referenced to the two chemical shifts in tetrakis(trimethylsilyl)silane (9.86 ppm and 135.34 ppm).[3] ^{27}Al data were collected using a 2.5 mm double resonance Chemagnetics MAS probe with a spinning rate of 20 kHz. A one-pulse experiment with a 1.0 µs long $\pi/6$ pulse and a 1.0 s recycle delay was used for the one-dimensional ^{27}Al spectra. Triple quantum ^{27}Al MQMAS experiments were conducted with the use of FAM-I conversion pulses[4] and a selective π pulse to generate a shifted echo for the purpose of whole echo data collection. An excitation pulse of 2.1 µs and a FAM-I sequence with four pulses, each with a pulse length of 0.6 µs, were used with a radio frequency field strength of 65 kHz. The selective π pulse had a pulse length of 4.8 µs using

a radio frequency field strength of 35 kHz. The dwell time in the indirect dimension was set for rotor-synchronized data collection. Ten data points were collected in the indirect dimension. A recycle delay of 0.9 s was used for all MQMAS experiments. All ^{27}Al spectra were referenced to aqueous aluminum nitrate (0 ppm). All data were processed with the program RMN.[5] Line shape fitting of the ^{27}Al and ^{29}Si 1D MAS spectra was performed using the program DMFIT.[6]

Brønsted site densities were determined by isopropylamine (IPA, Acros, 99%) temperature programmed desorption (TPD).[7] Typically, 60-80 mg of sample was added into a 1/2 inch quartz tube between two quartz wool (Grace) end plugs. The tube was placed in an Omega furnace. The temperature of the furnace was regulated by a process controller (Love, series 16A) and monitored by a type K thermocouple (Omega). All samples were calcined under air flow (50 sccm). A ramping protocol that prevents structural changes of the zeolites due to water evaporation was followed. The cell containing the samples was ramped to 373 (2 K min^{-1}) and was held at 373 K for 30 min. The cell was further heated at 393 K at the same rate and was held at 393 K for 30 min as well. Finally, the cell was ramped to 623 K (5 K min^{-1}) and was kept at that temperature for 300 min. The cell was subsequently cooled to 423 K, and purged in dry He flow (100 sccm) for more than 90 minutes. Catalysts were then dosed with isopropylamine in He flow. After saturation of IPA on the surface, He flow (400 sccm) removed physisorbed isopropylamine. The furnace temperature was then increased to 973K (10 K min^{-1}) under He including 1% Ar serving as an internal standard. Chemisorbed isopropylamine was converted into propene and ammonia during the temperature ramp. Throughout the entire process, a mass-selective residual gas detector (Stanford Instruments RGA 100) was used to track isopropylamine (m/z=44), propylene (m/z=41) and Ar (m/z=40) in the effluent. Evolved propylene was used to calculate Brønsted site density, assuming that one molecule of isopropylamine adsorbs per Brønsted site.

Brønsted acid sites to Lewis acid sites ratio was determined using pyridine Fourier transform infrared spectroscopy (FTIR, Nicolet 6700 DTGS detector). Approximately 15 mg of sample was pressed into a 13 mm pellet in a hydraulic press. The pellet was loaded into an in situ cell, designed and built in house. Catalysts were calcined as per the procedure described in the TPD experimental section. Subsequently, the cell was cooled to 423K, and purged under dry He flow (60 sccm). The pellet was then dosed with 4 torr of pyridine (Sigma Aldrich, 99%). After the pellet was fully saturated, the cell was purged under a He flow (200 sccm) at 423K to remove physisorbed pyridine. Spectra were collected at 423 K, and Brønsted to Lewis ratios were determined by the ratio of the integrated IR bands at 1545 cm^{-1} (pyridimium ion) and 1455 cm^{-1} (pyridine) respectively, by applying the appropriate molar extinction coefficients.[8] Lewis site density was calculated from isopropylamine TPD and pyridine FTIR by the following equation: L=B/(B/L ratio).

A.2. X-Ray Diffraction (XRD) of hot liquid water treated zeolites frameworks

X-ray diffraction (XRD) characterization was used to compare retained crystallinity of different zeolite frameworks after hot liquid water treatment, as described in Section SI-1.2. **Figure A.1** shows XRD diffractograms of calcined and hydrothermally treated HY, Hß, mordenite and ferrierite zeolite frameworks. Treatment temperatures were 300, 400, and 450 °C. **Figures A.1A** and **A.1B** compare the diffractograms of calcined and treated mordenite and ferrierite. Mordenite and ferrierite undergo significant crystallinity loss (approximately 50%) after treatment at 300 °C, as indicated by the decreased areas of all crystalline peaks between 5 and 40 2θ degrees in comparison with the calcined versions. After the 400 °C treatment, the mordenite diffractogram retains most of the crystalline features observed after at 300 °C treatment, but all crystalline peaks disappear after treatment at 450 °C. Instead of crystalline peaks, the diffractogram of mordenite treated at 450 °C consists of a single broad peak centered at 21 2θ degrees, indicative of complete
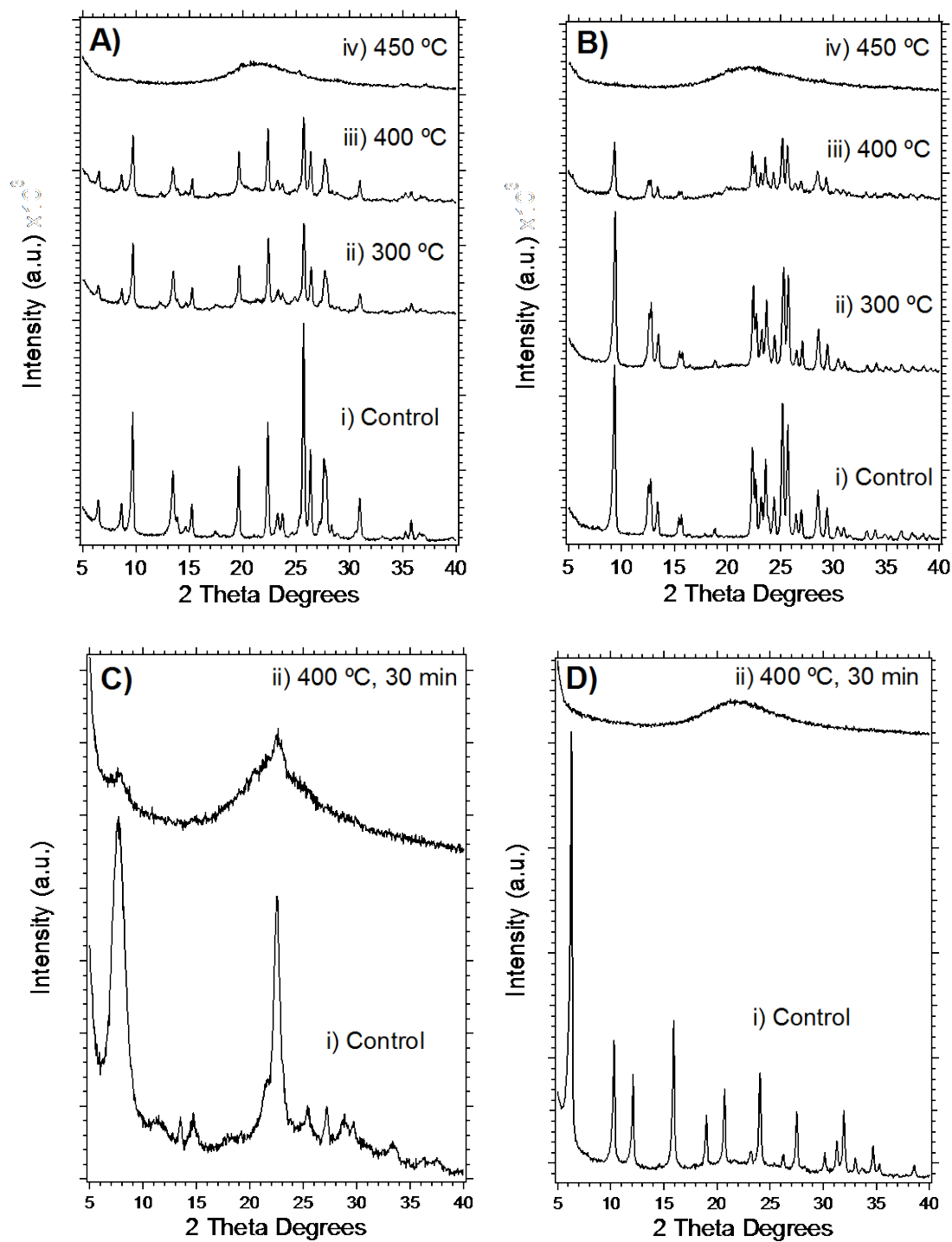
Figure A.1. XRD diffractograms of A) mordenite, B) ferrierite, C) H-Y or D) H-β zeolites when exposed to hot liquid water at varying treatment temperatures. Treatment times for A) and B) were 3 hours and in C) and D) the treatment times were 30 min, as indicated in the annotations.

amorphization. Ferrierite degradation increases with increasing temperature, again with complete dissolution observed at 450 °C. The results shown in **Figures A.1A** and **A.1B** reveal partial retention of the crystalline framework at 400 °C but complete dissolution at 450 °C.

Figure A.1C and **A.1D** contains diffractograms of calcined and hydrothermally treated H-Y and H-ß zeolite frameworks. The treatment temperature in **Figure A.1C** and **D** was 400 °C and the treatment time was 30 min. After the 30-min treatment, the H-Y and H-β diffractograms retain no evidence of crystallinity, indicative of complete dissolution. **Figure A.1** establishes ZSM-5 as the most stable of the common zeolite frameworks, extending the known data past the critical point of water.[9-11]

A.3. Scanning electron microscopy with energy dispersive x-ray spectroscopy (SEM-EDS)

EDS was used to determine if the surface features observed in the SEM images (Figure 2 in the main text) were composed of amorphous silica, amorphous alumina, or a crystalline silicate with composition similar to ZSM-5. **Figure A.2** shows representative EDS images of calcined ZSM-5 (**Figure A.2a**), ZSM-5 treated in hot liquid water at 250 °C (**Figure A.2b**), ZSM-5 treated in hot liquid water at 325 °C (**Figure A.2c**) and ZSM-5 treated in hot liquid water at 450 °C (Figure SI-2d). As expected, **Figure A.1a** shows uniform Al distribution on the surfaces of calcined ZSM-5. In contrast, the Al distribution on the surfaces of samples treated at 250 and 325 °C is non-uniform, exhibiting distinct regions of enhanced Al content (**Figures A.2b and c**). The surface Al distribution of the sample treated at 450 °C (**Figure A.2d**) is more uniform than the surfaces of ZSM-5 treated at 250 and 325 °C, lacking the regions of distinct Al enrichment. **Figure A.2** indicates that dealumination results in agglomerated alumina regions at temperatures equal to or less than 325 °C but not at 450 °C, possibly indicative of different mechanisms at the different conditions.
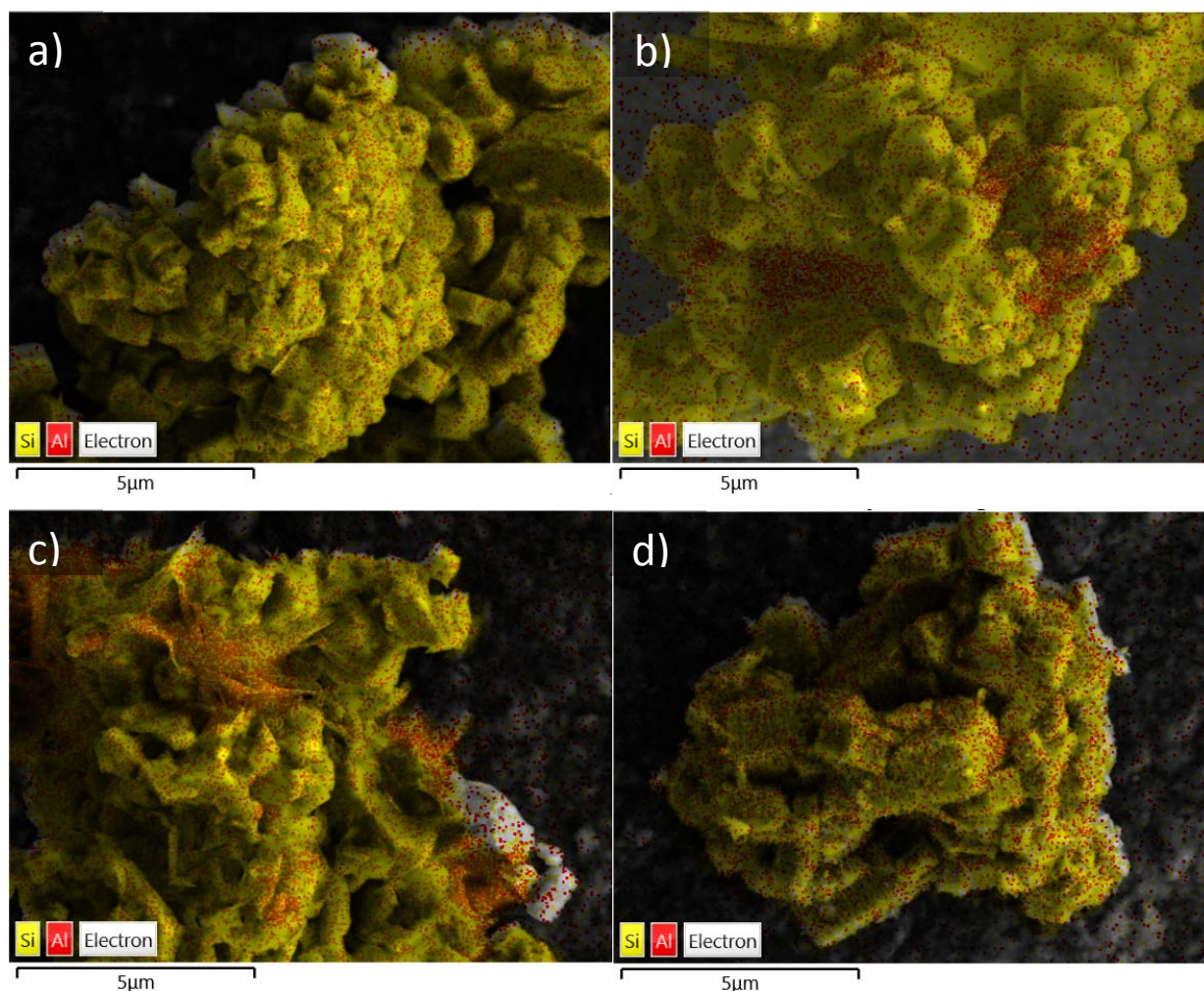
Figure A.2. SEM-EDS images of ZSM-5 samples a) untreated, b) 250 °C b) 325 °C and d) 450 °C treated samples in hot liquid water.
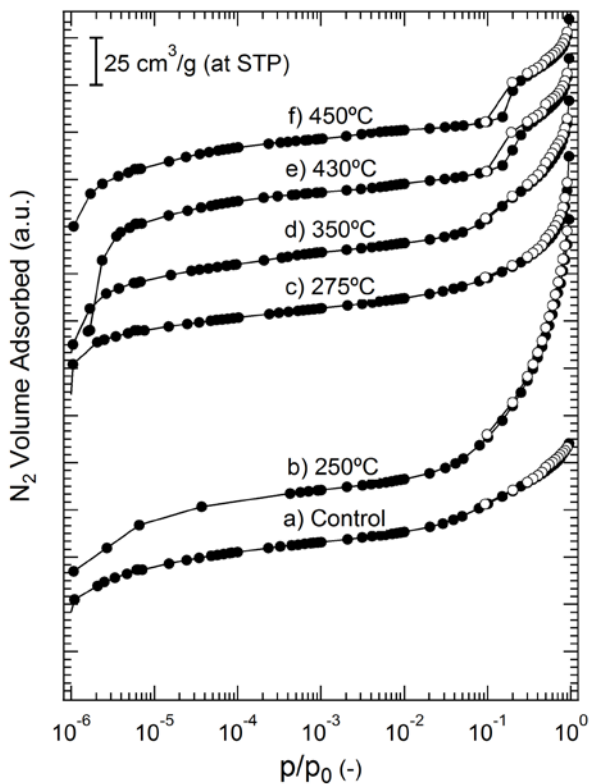
A.4. Nitrogen Sorption

Nitrogen sorption was used to investigate the effects of liquid water treatment on ZSM-5 surface area and micro/meso-porosity. Compared to STEM, nitrogen sorption is a bulk technique that accounts for the porosity of the entire sample. **Figure A.3** shows that the measured isotherms were consistent with IUPAC type II [12] characteristic of a microporous material. Nitrogen sorption isotherms of this type can be divided into 2 main regions, depending on the pressure (P/P_0). For $P/P_0 < 10^{-3}$, the isotherm is associated with gas-zeolite interactions within micropores. For $P/P_0 >$

0.1 the isotherm is associated with gas-gas molecular interactions within mesopores; in particular, curvature of the sorption isotherm for $P/P_0 > 0.1$ is attributable to mesoporosity. Qualitatively, the sorption isotherm of the parent ZSM-5 indicates that the majority of adsorption occurs in the low pressure region, with modest adsorption at $P/P_0 > 0.1$ consistent with a microporous solid lacking mesoporosity.[13] After treatment in hot liquid water, curvature in the pressure range of $P/P_0 = 0.1$-1.0 increases slightly, with evidence of minor adsorption-desorption hysteresis. A large increase of the curvature in the mesopore range has been attributed to ZSM-5 de-silication[14, 15] from alkaline treatment. The minor changes in the adsorption isotherms of treated ZSM-5 indicate that the framework remains largely microporous (>90%) with only modest mesopore formation. These observations are consistent with the STEM images shown in Figure 3.

The abundant literature on zeolite degradation under acidic and basic[15-21] conditions can provide insight on the trends observed in the N_2 sorption isotherms. Base catalysis by OH^- selectively cleaves siloxane framework bonds, leading to de-silication.[15, 17-21] Desilication of a zeolite in an alkaline medium will often initiate at internal sites[18] and propagate from hydroxyl nest defects introduced into the framework during synthesis or dealumination.[19, 20, 22, 23] The extent of zeolite desilication greatly depends on the zeolite structure and its Si/Al ratio.[24] The end result of base catalyzed desilication is increased curvature of the N_2 isotherm for $P/P_0 > 0.1$ and increased mesoporosity. This is the typical observation made of zeolites exposed to hot liquid water conditions, including H-β[25] and H-Y[26]. In contrast to base catalyzed desilication, numerous studies report that acids promote zeolite dealumination,[19-21, 24, 27-33] with minimal framework degradation. In acid solutions, dealumination occurs via a proton/hydronium catalyzed mechanism that selectively removes Al sites, forming a variety of extra-framework hydroxyaluminate complexes that impart Lewis acidity as well as mono, di and/or trivalent Al

cations.[24] The modest isotherm changes observed for liquid-treated ZSM-5 closely mirror those reported for acid-treated zeolites,[14, 17, 34] Dealumination of ZSM-5 could be consistent with the observation of Gardner et al.[35] that exposure of ZSM-5 to liquid water at 150 °C results in increased concentration of Al species in the water solution.

The final feature present in the gas sorption isotherms that merits discussion is the substep observed at approximately $P/P_0 = 0.1$ for ZSM-5 treated in liquid water at 430 and 450 °C. Minor qualitative differences were present in the isotherms of treated ZSM-5, specifically a minor change in the curvature of the isotherm in the mesopore region, which is consistent with retention of a structure dominated by micropores, and a minor substep in samples treated at 430 and 450 °C; the substep has sometimes been attributed to dealumination.[34, 36] Saito et al.[36] reported that a step in the N_2 isotherm appears and becomes more prominent as the Si/Al ratio of ZSM-5 increases. They attributed the observed phenomena to a fluid to solid transition of N_2 adsorbate.[36] The substep is less pronounced when aluminum is incorporated into the framework, which contributes electrostatic effects that cause surface energy heterogeneity that dampens the substep.[36] More specifically, Triantafillidis et al.[34] identified a similar substep for ZSM-5 with a Si/Al ratio >1000 and in ZSM-5 with an initial ratio Si/Al of 26.5 that was steamed at 790 °C for 6 hours to dealuminate the framework. In contrast, Triantafillidis et al.[34] did not observe a sub-step for ZSM-5 with Si/Al =27. As with the previous study,[34] the parent ZSM-5 (Si/Al = 38) did not exhibit a sub-step, whereas the liquid treated samples do. As with the other features of the N_2 adsorption curve and some of the features of the XRD spectra, the presence of a sub-step in the treated samples is therefore consistent with dealumination.

Figure A.3. H-ZSM5 nitrogen sorption isotherms for a) untreated, b) 250 °C treated, c) 275 °C treated, d) 350 °C treated, e) 430 °C treated, and f) 450 °C treated samples in hot liquid water

A.5. Analysis of Crystallinity and Textural Properties

The main text provides evidence of changes to ZSM-5 crystallinity and textural properties during exposure to HLW and SCW. Inter-comparison of ZSM-5 crystallinity, surface area, and pore volume reveals a complex relationship between framework and surface area stability of treated ZSM-5. **Figure A.4** plots surface area determined from N_2 sorption as a function of measured crystallinity. Total surface area, external surface area, and micropore area are all plotted as separate traces, and marker size are both labeled and rated to treatment temperature. Interestingly, in all cases, the relationship between crystallinity and surface area is complicated and non-monotonic. As a general trend, modest decreases in crystallinity (2-5%) lead to increases in surface area. Crystallinity decreases of 5-10% result in much larger decreases in surface area, ranging from 10-

40%. For further decreases in crystallinity of more than 10% the surface area remains nearly constant at the values obtained for 5-10% decreases in crystallinity. Lastly, the effect of temperature is complex, with all of the trends exhibiting non-monotonic relationships with temperature. These data help show the complexity of the changes in surface area and crystallinity of HLW and SCW treated ZSM-5.
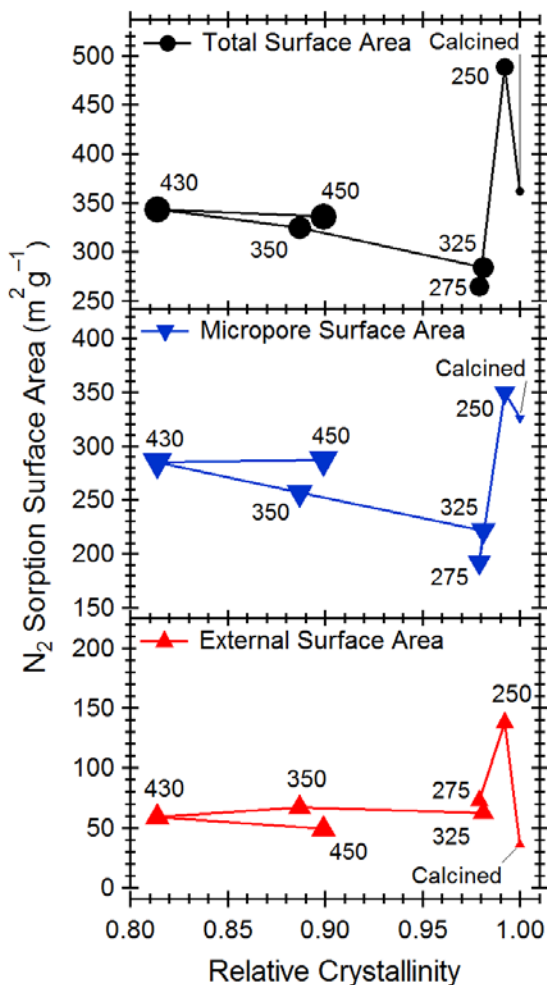
Figure A.4. Comparison of textural properties relative to the degree of crystallinity of hot liquid water treated ZSM-5. Textural properties are calculated from N_2 isotherms, including micropore area (blue triangle), external surface area (red triangle) and total surface area (black circle). Relative crystallinity is obtained based on XRD diffractograms. Marker size is rated to treatment temperature. Untreated ZSM5 samples are denoted with a star point and are labeled.

A.6. Si 2p XPS spectra

The main text provides Al XPS spectra obtained from analysis of treated and untreated ZSM-5 samples. Figure SI-5 provides similar spectra for the Si 2p band, showing that – unlike the Al band intensity which increases by more than an order of magnitude after treatment – the Si band intensity increases by approximately 30%. The data shown in Figure SI-5 where then used in conjunction with Figure 5 and known sensitivity factors[2] to determine the Si/Al ratios quoted in the text.
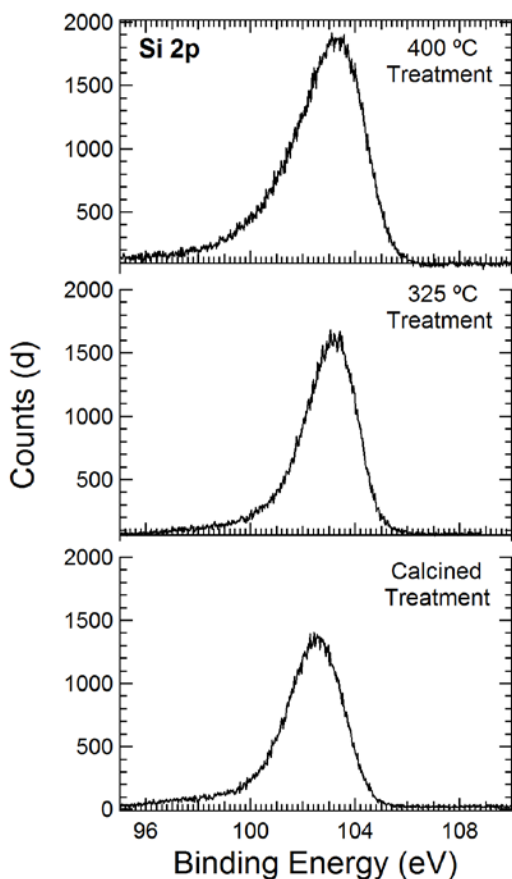

Figure A.5: Si 2p XPS spectra of H-ZSM5 treated for untreated, 325 °C treated, and 400 °C treated samples in hot liquid water.

A.7. ^{29}Si NMR

^{29}Si NMR was used to determine elemental connectivity and coordination of the silicon atoms present in ZSM-5. **Figure A.6** shows ^{29}Si NMR spectra fitted with Gaussian peaks for both ZSM-5 calcined powders and treated in hot liquid water. Considering first the calcined sample (**Figure A.6a**), the spectrum is fit with three distinct Gaussian curves with chemical shifts ($^{Si}\delta$) located at −116, −112 and −107 ppm. Peaks located at −116 and −112 ppm are assigned to Si atoms with 4 Si neighbors in their second coordination sphere (Q_4 sites), while the −107 ppm peak is assigned to Si atoms with 3 Si neighbors and either an Al atom or hydroxyl group in its second coordination sphere (Q_3 sites).[37]

^{29}Si NMR of the treated samples are consistent with dealumination inferred from DRIFTS and XPS analysis. Figures SI-6b-d show ^{29}Si NMR spectra of the treated samples. Focusing first on qualitative features, the ^{29}Si NMR spectrum of ZSM-5 treated at 250 °C (**Figure A.6b**) indicates only modest changes relative to the calcined sample, with a minor increase of the intensity of the Q_4 band at −116 ppm. The minor changes observed in the ^{29}Si NMR spectrum of ZSM-5 treated at 250 °C relative to the calcined version are consistent with the stability of the sample at these conditions indicated by XRD and microscopy. The intensity the Q_3 peak decreases after treatment at 325 °C and the peaks associated with Q_4 sites narrow (**Figure A.6c**). Narrowing of Q_4 peaks has been reported in studies of steam dealumination ZSM-5.[28, 38] Peaks in the ^{29}Si NMR spectra of ZSM-5 treated at 400 °C (**Figure A.6d**) are increasingly narrow; in fact, the spectra of ZSM-5 treated at 400 and 450 °C resemble silicalite,[38] suggesting near quantitative removal of Al atoms from the framework. Lastly, a new peak located at −92 ppm appears in the spectra of samples treated at 400 and 450 °C. This peak is attributed to Q_2 sites associated with Al-O-Si-O-Al bonding configuration with each aluminum in a tetrahedral coordination.[38] Although tetrahedral

aluminum sites are typically associated with framework aluminum, Ong et al.[31] has identified possible tetrahedral configurations for EFAL within steamed ZSM-5 that associate near framework aluminum sites. Again, all indications from the ^{29}Si NMR support dealumination of ZSM-5 under hot liquid water conditions.
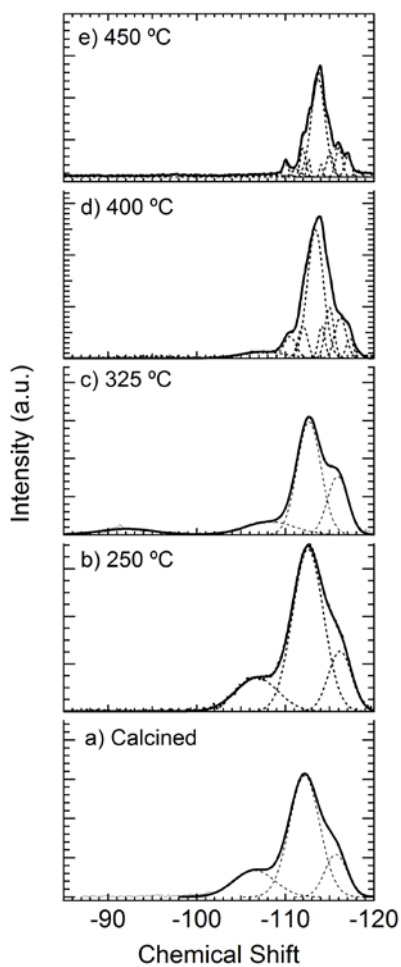
Figure A.6. 1-D ^{29}Si NMR spectra for a) untreated, b) 250 °C treated c) 325 °C treated, d) 400 °C treated, and e) 450 °C treated samples in hot liquid water.

A.8. 2D Al MQMAS

The ^{27}Al NMR spectra shown in Figure 6 contains peaks that can be assigned to both tetrahedrally coordinated framework aluminum and octahedrally coordinated extra-framework aluminum species. In addition to these Al species, the spectra contain a contribution from the aluminum rotor, which is centered at 10 ppm that does not arise from the sample itself. The rotor peak is more easily observable as the 2D Al MQMAS spectra shown in **Figure A.7**. The peak centered at F2 = 10 ppm is distinctly separate from the tetrahedral and octahedral oriented species in all 5 2D Al MQMAS plots (SI-7a to e). The untreated sample plotted in **Figure A.7a** shows that the framework aluminum peak centered at F2 = 50 ppm is the main species for ZSM-5 and the contribution of the rotor is expectedly small. Upon increasing hot liquid water treatment temperatures, the relative rotor contribution increases as ZSM-5 dealuminates and becomes relatively more siliceous. The rotor contribution in **Figure A.7e** (ZSM-5 treated at 450 °C) is the primary feature of the MQMAS spectra only as this sample lacks both framework and extra-framework aluminum species.
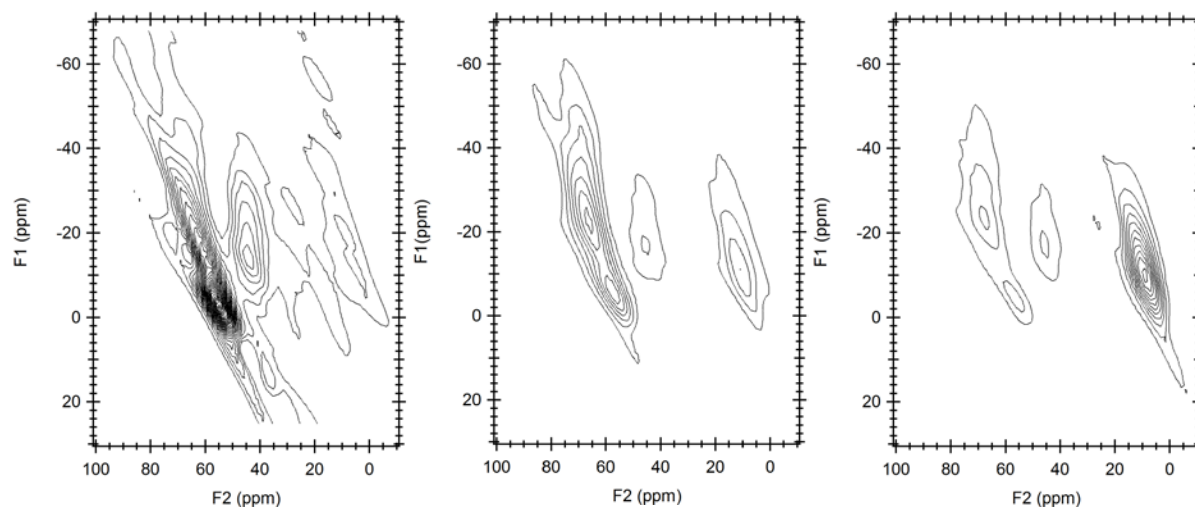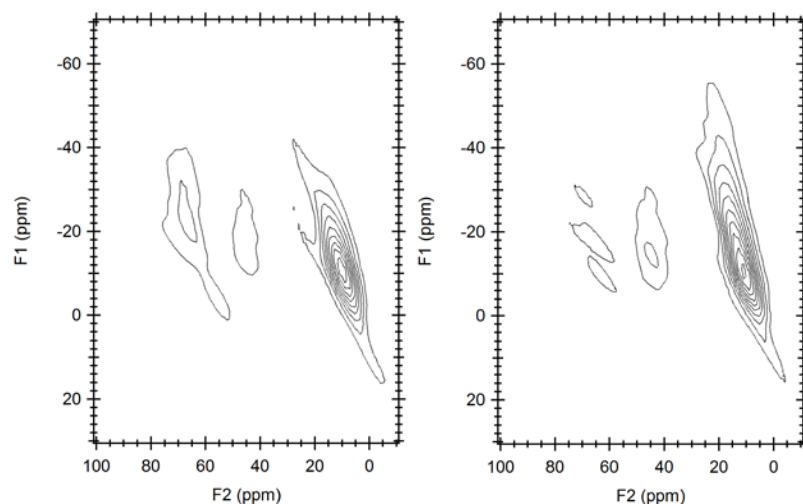
Figure A.7: 2D Al NMR: 2-D ^{27}Al NMR spectra for a) Calcined, b) 250°C treated, c) 325°C treated, d) 400°C and e) 450°C treated samples in hot liquid water

A.9. Pyridine Infrared Spectroscopy

The stacked pyridine IR spectra displayed in **Figure A.8** were performed to compare the relative amount of Bronsted acid sites (BAS) to Lewis acid sites (LAS) of calcined and HLW treated ZSM-5 samples. The FTIR spectra of pyridine-adsorbed ZSM-5 are similar to others reported in the literature,[39-41] with no major qualitative differences between calcined ZSM-5 and materials treated in liquid water. Bands associated with Brønsted and Lewis acids were integrated to estimate the ratio of the two acid types in ZSM-5. Specifically, the peak areas for stretching modes located at 1450 cm^{-1} and 1545 cm^{-1} are used to quantify the relative amount of LAS and BAS respectively and obtain a Brønsted to Lewis ratio (B/L ratio). The B/L ratio of calcined ZSM-5 is calculated to be 9.8; an expected result for synthesized ZSM-5 which is predominately Bronsted acidic. Upon HLW treatment at 350 °C, the B/L decreases to 3.8, which is likely due to contibuting factors of BAS loss and the corresponding formation of LAS species such as extra framework alumina. When

ZSM-5 is treated in 450 °C HLW, the B/L ratio continues to decrease, consistent with a continual loss in BAS with increasing temperature. Unlike ZSM-5 observed changes in framework degradation that vary with temperature dependant solvent effects, BAS density decreases monotonically with increasing temperature. The analysis shown in **Figure A.8** was used for the quantitative data provided in Table 2 in the main text.
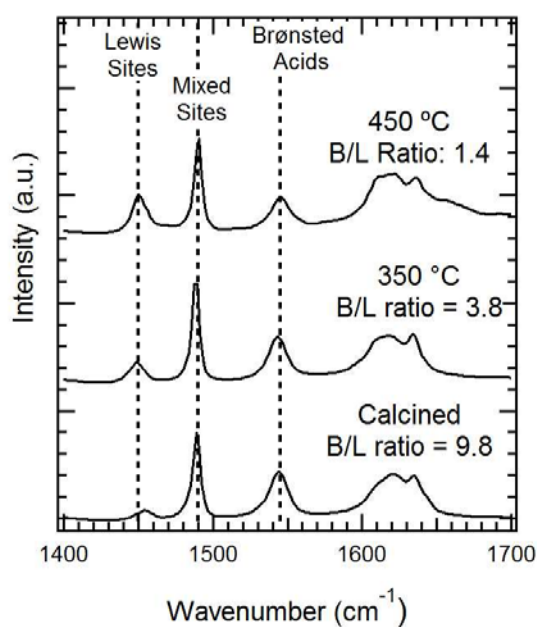

Figure A.8. Pyridine IR Spectra of untreated H-ZSM5 samples compared to samples treated in either 350 or 450 °C hot liquid water conditions. Calculated Brønsted to Lewis acid ratios (B/L ratio) are included in the figure.

A.10. Kinetic analysis of literature studies on degradation of MFI and other zeolite frameworks

Ravenelle et al.[11] obtained temporal data on the crystallinity loss of HY after hot liquid water treatment that follows a first-order degradation kinetics. This can be shown by transforming the temporal data obtained from their study into a first-order rate analysis:

$$ln\left[\frac{CI(t)}{CI(t=0)}\right] = -k_{app}t \qquad (1)$$

The degree of crystallinity data, CI, provided in Table SI-1 were fitted to estimate the apparent rate desilication rate constant, k_{app}, at different temperatures. The plot of the natural log of relative CI over time for HY from Ravenelle et al.[11] is provided in Figure SI-9. The data in Figure SI-9 has a strong linear fit, confirming a first order framework degradation rate.
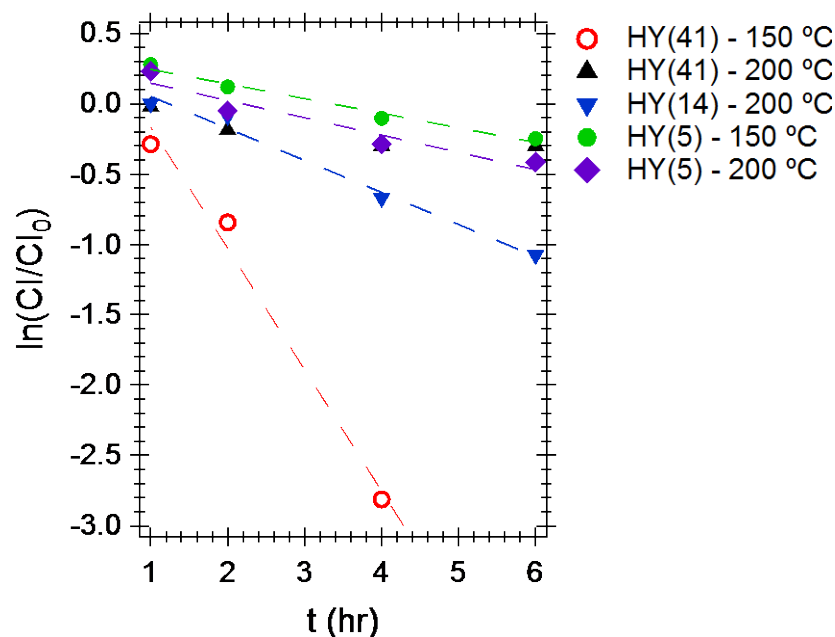
Figure A.9. First order rate plot of HY degradation under hot liquid water conditions (natural log of the relative retained crystallinity (CI/CI$_0$) versus time). Data points are denoted in the legend with their corresponding Si/Al ratios in parenthesis followed by treatment temperature.

Based on the first order degradation rate for HY, a similar framework breakdown is applied to other previous studies. Using Equation 1, the rate constants are calculated for each stability

study either based on the XRD diffractogram or reported relative crystallinity data. The calculated

rate constant is then used to calculate an expected relative crystallinity after 10 hrs of water

treatment using Equation 1. These calculations are included in Table SI-1 and plotted in Figure 8

of the main text.

Table A.1. Framework crystallinity results after hot liquid water treatment from this and previous studies on FAU, BEA, FER, MOR and MFI zeolites. 10 hr adjusted CI/CI_0 was calculated assuming first order degradation kinetics.

Author	Ravenelle et al.							
Material(Si/Al ratio) - Temperature	FAU(14) - 150				FAU(14) - 200			
Treatment Time (hr)	1	2	4	6	1	2	4	6
Relative Crystallinity (CI/CI_0 - %)	98.0	83.0	74.0	74.0	100.0	91.5	51.0	34.0
Calculated rate constant (hr^{-1})	0.0526				0.228			
10 hr adjusted CI/CI_0 (%)	59.1				10.2			

Author	Ravenelle et al. (cont.)							
Material(Si/Al ratio) - Temperature	FAU(5) - 150				FAU(5) - 200			
Treatment Time (hr)	1	2	4	6	1	2	4	6
Relative Crystallinity (CI/CI_0)	132	112.5	90	78	126	95	75	66
Calculated rate constant (hr^{-1})	0.104				0.123			
10 hr adjusted CI/CI_0 (%)	35.3				29.2			

Author	Prodinger et al.	Vjunov et al.		Ennaert et al.
Material(Si/Al ratio) - Temperature	BEA(14) - 160	BEA(150) - 160	BEA(25) - 160	HY(25) - 190
Treatment Time (hr)		48		24
Relative Crystallinity (CI/CI_0)	80	25	5	45
Calculated rate Constant (hr^{-1})	0.0046	0.029	0.062	0.033
10 hr adjusted CI/CI_0 (%)	95.5	74.9	53.6	71.7

Author	Ennaert et al. (cont.)			
Material(Si/Al ratio) - Temperature	USY(19) - 190	USY(16) - 190	USY(9) - 190	USY(6) - 190
Treatment Time (hr)		24		
Relative Crystallinity (CI/CI_0)	88	33	17	14
Calculated rate constant (hr^{-1})	0.0053	0.046	0.074	0.082
10 hr adjusted CI/CI_0 (%)	94.8	63.0	47.8	44.1

Author	This Study			
Material(Si/Al ratio) - Temperature	MOR(10) - 300	MOR(10) - 400	MOR(10) - 450	FAU(30) - 400
Treatment Time (hr)		3		0.5
Relative Crystallinity (CI/CI_0)	88.1	75	56.1	64.75
Calculated rate constant (hr^{-1})	0.042	0.095	0.19	0.87
10 hr adjusted CI/CI_0 (%)	65.6	38.3	14.6	0.017

Author	This Study (cont.)			
Material(Si/Al ratio) - Temperature	FER(10) - 300	FER(10) - 400	FER(10) - 450	BEA(19) - 400
Treatment Time (hr)		3		0.5
Relative Crystallinity (CI/CI$_0$)	94.4	76	60.2	56.7
Calculated rate constant (hr^{-1})	0.019	0.91	0.17	1.13
10 hr adjusted CI/CI$_0$ (%)	82.6	40.1	18.4	0.0012

A.11. Temperature effects on silica solubility

Zeolite solubility in subcritical and supercritical water could be a factor in observed zeolite decrystallization rates. The STEM images (**Figure 5.3** in the main text) suggest exfoliation of an external ZSM-5 amorphous silica layer after hydrothermal treatments of 325 and 400 °C but not after treatment at 450 °C. The loss of the amorphous overlayer after hot liquid water treatment at temperatures of $325 \leq T \leq 400$ °C is consistent with the known effects of temperature on the solubility of amorphous silica in liquid water.

While zeolite solubility is not well defined *per se*, water solubility of silica is highly temperature dependent and varies non-linearly with temperature. **Figure A.10** contains plots of aqueous solubility of amorphous silica at varying temperatures and pressures, using a correlation reported by Karásek et al,[42] which used thermodynamic correlations based on work by Dloejš and Manning.[43] The horizontal axis in **Figure A.10** is the reduced temperature, i.e., the thermodynamic temperature divided by the critical temperature of pure water. The isobaric solubility lines of amorphous silica at 6 and 12 MPa in **Figure A.10** terminate when the temperature equals the vaporization temperature.
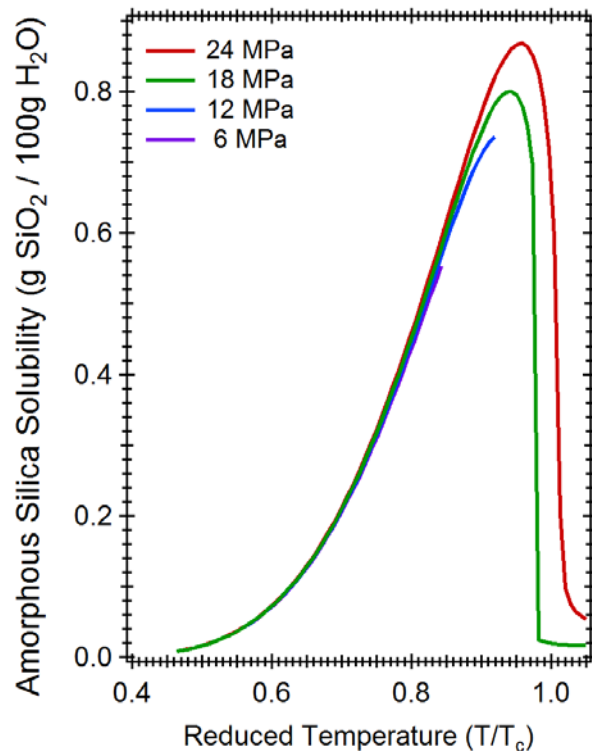
Figure A.10. Calculated amorphous silica solubilities in water at 6, 12, 18 and 24 MPa and varying water temperatures. Solubility data calculation are based on a thermodynamic model from Karásek et al.[43]

Figure A.10 reveals significant changes in amorphous silica solubility with water temperature, with only minor differences with water pressure between 6 and 24 MPa. In all cases, the solubility exhibits a maximum at temperatures less than the critical point, and the maximum solubility is at least 10 times greater than at ambient conditions. Interestingly, silica solubility at temperatures greater than the critical temperature is only about 2 times greater than the ambient value. Retention of an amorphous over layer at supercritical conditions but not at sub-critical conditions is consistent with the temperature variability of silica solubility as shown in **Figure A.10** and also the crystallinity retention behavior shown in **Figure 5.1**, in the main text.

The temperature dependence of silica solubility roughly parallels experimental measurements of zeolite degradation. However, if the temperature dependence of zeolite degradation is dominated by the thermodynamic driving force, similar behavior would be expected for all frameworks. Since this is not observed, instead, the temperature dependent silica solubility may explain the persistence of the amorphous silica overlayer at temperatures greater than 400 °C but not at temperatures less than 400 °C.

References

1.   ASTM, *Standard Test Method for Determination of Relative Crystallinity of Zeolite ZSM-5 by X-Ray Diffraction.* ASTM International: D4758-01, 2015. **05**: p. 3-5.

2.   Wagner, C.D., et al., *Empirical atomic sensitivity factors for quantitative analysis by electron spectroscopy for chemical analysis.* Surface and Interface Analysis, 1981. **3**: p. 211-225.

3.   Aliev, A.E., K.D.M. Harris, and D.C. Apperley, *Natural abundance high-resolution solid state 2H NMR spectroscopy.* Chemical Physics Letters, 1994. **226**: p. 193-198.

4.   Madhu, P.K., et al., *Sensitivity enhancement of the MQMAS NMR experiment by fast amplitude modulation of the pulses.* Chemical Physics Letters, 1999. **307**: p. 41-47.

5.   Grandinetti, P., *RMN, Version 1.3.0; The Ohio State University: Columbus, OH,.* 2005, The Ohio State University, Columbus.

6.   Massiot, D., et al., *Modelling one- and two-dimensional solid-state NMR spectra.* Magnetic Resonance in Chemistry, 2002. **40**: p. 70-76.

7.   Tittensor, J.G., R.J. Gorte, and D.M. Chapman, *Isopropylamine adsorption for the characterization of acid sites in silica-alumina catalysts.* Journal of Catalysis, 1992. **138**: p. 714-720.

8.   Emeis, C.A., *Determination of Integrated Molar Extinction Coefficients for Infrared Absorption Bands of Pyridine Adsorbed on Solid Acid Catalysts.* Journal of Catalysis, 1993. **141**: p. 347-354.

9.   Lutz, W., et al., *Investigation and modeling of the hydrothermal stability of technically relevant zeolites.* Adsorption, 2005. **11**: p. 405-413.

10.   Vjunov, A., et al., *Impact of aqueous medium on zeolite framework integrity.* Chemistry of Materials, 2015. **27**: p. 3533-3545.

11.   Ravenelle, R.M., et al., *Stability of zeolites in hot liquid water.* Journal of Physical Chemistry C, 2010. **114**: p. 19582-19595.

12.   Donohue, M.D. and G.L. Aranovich, *Classification of Gibbs adsorption isotherms.* Advances in Colloid and Interface Science, 1998. **76**: p. 137-152.

13.   Groen, J.C., L.A.A. Peffer, and J. Pérez-Ramírez, *Pore size determination in modified micro- and mesoporous materials. Pitfalls and limitations in gas adsorption data analysis.* Microporous and Mesoporous Materials, 2003. **60**: p. 1-17.

14.   You, S.J. and E.D. Park, *Effects of dealumination and desilication of H-ZSM-5 on xylose dehydration.* Microporous and Mesoporous Materials, 2014. **186**: p. 121-129.

15.   Groen, J.C., et al., *Mesoporosity development in ZSM-5 zeolite upon optimized desilication conditions in alkaline medium.* Colloids and Surfaces A: Physicochemical and Engineering Aspects, 2004. **241**: p. 53-58.

16. Fodor, D., et al., *Differences between individual ZSM-5 crystals in forming hollow single crystals and mesopores during base leaching.* Chemistry - A European Journal, 2015. **21**: p. 6272-6277.

17. Groen, J.C., et al., *Optimal aluminum-assisted mesoporosity development in MFI zeolites by desilication.* Journal of Physical Chemistry B, 2004. **108**: p. 13062-13065.

18. Verboekend, D. and J. Pérez-Ramírez, *Design of hierarchical zeolite catalysts by desilication.* Catalysis Science & Technology, 2011. **1**: p. 879.

19. Groen, J.C., et al., *Mechanism of hierarchical porosity development in MFI zeolites by desilication: The role of aluminium as a pore-directing agent.* Chemistry - A European Journal, 2005. **11**: p. 4983-4994.

20. Groen, J.C., J.A. Moulijn, and J. Pérez-Ramírez, *Decoupling mesoporosity formation and acidity modification in ZSM-5 zeolites by sequential desilication-dealumination.* Microporous and Mesoporous Materials, 2005. **87**: p. 153-161.

21. van Donk, S., et al., *Generation, Characterization, and Impact of Mesopores in Zeolite Catalysts.* Catalysis Reviews, 2003. **45**: p. 297-319.

22. Zhang, L., et al., *Factors that Determine Zeolite Stability in Hot Liquid Water.* Journal of the American Chemical Society, 2015. **137**: p. 11810-11819.

23. Bonilla, A., D. Baudouin, and J. Pérez-Ramírez, *Desilication of ferrierite zeolite for porosity generation and improved effectiveness in polyethylene pyrolysis.* Journal of Catalysis, 2009. **265**: p. 170-180.

24. Silaghi, M.C., C. Chizallet, and P. Raybaud, *Challenges on molecular aspects of dealumination and desilication of zeolites.* Microporous and Mesoporous Materials, 2014. **191**: p. 82-96.

25.   Prodinger, S., et al., *Improving Stability of Zeolites in Aqueous Phase via Selective Removal of Structural Defects.* Journal of the American Chemical Society, 2016: p. jacs.5b12785.

26.   Zapata, P.A., et al., *Silylated hydrophobic zeolites with enhanced tolerance to hot liquid water.* Journal of Catalysis, 2013. **308**: p. 82-97.

27.   Maier, S.M., A. Jentys, and J.A. Lercher, *Steaming of zeolite BEA and its effect on acidity: A comparative NMR and IR spectroscopic study.* Journal of Physical Chemistry C, 2011. **115**: p. 8005-8013.

28.   Niwa, M., S. Sota, and N. Katada, *Strong Brønsted acid site in HZSM-5 created by mild steaming.* Catalysis Today, 2012. **185**: p. 17-24.

29.   Beyerlein, R.a., et al., *Effect of steaming on the defect structure and acid catalysis of protonated zeolites.* Topics in Catalysis, 1997. **4**: p. 27-42.

30.   Nielsen, M., et al., *Kinetics of Zeolite Dealumination: Insights from H-SSZ-13.* ACS Catalysis, 2015. **5**: p. 7131-7139.

31.   Ong, L.H., et al., *Dealumination of HZSM-5 via steam-treatment.* Microporous and Mesoporous Materials, 2012. **164**: p. 9-20.

32.   Triantafillidis, C.S., A.G. Vlessidis, and N.P. Evmiridis, *Dealuminated H−Y Zeolites: Influence of the Degree and the Type of Dealumination Method on the Structural and Acidic Characteristics of H−Y Zeolites.* Industrial & Engineering Chemistry Research, 2000. **39**: p. 307-319.

33.   Masuda, T., et al., *Changes in catalytic activity of MFI-type zeolites caused by dealumination in a steam atmosphere.* Applied Catalysis A: General, 1998. **172**: p. 73-83.

34.   Triantafillidis, C.S., et al., *Effect of the degree and type of the dealumination method on the structural, compositional and acidic characteristics of H-ZSM-5 zeolites.* Microporous and Mesoporous Materials, 2001. **47**: p. 369-388.

35.   Gardner, D.W., et al., *Insights into the Hydrothermal Stability of ZSM-5 under Relevant Biomass Conversion Reaction Conditions.* ACS Catalysis, 2015. **5**: p. 4418-4422.

36.   Saito, A. and H.C. Foley, *High-resolution nitrogen and argon adsorption on ZSM-5 zeolites: effects of cation exchange and Si Al ratio.* Microporous Materials, 1995. **3**: p. 543-556.

37.   Maijanen, A., E. Derouane, and J. Nagy, *FT-IR and solid-state NMR investigation of surface hydroxyl groups on dealuminated ZSM-5.* Applied Surface Science, 1994: p. 204-212.

38.   Fyfe, C.a., G.C. Gobbi, and G.J. Kennedy, *Investigation of the conversion (dealumination) of ZSM-5 into silicalite by high-resolution solid-state 29Si and 27Al MAS NMR spectroscopy.* Journal of Physical Chemistry, 1984. **88**: p. 3248-3253.

39.   Rahimi, N. and R. Karimzadeh, *Catalytic cracking of hydrocarbons over modified ZSM-5 zeolites to produce light olefins: A review.* Applied Catalysis A: General, 2011. **398**: p. 1-17.

40.   Serrano, D.P., et al., *Influence of the calcination treatment on the catalytic properties of hierarchical ZSM-5.* Catalysis Today, 2012. **179**: p. 91-101.

41.   Jin, F. and Y. Li, *A FTIR and TPD examination of the distributive properties of acid sites on ZSM-5 zeolite with pyridine as a probe molecule.* Catalysis Today, 2009. **145**: p. 101-107.

42.   Karásek, P., et al., *Solubility of fused silica in sub- and supercritical water: Estimation from a thermodynamic model.* Journal of Supercritical Fluids, 2013. **83**: p. 72-77.

43.   Dolejš, D. and C.E. Manning, *Thermodynamic Model for Mineral Solubility in Aqueous Fluids: Theory, Calibration and Application to Model Fluid-Flow Systems.* Frontiers in Geofluids, 2011: p. 20-40.

Appendix B

Thermal and Temporal Effects on ZSM-5 Framework and Acid Site Stability under Hot Liquid Water Conditions

B.1 XRD Diffractogram
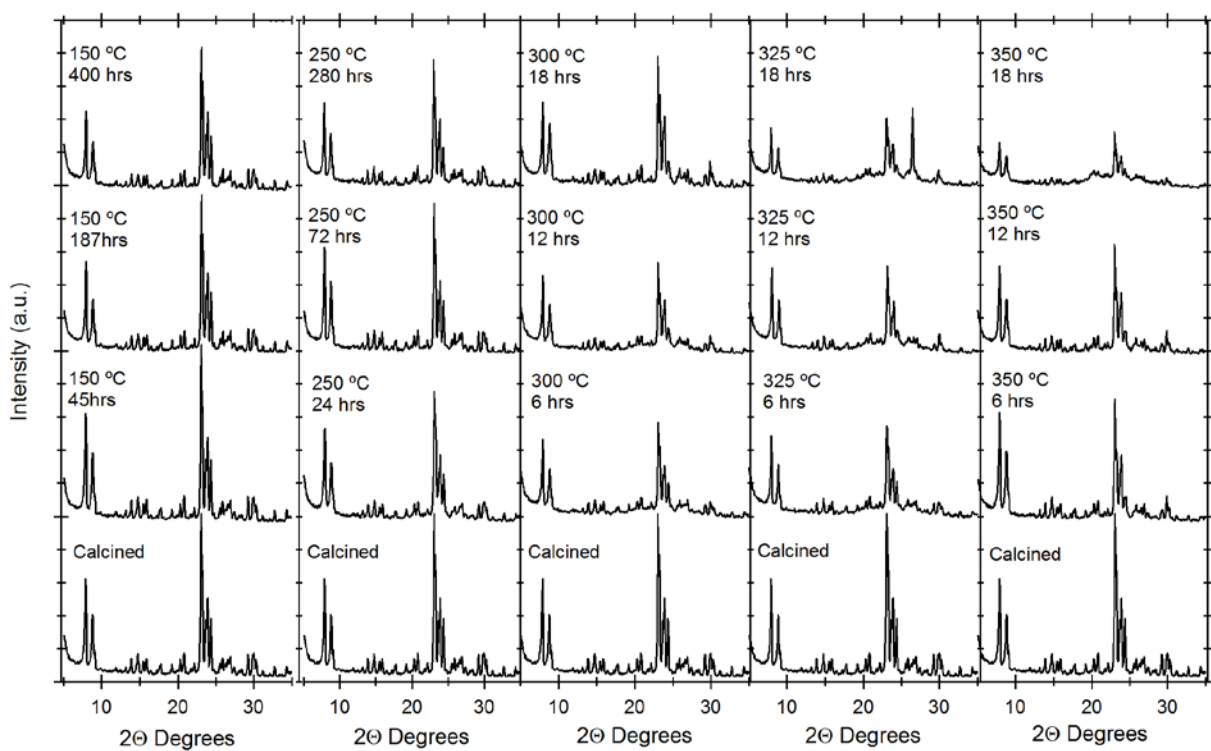
Figure B.1. XRD diffractograms of ZSM-5 samples treated in HLW conditions in a batch reactor for 6 – 400 hrs and 150 – 350 °C. treatment time and temperatures are denoted in each individual diffractogram

Figure B1 displays the XRD diffractogram of ZSM-5 samples treated in HLW conditions. With increasing treatment time and temperature, the peaks associate with bulk crystallinity between 22.5 and 25 2θ degrees decrease in intensity, consistent with a loss in crystallinity. The relative area of these peaks is related to an untreated ZSM-5 sample and used to calculate the degree of crystallinity used in Figure 6.1 of the main text.

B.2 N$_2$ sorption analysis - t-plot method

Table B.1 lists the micro/mesopore surface area and pore volumes for both untreated and treated ZSM-5 samples. Untreated ZSM-5 has a micropore and external surface area of 322 and 39 m^2 g^{-1}, respectively. Minor changes are observed in the micropore area and micropore volume after 400 hrs of 150 °C HLW treatment. Interestingly, the micropore to mesopore volume ratio (V_{micro}/V_{meso}) of untreated ZSM-5 decreased 3.0 to 1.8 for 400 hr treated ZSM-5 at 150 °C, attributable to the slight increase in external surface area and mesopore volume. Similarly to 150 °C treatment, ZSM-5 treated at 250 °C retains microporosity after 280 hrs, increases in external surface area and leads to a 60% loss in V_{micro}/V_{meso} ratio. Textural data extracted from N$_2$ isotherms of 150 °C and 250 °C are consistent with largely retained crystallinity observed from XRD analysis, with changes primarily occurring in the mesopore region.

Analysis of N$_2$ isotherms for ZSM-5 samples treated at HLW temperatures > 250 °C show more signs of framework degradation. Unlike samples treated at T ≤ 250 °C, samples treated at increased temperatures have a continual loss of micropore area and increase in external surface area with prolonged treatment times. ZSM-5 treated at 300 °C retained microporosity after 12 hours but dropped to a micropore surface area of 251 m^2 g^{-1} after 18 hours of HLW treatment. A similar drop in microporosity occurs at increased HLW treatment temperatures and shorter treatment times,

reaching micropore surface areas of 330 and 254 $m^2 g^{-1}$ after 6 hrs at 325 and 350 °C, respectively. In conjunction with a decrease in micropore area, a significant increase in external surface area of up to 58% is observed for all characterized treatment times at $T > 250$ °C. Similar decreasing micropore and increasing external surface area trends are shown for micropore and mesopores volumes, with V_{micro}/V_{meso} ratios between 0.07 and 1.21 for samples treated at temperatures > 250 °C.

Table B.1. t-plot analysis of sorption data for ZSM-5 samples either untreated or HLW treated at varying treatment temperatures and times

Sample Treatment	$S_{micro,t-plot}(m^2/g)$	$S_{ext,t-plot}(m^2/g)$	V_{micro} (t-plot) (cc/g)
Untreated	357	27.2	0.174
45 hr – 150 °C	367	33.1	0.179
188 hr – 150 °C	350	33.1	0.182
400 hr – 150 °C	330	38.8	0.174
635 hr – 150 °C	282	39.6	0.148
6 hr – 250 °C	314	21.5	0.164
12hr – 250 °C	303	30.6	0.164
48hr – 250 °C	348	22.2	0.165
72hr – 250 °C	368	22.6	0.177
150hr – 250 °C	344	30.1	0.167
280 hrs – 250 °C	333	59.9	0.184
3 hrs 300 °C	300	28.3	0.155
6hr – 300 °C	330	51.5	0.175
12hr – 300 °C	294	36.8	0.155
18hr – 300 °C	274	26.0	0.146
3 hr - 325C	254	33.6	0.127
6 hr – 325 °C	252	26.9	0.126
12 hr – 325 °C	235	37.1	0.108
18hr – 325 °C	94.7	47.9	0.060
3 hr – 350 C	177	42.4	0.102

|			
6hr – 350 °C	133	42.8	0.078
12 hr – 350 °C	58.0	31.6	0.039
18hr – 350 °C	47.6	31.7	0.030

B.3 Framework Degradation Rate Analysis

Previous transformations of temporal data for a first-order rate analysis was performed using the kinetic equation of the form:

$$\ln\left(\frac{CI(t)}{CI_0}\right) = -k_{app}\, t \qquad (1)$$

where CI/CI_0 is the crystallinity index obtained from XRD, t is the treatment time and k_{app} is the reaction rate constant for ZSM-5 degradation. The linearized first order degradation rate plot is included in **Figure B.2**
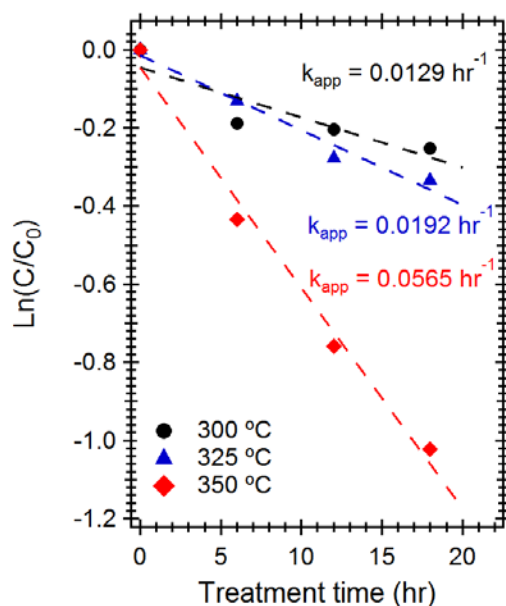

Figure B.2: First order rate plot of ZSM-5 degradation under HLW conditions (natural log of the relative retained crystallinity (CI/CI₀) versus time). Data points are denoted in the legend with their corresponding treatment temperatures.

256

A nonmonotonic temperature dependence on the decrystallization rate at treatment temperatures > 430 °C was attributed to unique thermochemical properties of water, including water's ionic product, on OH^- catalyzed framework desilication.

S.4 Arrhenius analysis on framework degradation

Estimating a first order framework degradation rate and normalizing the rate constant to the temperature dependent ionic product of water resulted in a linearized Arrhenius plot with a reasonable desilication activation energy of 144 kJ/mol, as shown in **Figure B.3.** Arrhenius analysis follows the same calculation method shown in Chapter 5.
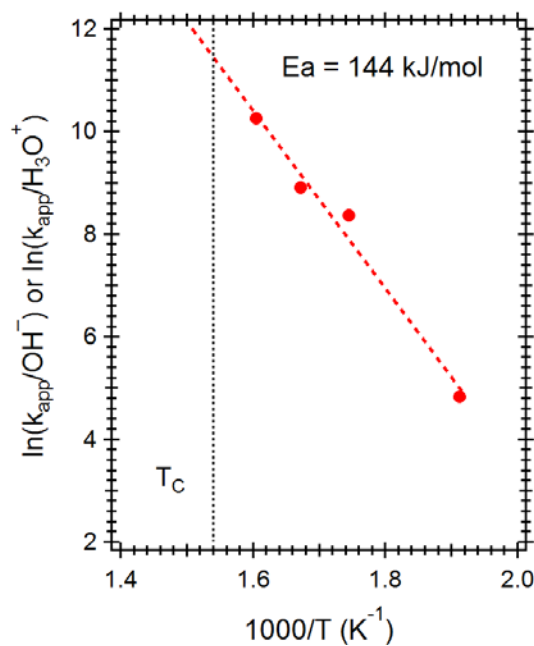
Figure B.3. Plots of ZSM-5 decrystallization rates assuming water as the sole source of OH^- or H^+ and accounting for the temperature dependence of K_W